Formation of supermassive black holes

Mélanie Habouzit

▶ **To cite this version:**

Mélanie Habouzit. Formation of supermassive black holes. Astrophysics [astro-ph]. Université Pierre et Marie Curie - Paris VI, 2016. English. NNT : 2016PA066360 . tel-01480290

HAL Id: tel-01480290
https://theses.hal.science/tel-01480290

Submitted on 1 Mar 2017

HAL is a multi-disciplinary open access archive for the deposit and dissemination of scientific research documents, whether they are published or not. The documents may come from teaching and research institutions in France or abroad, or from public or private research centers.

L'archive ouverte pluridisciplinaire **HAL**, est destinée au dépôt et à la diffusion de documents scientifiques de niveau recherche, publiés ou non, émanant des établissements d'enseignement et de recherche français ou étrangers, des laboratoires publics ou privés.

UPMC SORBONNE UNIVERSITÉS

IAP

THÈSE DE DOCTORAT
DE L'UNIVERSITÉ PIERRE ET MARIE CURIE

Spécialité Astrophysique

École Doctorale d'Astronomie & d'Astrophysique d'Ile-de-France

réalisée

à l'Institut d'Astrophysique de Paris

présentée par

Mélanie Habouzit

pour obtenir le grade de

DOCTEUR DE L'UNIVERSITÉ PIERRE ET MARIE CURIE

Sujet de la thèse :

Formation of supermassive black holes

soutenue le 15 septembre 2016

devant le jury composé de :

Benoit Semelin	Président du jury
Marta Volonteri	Directeur de thèse
Rachel Somerville	Rapporteur
Sadegh Khochfar	Rapporteur
Raffaella Schneider	Examinateur
Jenny Greene	Examinateur
Yohan Dubois	Examinateur

A mon petit Fanfan, mes parents et mes grand-parents.

Abstract

Supermassive black holes (BHs) harboured in the center of galaxies have been confirmed with the discovery of Sagittarius A* in the center of our galaxy, the Milky Way. Recent surveys indicate that BHs of millions of solar masses are common in most local galaxies, but also that some local galaxies could be lacking BHs (e.g. NGC 205, M33), or at least hosting low-mass BHs of few thousands solar masses. Conversely, massive BHs under their most luminous form are called quasars, and their luminosity can be up to hundred times the luminosity of an entire galaxy. We observe these quasars in the very early Universe, less than a billion years after the Big Bang, with masses as large as $10^8\,\mathrm{M}_\odot$ (Fan et al., 2006b ; Mortlock et al., 2011). BH formation models therefore need to explain both the low-mass BHs that are observed in low-mass galaxies today, but also the prodigious quasars we see in the early Universe. Several correlations between BH mass and galaxy properties have been derived empirically, such as the BH mass-velocity dispersion relation, they may be seen as evidence of BH and galaxy co-evolution through cosmic time. Moreover, BHs impact their host galaxies and vice versa. For example, BH growth is regulated by the ability of galaxies to funnel gas towards them, while BHs are thought to exert powerful feedback on their host galaxies. BHs are a key element of galaxy evolution, and therefore in order to study BH formation in the context of galaxy evolution, we have used cosmological hydrodynamical simulations. Cosmological simulations offer the advantage of following in time the evolution of galaxies, and the processes related to them, such as star formation, metal enrichment, feedback of supernovae and BHs.

BH formation is still puzzling today, and many questions need to be addressed: How are BHs created in the early Universe? What is their initial mass? How many BHs grow efficiently? What is the occurrence of BH formation in high redshift galaxies? What is the minimum galaxy mass to host a BH? Most of these questions are summarized in Fig 1, which represents a sample of local galaxies with their BHs, in blue points. The red shaded area represent the challenge of this thesis, which is to understand the assembly of BHs at high redshift and their properties. My PhD focuses on three main BH formation models. Massive first stars (PopIII stars) in mini-halos, at redshift $z = 20 - 30$ are predicted to collapse and form a BH retaining half the mass of the star, $\lesssim 10^2\,\mathrm{M}_\odot$ (Madau & Rees, 2001 ; Volonteri, Haardt & Madau, 2003). This is the *Pop III star remnants* model. *Compact stellar clusters* are also thought to be able to collapse and form a very massive star by stellar collisions, which can lead to the formation of a $\sim 10^3\,\mathrm{M}_\odot$ BH seed (Omukai, Schneider & Haiman, 2008 ; Devecchi & Volonteri, 2009 ; Regan & Haehnelt, 2009b). Finally, in the *direct collapse* model, metal-free halos, without efficient coolants (i.e. no metals, no molecular hydrogen), at $z = 10$ and later, can collapse and form a star-like supermassive object, which can collapse into a BH of $10^4 - 10^6\,\mathrm{M}_\odot$ (Bromm & Loeb, 2003 ; Spaans & Silk, 2006 ; Dijkstra et al., 2008).

As we will see in this thesis, we have investigated both the BH population in normal local galaxies, as well as the feasibility of BH formation model to explain the assembly of the high redshift quasar population. First of all, in order to fully understand the population of BHs we

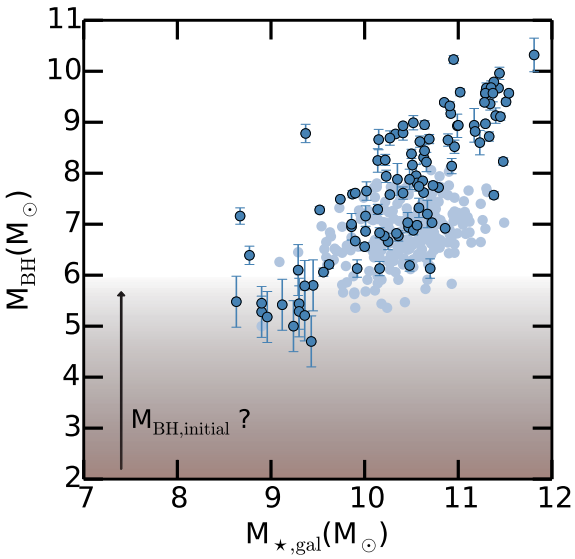

Fig. 1 – Sample of BHs in local galaxies in light and dark blue points. BH masses range from few $10^4\,M_\odot$ to $10^{10}\,M_\odot$. The shaded area represent the domain of BH mass at their formation time, in the early Universe.

observe in low-mass galaxies, we need a theoretical model able to predict the occupation fraction of BHs in low-mass galaxies, and the properties of both these BHs and their host galaxies. We have implemented a model accounting for the PopIII remnant and stellar cluster models, in the numerical code Ramses. We form BHs according to the theoretical models, and let these BHs evolve with time. So far, cosmological simulations were only used to reproduce the quasars luminosity function and study their feedback, simulations were therefore seeding BHs by placing a $10^5\,M_\odot$ BH in the center of massive galaxies. Our approach allows instead to study BH formation, and to cover the low-mass end of BHs. We then compare the simulated BHs to two different observational samples, local galaxies (Reines & Volonteri, 2015), and Lyman-Break Analogs (Jia et al., 2011a). Local low-mass galaxies are among the most pristine galaxies, because they have a quieter merger history. Therefore BHs in low-mass galaxies, are also thought to be pristine, and to not have evolved much from their birth, thus they can provide us precious clues on BH formation. Lyman-Break Analogs are galaxies very similar to their high redshift analogs, the Lyman-Break Galaxies, comparing our simulated samples to BHs found in these galaxies can therefore also provide us a promising new laboratory to study BHs in high redshift environment, but much closer to us.

The direct collapse model has been much studied recently, but there is no consensus on the number of BHs that form through this model yet. The number density of BHs, derived by different studies employing semi-analytic models (Dijkstra, Ferrara & Mesinger, 2014) or hybrid semi-analytic models (Agarwal et al., 2012, 2014) varies on several orders of magnitude. Hybrid semi-analytic models are very appealing because they use spatial information from cosmological simulations. However, only small simulated volumes allow one to achieve the high resolutions needed to resolve minihalos, and the early metal enrichment. These small boxes probe with difficulty the feasibility of the direct collapse BH formation model, lacking statistical validation. Instead, in this thesis, we chose to run simulations with different box sizes and resolutions, that allow us to test the impact of different processes such as metal enrichment and the impact of supernova feedback. The main advantage is also that employing large simulation boxes makes

possible to test different radiation intensity thresholds to destroy molecular hydrogen, which is of paramount importance for the direct collapse model.

Remerciements

Nous n'avons pas souvent l'occasion de remercier les personnes qui nous épaulent au quotidien, que ce soit professionnellement ou personnellement, ou bien même les deux. Sans elles, rien n'aurait été possible.

Mes premiers remerciements sont pour Marta, qui m'a fait partager son enthousiasme et sa soif de connaissance, merci pour sa patience et sa pédagogie, et pour m'avoir donné l'opportunité de travailler sur des projets passionnants. Nous avons cherché ensemble à répondre à quelques-unes des questions sur la formation et la croissance des trous noirs supermassifs, mais il en reste encore des milliers, et j'espère tout autant d'occasions de travailler de nouveau ensemble.
Deux autres chercheurs m'ont particulièrement apporté leur aide durant ma thèse. Je remercie Yohan Dubois pour sa disponibilité, pour m'avoir fait découvrir Ramses, et pour avoir répondu aux questions de physique, aussi bien qu'aux questions numériques que je me suis posée pendant ces trois années. Je remercie également Muhummad Latif pour m'avoir accompagnée sur les chemins sinueux du modèle *direct collapse* de formation des trous noirs, ainsi que pour sa disponibilité et ses conseils.
J'ai également une pensée pour les chercheurs avec qui j'ai débuté et qui m'ont toujours encouragée et apporté leur soutien, Claudia Maraston à Portsmouth (ICG), et bien sûr ici à Paris (IAP), Gary Mamon, Joseph Silk, et Sébastien Peirani. Je tiens également à remercier Jacques le Bourlot pour son soutien et tous les conseils judicieux qu'il a pu me donner.
Bien sûr ma thèse n'aurait pas été la même sans notre grande équipe, je remercie donc également Pedro Capelo, Andrea Negri, Salvatore Cielo et Alessandro Lupi pour le côté italien, Tilman Hartwig pour le côté allemand, et Rebekka Bieri pour le côté suisse de notre équipe.

Merci à Rachel Somerville et Sadegh Khochfar d'avoir accepté d'être les rapporteurs de ma thèse et d'avoir passé une partie de leurs vacances d'été à lire mon manuscrit, à Raffaella Schneider et Jenny Greene d'avoir accepté d'être examinatrices, et finalement Benoit Semelin d'avoir accepté de présider le jury de ma thèse. Ce sont des chercheurs exceptionnels et je suis vraiment fière qu'ils aient accepté de faire partie de mon jury de thèse, merci pour leur suggestions et remarques très constructives sur mon travail.

Pendant trois ans, j'ai eu la chance de travailler également au *Palais de la Découverte*, de donner des conférences le week-end, et d'écrire des articles pour la revue *Découverte* du musée. Je remercie Sébastien Fontaine de m'avoir donné cette chance. J'ai pu discuter avec le grand public des nombreuses grandes questions de l'astrophysique, m'émerveiller avec eux de toutes les réponses que nous avons déjà, rire avec toutes ces personnes de 7 à 77 ans qui viennent découvrir et apprendre au musée des sciences de Paris. Je ne peux ici pas citer toutes les personnes que je voudrais remercier, mais j'ai une pensée particulière pour Marc Goutaudier, Andy Richard, et Gaëlle Courty qui m'ont apporté une aide précieuse.

Evidemment je ne pourrais pas achever ma thèse sans remercier l'ensemble des doctorants, pour l'ambiance exceptionnelle qui règne à l'IAP. Je commencerais par les anciens, Alice (et sa joie de vivre communicative), Flavien (parce que nous avons découvert Cyclopatte ensemble), Thomas (qui partage un peu le même humour que moi), Vivien (pour le côté beau gosse de l'IAP), Nicolas (pour le côté plus que cool de l'IAP), Vincent (pour sa robe de chambre d'astrophysicien), Pierre (pour sa joie de vivre), Guillaume D. (pour sa bonne humeur et ses conseils sur les post-docs), Hayley (pour les "touffes" de galaxies), Guillaume P. et Manuel (pour leurs conseils sur la programmation). Ensuite les doctorants qui sont devenus docteur en même temps que moi, Julia, Alba, Rebekka, Laura (la plus sportive), Clotilde (pour son petit accent allemand quand elle parle en anglais), Jean-Baptiste (le seul homme de la promotion). Enfin tous les plus jeunes à qui je souhaite une très grande réussite, Tilman, Caterina, Federico, Nicolas, Erwan, Sébastien, Siwei, Céline, Jesse, Tanguy et Florian.

Je remercie particulièrement les drôles de dames du bureau 13. Il y aura eu un nombre absolument étourdissant de fous rires, de larmes, de moments de désespoir, de moments de joie, de danses, de chansons, et un mariage et demi. Ensemble nous avons vécu bien plus qu'une thèse. Je pense à Rebekka avec qui j'ai partagé tous les stressants meetings du mardi, avec qui nous avons écrit des équations ou des lignes de code Ramses sur un tableau noir, je la remercie pour tous ses encouragements dans les moments difficiles, et pour toute sa joie de vivre et sa folie (ce qui inclut des patches beauté dans le bureau, des siestes par terre, faire du yoga et manger des graines). Je remercie Alba et son sourire du Sud, son amour de la nourriture, je repense à toutes les fois où nous avons dîné ensemble (souvent gratuitement) le soir à l'IAP, sa connaissance de la grammaire française, des musées parisiens, son espoir de m'apprendre les verbes irréguliers en anglais ou m'apprendre à être plus positive. Et finalement Julia, que je connais depuis de très nombreuses années, et que j'adore depuis le premier jour pour son enthousiasme des travaux pratiques, et plus sérieusement pour son amitié, tous ses conseils, son soutien dans les moments difficiles, pour tous les potins que nous avons partagés (≈ 4000, à raison de deux par jour pendant 6 ans), et tout autant de fous rires.
Je remercie Clément pour tout le soutien qu'il m'a apporté durant ces trois années, et aussi pour toutes les fois où il a eu l'audace de me contredire, que ce soit pour la signification d'un poème de Baudelaire dans les jardins du Luxembourg, ou sur le fait que je pourrais ne pas avoir raison en toutes circonstances, ou encore sur le fait qu'il manquait quelque chose sur mes peintures, ou qu'il faille manger des légumes, ou ne pas inventer de nouveaux mots. Merci aussi pour toutes ses histoires abracadabrantes racontées au détour des ruelles de Paris une fois la nuit tombée, et pour son émerveillement de tout, de la philosophie aux documentaires Arte. Et aussi pour sa fascination des abeilles et des fourmis, et bien sûr sa joie de partager cela avec son entourage pendant les pauses café.
Merci également à Terry pour son soutien infaillible toutes ces années, spécialement dans les moments difficiles.

Pour finir, je suis infiniment reconnaissante à ma grande et belle famille de m'avoir accompagnée depuis toutes ces années, et particulièrement d'avoir fait le déplacement pour assister à ma soutenance de thèse. Il en faut de la patience pour attendre avec moi le passage des étoiles filantes, tous les ans, pendant les longues soirées d'été. Et du courage pour braver les obscurs chemins de la campagne pour tenter, enfin, d'observer la Voie Lactée. Du courage il en aura fallu aussi pour supporter la scientifique que je suis, les feuilles d'équations, de calculs, de schémas, les piles de livres à n'en plus finir, les longues soirées à réfléchir, et à garder la lumière allumée

une bonne partie de la nuit.

Je suis on ne peut plus reconnaissante à mes grand-parents de m'avoir offert mon petit lieu de paradis, où le chant des oiseaux se mêle aux parfums des fleurs du jardin, où l'on peut se réveiller à midi et déguster des crêpes pour le dessert, où l'on peut s'amuser en taillant les arbustes du jardin, ou en ramassant des pommes dans le verger. Il serait difficile de dire en quelques mots ici tout ce que je dois à mes parents, et à quel point je les remercie, tout leur amour et tout leur soutien depuis mon enfance sont, et seront toujours, une force indispensable. Et finalement je remercie mon petit Fanfan, qui a bien grandi, pour son intelligence, sa culture, ses blagues, ses fous rires du dimanche, sa bonne humeur, pour son soutien et ses conseils (on se demande parfois qui est le petit frère et qui est la grande soeur), et surtout notre amour partagé du gâteau aux petits-beurre.

Paris, septembre 2016.

Contents

Chapter 1

Introduction

In this chapter, after giving a brief introduction of the historical discoveries that lead us to our modern conception of the evolution of the Universe, we describe the formation and evolution of large-scale structures, from the collapse of dark matter halos to the formation of the first stars, and galaxies. Black holes (BHs) are a key component of galaxies today, most of the local galaxies indeed host a BH, including our Milky Way. The discovery of quasars, powered by massive BHs, indicates that they were already in place less than 1 Gyr after the Big Bang. Moreover, these BHs are also thought to play an important role in galaxy evolution, through powerful feedback processes. BHs are therefore a key ingredient of galaxy evolution. However, there is still no consensus on the formation of BHs. We describe the main theoretical scenarios of BH formation at the end of this chapter, and the main questions that still need to be investigated.

Contents

1.1 Brief historical introduction

The cosmological framework of galaxy formation and evolution, is the culmination of many discoveries over the last centuries. In this brief section, we review the most important developments in our knowledge of the Universe, and their implications.

Starting in 1771, the French observer Messier, referenced about 100 luminous objects in the sky (Messier, 1781), that were called *spiral nebulae*. One century later, these objects were still the purpose of intense investigations, Herschel published a new catalog of these objects in 1864 (Herschel, 1864), with this time more than 5000 objects. Their nature was, however, still debated at that time, between galactic objects (luminous clouds inside the Milky Way) or extragalactic sources, the well-known *island Universes* as called by the philosopher Kant one century before. The debate in 1920 between those in favor of island Universes, led by Curtis and the other led by Shapley, has became most famous, and is now referred to the *great debate*. The answer is given by Hubble (1925). Using Cepheid variables (standard candles to derive cosmological distances), he derived the distance to the Andromeda nebula, which appeared to be at a distance beyond the size of the Milky Way: nebulae are extra-galactic objects. This result has taken advantage of Leavitt's work (Leavitt, 1908), which established that Cepheids' period is related to their luminosity, with a catalog of 1777 variable stars in the Magellanic Clouds. The relation between Cepheids' period and their luminosity, allowed Hubble to estimate the distance to the Andromeda nebula. Advances in observational physics made us realize that the Milky Way is not a unique entity, but that there are thousands of similar galaxies around us in the Universe. In 1929, Hubble made a second unprecedented discovery: by spectral analysis, he realized that galaxies are redshifted, i.e. they are moving away from each other (Hubble, 1929). Recession velocities of galaxies are linearly related to their distances, which is now known as the *Hubble law*.

Theoretical physics was also experiencing a revolution at that time. In 1916, Einstein provided the mathematical framework of modern cosmology: *general relativity*. When the Universe was thought to be static, Einstein developed calculations concluding that the Universe was either expanding or contracting. This was also found by Friedmann (1922), and Lemaître (1927). The idea of an expanding Universe, where galaxies move away from each other, was already studied by Slipher in 1917 (he was observing nebulae that were receding with a given velocity, Slipher, 1917). Measurements of Slipher were actually used by Hubble (Hubble, 1929) and also by Lemaître (Lemaître, 1927) to conclude that the Universe was expanding.

In 1933, Zwicky advanced the idea of a missing mass in the Universe (Zwicky, 1933). This has been shown by measuring the orbital velocity of galaxies in galaxy clusters, and particularly in the Coma cluster, where the mass derived from the luminosity was a few hundred times lower than the mass derived from the orbital velocities. The fast orbital velocities could, however, be explained if a *dark matter* component was increasing the mass, and keeping the cluster as a bound object. The existence of dark matter has been also deduced from the velocity of stars in spiral galaxies, and gravitational lensing, for example.

Gamow and Alpher, in the 1940s [1], also bring further interesting elements of our modern picture of the Universe, with the idea that chemical elements were created (partly) in an early stage of the Universe history by thermonuclear reactions, through what we called the *nucleosynthesis*. This coincides with the discovery of thermonuclear reactions at that time. If the Universe is expanding, it should have been denser and hotter in the past, and this would have led to a residual heat, which could be visible today. In 1965, we have observed a background temperature

[1] The paper has been released on April, 1st, 1948, and is know as the alpha-beta-gamma paper.

of the Universe, of a few Kelvin, with a peak in the microwave wavelength, as predicted by Gamov. This cosmological microwave background is today referred to as CMB. During the 1950s and 1960s, the theory of *the Hot Big Bang model*[2], which relies on Gamov's idea that the Universe was expanding from a hotter and denser initial state, became commonly accepted by the community with the measurement of the CMB. Penzias & Wilson (1965), and Dicke et al. (1965) showed that the temperature of this relic of density perturbations in the cosmic field from the beginning of the Universe, is perfectly consistent with the Hot Big Bang model. Penzias & Wilson (1965) observed by chance the excess of temperature in the 4080 MHz antenna. This excess was looked for by Dicke and collaborators, and they finally observed it one year later (Dicke et al., 1965).
However, later on, between 1960s and 1970s, the model faced three problems, the non-uniform and isotropic distribution of matter, the flatness problem and the horizon problem, to which the Hot Big Bang theory has no solution. A major advance is the idea of Guth (1981), that these problems of the model can be solved by considering an accelerated period of the Universe. This early period of exponential expansion of the Universe, called *inflation*, is driven by the vacuum energy of some quantum field. The theory is slightly modified one year later by Linde (1982) and Albrecht & Steinhardt (1982), to fulfill all the conditions, such as homogeneity and isotropy, for example. In the 1980s, we also realized that the inflationary period could have generated density seed perturbations that could have lead to the formation of dark matter halos and galaxies.

With these discoveries, we have constructed a mathematical and cosmological framework, namely general relativity and the standard cosmological model, to study the history of the Universe. We have also realized that the Universe is not in a steady state, but exhibits temporal evolution, and is the result of a succession of several distinct periods. In the following we briefly recall the main ages of the Universe and their main characteristics.

Inflation 10^{-3} s. The Universe experiences an early period of expansion driven by the vacuum energy of some quantum field, that generates the seed density fluctuations.
Recombination 400,000 years ($z = 1100$). So far, electrons were interacting with photons through Thomson scattering, this couples matter and radiation. The Universe expands, and so become cooler, down to 3000 K, where electrons and atomic nuclei combined to form neutral atoms. Photons stop being in thermal equilibrium with matter, photons stop interacting with matter, and thus the Universe becomes transparent. Microwave background is produced at that time.
Dark ages 400,000 years - 150 Myr ($z \approx 1100 - 20$). This period consist on the transition period between the recombination and the formation of the first light in the Universe.
Reionization 150 Myr - 1 Gyr ($z \approx 20 - 6$). The first stars (first generation of stars) start to form, and to emit ionizing radiation that will reionize the Universe. Stars emit ionizing radiation in HII regions, which will expand individually until they overlap, and fully ionized the Universe. Powerful sources, such as quasars, are thought to also play a role in the reionization process.
Galaxy formation and evolution 150 Myr - 10 Gyr ($z \approx 20 - 0$). The Universe globally expands, but small pockets, denser than the background field, can slow the expansion down, and turn it around, to become even denser and collapse due to their own gravity, forming galaxies.
Present time Astrophysicists trying to figure out, to capture, what was the previous epochs features, and how our Universe evolve until today.
In this thesis, we focus on the time after the "dark ages" and before the peak of galaxy formation.

[2]Big Bang is the name that was given to this theory, mockingly, by Fred Hoyle.

1.2 Structure formation in a homogeneous Universe

1.2.1 The homogeneous Universe

Cosmology gives us a framework to work with, but also initial conditions for the formation of the first objects in the Universe, among which, galaxies, stars, black holes. Everything starts with the observation that on large scales, the Universe can be spatially considered as homogeneous (which means invariance by translation) and isotropic (meaning invariance in rotation), this is known as the *cosmological principle*. The properties of a homogeneous and isotropic Universe are described by the space-time metric (the most common being the *Robertson-Walker metric* or *Friedmann-Lemaître-Robertson-Walker metric*), which can be written as:

$$ds^2 = (c\,dt)^2 - a(t)^2 \left[\frac{dr^2}{1-Kr^2} + r^2\left(d\theta^2 + sin^2\theta\, d\phi^2\right)\right], \tag{1.1}$$

with c the speed of light, ds the space-time interval, (r,θ,ϕ) the comoving coordinates of an observer, t the proper time, $a(t)$ a cosmological time-dependent scale factor, K the curvature. K is a constant, which can be equal to -1 (open or hyperbolic geometry), 0 (flat geometry) or 1 (closed or spherical geometry). The time-dependence of the scale factor a is derived in general relativity from the metric and the equation of state for the matter content of our Universe. For the time-time component[3]:

$$\frac{\ddot{a}(t)}{a(t)} = -\frac{4\pi G}{3}\,(\rho + 3p) + \frac{\Lambda}{3}, \tag{1.2}$$

and for the space-space component:

$$\left(\frac{\dot{a}(t)}{a(t)}\right)^2 = \frac{8\pi G}{3}\rho - \frac{\mathrm{K}}{a(t)^2} + \frac{\Lambda}{3}, \tag{1.3}$$

with Λ the dark energy constant, ρ the energy density, and p the pressure. These two equations are known as Friedmann's equations. An expanding Universe is characterized by $\dot{a} > 0$, a collapsing Universe by $\dot{a} < 0$, and a static Universe by $\dot{a} = 0$. To close this system of equations, one needs to choose an equation of state, which connects the pressure p and density ρ, and therefore gives the energy content of the Universe (e.g., radiation or matter-dominated era). The equation of state depends on the different phases of our Universe, but always follows a single barotropic fluid equation $p = w\,\rho$, with w a constant.

In the very early stage, the Universe is in a radiation phase (also referred as relativistic matter), the equation of state is $p = \rho/3$, therefore the energy density scales with a^{-4}, and the scale factor $a(t)$ with $t^{1/2}$.
The Universe expands and enters a second phase, the matter-dominated phase, where $p = 0$, the energy density decreases, and now scales with a^{-3}.
For the vacuum energy $p = -\rho$, therefore ρ and H are constant, and $a(t) \propto e^{H(t)\times t}$.

The Hubble parameter is defined as the rate of change of the proper distance between two fundamental observers at a given time t, in other words $H(t)$ measures the rate of expansion, and can be expressed as:

$$H(t) = \frac{\dot{a}(t)}{a(t)}. \tag{1.4}$$

[3]The Friedmann's equation can be deduced from the time-time (or 0-0) component of Einstein's equation $R_{\nu\mu} - (1/2)g_{\nu\mu}R + \Lambda g_{\nu\mu} = T_{\nu\mu}$, where $R_{\nu\mu}$ is the Ricci tensor, R the Ricci scalar, $g_{\nu\mu}$ the metric tensor. One can also deduce the three space-space components. Off-diagonal components are equal to zero.

The scale factor is normalized to unity at the present day t_0, $a(t_0) = 1$. It is more convenient to express the equations as a function of the cosmological redshift $z(t)$ (that we measure today, at the given time t). Because the Universe is expanding, the photons which are emitted at a wavelength λ are observed today at a redshifted wavelength $\lambda_{\rm obs} = \lambda \times \dfrac{a(t_0)}{a(t)}$. The cosmological redshift is directly related to the scale factor by:

$$1 + z(t) \equiv \frac{\lambda_{\rm obs}}{\lambda} = \frac{a(t_0)}{a(t)}. \tag{1.5}$$

We call $\rho_{\rm c}$ the critical density:

$$\rho_{\rm c}(t) = \frac{3H^2(t)}{8\pi G}, \tag{1.6}$$

which is the density of the Universe considering that its spatial geometry is flat. Therefore, we define the dimensionless density parameters, the non-relativistic matter (dark matter and baryons) density parameter $\Omega_{\rm m}$, the dark energy density parameter Ω_Λ (vacuum energy, or cosmological constant Λ), the relativistic matter density parameter $\Omega_{\rm r}$ (such as photons, known as radiation component), as follows:

$$\Omega_{\rm m} = \frac{\rho_{\rm m}(t)}{\rho_{\rm c}(t)} = \frac{8\pi G\rho_{\rm m}}{3H^2(t)} \tag{1.7}$$

$$\Omega_\Lambda = \frac{\rho_\Lambda(t)}{\rho_{\rm c}(t)} = \frac{\Lambda(t)}{8\pi G\rho_{\rm c}(t)} = \frac{\Lambda}{3H^2(t)} \tag{1.8}$$

$$\Omega_{\rm k} = \frac{\rho_{\rm k}(t)}{\rho_{\rm c}(t)} = -\frac{Kc^2}{a^2(t)H^2(t)} \tag{1.9}$$

$$\Omega_{\rm r} = \frac{\rho_{\rm r}(t)}{\rho_{\rm c}(t)} = \frac{8\pi G\rho_{\rm r}}{3H^2(t)} \tag{1.10}$$

where we have the constraint $1 = \Omega_{\rm m,0} + \Omega_{\Lambda,0} + \Omega_{\rm k,0} + \Omega_{\rm r,0}$.

We can now express the second Friedmann's equation, which gives the evolution of the expansion rate H(t), as a function of the cosmological redshift and the dimensionless density parameters:

$$H(z) = \frac{\dot{a}(z)}{a(z)} = H_0 \times E(z) = H_0 \times \sqrt{\Omega_{\rm r,0} \times (1+z)^4 + \Omega_{\rm m,0} \times (1+z)^3 + \Omega_{\rm k,0} \times (1+z)^2 + \Omega_{\Lambda,0}}. \tag{1.11}$$

To solve $a(t)$, one must know H_0, and the mass content of the Universe today, through the dimensionless density parameters $\Omega_{\rm r,0}$, $\Omega_{\rm m,0}$, and $\Omega_{\Lambda,0}$ at time t_0.

Hubble constant H_0, and cosmological parameters

Determining the cosmological parameters relies on measuring the geometrical properties of the Universe. The redshift-distance relation in our Universe, which links the galaxy recession speed to the distance of the galaxy from an observer, is expressed by:

$$d(z) = \frac{c\,z}{H_0}\left[1 + F(z, \Omega_{\rm i,0})\right] \tag{1.12}$$

where F represents the second order of d and depends on the cosmological parameters. d can represent the luminous distance $d_{\rm L}$, where the luminosity L of an object is related to its flux f and luminosity distance by $L = 4\pi d_{\rm L}^2 f$. It can also represent the angular diameter $d_{\rm A}$, where the physical size of an object D is related to its angular size θ by $D = d_{\rm A}\theta$.

At $z << 1$, the distance-redshift relation can be written as $d(z) = cz/H_0$ (*Hubble expansion law*). The Hubble constant can therefore be obtained by measuring both the distance of an object and its redshift (through $\lambda_{\rm obs}/\lambda$, that we obtain from the object spectra). For $z \geqslant 1$, one needs to use the second order of the distance-redshift relation, with the function F (Eq. 1.12), depending on the other cosmological parameters.
Cosmological parameters have been obtained by measuring the light curves of type Ia SNe in distant galaxies (Perlmutter et al., 1999), or by measuring the angular spectrum of the CMB temperature fluctuations. The *Planck* mission has made large progress in the determination of these parameters (from Table 4., last column of Ade et al., 2015, corresponding to TT,T,EE+low P+lensing+ext, 68% limit):

- $H_0 = 67.74 \pm 0.46$
- $\Omega_{\rm m,0} h^2 = 0.14170 \pm 0.00097$
- $\Omega_{\rm m,0} = 0.3089 \pm 0.0062$
- $\Omega_{\rm b,0} h^2 = 0.02230 \pm 0.00014$
- $\Omega_{\lambda,0} = 0.6911 \pm 0.0062$
- $\Omega_{\rm r,0} = 10^{-5}$
- $\Omega_{\rm k,0} = 0.000 \pm 0.005$ (95%, Planck TT+lowP+lensing+BAO)

Mass content of the Universe
From the CMB measurement, the baryonic component represents $\sim 15 - 20\%$ of the total matter content of the Universe. Matter is mostly dominated by dark matter. The total matter component $\Omega_{\rm m,0} \sim 0.3$ ($\sim 30\%$) is supported by many other measurements, such as cosmic shear, the abundance of massive clusters, large-scale structure, peculiar velocity field of galaxies. This is also in agreement with independent constraints from nucleosynthesis, and the abundance of primordial elements. All of this leads us with the idea that $\sim 70\%$ of the mass-energy of the Universe is composed of dark energy. This dark energy component is still an open question of modern cosmology, as well as dark matter. One of the model used to model dark energy is the cosmological constant Λ, which leaves us with the cosmological model ΛCDM.

1.2.2 Linear growth of perturbations and spherical collapse model

The Universe is composed of large structures, dark matter halos, and galaxies. However, the cosmological principle predicts an uniform and isotropic distribution of matter in the Universe. If so, no structure formation can happen. Therefore, in order to form large scale structures, one needs to introduce fluctuations in the history of the Universe. The Hot Big Bang theory has no explanation for the non-uniform and isotropic distribution of matter, and it is one of the so-called *problems* of this theory (the two others being the flatness problem and the horizon problem). The standard description of the Universe, driven by general relativity, is expected to break down when the Universe is so dense that quantum effects may be more than important to consider.
Inflation has been considered to be a natural physical process solving Hot Big Bang theory's problems. The first model of inflation is introduced in 1981 by Guth (1981). In addition to solve the Hot Big Bang problems, this accelerated period of our Universe allows the introduction of these quantum processes, which can produce the necessary spectrum of primordial density perturbations, that *gravitational instability* accentuates to produce the large structures we observe today, namely dark matter halos, clusters of galaxies and galaxies. Structure seeds or overdensities

will grow with time, the overdense regions will attract their surroundings and become even more overdense. Conversely, the underdense regions will become even more underdense because matter in these regions flows away from them, leading to the formation of voids.
In the following, we describe the growth of the density perturbations.

Growth of density perturbations
The density contrast $\delta(x,t)$ can be expressed as a function of the local density $\rho(x,t)$, and the background density of the Universe $\bar{\rho}(t)$ (which is equal to the previous $\rho_{\rm m}(t)$). $\delta(x,t)$ measures the deviation from a homogeneous Universe (for which $\delta(x,t)=0$):

$$\delta(x,t) = \frac{\rho(x,t) - \bar{\rho}(t)}{\bar{\rho}(t)}. \tag{1.13}$$

The density field $\delta(x,t)$ can also be expressed in the Fourier space, by:

$$\delta(k,t) = \frac{1}{(2\pi)^2} \int dx e^{-ik.x} \delta(x,t). \tag{1.14}$$

Statistical properties of the density field are described by the power spectrum $P(k,t)$, which is the Fourier transform of the two-point correlation function:

$$P(k,t) = \langle |\delta(k,t)|^2 \rangle. \tag{1.15}$$

The perturbative density field is predicted to be Gaussian, which is consistent with the measurement from the CMB (Planck Collaboration et al., 2015a). A discussion on the possible existence of non-Gaussian primordial density fluctuations at small scale, and the consequences for the assembly of dark matter and galaxies, is carried in chapter 5. The simplest initial power spectrum is the Harrison-Zeldovich spectrum (Peebles & Yu, 1970 ; Harrison, 1970 ; Zeldovich, 1972) (or scale-invariant power spectrum), defined by $P(k, t_{\rm initial}) \propto k^{n_{\rm s}}$, with the spectral index $n_{\rm s} = 1$ ("scale free")[4], is in good agreement with the CMB measurements. This initial spectrum evolves with time. We usually express the evolution with a transfer function $T(k)$, which encodes the Universe geometry and the nature of matter (for example, the type of dark matter particles), to obtain $P(k,t) = T^2(k,t) \times P(k, t_{\rm initial})$.

To describe the evolution of perturbations, we use the ideal fluid description in the Newtonian theory. Baryons can be described by an ideal fluid, because collisions between particles are frequent, which leads to the establishment of local thermal equilibrium. (If we consider density fluctuations on characteristic length scales smaller than the Hubble length c/H, and weak gravitational field). The evolution of an ideal fluid in the Newtonian theory, is given by the 3 following equations (equation of continuity, Euler's equation, and Poisson's equation), which can be rewritten to take into account the expansion of the Universe. Because the Universe is expanding we move from proper distance $x_{\rm proper}$ to comoving distance x, by taking $x_{\rm proper} = a(t)x$. The proper velocity is expressed as $v_{\rm proper} = \dot{a}(t)x + a(t)\dot{x} = \dot{a}(t)x + v$ with $\dot{a}(t)x$ the Hubble velocity, and v the peculiar velocity (which describes the movement of the fluid with respect to a fundamental observer), that is used in the following 3 equations:

$$\text{Equation of continuity:} \qquad \dot{\delta} + \frac{1}{a}\nabla.(1+\delta)v = 0 \tag{1.16}$$

[4]Power spectrum with $n_{\rm s} > 1$ as refereed to as "red tilt" (more power on small scales), whereas those with $n_{\rm s} < 1$ as "blue tilt" (less power on small scales).

$$\text{Euler's equation:} \qquad \dot{v} + \frac{1}{a}(v.\nabla)v + \frac{\dot{a}}{a}v = -\frac{1}{a}\nabla\Phi \tag{1.17}$$

$$\text{Poisson's equation:} \qquad \nabla^2\Phi = 4\pi G\bar{\rho}\delta a^2. \tag{1.18}$$

The density perturbations grow by self-gravity, if these perturbations stay small, we can model their growth in the linear perturbation regime ($\delta << 1$). From the 3 equations above, we obtain the equation describing the growth of perturbations [5]:

$$\ddot{\delta} + 2\frac{\dot{a}}{a}\dot{\delta} = 4\pi G\bar{\rho}\delta. \tag{1.19}$$

The evolution of perturbations in the density field depends on the phases of the Universe. For the radiation phase, the solution of the equation of perturbation growth is $\delta(x,t) = A(x)\ln(t) + B(x)$. Perturbations grow very slowly during that phase of the Universe, they will really grow during the matter-dominated phase. For the matter-dominated phase, the solution is $\delta(x,t) = A(x)t^{2/3} + B(x)t^{-1}$. The first term indicates that perturbations grow with time, with the expansion of the Universe, whereas the second term is a decaying term, which is generally not considered because it vanishes with time. Finally, today the perturbations are not growing anymore, the solution can be expressed by $\delta(x,t) = A(x) + B(x)\mathrm{e}^{-2\mathrm{H}\times\mathrm{t}}$.

Spherical collapse

As we just said, at the early stage, when perturbations are still in a linear regime ($\delta << 1$), the overdense regions expand with the expansion of the Universe. At some point, when $\delta \sim 1$, the perturbations segregate from the expansion of the Universe, and over dense regions start to collapse. This phase is referred to as the *turn-around*, the regime becomes strongly non-linear. The growth of perturbations can not be treated anymore in the linear perturbation regime. This leads to an increase of δ, the overdense regions will attract their surroundings and become even more overdense, and will inevitably collapse under their own density due to gravity. The evolution of these overdense regions is independent of the global background evolution of the Universe; they can therefore be seen as small Universes, denser than the background density $\bar{\rho}$, that collapse. To treat them we use the spherical collapse model. It assumes that the overdensity inside a sphere of radius r, is homogeneous, and describes the evolution of the radius as a function of time. The sphere is supposed composed of matter shells, which do not cross.

The newtonian equation describes the evolution of a mass shell in a spherically symmetric density perturbation:

$$\frac{d^2r}{dt^2} = -\frac{G\mathrm{M}}{r^2} \tag{1.20}$$

where M is the mass within the shell, and is constant, and r is the radius of the shell. Because M is constant and so independent of t (before shell crossing), we can integrate the previous equation:

$$\frac{1}{2}\left(\frac{dr}{dt}\right)^2 - \frac{G\mathrm{M}}{r} = E \tag{1.21}$$

[5] Here, we have used the simple form of the Euler equation, we have neglected the pressure term $-\frac{\nabla p}{a\rho(1+\delta)}$ that can be added on the right side of the equation. Without neglecting the pressure term, Eq. 1.18 will have the additional terms $\frac{c_\mathrm{s}^2}{a^2}\nabla^2\delta$ and $\frac{2\bar{T}}{3a^2}\nabla^2 S$, where c_s is the sound speed, $\bar{T}$ the mean temperature background, and S the entropy.

with E the specific energy of the shell. One can solve the equation for the different values of E, $E = 0$, $E > 0$ or $E < 0$. We focus on the last case, which corresponds to the collapse case. The motion of the shell is described by the system:

$$r = A(1 - \cos(\theta)) \quad \text{and} \quad t = B(\theta - \sin(\theta)). \tag{1.22}$$

Parameters A and B can be expressed as a function of r_i, t_i, the density contrast δ_i, and the density parameter of the overdense region Ω_i. Therefore the motion of the mass shell is entirely described by r and t, and the initial conditions on the radius r of the shell, and the mean overdensity enclosed in it. We can therefore compute the maximum expansion of the shell, for $\theta = \pi$, which corresponds to $r_\mathrm{max} = 2A$, and $t_\mathrm{max} = \pi B$. After that, the mass shell turns around and starts to collapse, the mass shell can cross the other mass shells that were initially inside it. By the time $t_\mathrm{col} = 2t_\mathrm{max}$, all the mass shells have crossed each other many times, and have formed an extended quasi-static virialized halo. The time of virialization is the time at which the virial theorem is satisfied, so when the spherical region has collapsed to half its maximum radius, thus $t_\mathrm{col} = t_\mathrm{vir}$ here.
From this theory, it is possible to estimate the density contrast at which the turnaround happens, namely $\delta = 1.06$, and at which the collapse happens, $\delta = 1.69$. Therefore the global picture is the following, when the density contrast of a perturbation exceeds unity, it turns, and starts to collapse when it reaches $\delta = 1.69$.

Virialization of halos
The collapse does not go to a singular point, but it is halted before reaching that stage, by what we call the *virialization*. Because dark matter is composed by collisionless, non or weakly interacting particles, it can not release the gravitational potential energy through radiation or shocks, therefore the virial theorem tells us that this energy is converted into a kinetic energy for the particles. Eventually the other particles will exchange with DM particles this kinetic energy, by relaxation processes, leading to a pressure supported *virialized* halo where finally particles will reach an equilibrium state. The overdensity at the virialization time can be derived from the theory, $\delta(t_\mathrm{vir}) = 178$ (here we have assumed $\Omega_{\mathrm{m},0} = 1$, otherwise we would have a weak dependence on the density parameters).

1.3 Formation of galaxies and first stars

As we have seen, baryons only represent a small fraction of the matter density in the Universe, but are present in all the structures we observe today. Therefore it is also important to treat the evolution of perturbations in the baryonic fluid, still in the Newtonian regime. Compared to the dark matter (DM) growth of perturbations, the perturbation growth in the baryonic fluid equation is slightly different, because a term $\nabla P/\rho$ corresponding to the pressure support is added in the Euler's equation. The equation of perturbations growth for the baryonic fluid is now expressed by:

$$\ddot{\delta_\mathrm{B}} + 2\frac{\dot{a}}{a}\dot{\delta_\mathrm{B}} + \left(\frac{k^2 c_s^2}{a^2} - 4\pi G\bar{\rho}_\mathrm{B}\right)\delta_\mathrm{B} = 4\pi G\bar{\rho}_\mathrm{DM}\delta_\mathrm{DM}. \tag{1.23}$$

The differences with Eq. 1.19, is that now we have two terms coming from baryonic and dark matter gravitational potential (terms $4\pi G\bar{\rho_\mathrm{B}}\delta_\mathrm{B}$, and $4\pi G\rho\bar{_\mathrm{DM}}\delta_\mathrm{DM}$), and a term $\dfrac{k^2 c_s^2}{a^2}$ from the pressure gradient of the baryonic fluid. From this equation, one can define a characteristic scale,

the Jeans wave number $k_{\rm J}$:

$$k_{\rm J} = \sqrt{\frac{4\pi G\bar{\rho_{\rm B}}}{c_{\rm s}^2}}, \tag{1.24}$$

which is associated with the *Jeans length*, defined as $\lambda_{\rm J} = (2\pi/k_{\rm J})a(t)$:

$$\lambda_{\rm J} = \sqrt{\frac{\pi c_s^2}{G\bar{\rho}}}. \tag{1.25}$$

Perturbations with a physical length larger than the Jeans length ($\frac{2\pi}{k}a(t) > \lambda_{\rm J}$) can grow, whereas perturbation modes with a smaller physical length ($\frac{2\pi}{k}a(t) < \lambda_{\rm J}$) can not.
Here again, the evolution of perturbations in the density field, depends on the Universe history epochs. In the radiation-dominated phase, DM perturbations are growing logarithmically, the evolution is dictated by the term due to expansion $2\frac{\dot{a}}{a}\dot{\delta}$ (damping term), which dominates over the gravitational potential term. However, the baryonic fluid is affected by the pressure gradient. Pressure support prevents the growth of baryonic perturbations. After the matter-radiation decoupling time (recombination), baryonic perturbations can grow, and closely follow the growth of DM perturbations.
From this, we see that baryonic perturbations follow the perturbations of the DM fluid. Without DM, the baryonic perturbations would still be in the linear regime today, making the assembly of galaxies difficult.
A characteristic mass, the *Jeans mass*, can be defined as the amount of baryonic mass within a sphere a radius $\lambda_{\rm J}/2$ (the Jeans scale length is used as a characteristic diameter of the sphere):

$$\mathrm{M_J} = \frac{4\pi}{3}\left(\frac{\lambda_{\rm J}}{2}\right)^3 \bar{\rho}. \tag{1.26}$$

The Jeans mass is of order $10^{16}\,\mathrm{M_\odot}$ during the radiation dominated phase, which roughly correspond to galaxy clusters scale. But after matter-radiation decoupling, there is no more presure support provided by photons, the baryonic gas only resists gravity by its normal gas pressure, and therefore the pressure drops significantly, the Jeans mass drops to the scale of globular cluster mass, with $\mathrm{M_J} \sim 10^5\,\mathrm{M_\odot}$.

In order to form galaxies, we often refer to two different stages: the assembly of mass, and the formation of stars. The assembly of mass is a long process, cold gas falls into potential well of dark matter fluctuations, increases the local density, which leads to the formation of molecular hydrogen. H_2 will lead to the cooling of dense regions, then will condense and fragment. Molecular gas cloud fragmentation allows the conversion of gas into stars.
In the very early Universe, in the absence of any heavy element (metals, which are created by stellar processes), atomic and molecular hydrogen are the only coolants. At temperatures $\mathrm{T_{vir}} < 10^4\,\mathrm{K}$, the cooling is done by radiative transitions of H_2, which can cool the gas down to a few hundred kelvin. Contrary to H, the excitation temperature of H_2 is sufficiently low (low energy levels). When $\mathrm{T_{vir}} > 10^4\,\mathrm{K}$, H is able to cool the gas.
Tegmark et al. (1997) compute the necessary molecular hydrogen abundance for a halo to collapse, by computing the abundance needed to have a cooling time smaller than the Hubble time. Molecular hydrogen form through two channels, the first one is based on H^- ion, the second one on H_2^+.
Channel H^-:

$$\mathrm{H} + \mathrm{e}^- \rightarrow \mathrm{H}^- + \mathrm{h}\nu$$

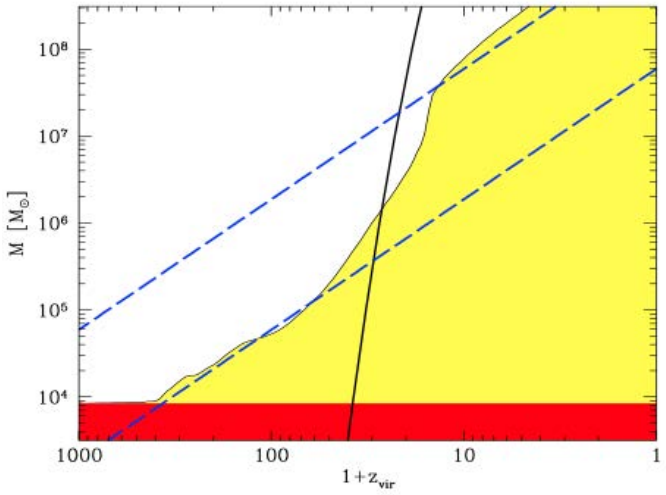

Fig. 1.1 – Mass needed to collapse and form luminous objects at a given virialization redshift (Tegmark et al., 1997). Only clumps whose parameters ($z_{\rm vir}$,M) lie above the shaded area can collapse and form luminous objects. The dashed straight lines corresponding to $T_{\rm vir} = 10^4$ K and $T_{\rm vir} = 10^3$ K are shown for comparisons. The dark-shaded region is that in which no radiative cooling mechanism whatsoever could help collapse, since $T_{\rm vir}$ would be lower than the CMB temperature. The solid line corresponds to a 3-σ peak in standard CDM model.

$$\mathrm{H^+ + H^- \rightarrow H_2 + e^-}$$

$$\mathrm{H^- + h\nu_{CMB} \rightarrow H + e^-} \text{ (destruction of } \mathrm{H^-} \text{ by CMB photons)}$$

Channel $\mathrm{H_2^+}$:

$$\mathrm{H^+ + H \rightarrow H_2^+ + h\nu}$$

$$\mathrm{H_2^+ + H \rightarrow H_2 + H^+}$$

$$\mathrm{H_2^+ + h\nu \rightarrow H + H^+} \text{ (photodissociation).}$$

The channel based on $\mathrm{H_2^+}$ is efficient for $100 < z < 500$. Conversely, at $z < 100$, $\mathrm{H_2}$ is mostly produced by the $\mathrm{H^-}$ mechanism. Indeed the last reaction which represents the destruction of $\mathrm{H^-}$ by CMB photons is not predominant, because photodetachment of $\mathrm{H^-}$ becomes inefficient due to the decline of the cosmic background radiation.
Based on the 2 mechanisms $\mathrm{H^-}$ and $\mathrm{H_2^+}$, Tegmark et al. (1997) show that the $\mathrm{H_2}$ abundance needed for a halo to collapse is 5×10^{-4}, which only differs slighty with the redshift of virialization (in the range $100 > z_{\rm vir} > 25$). These results are encoded in Fig. 1.1, only halos in the non-shaded region can collapse at a given corresponding virialization redshift. In this region, the virial temperature is sufficiently high that enough $\mathrm{H_2}$ form for the cooling time to be smaller than the Hubble time. Halos can cool, and collapse. However, in the red shaded area, there is no radiative cooling mechanism to help the collapse, the temperature there is indeed smaller than the CMB temperature. Finally, at $z_{\rm vir} \sim 30$, only halos more massive than $10^5\,\mathrm{M_\odot}$ are able to collapse, and to form luminous objects.

We also mention here, that at high enough densities, of around $10^8 - 10^9\,\mathrm{cm}^{-3}$, the formation of H_2 by 3-body reactions (Palla, Salpeter & Stahler, 1983) becomes significant:

$$H + H + H \rightarrow H_2 + H,$$

$$H + H + H_2 \rightarrow H_2 + H_2,$$

$$H + H + H_e \rightarrow H_2 + H_e.$$

At this stage of the gas collapse, most of the hydrogen is converted into H_2, but this does not increase the cooling of the gas, because the binding energy of every H_2 molecule that forms (4.48 eV) is converted in thermal energy, that contributes to heat the gas.

The first generation of stars , the so-called population "PopIII", is predicted to form in $10^5\,M_\odot$ halos, often referred as "mini-halos". With H_2 cooling, primordial star-forming clouds of $\sim 1000\,M_\odot$ collapse until a quasi-hydrostatic protostellar core of around $\sim 0.01\,M_\odot$ forms in the inner part of these clouds (Yoshida, Omukai & Hernquist, 2008).
The question of the initial mass function of the PopIII stars is still discussed today. The number of star(s) which form in mini-halos, and the initial mass of stars, are among of the most challenging issues. This field of research has been investigated with simulations over the last decade. Several numerical works have followed protostellar formation process (Abel, Bryan & Norman, 2002 ; Yoshida, Omukai & Hernquist, 2008 ; Greif et al., 2012). On the number of stars per halos, Greif et al. (2012) ; Latif et al. (2013b), recently showed that the protostellar disks can fragment into several gas clumps, each being able to form star. The final halo could therefore host more than one single star. Small traces of metals can also lead to forming several stars in the same clump because of first dust cooling (Schneider et al., 2002 ; Omukai et al., 2005 ; Schneider et al., 2006a), therefore decreasing individual star mass.
Assuming a single star per halo, Hirano et al. (2014) derive the initial mass function of primordial stars by simulating 110 halos. They first use SPH simulations to study the formation in primordial clouds in the central part of halos, that range in $M_{vir} = 10^5 - 10^6\,M_\odot$ for $z = 35 - 11$. Radiative hydrodynamical simulations are used to follow the accretion phase of protostars. They find that PopIII star masses could range from ~ 10 to $\sim 1000\,M_\odot$ (this can be seen as an upper limit on the mass, because they assume that only one star forms in each halo). The mass of PopIII stars is also dictated by their radiative feedback into their surrounding gas, it can halt the accretion into the stars, and therefore regulating their growth (Bromm, 2013 ; Greif, 2015).

In the standard ΛCDM model, the first "galaxies" form after the first generation of stars. Mini-halos, which host the first PopIII stars, may indeed not be massive enough to retain the gas pushed away by the first SNe, through mechanical feedback (shock waves from SN). Potential wells may also not be deep enough to retain the gas heated by SN (thermal feedback of SN) and stellar feedback, such as photoionization by stellar radiation. This depletion of gas in mini-halos can devoid them of gas, and consequently can prevent and delay the next episode of star formation for a long time of few 10^7 years.
Therefore the formation of the first stars has a non-negligible impact on the Universe through different processes, which affect more than their own dark matter halos. First of all, they emit UV radiation, which can dissociate molecular hydrogen, and therefore delay star formation in neighboring halos. Second, these stars will produce and release metals in their surrounding,

therefore enriching the intergalactic medium with metals. Star and BH formation will be strongly affected by the feedback from this first population of stars, we discuss the consequences of these two particular feedback processes on the formation of BHs in section 1.7.
Once gas is able to cool again, it collapses in the potential wells of halos, which have by that time, grown in mass through accretion and mergers, to $10^8\,M_\odot$. Because mini-halos are the progenitors of these massive halos, the gas is normally metal-enriched by the first population of stars, and therefore can cool even more efficiently to lower temperatures to form lower mass stars, that constitute the second generation of stars, called PopII stars.

Early metal-enrichment of the medium due to PopIII stars has been discussed in the literature (Yoshida, Bromm & Hernquist, 2004 ; Tornatore, Ferrara & Schneider, 2007 ; Greif et al., 2008), but it is generally assumed that the first galaxies are the main drivers of metal-enrichment. Radiation from the first stars, and galaxies, is also among the most commonly assumed source of radiation for the reionization of the Universe. High redshift galaxies are indeed thought to be the most important contributors of ionizing photons (Robertson et al., 2010, 2013). It is worth mentioning here, that thanks to improvements in observations, the next generation of telescopes will help us to push further our understanding of high-redshift galaxies, and their consequences on the Universe evolution. So far, we have been able to observe high redshift galaxies in the range $6 < z < 10$ (Bouwens & Illingworth, 2006 ; Bouwens et al., 2015), when the Universe was less than a 1 Gyr old. James Webb Space Telescope (JWST) will open a new window on cosmic reionization, it will help us to better constrain the contribution of high redshift galaxies, in terms of the evolution of ionizing photons emitted by galaxies at $z > 10$, their number density, the evolution of ionized gas bubbles, and the identification of sources producing ionizing radiation. The sensitivity of JWST should ensure us to capture sources with stellar mass higher than $\sim 10^5 - 10^6\,M_\odot$, which is unfortunately not enough to observe the first PopIII stars (Bromm, Kudritzki & Loeb, 2001), but is still very impressive as we should observe starbursts in the first galaxies. Another source of ionizing photons is thought to be AGN, which are powered by powerful BHs. The Square Kilometre Array (SKA) will give us a better idea of the abundance of AGN at $z > 6$, and whether there is a faint population of AGN at such high redshift, which would favor the contribution of AGN to the reionization. In the next sections, we will focus on BHs, and their evolution within their host galaxies.

1.4 Black holes as a key component of galaxies

In this section, we will see that BHs are a key component of galaxies. Indeed most of the local galaxies host a massive BHs, including the Milky Way and some dwarf galaxies. The discovery of luminous quasars at $z > 6$, 15 years ago (Fan, 2001 ; Fan et al., 2003, 2006b), showed us that massive BHs were already in place at the end of reionization epoch.

1.4.1 BHs and AGN

The general relativity of Einstein led us with the necessary framework, to predict theoretically the existence of BHs, immediately after 1915. The solution of Einstein's equation derived by Schwarzschild in 1916, led us with the idea that the mass of an object can collapse to a singularity of infinite density, a *black hole*, from which light can not escape anymore[6]. The observational

[6]The existence of black holes has been thought/introduced earlier by Mitchell in 1784, and Laplace in 1796, but also Eddington, who predicted that "*the star apparently has to [...] contracting, and contracting until, I suppose,*

first detection of a serious candidate BH took some time from the theoretical prediction, but in 1970, the X-ray source Cygnus X-1 is observed, with a mass of more than $6\,M_\odot$ indicating that the only possible explanation was a BH.
The first detections of supermassive BHs where through AGN observations, where the inner part of some galaxies were identified as *active nuclei*. We briefly remain here the main characteristics of AGN. Spectra of some galaxy nuclei present strong emission lines produced by the transitions of excited atoms. The emission lines can be broad or narrow. Broad lines correspond to high Doppler-broadening velocities of $> 10^3\,\mathrm{km\,s^{-1}}$, and generally correspond to permitted lines. Narrow lines with lower velocities of $10^2\,\mathrm{km\,s^{-1}}$ are also observed, and correspond either to permitted or forbidden lines. These emission lines give us crucial information on the surroundings of BHs: broad lines are produced close to the BH, where the gas densities and velocities are high because of the potential generated by the BH, we call this region the broad line region, narrow lines are produced in more extended regions, where gas densities and velocities are lower. We call this region the narrow line region. The global picture of AGN today, is that BHs are surrounded by an accretion disk, which is itself surrounded by a small inner broad line region, around which there is a clumpy extended narrow line region. The presence of an obscuring torus, around the broad line region, is thought to hide the emission from the broad line region, depending on the axis of the line-of-sight. Broad lines in a galaxy spectrum are a diagnostic for the presence of an AGN, and they are also used to estimate the mass of BHs in AGN through the virial method. The width of the broad lines is assumed as a proxy of the Keplerian rotational velocity. Conversely, the presence of narrow emission lines does not necessarily imply the presence of an AGN, because star forming galaxies can also present narrow emission lines due to HII regions around young massive stars. Line ratios are used to distinguish between AGN and star-forming galaxies. For example, [OIII]/Hβ indicate the level of ionization and temperature, whereas ratios like [NII]/Hα give an information on the ionized zone produced by high energy photoionization. For an AGN, the level of ionization and the temperature of the emitting gas are both higher, and because the photons are more energetic, the ionized region is also expected to be larger in the case of an AGN than for a star-forming galaxies. Therefore in a line ratio diagram (BPT diagram, Baldwin, Phillips & Terlevich, 1981), high [OIII]/Hβ vs [NII]/Hα are more likely to represent an AGN.

1.4.2 Local galaxies

Evidence for the presence of supermassive black holes in the center of galaxies has accumulated over the last decades. Because the first observations of BHs were through AGN, we have first drawn a picture of BH that was mostly based on the most massive BHs, the most bright and accreting ones. In this section, we will see that low-mass BHs have been observed, or at least an upper limit on their mass has been estimated for some of them, with the advance of observational abilities. This has strong consequences on our vision of BH formation and evolution over cosmic time.

Massive BHs are harbored in the center of most local galaxies, some examples can be found

it gets down to a few kilometers radius when gravity becomes strong enough to hold radiation and the star can at least find peace", through not very convinced by himself "*I think there should be a law of Nature to prevent the star from behaving in this absurd way.*". Finally, the first real calculation of the black hole is realized by Openheimer and Snyder in 1939, they show that an homogeneous sphere (without pressure) which gravitationally collapses, ends up its life without being able to exchange information with the rest of the Universe anymore. The term *black hole* is introduced later by Wheeler in 1968.

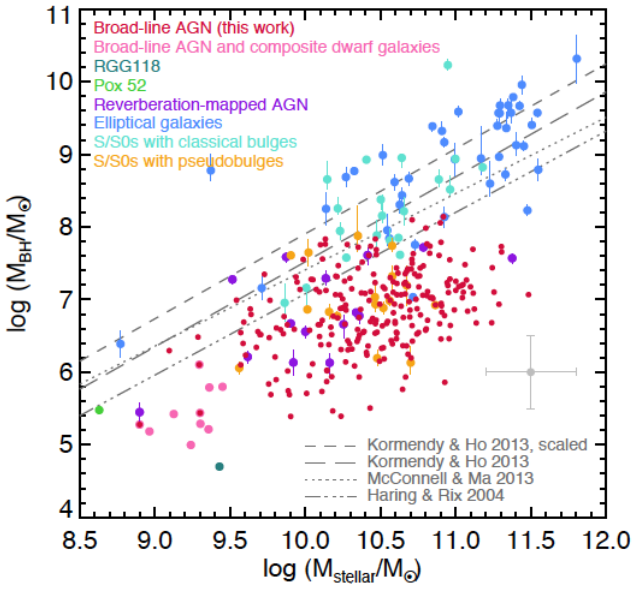

Fig. 1.2 – Relation between BH mass and the total stellar mass of local host galaxies (Reines & Volonteri, 2015). This consist of a sample of 244 broad-line AGN from which the virial BH masses are estimated through the single-epoch virial mass estimator (Reines, Greene & Geha, 2013) and shown as red points. Pink points represent 10 broad-line AGN and composite dwarf galaxies. Dark green point represents the dwarf galaxy RGG 118 with its 50,000 $M_\odot$ BH. Light green point is Pox 52. Purple points represent 15 reverberation-mapped AGN. Blue dots represent dynamical BH mass measurements. Turquoise dots represent the S/SO galaxies with classical bulges. Orange dots the S/SO galaxies with pseudobulges. Grey lines show different BH mass- bulge mass relations.

in Kormendy & Ho (2013). For instance, galaxies NGC 1332, NGC 3091, NGC 1550, and NGC 1407, have dynamical BH mass measurement of $M_{BH} > 10^9\,M_\odot$ (Kormendy & Ho, 2013). Reines & Volonteri (2015) provided a sample of local galaxies hosting BHs, at $z < 0.055$, that we reproduce in Fig 1.2. Blue points represent BHs in quiescent galaxies, whereas red points show AGN. On Fig 1.2, we see that indeed massive galaxies can host very massive central BHs of few $10^9\,M_\odot$. It is important to keep in mind that we have focussed so far on understanding what we were able to see until today, namely powerful BHs and massive galaxies. We have only observed the massive end of the BH and galaxy story. Understanding the BH population requires to now move on observing the low-mass end on the BH distribution, specifically the BHs that could reside in low-mass galaxies. Such observations need the support of theoretical models, such as those developed in this thesis.

Observing low-mass BHs in low-mass galaxies

That being said, observing the BH population in low-mass galaxies is not at all an easy task, for many reasons. First of all, if we simply extrapolate the BH-galaxy mass relation to low-mass galaxies, BH mass in low-mass galaxies would be lower that the ones in more massive galaxies, which makes their detections more challenging. In the hierarchical structure formation model, massive galaxies grow in mass partly because of galaxy-galaxy mergers. Low-mass galaxies, instead, do not experience as many galaxy-galaxy mergers as massive galaxies, their growth is limited compared to their massive counterparts. BH mass growth is boosted when a galaxy-galaxy merger occurs. BH in low-mass galaxies, are instead not expected to have grown much over

cosmic time.
Low-mass BHs are more difficult to observe than their massive counterparts, their gravitational force is weaker, stars or gas moving around such low-mass BHs will be difficult to identify/observe.
Stellar and gas dynamics method:
Galaxies beyond the Milky Way, are too far for us to resolve individual stars trajectories around the central BH. In the local Universe, we therefore need to study quantities which are averaged over stars, such as the averaged velocity of stars. In the inner part of a galaxy hosting a BH, there is an additional contribution to the gravitational potential from the BH, stars will move faster in the presence of a BH, resulting in a higher peak in the velocity curve. However, this peak is proportional to the mass of the BH, the more massive the BH is, faster is the velocity of the stars. The velocity dispersion σ along the line of sight and the surface density, and so the stellar density, can be measured and we can deduce the BH mass component. Gas dynamics is also used in a similar way, it allows one to measure the motion of ionized gas, this method mostly focuses on low-luminosity AGN.
Accreting BH signatures:
In addition to the gas moving around BHs, which provides precious clues for the detection of BHs, for example emission lines. BHs are often enclosed in an accretion disk. An accreting (potentially low-mass) BH can be detected via its accretion signatures. Matter that is accreted into the accretion disk of the BH, dissipate most of its energy in the UV wavelengths. Further BH signatures can be identified, such as X-ray emission, resulting from the interaction of high energy particles. The emission from these BHs is also thought to be weaker too, reducing our chance to detect them.

The properties of low-mass galaxies can also complicate the detection of low-mass BHs. Low-mass galaxies contain more gas, more dust and more on-going star formation (Greene, 2012). The dust can obscure/absorb the emission (which is already suspected to be weak) from an accreting BH. The on-going star formation emission will also make a BH detection difficult, because contaminating the diagnostics in optical, IR, and UV.
Multi-wavelength search helps to select BH low-mass galaxies sample, as X-ray, radio (Gallo et al., 2008, 2010; Reines et al., 2011; Reines & Deller, 2012; Miller et al., 2012; Schramm et al., 2013; Reines et al., 2014) and mid-infrared wavelengths (Izotov et al., 2014; Jarrett et al., 2011). X-ray photons from the nucleus are so energetic that they can be observed despite the gas-rich content of the galaxy, whereas radio and mid-infrared wavelength emissions are also less impacted by dust absorption. A combination of different wavelengths is a good method to detect BHs in low-mass galaxies, we give a non-exhaustive list of new BH search using multi-wavelengths method, at the end of this section. Combination of X-ray and an another wavelength can, for example, avoid a contamination by X-ray binaries (XRBs). Indeed, the ratio of radio to hard X-ray emission is larger for accreting BHs than for stellar mass BHs (Merloni, Heinz & di Matteo, 2003). Mid-IR observations allow one to detect luminous AGN (Stern et al., 2012; Assef et al., 2013), even if it is much more complicated to use it as an observational diagnostic to make a sample of dwarf galaxies (Izotov et al., 2014; Jarrett et al., 2011), because of the contamination from star-forming galaxies, which also emit mid-IR emission.

To conclude, low-mass BHs are complicated to observe, first because stellar or gas kinematics method are less sensitive to these low-mass objects. Accreting BHs offer a better chance to be observed. However, many sources of contamination exist, for example from the host galaxies, and make their detection difficult. New observational diagnostics emerge to detect these objects, as the combination of different wavelength search, that can avoid pollution from star-forming

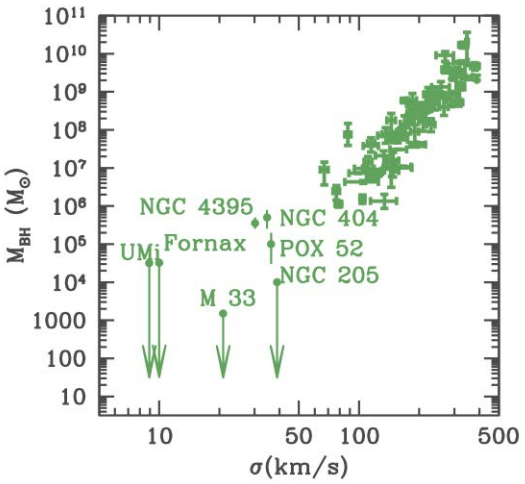

Fig. 1.3 – Low-mass BHs detected in galaxies, showed here in the BH mass - galaxy velocity dispersion diagram. Not only massive galaxies harbor a BH, BHs are also found in low-mass galaxies, some galaxies may be bereft of BHs.

galaxies, and from XRBs, for example. In the following, we list some of low-mass BHs that have been detected, and we review the search for new samples of BHs in low-mass galaxies.

Examples of low-mass BHs observed in low-mass galaxies

Over the last decade we have accumulated a good deal of observational evidence of the presence of BHs in low-mass galaxies in the local Universe. Below, we list some of the BHs that have been detected, or not, in low-mass galaxies. We start by listing two particularly interesting cases of nearby low-mass galaxies, which do not show any evidence for the presence of a BH, upper limits have been assigned to these BHs. Gebhardt et al. (2001) derive an upper limit for the BH mass in M33 of 1500 $M_\odot$ through stellar kinematics, with a best fit of the light profile indicating an absence of BH. For the same galaxy Merritt, Ferrarese & Joseph (2001) find an upper limit of 3000 $M_\odot$. Using the same method, Valluri et al. (2005) find an upper limit of 2.2×10^4 $M_\odot$ for the dwarf elliptical NGC 205. These very low upper limits possibly indicate that these galaxies are lacking a BH, or at least that they contain very low-mass BHs.
Low-mass BHs have been observed in several galaxies, here we list some of them in a chronological order. NGC 4395 shows clear evidence for a $10^4 - 10^5\,M_\odot$ BH (Filippenko & Ho, 2003; Peterson et al., 2005; Edri et al., 2012) (Hβ linewidth-luminosity-mass scaling relation), with rapid variability in the X-rays (Shih, Iwasawa & Fabian, 2003), and a radio-jet (Wrobel & Ho, 2006). The galaxy POX 52 is thought to host a low-mass BH of $\sim 10^5\,M_\odot$ as well (Barth et al., 2004). Barth et al. (2009) find that the galaxy NGC 3621 could host a $3 \times 10^6\,M_\odot$ BH, accretion evidence is also found. The presence of a $5 \times 10^5\,M_\odot$ has been reported in the galaxy NGC 404 by Seth et al. (2010), also with kinematics method and a set of other methods (near-IR integrated-filed spectroscopy, optical spectroscopy, imaging, etc).
Some low-mass galaxies host an accreting BH, as revealed in Reines et al. (2011) by X-ray and radio emission from the dwarf galaxy Henize 2-10, the mass of the BH is estimated at $2 \times 10^6\,M_\odot$. The dwarf galaxy M6-UCD1 indicates signatures of a $2.1 \times 10^7\,M_\odot$ BH. Yuan et al. (2014) identify 4 candidates with BH mass of $\leqslant 10^6\,M_\odot$, two of which show signatures of X-ray emission.
Baldassare et al. (2015) report the lowest-mass BH ever discovered, with a mass of 50,000 $M_\odot$,

derived through virial BH mass estimate techniques.

Search for more objects in low-mass galaxies

Despite these famous examples of low-mass BHs, in recent years, many studies have started looking for evidence of the presence of BHs in low-mass galaxies, in a systematic way, with stellar mass of $M_\star \sim 10^9\,M_\odot$. The SDSS survey is an optical spectroscopic galaxy survey (York et al., 2000). It has been used to look for evidence for accreting BHs with broad Hα line. Greene & Ho (2004) identify 19 objects (using the first release of SDSS data), which correspond to broad-line AGN, with a BH mass in the range $8 \times 10^4 - 10^6\,M_\odot$. Mass of BHs were determined using a linewidth-luminosity-mass scaling relation method, which links the BH mass to the AGN luminosity at a given wavelength (at 5100 Å), and the FWHM of the broad Hβ line.
Greene & Ho (2007a) estimate BH masses of AGN in low-mass galaxies though the virial method (1.27), which is a method "extrapolating" the results from reverberation mapping to single-epoch spectra. The BH mass is expressed by:

$$M_{BH} = \frac{f v^2 R_{BLR}}{G}, \tag{1.27}$$

where f is a scaling factor accounting for the unkown broad line region (BLR) geometry (see Greene & Ho, 2005). The broad line region velocity dispersion is measured from the line width. The radius of the BLR region is estimated from the AGN luminosity using a radius-luminosity empirical relation derived by reverberation mapping of a sample of AGN. With the reverberation method, the radius R_{BLR} of the broad-line region is determined by measuring the time delay Δt between variations in the BLR emission and in the AGN photoionizing continuum. This sample increases by one order of magnitude the number of BHs with $M_\odot < 2 \times 10^6\,M_\odot$. From this sample, Dong, Greene & Ho (2012) study the X-ray properties of 49 sources in the BH mass range $10^{5-6}\,M_\odot$, and find several weak X-ray sources. Evidence for narrow-line AGN in low stellar velocity dispersions (favoring the presence of a low mass BH) have been found (Barth, Greene & Ho, 2008). However, because of small volume surveys, or for example SDSS spectroscopic selections which favor a selection of luminous galaxies, and the low number of galaxies with $M_\star < 10^9\,M_\odot$, these samples did not give us all the clues needed to understand BH population in low-mass galaxies, but have paved the way for the following low-mass BH search. Reines, Greene & Geha (2013) performed a new systematic search for BHs (of $10^{5-6}\,M_\odot$) in galaxies with stellar mass of $M_\star < 3 \times 10^9\,M_\odot$. They found 136 dwarf galaxies harboring evidences of active BHs, in the SDSS survey. The identification is made on the detection of narrow-line photoionization signatures, and/or broad Hα emission lines. Lemons et al. (2015) recently identify a new sample of BHs using hard X-ray diagnostics, meaning that this could be an interesting diagnostics for AGN in dwarf galaxies. More recent works use, as we have said before, X-ray and radio observations to search for weakly accreting BHs (Reines, 2015). This allows to avoid a confusion in optical wavelengths, for example with star-forming region emission. However, recently Moran et al. (2014) show that optical detections have still a role to play in the low-mass BHs detection, by identifying 28 AGN in the SDSS survey, with BH mass estimated in the range $10^3 - 10^4\,M_\odot$, a sample for which only few of the objects have been also identified via emission that can be associated to BH accretion in other bands than optical, for example at radio and X-ray wavelengths.

Massive BHs are found in many local galaxies, from massive galaxies, to low-mass galaxies, when other galaxies seem to be lacking of BHs. In this section, we have seen that today we

are pushing the observational limits to identify more and more BHs in low-mass galaxies. Our ability of observing galaxies keeps increasing, so no doubt that many more signatures of BHs in low-mass galaxies will emerge.

1.4.3 Population of quasars at $z = 6$

In the 1960s, several observational studies proposed the idea of *quasi-stellar radio sources*, *quasi-stellar sources*, that we commonly call *quasars* today. Observations of more and more very luminous objects, with powerful radio emission, showing broad emission lines at uncommun wavelengths, but also variability, and excess of ultraviolet emission compared with normal stars[7]. Among the most famous objects, there is 3C295, which was studied by Minkowski, who showed that 3C295 was 10 times smaller than Cyg A, and the presence of a redshifted line allowed him to deduce that the object was 10 times farther than Cyg A. In 1961, Matthews and Sandage, studied 3C48, which was thought to be a small blue star, with broad emission at unkown wavelenghts. In 1962, Hazard determined the position of 3C273, and the structure of an associated elongated radio source, similar to a jet. Schmidt and Oke observed the source and also found redshifted lines, as in 3C48. These objects were all showing highly redshifted lines in their spectra, were very luminous, and were also for some of them showing variability (3C48, 3C273), indicating that the sources were actually small. A series of papers in 1963 (Hazard, Mackey & Shimmins, 1963 ; Schmidt, 1963 ; Oke, 1963 ; Greenstein, 1963), were addressing the nature of quasars, as either unusual galactic stars, or extra galactic sources at larger redshifts. It has been quite difficult for the community to accept that the redshifts indicated by these lines, were cosmological redshifts and that these sources were far away powerful extragalactic sources. Rapidly, in order to explain the features of such quasar objects, central mass of $10^9\,M_\odot$ are proposed (see Matthews & Sandage, 1963 ; Smith & Hoffleit, 1963, for example), definitely too massive to be normal stars.

Today, we observe these quasars up to redshift $z = 7$ (Fan et al., 2006a ; Jiang & et al.,, 2009 ; Mortlock et al., 2011), and they represent the active tail of BHs distribution. The oldest quasar ever observed is ULAS J1120+0641 (Mortlock et al., 2011), which was already in place only 770 Myrs after the Big Bang, at redshift $z = 7.085$. The mass of the BH powering this quasar is $M_{BH} \sim 2 \times 10^9\,M_\odot$ (estimated from the quasar luminosity and its MgII line width). Other high redshift quasars have been observed before but at lower redshift than ULAS J1120+0641, among which CFHQS J0210-0456 at $z = 6.44$ (Willott et al., 2010a), SDSS 1148+5251 at $z = 6.42$ (Fan et al., 2003), and CFHQS J2329+0301 at $z = 6.42$ (Willott et al., 2007). A sample of 19 high redshift luminous quasars, in the redshift range $5.74 < z < 6.42$, and magnitude of $z_{AB} \leqslant 20$ (corresponding to a magnitude of $M_{1450\text{Å}} \sim -27$ at 1450 Å) has been described in a series of papers (Fan et al., 2003, 2006a). This sample has been made using the SDSS. Fainter objects have been observed, again in the SDSS survey, with magnitude $21 < z_{AB} < 22.16$ (corresponding to magnitudes in the range $-28 < M_{1450\text{Å}} < -25$). These are 6 quasars in the redshift range $5.78 < z < 6$, their magnitude is 2 order of magnitude fainter than the previous $z \sim 6$ known quasars found in SDSS. Their weak Lyα emission lines could be due to small black hole masses and high Eddington luminosity ratios, indicating that these BHs grow on short time scales. Some of the high-redshift quasars cited in this section are shown in Fig 1.6.

[7]For a very interesting review which retraces the history of the discovery of quasars, see https://ned.ipac.caltech.edu/level5/Sept04/Shields/Shields3.html. See also the book of Suzy Collin-Zahn, *Des quasars aux trous noirs*.

The discovery of quasars at very high redshift, $z > 6$, also triggered new questions regarding the role of powerful BHs in the early Universe, both on the evolution of galaxies, and on the evolution of the IGM. Quasars spectra allow us to answer some of these questions, particularly concerning the reionization of the Universe. Constraints on cosmic reionization mainly comes from IGM properties, how the IGM absorb and react to the radiation coming from background sources. The fraction and distribution of neutral hydrogen along the line-of-sight is inferred from quasar observations. Observing spectra of ionizing sources provide a crucial information on the properties of the IGM (density, composition, and so on). In the most easy case, namely when the emission from the IGM is negligible, the number of photons in a line-of-sight from the source to us, can only decrease. Photons can indeed only be absorbed by the IGM, and re-emitted under a random direction, and then may be scattered away from the line-of-sight. This defines the mean optical depth of the IGM, and can be probed by measuring the absorption in the spectra of quasars at high redshifts. In practice, it consists in measuring the flux decrement caused by the IGM, which is the mean value of the ratio between the observed continuum flux ($F_{\rm obs}(\lambda)$) and the expected continuum flux in the absence of absorption ($F_{\rm cont}(\lambda)$). This effect is known as the *Gunn-Peterson effect*. Using quasars spectra, Fan et al. (2006a) show that, at $z > 6$, the effective optical depth increases rapidly with increasing redshift, therefore indicating a rapid increase in the neutral density of the IGM at $z > 6$ (see also, Becker et al., 2001 ; Djorgovski et al., 2001 ; Fan et al., 2002 ; White et al., 2003). A rapid increase of HII regions size suggesting that HI fraction of the IGM has increased by a factor of $\geqslant 10$ from $z = 6.4$ to $z = 5.7$ is also shown (Fan et al., 2006a).
With the observation of the *Gunn and Peterson trough effect*, caused by neutral hydrogen in the IGM, in high redshift quasars, we start dating the end of the reionization period, around $z \sim 6$. However, the time evolution is difficult to investigate, from this we can not know wether the IGM become neutral just after $z > 6$ and therefore is a rapid process, or if the reionization is a slow process occuring at redshift much higher than $z = 6$. The impact of accreting BHs at such high redshift, whether BHs play a predominent role in the reionization process of the Universe, is still debated today.

In this section, we have seen that BHs are present both in high redshift galaxies, and in the present local Universe. Moreover these BHs span a large range of mass, from the smallest central BHs observed, with $\mathrm{M_{BH}} = 50,000\,\mathrm{M_\odot}$ (Baldassare et al., 2015) to the large mass of quasars we observe at high redshift. The most massive BH ever observed has a mass of $\mathrm{M_{BH}} > 10^{10}\,\mathrm{M_\odot}$ (McConnell et al., 2011). The mass distribution of BHs is a challenge for theoretical models of BH formation, which must explain both the low-mass and high-mass ends of BH distribution. High redshift quasars are also challenging for BH growth models, because they are observed less than 1 Gyr after the formation of the first BHs, and therefore they must have acquired large amount of mass in a short time. The detection of such massive objects at high redshift is the first constraint that we have for BH formation and evolution, it also helped to investigate reionization, and trigger new questions regarding BH feedback. In the next section, we focus on the co-evolution of BHs and their host galaxies, and the different mechanisms of BH feedback.

1.5 Black holes as a key component for galaxy evolution

We have seen that BHs are an important ingredient of galaxies, in the local Universe, but also at high redshift, which is probed by the observation of quasars. The comoving density of quasars at high redshift ($z \sim 6$) is 40 times smaller than the one at $z \sim 3$ (Fan et al., 2006b), this

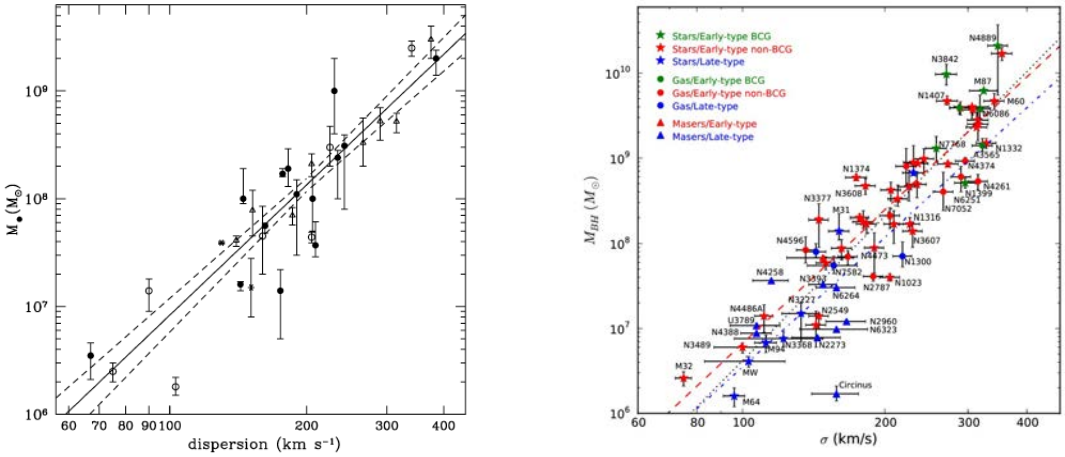

Fig. 1.4 – Relation between BH mass and the velocity dispersion of the host galaxy, from Tremaine et al. (2002), and McConnell & Ma (2013) 10 years later.

suggests that we are actually tracing the initial rise of the BH evolution history, and with this the premise of their co-evolution with their host galaxies. We will describe in the next section, the empirical relations between BH masses and the properties of their host galaxies, which indicate this co-evolution. Powerful BHs are also thought to impact their galaxies, by means of several feedback mechanisms, that we describe in the second section.

1.5.1 Co-evolution between BHs and their host galaxies

Several empirical relations have been found between BHs and their host galaxies. First of all, the luminosity of the stellar component of the host galaxies (the entire galaxies or their bulges) correlates with the mass of their central massive BHs (Kormendy & Richstone, 1995). BH masses also correlate with the mass of their host galaxy bulge (Kormendy & Richstone, 1995 ; Magorrian et al., 1998 ; Ferrarese & Merritt, 2000 ; McLure & Dunlop, 2001 ; Marconi & Hunt, 2003), with the relation $M_{BH} \propto 10^{-3} M_{bulge}$. An even tighter empirical relation is derived between BH masses and the velocity dispersion of the spheroids (Gebhardt et al., 2000 ; Ferrarese & Merritt, 2000 ; Tremaine et al., 2002). We show in Fig 1.4, the BH mass - galaxy velocity dispersion of Tremaine et al. (2002) and the one derived by McConnell & Ma (2013) 10 years later. Coevolution between BHs and their host galaxies is still a hot topic in the field of galaxy evolution today. This is perceivable in the debate regarding the power of the relation between BH mass and the galaxy velocity dispersion, $M_{BH} \propto \sigma_{gal}^{\alpha}$ with an incertitude on the power parameter $\alpha = 4 - 5$. Finally, a possible relation between BH masses and dark matter halos has been proposed by Ferrarese (2002), whereas Kormendy & Bender (2011) disagree on this relation, and claim that BHs only correlate with bulge, and do not correlate directly with either dark matter halo or galactic disks.

BHs and their host galaxies are co-evolving, as indicated by the empirical correlations $M_{BH} - M_{bulge}$, and the BH mass - galaxy velocity dispersion, and the debated BH - dark matter halo relation. BH growth must have been impacted by host galaxies properties, but BH evolution may also have influenced galaxy evolution as well, through what we call feedback processes. In the next section, we focus on the mechanism of BH feedback on the host galaxies.

1.5.2 AGN feedback

When gas is accreted onto a BH, there is a release of rest-mass accreted energy back to the galactic gas, which can impact the host galaxy by feedback processes (Silk & Rees, 1998). AGN feedback acts as an interaction between the energy, radiation produced by gas accretion onto the central BH, and the gas in the host galaxy. Theoretically, the energy released by the BH, can be sufficient to entirely unbind the gas of its host galaxy. If BH growth is dictated by accretion, the BH energy is expressed as $E_{BH} = (\epsilon/1-\epsilon)M_{BH}\,c^2$, whereas the binding energy of the galaxy is expressed by $E_{gal} = M_{gal}\,\sigma^2$. The ratio between the energy released by the BH and the binding energy of the host galaxy is:

$$\frac{E_{BH}}{E_{gal}} = \frac{\epsilon}{1-\epsilon}\left(\frac{M_{BH}}{M_{gal}}\right)\left(\frac{c}{\sigma}\right)^2 > 60 \tag{1.28}$$

if we assume the radiative efficiency to be $\epsilon \sim 0.1$. If only a small fraction of the BH accretion energy was released as kinetic energy transferred to the gas, AGN feedback would be able to unbind the gas of the galaxy.
Three main mechanisms can alter the galaxy gas content through AGN feedback: radiation feedback, kinetic feedback, and the ejection of energetic particles. These mechanisms have been implemented and tested in both isolated and cosmological simulations, leading to both *negative* and *positive* feedback. In the following, we explain the different modes of AGN feedback, and how they have been implemented in numerical simulations. We then explain the positive and negative feedback effects, and review some studies which result in either one or the other aspects of AGN feedback, and their implications.

Radiative feedback or quasar mode

The first one is *radiative feedback*, through both radiation pressure and radiative heating. Radiative pressure is the force exerted on the galaxy gas through different processes such as electrons scattering, or scattering and absorption on dust for example (see many papers by Mitch Begelman, or the corresponding review Begelman, 2004). This is what we call the *quasar mode* of AGN feedback. Quasar mode is thought to happen after an episode of high gas accretion onto a BH, which can take place mostly in high redshift galaxies, which are gas-rich, and therefore provide a gas reservoir to feel the BH. AGN feedback through the radiative mode, is thought to push cold gas outward, when the accretion onto the central BH is close to the Eddington limit ($\dot{M}_{BH}/\dot{M}_{Edd} > 0.01$). Deposition of internal energy by increasing the gas temperature, has been used in cosmological simulations to mimic the heating of the gas in the surrounding of BHs (Di Matteo et al., 2008 ; Teyssier et al., 2011 ; Dubois et al., 2012a).

Mechanical feedback or radio mode

Observationally, the *kinetic or mechanical feedback* is the easiest to observe (through X-ray and radio observations), because responsible for the ejection of powerful jets, and bubbles/cavities discovered in the cores of clusters (see for example the Perseus cluster, Fabian et al., 2006). In numerical simulations, this mode is modeled for low Eddington fraction ($\dot{M}_{BH}/\dot{M}_{Edd} \leqslant 0.01$), with a momentum-driven kinetic bipolar outflow, where the mass, energy, and momentum are deposited in the surroundings within a cylinder (Dubois et al., 2010, 2011, 2012a). The orientation of the outflow is determined by computing the gas angular momentum around BHs.

Ejection of energetic particles

Finally AGN feedback is also responsible for *ejecting energetic particles* in the surroundings,

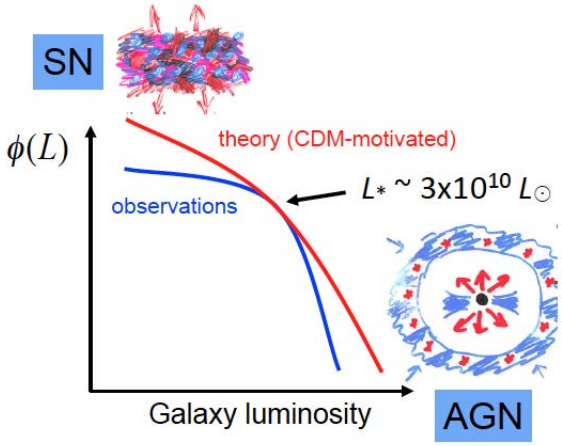

Fig. 1.5 – Cartoon from Silk & Mamon (2012), showing the theoretical galaxy mass function, and the observational one. Discrepancies appear at both the low-mass and high-mass ends of galaxy distribution. Feedback from SN and AGN have been advocated to regulate the star formation in galaxies at low and high-mass end respectively.

which can be either charged (cosmic rays), or neutral (relativistic neutrons or neutrinos).

AGN feedback can be negative, the gas is heated, which inhibits star formation in the galaxy, but also dispersed and pushed out of the galaxy, which limit the gas mass available to form stars as well. Conversely, AGN feedback can impact the host galaxy in a positive way, by triggering star formation. Negative and positive AGN feedback are not excluding each other, and may both exist at different times or different parts of the host galaxy (Silk, 2013).
When we compare theoretical models and cosmological simulations to observations of galaxies in the nearby Universe, we see that the models lead to an overestimate of the number of small galaxies, and of the number of high mass galaxies. In other words, in galaxy evolution models, galaxies and dark matter halos retain too many baryons, and produce too many stars. This is known as the *overcooling* problem. At the low-mass end of the galaxy stellar mass function, stellar feedback, by means of SN winds, are able to drive baryons out of halos. However, when we consider much more massive galaxies, winds from SN may not be sufficiently strong to push baryons out of the galaxy. Only powerful BHs are thought to be strong enough, to remove baryons or suppress accretion from the cosmic web, therefore decreasing the ability of galaxies to form stars, which leads to a decrease of the galaxy luminosity function at the high-mass end. The evolution between star formation and dark matter halo mass appears to be more complex than what models and simulations predict, this is partially due to our lack of knowledge in star formation, and mechanism of galaxy regulation, as stellar and BH feedbacks. AGN regulating star formation in their host galaxies, what we call the *quenching of galaxies*, have been reproduced in cosmological simulations. Di Matteo et al. (2008) and Dubois et al. (2012a), model the radiative (or quasar) AGN feedback mode, by depositing internal energy into the surrounding of BH, and find that AGN feedback regulate star formation, and therefore have a negative feedback. In addition to quench star formation in massive galaxies, AGN feedback is also thought to limit their own BH accretion by depositing energy in the surroundings (Silk & Rees, 1998 ; Fabian, 1999), and to drive/regulate the coevolution between BHs and their host galaxies.

Regarding the positive impact of AGN feedback, theoretical studies (Begelman & Cioffi, 1989 ;

Rees, 1989) have shown that outflow or jets propagating in an inhomogeneous ISM of galaxy may boost or even trigger star formation. This have been also demonstrated in simulations of massive galaxy composed by a multi-phase ISM, and including a powerful jet (Gaibler et al., 2012). The jet is able to change the shape of the density probability distribution function, and pressurize the galactic disk, which compresses gas clumps, and increases their densities up to the limit to form stars. Positive AGN feedback has also been found in isolated galaxy hydrodynamical simulations including an ambient external pressure in the galactic disk (Bieri et al., 2016).

The radiative mode is the AGN feedback mode dedicated to high accretion rate onto the BH (close to the Eddington limit), and could therefore be the mode responsible for the co-evolution between for example the BH mass and the galaxy stellar velocity dispersion, and may be the predominant mode at early times because of the large reservoirs of cold gas available to fuel central BHs. Conversely, the kinetic mode responsible for driving large outflows, may be the main AGN feedback mechanism at later times, as observed today in nearby galaxies. At later times, gas has been consumed and pushed away by previous AGN feedback episodes, and star formation episodes, therefore the BHs accrete at a lower Eddington fraction (see also Churazov et al., 2005). We are still far from understanding the whole mechanisms of AGN feedback, and whether it has a positive and negative effect of the host galaxies, or a contribution of the two at different places, and times, and whether a given mode of AGN feedback is associated to a given positive or negative effect.

In the two previous sections, we have discussed the presence of massive BHs in most of the nearby massive galaxies, but also the discovery of quasars, which tells us that powerful BHs were already assembled and in their powerful age already at high redshift. We also pointed out that we have several clues on the co-evolution of these BHs with their host galaxies (from high redshift to the local Universe), through empirical relations between BH mass and galaxy properties. We have discussed the capability of BHs to interact and regulate their host galaxies evolution, through radiative or kinetic feedback mechanisms. In the next section 1.6, we focus on BH growth.

1.6 Black hole growth over cosmic time

More than 50 high redshift quasars ($z > 5$, Fan, 2006) have been observed so far. They help us to constrain the high redshift Universe, and periods that are hardly accessible with observations, such as the reonization. The observation of quasars at high redshift is one of the main clues on BH formation and growth we have today. The $z = 6$ quasars are among the most luminous objects that we have observed, at all redshifts. Their apparent magnitudes can be up to ~ 19, even for redshift higher than $z > 6$. As we have seen, the SDSS survey strongly helped us to understand better the powerful quasars (Fan, 2001 ; Fan et al., 2003), and let us with a puzzeling population of massive powerful BHs less than 1 Gyr after the Big Bang. The fact that we observe them at very high redshift gives us precious clues: BHs must have formed in the early Universe in order to assemble within 1 Gyr after the Big Bang, and to grow very efficiently up to $> 10^9\,M_\odot$ by $z = 6$ for some of them. How can BHs grow of several order of magnitude within 1 Gyr? Is their grow limited?

Eddington limit

It exists a luminosity limit, the so-called Eddington luminosity, for which the radiation pressure

is higher than the gravity, a wind is formed, and matter is pushed away from the BH. If we consider the luminosity which can be emitted by an object via a static photosphere in a spherical geometry, with a small volume at the surface dV, and r the radius of the photosphere, we can express the gravitational force as:

$$\frac{\mathrm{d}\boldsymbol{F}_{\mathbf{grav}}}{\mathrm{dV}} = -\frac{G\mathrm{M}m_{\mathrm{p}}n}{r^2}\boldsymbol{u_r}, \tag{1.29}$$

with M the mass of the object, which is the BH here, m_p the proton mass. We assume that the matter which is accreted is only composed of hydrogen (in neutral or ionized state). The radiation flux interacts mainly with the matter by Thomson scattering on electrons, so the force of radiation pressure is expressed by:

$$\frac{\mathrm{d}\boldsymbol{F}_{\mathbf{rad}}}{\mathrm{dV}} = -\frac{n\sigma_{\mathrm{T}}}{c}\frac{L}{4\pi r^2}\boldsymbol{u_r}, \tag{1.30}$$

with σ_{T} the Thomson cross-section. The resulting force is:

$$\frac{\mathrm{d}\boldsymbol{F}}{\mathrm{dV}} = -\left(1 - \frac{L\sigma_{\mathrm{T}}}{4\pi G\mathrm{M}m_{\mathrm{p}}c}\right)\frac{G\mathrm{M}m_{\mathrm{p}}n}{r^2}\boldsymbol{u_r}. \tag{1.31}$$

We therefore define the luminosity limit, for which the radiation pressure is higher than the gravity, the photosphere is not static anymore, which leads to the formation of a wind:

$$L_{\mathrm{Edd}} = \frac{4\pi G\mathrm{M}m_{\mathrm{p}}c}{\sigma_{\mathrm{T}}} = 3.4\times10^4\left(\frac{\mathrm{M}}{\mathrm{M}_\odot}\right)L_\odot. \tag{1.32}$$

We commonly define the Eddington timescale, or the Salpeter timescale, as:

$$L_{\mathrm{Edd}} = \frac{\mathrm{M}_{\mathrm{BH}}c^2}{t_{\mathrm{Edd}}} \quad \text{with} \quad t_{\mathrm{Edd}} = \frac{\sigma_{\mathrm{T}}c}{4\pi G m_{\mathrm{p}}} = 0.45\,\mathrm{Gyr}. \tag{1.33}$$

A BH accretes at a fraction f_{Edd} of this Eddington limit:

$$L = \epsilon\dot{\mathrm{M}}_{\mathrm{acc}}c^2 = f_{\mathrm{Edd}}L_{\mathrm{Edd}}c^2, \tag{1.34}$$

with ϵ the efficiency with which accreted matter is converted into radiation, f_{Edd} is the ratio of the luminosity and the maximum Eddington luminosity.

$$\dot{\mathrm{M}}_{\mathrm{acc}} = \frac{f_{\mathrm{Edd}}L_{\mathrm{Edd}}}{\epsilon} = \frac{f_{\mathrm{Edd}}\mathrm{M}_{\mathrm{BH}}\mathrm{c}^2}{\epsilon\, t_{\mathrm{Edd}}} \tag{1.35}$$

$$\mathrm{dM}_{\mathrm{BH}} = (1-\epsilon)\mathrm{dM}_{\mathrm{acc}} \tag{1.36}$$

$$\frac{\mathrm{dM}_{\mathrm{BH}}}{\mathrm{dt}} = \frac{(1-\epsilon)}{\epsilon}f_{\mathrm{Edd}}\frac{1}{t_{\mathrm{Edd}}}\mathrm{M}_{\mathrm{BH}} \tag{1.37}$$

$$\frac{\mathrm{dM}_{\mathrm{BH}}}{\mathrm{M}_{\mathrm{BH}}} = \frac{(1-\epsilon)}{\epsilon}f_{\mathrm{Edd}}\frac{\mathrm{dt}}{t_{\mathrm{Edd}}}. \tag{1.38}$$

After integration, we obtain the time evolution of the BH mass:

$$\mathrm{M}_{\mathrm{BH}}(t) = \mathrm{M}_{\mathrm{BH}}(t=0)\exp\left[\frac{(1-\epsilon)}{\epsilon}f_{\mathrm{Edd}}\frac{t_{\mathrm{growth}}}{t_{\mathrm{Edd}}}\right], \tag{1.39}$$

and the corresponding time of growth:

$$t_{\mathrm{growth}} = t_{\mathrm{Edd}}\frac{\epsilon}{(1-\epsilon)}\frac{1}{f_{\mathrm{Edd}}}\ln\left[\frac{\mathrm{M}_{\mathrm{BH}}}{\mathrm{M}_{\mathrm{BH}}(t=0)}\right]. \tag{1.40}$$

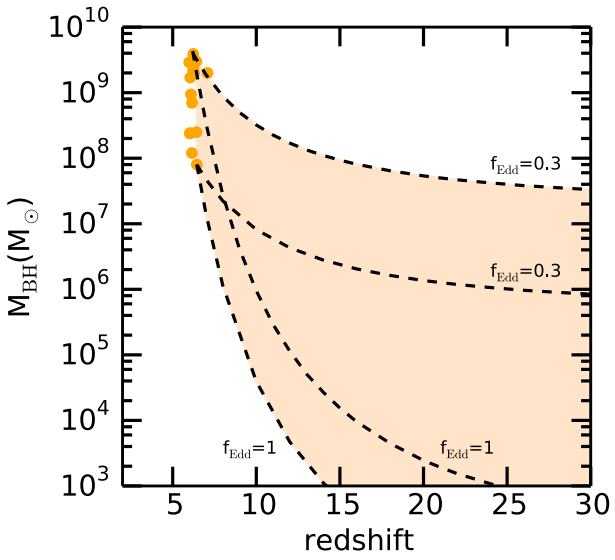

Fig. 1.6 – Theoretical growth of high redshift quasars. The sample of some high redshift quasars is represented in orange dots. Black dashed lines indicate theoretical growth of two of these objects, assuming $\epsilon = 0.1$, and a constant growth at either $f_{\rm Edd} = 0.3$ or $f_{\rm Edd} = 1$.

From this last equation, if we consider a quasar of $10^9\,{\rm M}_\odot$ as a $z = 6$, which had accreted at the Eddington limit its entire life ($t_{\rm growth} = 1$ Gyr), and considering $t_{\rm Edd} = 0.45$ Gyr, we find that the initial mass of the BH is ${\rm M_{BH}(t = 0)} \sim 2\,{\rm M}_\odot$. From the mass of quasars at high redshift we can then infer different configurations for BH formation and BH growth together. We can already notice that accreting at the Eddington rate from the beginning of the Universe is a strong assumption, therefore BH seeds forming with masses in the range $100 - 10^5\,{\rm M}_\odot$ seem more realistic. In Fig. 1.6, we show a sample of few high-redshift quasars, among which those we have presented in the previous section, in orange dots. Black dashed lines indicate the theoretical growth of the BHs powering two of these quasars, assuming $\epsilon = 0.1$, and either $f_{\rm Edd} = 0.3$ or $f_{\rm Edd} = 1$. In the next section, we will describe the main theoretical scenarios that have been advanced for the formation of such massive BH seeds in the early Universe. Before coming to the formation of BHs, we here briefly review different modes of BH growth.

BH growth

Several processes participate to the growth of BHs: gas accretion, and BH-BH mergers. However, it has been shown that BH growth is mainly driven by gas accretion, rather than BH-BH mergers. This comes from both the hard X-ray background measurement (Fabian & Iwasawa, 1999) (which gives the mass density in BHs), and Soltan's argument (Soltan, 1982; Yu & Tremaine, 2002), which compares the mass of BHs today to the AGN/quasar population (through their luminosity functions) integrated over luminosity and redshift. This total energy can be converted into a total accreted mass, and appears to be close to the total mass of BH today. This tends to say that most of BH growth is done by radiatively efficient gas accretion. The luminosity L of a BH is defined by:

$$L = \frac{\epsilon}{1-\epsilon} c^2\,\dot{\rm M}_{\rm acc}, \tag{1.41}$$

and can be related to the accreted mass energy E of a BH, which is then expressed by:

$$E = \frac{\epsilon}{1-\epsilon} c^2\,{\rm M}_{\rm acc}. \tag{1.42}$$

The density $\rho_{\rm acc}$ is obtained by:

$$\frac{E}{V} = \frac{1}{V}\frac{\epsilon}{1-\epsilon}c^2\,{\rm M_{acc}} = \frac{\epsilon}{1-\epsilon}{\rm c}^2\rho_{\rm acc}, \tag{1.43}$$

with V the volume. The luminosity function of quasars and AGN gives the number of objects N with the luminosity L, for the volume V:

$$\Phi(L,t) = \frac{dN}{dL\,dV}. \tag{1.44}$$

Soltan's argument is to integrate the observed luminosity function of quasars/AGN over luminosity and time, to obtain the total energy density emitted by accreting BHs $u_{\rm acc}$:

$$u_{\rm acc} = \int_t^0 dt \int_0^\infty \Phi(L,t)LdL, \tag{1.45}$$

or to integrate over redshift:

$$u_{\rm acc} = \int_z^\infty \frac{dt}{dz}dz \int_0^\infty \Phi(L,t)LdL. \tag{1.46}$$

Finally, a comparison is established between the density of accreted mass $\rho_{\rm acc}$ to the total energy emitted by known accreting BHs $u_{\rm acc}$:

$$\rho_{\rm acc} = u_{\rm acc}\,\frac{1}{c^2}\frac{1-\epsilon}{\epsilon} = \frac{1}{c^2}\frac{1-\epsilon}{\epsilon}\int_z^\infty \frac{dt}{dz}dz \int_0^\infty \Phi(L,t)LdL. \tag{1.47}$$

The derived local mass density of accreted matter, gives us the total amount of matter that have been accreted by quasars. However, it is based on the observed luminosity function of quasars, and therefore may be underestimated, because of the presence of potential obscured AGN that are missed by observations, and the presence of normal BHs (quiescent, non-accreting BHs). Therefore the Soltan's argument gives a lower limit of the relic BHs that we could find in local galaxies today. Soltan (1982) find that the mass accumulated in quasars is $\epsilon^{-1}\,4.7\times10^{12}\,{\rm M_\odot Gpc^{-3}} = \epsilon^{-1}\,4.7\times10^{3}\,{\rm M_\odot Mpc^{-3}}$, which translates into $4.7\times10^{13}\,{\rm M_\odot Gpc^{-3}} = \epsilon^{-1}\,4.7\times10^{4}\,{\rm M_\odot Mpc^{-3}}$ when we assume $\epsilon = 0.1$. At that time, the quasar luminosity function was not as well-know as today, and the local mass density found by Soltan (1982) was therefore underestimated, and already quite large, and interestingly similar to the mass in BHs today. Yu & Tremaine (2002) derive:

$$\rho_{\rm acc}(z=0) = 2.1\times10^5(C_{\rm B}/11.8)[0.1\frac{1-\epsilon}{\epsilon}]\,{\rm M_\odot Mcp^{-3}} \tag{1.48}$$

This means that taking into account the total accretion onto quasars, we find that every $1\,{\rm Mpc}^3$, there must exist $\geqslant 10^5\,{\rm M_\odot}$ mass of BH(s), which is similar to what we observe today. Therefore the growth of BHs is mainly driven by gas accretion.

Regulation of BH growth

We have seen that BHs mostly grow by gas accretion, however, the accretion can be regulated by different processes, at small scales in the close environment of the BH, and at larger scales.
BH growth can be regulated in the first place immediately after the BH formation. The SN explosion of the stellar progenitor produces two types of feedback. Feedback can be mechanical, the explosion can push the gas outward, and lead to a low-density medium around the newly formed BH, particularly for high-redshift mini-halos with shallow potential well (Johnson & Bromm, 2007; Pelupessy, Di Matteo & Ciardi, 2007; Alvarez, Wise & Abel, 2009). It can be thermal, the SN explosion also certainly heats the gas. Finally, the star can also have produced

ionizing radiation. Pop III stars are thought to produce large amount of ionizing radiation (Schaerer, 2002) before collapsing into a BH. The initial growth of the BH seed can therefore be delayed for $\sim$ 100 Myr (Johnson & Bromm, 2007; Alvarez, Wise & Abel, 2009; Johnson et al., 2013), due to the low-density region it is formed in. Conversely, BHs formed through supermassive stars (we will describe BH formation models in the next section), have more chance to grow. Indeed, emitted ionizing radiation from supermassive stars could be weaker, as well as their radiative feedback (Hosokawa et al., 2013; Schleicher et al., 2013), resulting in a more favorable environment for the newly formed BH to accrete gas. Early growth of BHs depends on BH formation models, namely the BH progenitors properties, the initial mass of BH, and the close environment they are born in. Accretion onto the BH itself can also favor the production of ionizing radiation, decreasing the early accretion into BHs. Unfortunately, these phenomena are difficult to capture within simulations, requiring sub-parsec resolutions.

Larger scale environment also strongly influence the growth of BHs. Cosmological simulations (Bromm & Loeb, 2003; Greif et al., 2008; Wise, Turk & Abel, 2008) have shown that an important reservoir of gas can be produced in the inner part of proto-galaxies by the gravitational collapse of the gas. This reservoir could start or at least increase the accretion onto BHs after their formation, counteracting the potential negative feedback from the BH stellar progenitor. At even larger scales, the growth of BHs is sustained by cold filamentary infall (Di Matteo et al., 2012; Dubois et al., 2012b). At later times, galaxy mergers can also boost the accretion onto BHs by redistributing the gas within the resulting galaxy. Several simulations have shown that when a galaxy merger occurs, gravitational tidal fields produce large inflows to galaxies center (Barnes & Hernquist, 1991, 1996, e.g. the early work), boosting the accretion onto the central BH (Di Matteo, Springel & Hernquist, 2005; Di Matteo et al., 2008; Hopkins et al., 2006).

We have seen that to explain the massive end of the BH distribution, high accretion episodes or super-Eddington accretion episodes, have been envisaged (e.g. Collin et al., 2002; Abramowicz, 2005). Supercritical accretion onto BHs at high redshift have been studied (Volonteri, Silk & Dubus, 2015; Pacucci, Volonteri & Ferrara, 2015; Pacucci et al., 2015; Inayoshi, Haiman & Ostriker, 2016). The formation of accretion disks around BHs depend on the accretion rate, here $\dot{m}$ denotes the normalized accretion rate, with $\dot{m} = \dot{\mathrm{M}}_{\mathrm{BH}}/\dot{\mathrm{M}}_{\mathrm{Edd}}$. For low accretion rates, $\dot{m} \leqslant 0.01$, cooling is inefficient, the disk is expanded and radiatively inefficient (Abramowicz & Lasota, 1995). For higher accretion rates, $0.01 \leqslant \dot{m} \leqslant 1$, cooling is more efficient, the accretion disk is geometrically thin and optically thick (Shakura & Sunyaev, 1973). Finally, for much higher accretion rates, $\dot{m} >> 1$, a slim accretion disk forms (Abramowicz et al., 1988). For a slim disk, the luminosity is proportional to:

$$\frac{L}{L_{\mathrm{Edd}}} \propto 1 + \ln(\dot{m}) \propto 1 + \ln(\frac{\dot{\mathrm{M}}}{\dot{\mathrm{M}}_{\mathrm{Edd}}}), \tag{1.49}$$

instead of $\propto \dot{m}$, meaning that the disk is radiatively inefficient, and the luminosity is contained. Super-Eddington accretion does not imply super-Eddington luminosities. The phenomenon occurring here is the trapping of the radiation. For low-angular momentum gas in the center of galaxies, a compact accretion disk (slim accretion disk model) can form out of the low angular momentum infalling gas. The high compactness of the disk, implies the trapping of photons, which can not escape in a time shorter than the timescale for accretion, the luminosity remain lower than the Eddington limit. BH growth could be boosted by a factor of few times the Eddington limit. Using this slim disk model, Volonteri, Silk & Dubus (2015) predict that long-lived super-Eddington accretion occurs only in galaxies with copious low-angular momentum

gas. They are the only galaxies able to fuel central BHs at supercritical rates for sufficiently long times, by forming a slim disk around BHs, which is able to trap radiation for long times. The commonly used Eddington limit may therefore not be a real limit for BH growth.

1.7 Theoretical models for black hole formation in the early Universe

Currently, three main models are popular to explain theoretically the formation of massive BH seeds in the early Universe (Rees, 1978, 1984): the PopIII remnants model, the compact stellar cluster model, and the direct collapse model.
These three models for BH formation rely on different physical processes, but the main idea is to form a massive BH out of a massive star. The mass of the star that forms out of the gas, is relied to the Jeans mass of the medium, that we can write as:

$$\mathrm{M_J} \approx 700 \mathrm{M_\odot} \left(\frac{T}{200\,\mathrm{K}}\right)^{3/2} \left(\frac{n}{10^4\,\mathrm{cm^{-3}}}\right)^{-1/2}. \tag{1.50}$$

The composition of the gas, and so its temperature, sets the Jeans mass. For exemple, in minihalos of $\mathrm{M_{mini\,halo}} \approx 10^{5-6}\,\mathrm{M_\odot}$, where cooling is done by molecular hydrogen, the temperature of the gas goes below 10^4K (see left panel of Fig 1.7). If we assume $T = 200\,\mathrm{K}$, the Jeans mass is $\mathrm{M_J} \approx 700\,\mathrm{M_\odot}$. We will see that massive stars of the first generation are predicted to form in minihalos.
However, in atomic cooling halos of $\mathrm{M_{halo}} \approx 10^{7-8}\,\mathrm{M_\odot}$, where the temperature can be $T = 5000\,\mathrm{K}$ for example, the Jeans mass is much higher $\mathrm{M_J} \approx 10^5\,\mathrm{M_\odot}$, which can lead to the formation of an even more massive star, which may collapse into a direct collapse BH.
Finally if the gas is metal-enriched, cooling is more efficient. Indeed on Fig 1.7 right panel, we see that the cooling curve for metal-enriched gas is above the cooling curve for a primordial composition of the gas. In the presence of metals, the gas can also cool to lower temperatures. Molecules made of heavy elements are responsible for lowering the temperatures to a few K. Therefore the Jeans mass will be much lower. For example, for $T = 10\,\mathrm{K}$, the Jeans mass is around $\mathrm{M_J} \approx 10\,\mathrm{M_\odot}$. This is an intermediate model between the two previous ones, which is called stellar compact cluster model. A compact stellar cluster can form in the central region of proto-galaxies, stars are very close to each other, and can merge together to form a very massive star, that can collapse and form a massive BH.

1.7.1 Remnants of the first generation of stars

In the *PopIII star remnants* model, BHs are predicted to form in mini-halos ($\mathrm{M_h} \approx 10^5\,\mathrm{M_\odot}$) with gas below a critical metallicity ($Z < 10^{-3.5}\,\mathrm{Z_\odot}$, Bromm et al., 2001 ; Schneider et al., 2002) at redshift $z = 30 - 20$ from the remnants of the first generation of stars (PopIII stars, Carr, Bond & Arnett, 1984 ; Madau & Rees, 2001 ; Volonteri, Madau & Haardt, 2003). As we have said in Section 1.3, observational evidence on the initial mass function (IMF) of PopIII stars are lacking, but theoretical studies suggest that they could have masses in the range $10 - 1000\,\mathrm{M_\odot}$ (Bromm & Yoshida, 2011 ; Hirano et al., 2014). A massive star $\mathrm{M_\star} \gtrsim 260\,\mathrm{M_\odot}$ can lead to the formation of a BH seed of $\approx 100\,\mathrm{M_\odot}$ (Fryer, Woosley & Heger, 2001), which retained at least half the mass of the star.

The fate of primordial stars

We have not observed any zero-metallicity star yet. However, their existence has been studied theoretically. In the very early Universe, in the absence of any heavy element (metal), atomic

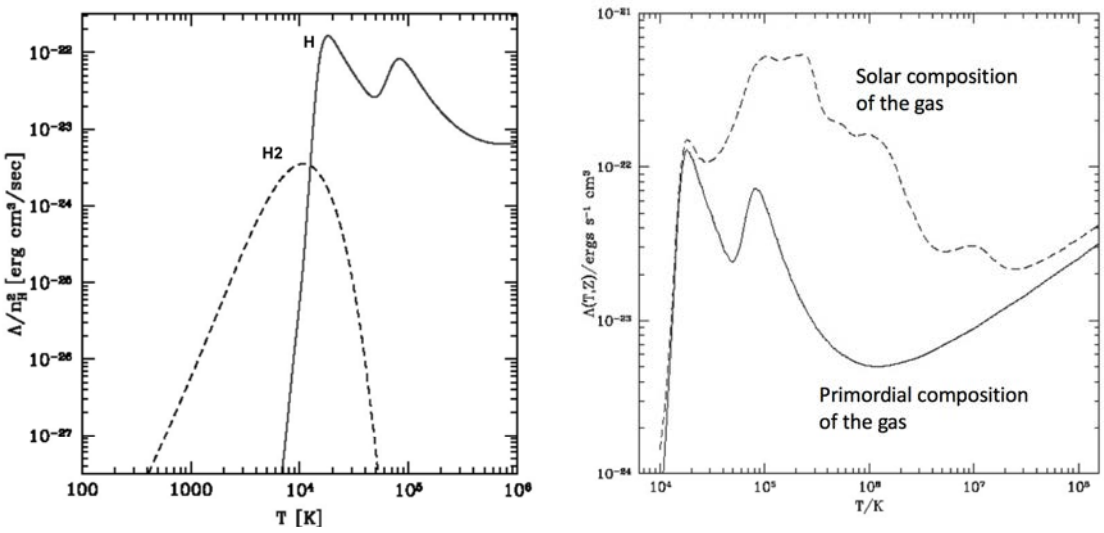

Fig. 1.7 – Left panel: cooling curves for primordial composition of the gas. Right panel: cooling curves for primordial composition of the gas (solid line) and solar composition of the gas (dashed line).

and molecular hydrogen are the only coolants. Then, it was rather difficult for primordial clouds to cool efficiently. Clouds and proto-stars were therefore able to grow in mass (because the Jeans mass, which is proportional to the temperature, was still high), for the gravitational force to balance the internal energy of the gas, and collapse. As a result these stars are predicted to be massive (Bromm & Yoshida, 2011), and to end their life within few Myrs. From Fig. 1.8, we can distinguish 4 domains for the zero-metallicity stars based on their final fate: stars with a mass $M_\star < 25\,\mathrm{M}_\odot$, $25\,\mathrm{M}_\odot < \mathrm{M}_\star < 140\,\mathrm{M}_\odot$, $140\,\mathrm{M}_\odot < \mathrm{M}_\star < 260\,\mathrm{M}_\odot$, and $260\,\mathrm{M}_\odot < \mathrm{M}_\star$.

For the $M_\star < 25\,\mathrm{M}_\odot$ regime:
Stars with mass lower than $8\,\mathrm{M}_\odot$ form white dwarfs. Stars which are more massive than $8\,\mathrm{M}_\odot$ form neutron stars.

For the $25\,\mathrm{M}_\odot < \mathrm{M}_\star < 140\,\mathrm{M}_\odot$ regime:
We can distinguish 3 different mass regimes here. First of all, for stars less massive than $M_\star \leqslant 35\,\mathrm{M}_\odot$, a BH can form by *fallback*. A first explosion of the star, an explosion of SN type, pushes away a significant fraction of the stellar mass by winds, which falls back and collapses to a BH keeping 10% of the initial stellar mass. For more massive stars, however, the helium core is more massive, as well as the oxygen and silicon core masses which prevents a potential SN explosion because of their large infall toward the center. No SNe are formed, and instead a BH forms directly. Finally the last regime consists of the stars more massive than $\sim 100\,\mathrm{M}_\odot$. For this regime, the star experiences the *electron-positron pair creation instability* (that we explain in more detail in the next regime). γ photon collide with atoms of the star, and create e^-/e^+ pairs. The radiation pressure of the star decreases, because a part of γ photons do not contribute anymore to the pressure. Infall starts, and stops when enough energy is released, which leads to a SN explosion. For $\mathrm{M}_\star < 140\,\mathrm{M}_\odot$ stars, however, the explosion is not strong enough to totally disrupt the star, the core can collapse and form a BH directly. The BH will keep less than half the initial mass of the star.

For the $140\,\mathrm{M}_\odot < \mathrm{M}_\star < 260\,\mathrm{M}_\odot$ regime:
Hydrogen forms helium by fusion. Helium in the core of the star also enters fusion reaction, that

we call the *central helium burning* phase. When helium is fully consumed, the temperature and density of the star are sufficiently high for *electron-positron pair creation*, meaning that e^-/e^+ pairs are created in significant proportions. These e^-/e^+ pairs are the result of collisions between atoms present in the star and photons γ, which are abundant in massive stars. This happens when the energy of γ photons is higher than the energy of the created pair, for $E_\gamma > E_{e^-} + E_{e^-}$, the exceeding energy of γ photons is given to the pairs. A part of the internal energy is therefore converted into rest mass energy through the e^-/e^+ pairs. However, photons that participate the reaction, do not contribute anymore to the radiation flux going outwards. Radiative pressure decreases, and can not balance gravity anymore. The star enters an unstable phase, and contracts. The collapse increases the number of pairs annihilations, which leads to an amplification of the photon production, which also increases the temperature of the star. Therefore more e^-/e^+ pairs are created, and so on. High temperature of the star, can lead to the creation of heavier elements depending of the star mass (oxygen, silicium, ...), and could stop its collapse. Under the explosive combustion of these elements, the star ends up its life in an nuclear-powered explosion. In this regime, the energy of the explosion is higher, and can even reach $\sim 10^{53}\,\mathrm{erg\,s^{-1}}$, and leave no compact object behind, all the metals are ejected in the surrounding ISM.

For the $M_\star > 260\,\mathrm{M}_\odot$ regime:
For the massive end of the stellar distribution of metal-free stars, the *photodisintegration* process allows the star to avoid the last explosive combustion phase. Because of the high temperature and pressure in the core, atoms can absorb very energetic photons. Atoms enter an excited state, their desexcitation is done by the emission of protons, neutrons, and α particles. The energy produced by the combustion of elements is therefore converted, and the star can avoid the final explosion and disruption. Temperature and pressure are decreased by the *photodisintegration* process, which favors the collapse, and the formation of a compact BH, able to retain at least half the initial stellar mass.

Difficulties and incertainties of the PopIII remnants scenario
First of all, large uncertainties remain on the first generation of stars, regarding their initial mass (properties of accretion into the core, external effects may also play an important role, such as feedback from UV radiation, CMB temperature), their number density in the early Universe, and the distribution of their formation (single stars or stellar cluster in minihalos).
The incertainty on the initial mass of BHs formed through the PopIII remnants model is a problem. Low-mass BHs will not be able to reach the center of the galaxy's potential well, they will instead interact dynamically with other objects as BHs and stars, and wander into their host galaxy, which does not favor high accretion rate into BHs. They would hardly accrete enough mass to form the population of quasars we observe at $z = 6$ (e.g. Pelupessy, Di Matteo & Ciardi, 2007).
This is even worse if we consider that they produce large ionizing radiation, which can heat the surrounding gas, and leave a potential BH in a low density environment, not very propitious for high accretion episodes of the seed. Simulations with radiative transfer coupled to the hydrodynamics (Alvarez, Wise & Abel, 2009), modeling the radiation form the PopIII star progenitor, have allowed one to study BH growth immediately after the death of the PopIII progenitor. BH growth is regulated by radiative feedback, which alters the accretion flow from large scales (see also, Milosavljevic et al., 2009), and keeps the BH in a low-density and high temperature gas environment, resulting in a low accretion rate into the BH. Therefore, radiative feedback makes even more difficult the growth of BH (Alvarez, Wise & Abel, 2009).

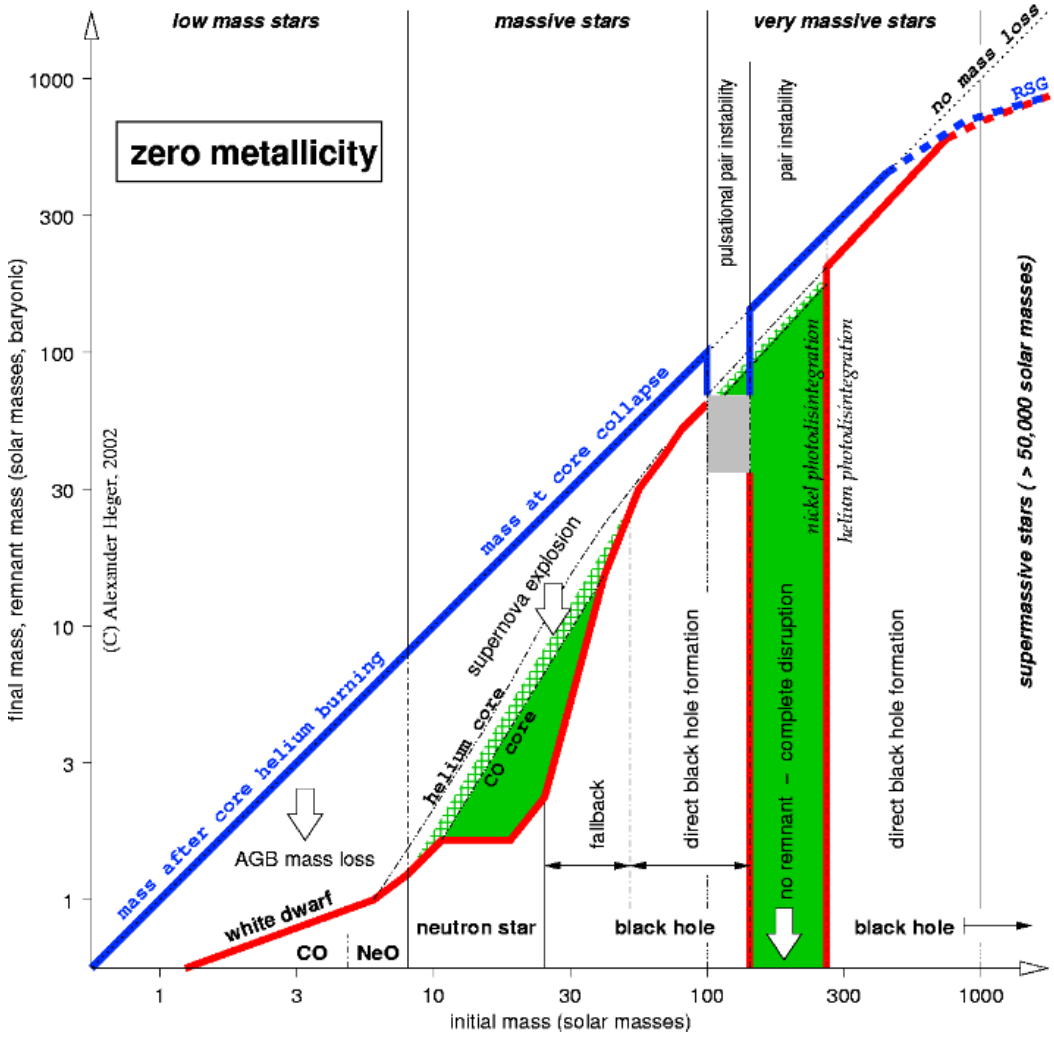

Fig. 1.8 – The fate of primordial stars (zero metallicity, non-rotating), from Heger et al. (2003). The figure shows the initial mass of primordial stars (x-axis), the stellar mass at time of final explosion/remnant formation (thick blue line), and the mass of the remnant object that is left behind after the death of the star (y-axis, thick red line). Metals released are shown in green filled and hatched regions. Four mains cases are distinguished based on their final fate: the fate of stars $M_\star < 25\,M_\odot$ leads to the formation of white dwarfs and neutron stars, stars within the range $25\,M_\odot < M_\star < 140\,M_\odot$ will form a BH, stars within the range $140\,M_\odot < M_\star < 260\,M_\odot$ will leave no compact remnant behind, and finally stars $260\,M_\odot < M_\star$ will lead to the formation of massive BHs.

However mechanisms for super-Eddington accretion have been developed (Volonteri, Silk & Dubus, 2015 ; Madau, Haardt & Dotti, 2014 ; Lupi et al., 2016). Episodes of super-Eddington accretion could allow PopIII remnant BHs to reach mass consistent with high redshift quasars. Lupi et al. (2016) simulate a idealized cluster of stellar mass BHs orbiting the inner part ($\sim 200\,\mathrm{pc}$) of a gas-rich galaxy. They model BH thermal feedback, which allows for different periods of radiatively inefficient accretion burst, during which the BHs can accrete mass at super-Eddington accretion rate. They find that the growth of the simulated BHs, acquiring $\sim 10^{3-4}\,\mathrm{M}_\odot$ on Myr timescales, is consistent with the the mass that should have quasars progenitors.

1.7.2 Compact stellar clusters

The death of the first generation of stars, inevitably leads to the release of metals into the surroundings, galactic winds can then push these metals farther, and pollute nearby halos. In the presence of metals, cooling is more efficient, ensuring fragmentation in these nearby halos. The formation of a second generation of stars is therefore initiated (Omukai, Schneider & Haiman, 2008), these PopII stars are less massive than the PopIII stars. Indeed, gas cooling is more efficient due to the presence of metals and molecules, and therefore the Jeans mass is smaller, the gas fragments and leads to the formation of less massive PopII stars.
Compact nuclear clusters often inhabit the center of galaxies. Such a cluster in the inner part of galaxies at high redshift, in relatively metal-poor environments, could have collapsed and form a very massive star, up to $\sim 1000\,\mathrm{M}_\odot$, by stellar collisions.
At high redshift, dense regions in proto-galactic disks, distributed uniformly in the entire disk, would fragment into several clumps, when their mass reaches the Jeans mass, and therefore would lead to star formation in the entire disk. In Toomre-unstable disks, instead, instabilities can lead to mass inflow toward the disk center, no fragmentation happens. Therefore the density of the central part of the disk increases, and star formation only occurs at the center of the galaxy. A compact stellar cluster forms in the central region. For metallicity of $10^{-4} - 10^{-5}\,\mathrm{Z}_\odot$, the typical mass of the cluster is $10^5\,\mathrm{M}_\odot$, the half mass radii is ~ 1pc (Devecchi & Volonteri, 2009 ; Regan & Haehnelt, 2009a ; Volonteri, 2010).
The stars and the parent cluster evolve on more or less the same timescales, the evolution of stars and the cluster dynamics are coupled, and therefore difficult to study. Portegies Zwart et al. (1999) use N-body simulation to study the evolution of young compact stellar clusters. A cluster of different mass stars is more likely, in this case massive stars will segregate from the others less massive ones, because of dynamical friction, then increasing the probability for these stars to collide. Runaway collisions between stars can happen, leading to the formation of a very massive star, which can collapse into a BH.
Metallicity appears to be a crucial parameter in this scenario, for two main reasons. First of all, because in metal-poor environment stars are more massive, and stars $> 40\,\mathrm{M}_\odot$ are predicted to collapse directly into a BH without exploding in SN (Heger et al., 2003). The second reason is that runaway collisions between stars lead to a significant mass loss (Portegies Zwart et al., 1999).
However, for metal-poor stars, mass loss is reduced. The metal-poor conditions are therefore related to mass losses through winds. Yungelson et al. (2008) study the stellar evolution of solar composition stars in the mass range $60 - 1000\,\mathrm{M}_\odot$. They find that they shed most of their mass via winds and are expected to end their lives as BHs less massive than $\sim 150\,\mathrm{M}_\odot$. At low metallicity, instead, mass loss due to winds is much more reduced, thus increasing the mass of the final remnant (Heger et al., 2003 ; Vink, 2008 ; Mapelli, Colpi & Zampieri, 2009 ; Belczynski

et al., 2010; Mapelli et al., 2013; Spera, Mapelli & Bressan, 2015).
A metal-poor environment therefore favors the formation of a more massive star at the beginning, but also its growth. A BH seed of $10^3\,M_\odot$ can be formed in this nuclear cluster model (**?**Devecchi & Volonteri, 2009; Regan & Haehnelt, 2009b; Katz, Sijacki & Haehnelt, 2015). Devecchi & Volonteri (2009) find that 5% of protogalaxies at $z = 20-10$, could form a BH by this mechanism.

1.7.3 Direct collapse of gas

One recent way of solving the problem of the formation of such massive objects is by the direct collapse of pristine gas triggered by dynamical processes (Loeb & Rasio, 1994; Eisenstein & Loeb, 1995; Koushiappas, Bullock & Dekel, 2004; Begelman, Volonteri & Rees, 2006; Lodato & Natarajan, 2006; Mayer et al., 2010), or invoking isothermal collapse in primordial halos (Bromm & Loeb, 2003; Spaans & Silk, 2006; Dijkstra et al., 2008; Latif et al., 2013a) . This scenario has become very popular, as it can lead to the formation of $10^4 - 10^6\,M_\odot$ seeds, making it easier to reproduce the quasar population at $z > 6$. All these models rely on different physical processes and have so different requirements, among which avoiding the fragmentation of the gas, angular momentum transport, metal-poor environment, large inflow rate of gas. We first describe models which can be classified as dynamical processes, and then move to isothermal collapse models.

Direct collapse model requires to avoid the fragmentation of the gas, and also the accumulation of mass in halo center, to form only one massive object in the center. Several models based on dynamical processes have been studied.
Turbulent systems (with supersonic turbulence), metal-free or not, have been shown to suppress the fragmentation of the gas (Begelman & Shlosman, 2009). The non-requirement of metal-free or metal-poor conditions of halos, makes this model feasible at lower redshift and in metal-rich halos. The formation of BHs in metal-rich galaxies has also been investigating more recently (Mayer et al., 2010, 2014). In this model, a stable compact nuclear disk forms, and is fulfilled with large accretion rate of $\sim 10^4\,M_\odot$, as a result of metal-rich galaxy merger. The disk can then collapse and form a BH. We will see later than the fragmentation of the gas can also be prevented in the presence of LW radiation, that suppress H_2.
Angular momentum transport is crucial to form a massive object in halo center, mass needs to travel inwards, and the angular momentum outwards. Indeed, to form a unique and massive object, mass needs to accumulate at the center of the halo. Gravitational systems, such as halos, are thought to possess a given degree of rotational support, which is described by the spin parameter $\lambda_{\rm spin} = J|E|^{1/2}/GM_{\rm h}^{5/2}$, with J the angular momentum of halos, E the total energy, and $M_{\rm h}$ the mass of halos. The angular momentum of a halo, or its baryonic central region, is thought to be the result of clustering/surrounding neighbors applying tidal torques on the given halo (Peebles, 1969). Before collapsing into a single massive object, the gas needs to settle into a rotationally supported proto-galactic disk (for example, see Oh & Haiman, 2002). BH formation in low angular momentum environment is supported by analytical models. Eisenstein & Loeb (1995) used an analytical model to investigate the origin of BHs from the collapse of low-spin cosmological perturbations. They derived the spin distribution of halos, and found that enough low-spin halos to explain the population of BHs. Koushiappas, Bullock & Dekel (2004) studied instead the formation of BHs in low angular momentum gas, present in all halos massive enough to host an unstable self-gravitating disk. They only consider the low angular momentum tail of material of halos. A fraction of low-spin gas should lead to an infall of gas in the central region, and to its collapse. Transport of angular momentum to lead to large infall of mass through the

center of the disk is generally still needed.
Dynamical instabilities, either global (Shlosman, Frank & Begelman, 1989 ; Begelman, Volonteri & Rees, 2006) or local (Lodato & Natarajan, 2006), are among the processes to transport angular momentum. *Bars within bars* model is one of the angular momentum transport mechanisms (Begelman, Volonteri & Rees, 2006). Halo gas cools and collapses gradually until rotational support halts the collapse. When rotational support becomes important, self-gravitating gas clouds can become *bar-unstable*. Therefore, gravitational and hydrodynamical instabilities lead to angular momentum transport along the bar. Because the gas is able to cool, the system contracts, more instabilities are therefore created within the system, a new bar is formed, and so on. The transport of the angular momentum outwards allows the mass to travel inwards. The mechanism forms a supermassive star, its core can collapse into a BH of $10 - 20\,\mathrm{M}_{\odot}$. Accretion forms the envelope can lead to high accretion rate into the BH, located in the core. The BH growth is limited by the Eddington limit of the whole system (BH in the core and the whole quasi-star), and therefore high accretion into the BH are possible while the BH mass is lower than the mass of the envelope (Begelman, Volonteri & Rees, 2006).
Redistribution of angular momentum and mass, can also be achieved via local instabilities (Lodato & Natarajan, 2006), for marginally stable disks in protogalaxies (stability of the disk is determined via the Toomre parameter), when the disk gets massive enough to be stable. When the Toomre parameter of the disk is close to the limit for stability, the disk experiences gravitational instabilities, that can lead to mass infall to the center of the disk, instead of gas fragmentation. Once enough mass has been transported to make the disk stable again, the process stops, and a massive star-like object can form in the center.

The physical conditions (listed below) required for isothermal collapse in primordial halos, which has become the most popular version of direct collapse in the last couple of years, and whose BH seeds are typically referred to as "DCBHs", are numerous. First, one needs a halo that has reached the atomic cooling threshold, $\sim 10^7 - 10^8\,\mathrm{M}_{\odot}$, but it is still pristine, i.e., metal-free (metal-free or metal-poor were not required for most of the scenarios listed in the previous section). A large inflow rate of gas at the center of the halo is also required. Angular momentum transport has also an important role, as discussed in the previous section. In the following, we develop in more detail these conditions for the isothermal collapse model.
One needs that the molecular hydrogen formation has been suppressed throughout the halo's evolution. The presence of metals and molecular hydrogen would decrease the temperature of the gas, and so the Jeans mass. This could lead to the fragmentation of the gas cloud, therefore the formation of only one massive object is unlikely, and the formation of several less massive objects, namely PopIII stars, is instead expected.
The destruction of molecular hydrogen can be accomplished by strong photo-dissociating radiation (Lyman-Werner, LW, photons with energy between 11.2 eV and 13.6 eV), and its prevention by photo-detachment of H^-. The destruction of H_2 is characterized by the reaction:

$$\mathrm{H}_2 + \gamma_{\mathrm{LW}} \rightarrow \mathrm{H} + \mathrm{H} \tag{1.51}$$

In this channel, which is based on the Solomon process, photons in the energy range $11.2 - 13.6\,\mathrm{eV}$ can be absorbed by H_2 (in the LW band), H_2 accedes an excited state, and photodissociates the molecule. For the photo-detachment of H^-, we have the following reaction:

$$\mathrm{H}^- + \gamma_{0.76\,\mathrm{eV}} \rightarrow \mathrm{H} + \mathrm{e}^- \tag{1.52}$$

The rate of H^- decreases, this prevents the formation of H_2 via the H^- channel.
Trapping of Lyman α photons could increase the temperature of the gas, therefore destroying

H_2, it would also stiffen the equation of state, and make more difficult the fragmentation of the gas (Spaans & Silk, 2006).

Radiation intensity J_{crit}:
J_{crit} (in units of $10^{-21}\,erg\,s^{-1}\,cm^{-2}\,Hz^{-1}\,sr^{-1}$) defines the level of LW radiation intensity required to dissociate a critical fraction of H_2, and depends on the stellar population, namely the black-body curves, and the ratio of 0.76 eV photons to LW photons produced by these stellar populations (Shang, Bryan & Haiman, 2010; Wolcott-Green, Haiman & Bryan, 2011).
Omukai (2001) use a 1D-zone model where spherical clouds are irradiated by photodissociating radiation, and find that when $J_{crit} \sim 10^5$, both suppression of H_2 formation, and photodissociation of H_2, prevent H_2 cooling. Bromm & Loeb (2003) use 3D hydrodynamical simulations and show that for a thermal spectrum with $T_{\star,III} = 10^5\,K$, $J_{crit} \geqslant 10^5$, and for a lower temperature $T_{\star,II} = 10^4\,K$, $J_{crit} \geqslant 10^3$, which is consistent with the previous 1D analysis of Omukai (2001). Temperature $T_{\star,III} = 10^5\,K$ refers to a Pop III population, whereas $T_{\star,II} = 10^4\,K$ refers to a PopII population. Shang, Bryan & Haiman (2010) using 3D hydrodynamical simulations of halos and a 1D model similar to Omukai (2001), find lower values (by a factor up to 10) for the critical radiation intensity, which can be due to a more accurate rate of H_2 collisional dissociation.
From this model, it is commonly admitted that a PopIII stellar population ($T_{\star,III} \sim 10^5$ K) leads to $J_{crit} = 10^3 - 10^4$, whereas a PopII population ($T_{\star,II} \sim 10^4$ K) to $J_{crit} = 30 - 100$ (Shang, Bryan & Haiman, 2010).

The difference in the critical radiation intensity for PopIII and PopII stars is also due to the abundance of 0.76 eV photons with respect to the LW photons. H^- is photodetached via reaction 1.52. More 0.76 eV photons are produced for PopII stars than PopIII stars, compared to LW photons (Omukai, Schneider & Haiman, 2008), offering another channel for the destruction of H_2 molecules. Therefore, the contribution of LW photons, which is encoded in the critical radiation intensity J_{crit}, does not need to be as high for PopII stars as for PopIII stars.
A single value for the critical radiation intensity is unlikely, instead a spread on a distribution of possible values is expected, as discussed by Sugimura, Omukai & Inoue (2014); Agarwal & Khochfar (2015); Agarwal et al. (2015b).
In any case, the value derived by the models cited above (i.e. $J_{crit} = 30 - 100$), are much lower than the radiation intensity that is required in 3D cosmological hydrodynamical zoom-in simulations. A radiation intensity of $J_{crit} > 500 - 1000$ is found in Regan, Johansson & Wise (2014); Latif et al. (2014, 2015).
The star-forming galaxies that can provide photo-dissociating LW radiation, are susceptible to also provide X-ray radiation, which can travel in the inner part of halos, and ionize the gas. This leads to an enhancement of the formation of H_2. Inayoshi & Tanaka (2015) show that taking into account X-ray ionization can indeed increase the critical flux to even higher values, and therefore decreasing the number density of BHs (see also Latif et al., 2015).

PopIII vs PopII
The LW radiation intensity is expected to be mainly driven by PopII stars, for different reasons. First, a small radiation background will impact stellar formation, H_2 is photo dissociated, which decreases the cooling and the formation of PopIII star (Agarwal et al., 2012; Johnson et al., 2012). Agarwal et al. (2012) use a semi-analytical model of radiation intensity variation on top of a DM simulation. They compute the star formation rate of PopIII stars, which drops at $z = 16$, when PopII stars start forming. Johnson, Dalla Vecchia & Khochfar (2013) run

cosmological simulations with and without LW radiation. Here again PopIII star formation drops at $z \sim 11 - 12$. PopIII star formation rate appears to be regulated by LW feedback.
Second, the life time of PopIII stars is shorter than the PopII star, their contribution to provide a high radiation intensity is certainly limited. The lifetime of a PopIII star is ~ 10 Myr. Since one halo must be illuminated by the LW radiation for at least one free-fall time to collapse and form a DCBH, one can compute the redshift at which the free-fall time is approximately equal to ~ 10 Myr, which is $z \sim 45$. If a DCBH forms in a halo illuminated only by Pop III stars, it should form at very early time around $z \sim 45$.
Another argument is that the radiation flux produced by Pop III stars only, does not provide enough radiation intensity to provide the critical intensity J_{crit} commonly assumed for DC scenario (Agarwal et al., 2012). Finally, the abundance of PopII stars is higher than the PopIII one, and therefore they are also expected to contribute more to the radiation intensity for this reason.

A large inflow rate of gas

A large inflow rate of gas at the center of the halo, higher than $0.1\,M_\odot$/yr, and sustained for at least 10 Myr, is also needed to form a supermassive star-like object in the nucleus (Begelman, Volonteri & Rees, 2006; Begelman, Rossi & Armitage, 2008; Begelman, 2010; Ball et al., 2011; Hosokawa, Omukai & Yorke, 2012; Hosokawa et al., 2013; Schleicher et al., 2013). An additional argument for the few Myr time scale for the accretion time scale is the life time for massive stars. Basically all the mass must accrete before the main-sequence life time is up. In the absence of H_2, the collapse proceeds isothermally at the temperature of ~ 8000 K, the accretion onto the central region is driven by warm gas flows, with an accretion rate of order the free-fall rate:

$$\dot{m} \sim \frac{c_s^3}{G} \sim 0.1 \left(\frac{T}{8000\mathrm{K}}\right)^{3/2} M_\odot/\mathrm{yr} \tag{1.53}$$

with c_s the sound speed, T the temperature of the gas. The BH mass can be up to 90% of the stellar mass.

Number density of DCBH

Because of all the strict conditions that we have enumerated, namely the absence of efficient coolants as molecular hydrogen or metals, and therefore the destruction of H_2 by a strong photo-dissociating flux, but also a high accretion rate into the halo center, the DCBH scenario is predicted to be quite rare. The scenario predicts the formation of very massive seeds of about $\sim 10^5\,M_\odot$, which are the perfect candidates for the population of quasars we see up to $z = 6 - 7$. Over the last decade, the question of the number density of BH formed through the DC scenario has therefore been studied, and via different methods: semi-analytic models, or recently hybrid models where the spatial distribution of halos is taken from cosmological simulations. Among the semi-analytical models, Dijkstra et al. (2008) derive a number density of $10^{-6} - 10^{-8}\,\mathrm{cMpc}^{-3}$. Dijkstra, Ferrara & Mesinger (2014) investigate several physical processes, among which metal-polluted galactic winds, and derive the number density of DCBHs for different J_{crit}. In Fig. 1.9, we show the number density derived by Dijkstra, Ferrara & Mesinger (2014), for various models. Few studies have taken advantage of the spatial information that cosmological simulations offer (Agarwal et al., 2012; Habouzit et al., 2016b, for dark matter only simulations), specially hydrodynamical ones when one can track metal-enrichment (Agarwal et al., 2014; Habouzit et al., 2016a). Agarwal et al. (2012) find a higher number density than the previous pure semi-analytical models, around $10^{-1}\,\mathrm{cMpc}^{-3}$ for $J_{crit} = 30$, for the same critical intensity Agarwal et al. (2014)

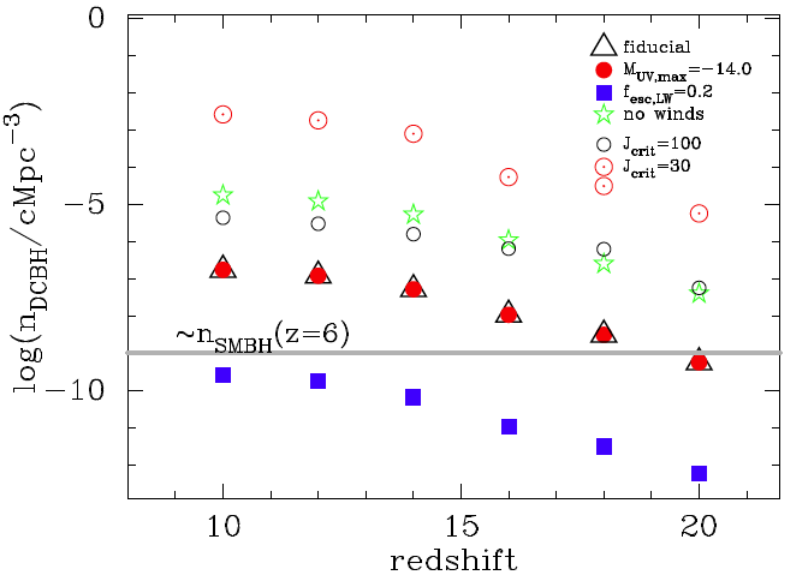

Fig. 1.9 – Number density of DCBHs from Dijkstra, Ferrara & Mesinger (2014). Triangles represent their fiducial model, with $J_{crit} = 300$, star formation occurring in all dark matter halos with $T_{vir} > 10^4$ K, escape fraction $f_{esc} = 1$, including metal-pollution from galactic winds. Green stars represent the same model without taking into account pollution by galactic winds. Black circles represent the fiducial model, but decreasing the critical radiation intensity to $J_{crit} = 100$, and for red circles to $J_{crit} = 30$. Blue squares represent the fiducial model, decreasing the escape fraction to $f_{esc} = 0.2$.

find a number density of the same order.
We do not develop further the number density of DCBH in this section, neither the large spread of values that have been derived by the various models cited above. We will assess these questions in detail in chapter 3.

1.7.4 Other models

Other BH formation models have been studied, such as primordial BHs. Those are predicted to form before the epoch of galaxy formation in regions where high density fluctuations are large, the whole region is predicted to collapse to form a BH. These primordial BHs would have mass of order the particle horizon mass at their formation time (Carr, 2003):

$$M_{PBH}(t) \sim \frac{c^3 t}{G} \sim 10^{15} \left(\frac{t}{10^{-23}\,\mathrm{s}} \right) \mathrm{g}. \tag{1.54}$$

Therefore if primordial BHs form at the Planck time ($t = 10^{-43}$ s), there initial mass would be equal to the Planck mass ($M_{PBH} = 10^{-5}$ g). If BHs form at 1 s, there mass would be much higher ($M_{PBH} = 10^5\,M_\odot$).

1.8 Diagnostics to distinguish between BH formation scenarios

BHs form in the early Universe, out of any possible observation with current facilities. Investigating the formation of BHs, therefore requires to derive observational diagnostics on the galaxies we can observe today, the local galaxies, in analogy with galactic archeology. Two theoretical diagnostics to distinguish between the different BH formation models, have been discussed in the literature (Volonteri, Lodato & Natarajan, 2008 ; Volonteri & Natarajan, 2009 ; van Wassenhove

et al., 2010).
The BHs we observe today, have grown over cosmic time from lower-mass BH seeds. Initial conditions are likely to be erased if accretion onto BHs is efficient. BHs grow by accretion and BH-BH mergers. Accretion onto a BH is boosted when galaxy-galaxy major mergers occur. Massive galaxies have a high probability that their central BH is not pristine anymore. The central BH may indeed have increased its mass through accretion, which is boosted by several major mergers of the host galaxy, but also BH-BH mergers and dynamical interactions. Clues on the BH initial mass are erased. However, low-mass galaxies, which have a much quieter cosmic evolution, host a BH today with a mass that is expected to only differ slightly from the initial BH seed mass. Therefore the mass of BHs in today's low-mass galaxies can provide us crucial information on the initial BH mass distribution.

Accretion and mergers alter the initial mass of BHs. The presence of a BH or not within a galaxy is, however, not affected. The probability for a galaxy to host a BH, the *BH occupation fraction*, is therefore a sensitive clue on the efficiency of BH formation mechanisms at high redshift. Moreover, signatures in low-mass galaxies are even stronger (Volonteri, Lodato & Natarajan, 2008). This can help us to distinguish between BH formation models, as illustrated in Fig. 1.10 reproduced from Greene (2012). On the top, the two most popular scenarios to form BHs are reproduced. On the left, the direct collapse scenario is predicted to form BHs only in few massive halos, because of the many conditions required by the scenario. On the right, we see that many galaxies will host a PopIII remnants BH: conditions to form these BHs are less strict. Using semi-analytical models, associated with the extended Press-Schechter formalism, Volonteri, Lodato & Natarajan (2008) study comparisons of the BH mass - galaxy velocity relation for different seeding models, and show that the fraction of galaxies without BH increases with decreasing halo mass at $z = 0$. Moreover, while PopIII remnants scenario leads to populate nearly all $z = 0$ galaxies, the direct collapse scenario has a much smaller efficiency to establish BH in galaxies. van Wassenhove et al. (2010) use similar techniques to simulate specifically the evolution of BHs in satellite galaxies of a Milky Way size halo, and study the properties of BHs in satellites surviving until today. They seed the high redshift progenitor halos with BH seeds, formed through the PopIII remnants and direct collapse models. They find that the direct collapse BH population is present in only a few percent of dwarf galaxies, but that they are more massive, and could be detected more easily. Whereas the PopIII remnant BHs are more abundant in low-mass galaxies, but they are predicted to be difficult to observe because of their very low masses.
Finally, the idea of a *plume* emerges in Volonteri & Natarajan (2009). Stellar remnant-like scenarios predict the formation of *light* seeds ($M_{BH,ini} \sim 100\,M_\odot$), the direct collapse scenario, instead, predicts the formation of *heavy* seeds ($M_{BH,ini} \sim 10^{4-6}\,M_\odot$). As discussed earlier, crucial clues on BH formation can remain in low-mass present-day galaxies, BHs there are predicted to not have grown much over cosmic time. Therefore, if the direct collapse model was the predominant model of BH formation, we should detect in low-mass galaxies a threshold for the minimal mass of BHs, which would correspond to an asymptote, or a plume, in the BH mass - galaxy velocity dispersion diagram, when moving to lower galaxy velocity dispersions. Investigating this plume requires to have the resolution to detect large samples of low-mass galaxies, and to go to lower and lower galaxy mass, what we are starting to do (Reines, Greene & Geha, 2013).

In practice, many difficulties appear when trying to determine the BH mass distribution in

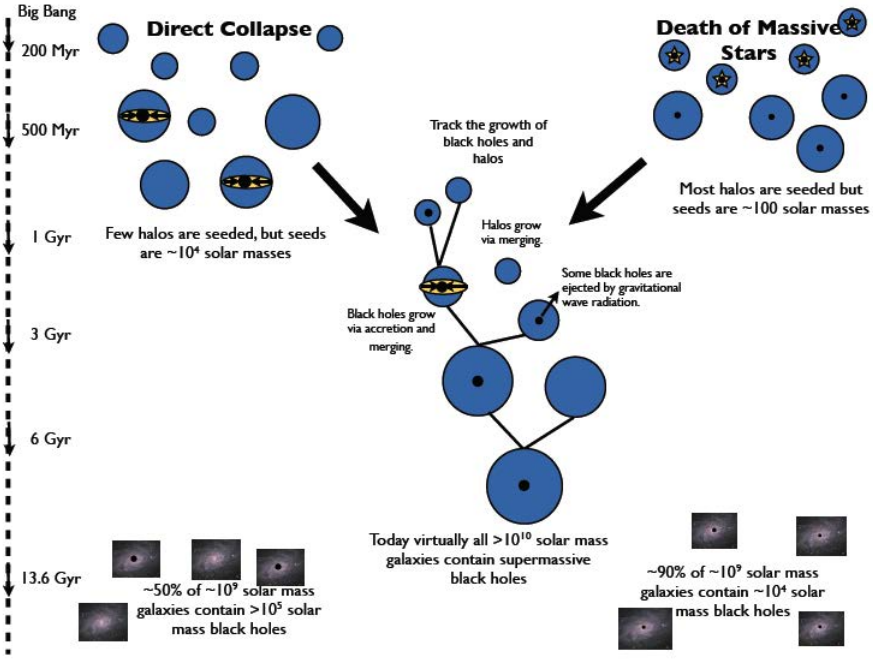

Fig. 1.10 – BH occupation fraction is one of the diagnostics to distinguish between BH formation scenarios. In the cartoon (Greene, 2012), on the top, the two most popular scenarios to form BHs are reproduced. On the left, the direct collapse scenario is predicted to form only in few massive halos, because of the many strict conditions required by the scenario. On the right, we see that many galaxies will host a PopIII remnants BH, conditions are less strict. The Universe evolve, halos and galaxies merge. The bottom pictures show two realizations of today's Universe. On the left, only 50% of the galaxies $M_{gal} < 10^9\,M_\odot$ host a direct collapse BH, on the right, instead, up to 90% $M_{gal} < 10^9\,M_\odot$ galaxies host a BH.

low-mass galaxies, and the occupation fraction (Greene, 2012 ; Reines, Greene & Geha, 2013). Difficulties to detect BHs in low-mass galaxies have already been discussed in section 1.4.1., we only recall, here, the main ideas. Observationally, we are always biased by luminous objects, observing faint objects is of course more challenging. Samples are often made with optical diagnostics, which are only sensible to powerful accreting BHs. We are missing BHs which are accreting at low accretion rate. Low-mass BHs are quite faint, even if they are accreting at the Eddington limit. Small galaxies are not the easiest galaxies to observe either, they are often showing signatures of on-going star formation, therefore one has to distinguish between emission lines due to the presence of a BH and of the star formation episode. The presence of gas and dust in abundance is also problematic because absorbing or masking the accretion properties of BHs. In section 1.4.1., we have highlighted recent works, that provide alternative observational diagnostics to detect galaxies hosting a central BH, and that will be used in the future to make larger samples.

Measuring the occupation fraction is even more challenging. Recently, Miller et al. (2015) investigate the occupation fraction of $M_{gal} < 10^{10}\,M_{\odot}$ within the AMUSE survey (X-ray detection) of early-type galaxies. They find a lower limit of $> 20\%$ for the occupation fraction of these galaxies. On Fig. 1.11, we show the occupation fraction derived by Miller et al. (2015). This thesis aims to provide a theoretical framework of BH formation models, and to derive theoretically several properties as the distribution of BH mass, and the occupation fraction in low-mass galaxies, that can be compare to the future observational data.

Finally, several works have recently look beyond the local Universe to investigate the population of BHs in low-mass galaxies Mezcua et al. (2016) realize an X-ray stacking analysis of dwarf galaxies with $M_{\star} \leqslant 3 \times 10^{9}\,M_{\odot}$ in the COSMOS field for $z < 1.5$. An X-ray excess, which is an evidence for accreting BHs, is found in each bin from $z = 0$ to $z = 1.5$, used for the stacking method. BH masses are estimated to $\sim 10^{5}\,M_{\odot}$. This show that BHs in low-mass galaxies exist in that redshift range, however stacking analysis does not allow an estimation of the BH occupation fraction. Pardo et al. (2016) perform a search for BHs in dwarf galaxies $M_{\star} \leqslant 10^{9}\,M_{\odot}$ beyond the local Universe, up to $z \leqslant 1$, to quantify the AGN fraction in galaxies. This approach gives an upper limit on the occupation fraction of BHs in dwarf galaxies. This study use X-ray data, and also multi-wavelength method is used to derive galaxies properties. BH masses are estimated using the empirical relation between BH mass and stellar mass, which lead to masses in the range $M_{BH} \sim 10^{5} - 10^{6}\,M_{\odot}$. They find an AGN fraction of 0.6-3% for galaxies in the range $10^{9}\,M_{\odot} \leqslant M_{\star} \leqslant 3 \times 10^{9}\,M_{\odot}$, and $0.1 \leqslant z \leqslant 0.6$, which is in agreement with what is found in the local Universe (Reines, Greene & Geha, 2013 ; Miller et al., 2015). This is also in agreement with semi-analytical models which study jointly BH and galaxy formation and evolution (Somerville et al., 2008 ; Hirschmann et al., 2012a), and allow one to predict the BH occupation fraction or the AGN fraction, for example. Our work, specifically chapter 3 is a complementary approach to the one used in semi-analytical models (see Hirschmann et al., 2012a, for a comparisons between hydrodynamical simulations, and semi-analytical models, in terms of galaxy content evolution), physical processes (metal enrichment, stellar and BH feedback, etc) evolve self-consistently within cosmological hydrodynamical simulations, and also allow one to predict the BH occupation.

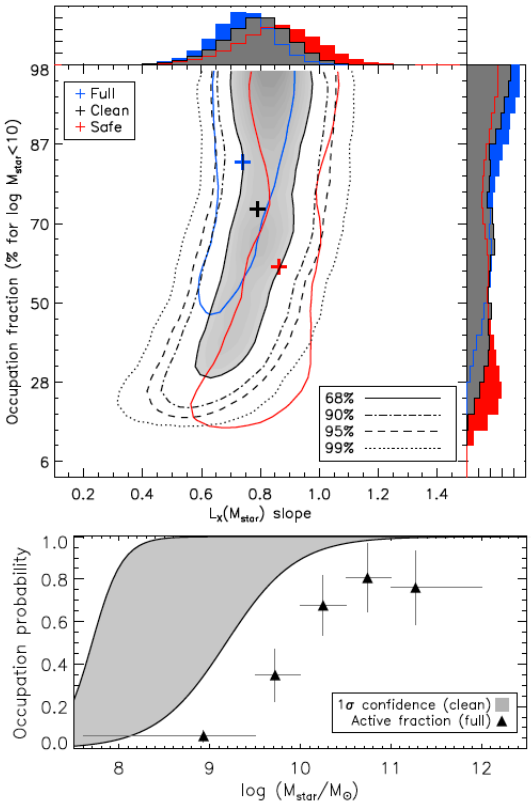

Fig. 1.11 – BH occupation fraction is one of the diagnostics to distinguish between BH formation scenarios. Miller et al. (2015) investigate the occupation fraction of $M_{gal} < 10^{10}\,M_{\odot}$ within the AMUSE survey (X-ray detection) of early-type galaxies. They find an lower limit of $> 20\%$ for the occupation fraction of these galaxies.

1.9 Organization of the thesis

The thesis is organized as follows. The present chapter gave an introduction of the physics and processes needed for the evolution of large-scale structures, the formation of the first stars and galaxies, and gives an introduction of the observational discovery of quasars and active galactic nuclei. We have described the main features of supermassive black holes, which are thought to power the powerful objects cited above, including their growth and their formation through the main popular mechanisms that have been derived theoretically.

Chapter 2 gives an overview of the main numerical tools used in this thesis. We describe the numerical code RAMSES, which has an hydrodynamical solver, with adaptive mesh refinement. We also briefly mention the other simulation code GADGET used in this thesis.

In chapter 3, we describe our implementation of BH formation models in the cosmological hydrodynamical code RAMSES, accounting for the PopIII stellar remnants and stellar cluster theoretical scenarios (*light seed* models). In this chapter, we investigate BH formation, and the distribution and early growth of BH seeds. We also perform a comparison of three different SN feedback implementations in order to understand the impact of SNe on the formation and growth of BHs. We compare the simulated BHs to observations of Lyman-Break Analogs and BHs of a local sample. We also describe the next step of this analysis, which is to understand what triggers the mass accretion onto BHs, to do so we follow in time BHs in the simulations.

Chapter 4 focuses on another BH formation scenario (*heavy seed* model), the direct collapse mechanism, which can lead to the formation of $10^5\,M_\odot$ BHs at early time of the Universe. We perform cosmological hydrodynamical simulations of different sizes and resolutions, with the code RAMSES. This allows us to investigate the impact of different physical processes, such as SN feedback, or critical radiation intensity, for example. We also directly investigate the question of DCBHs as the precursors of the quasars we observe at $z = 6$, with the large scale simulation, Horizon-noAGN. It consists of the largest simulation box used to study the DC scenario so far, and gives a first global view of the scenario. We derive the number density of DCBHs for all the simulations used in this work. We perform a comparison between different previous studies, including pure semi-analytical and hybrid models, and investigate the discrepancies between them.

In chapter 5, we investigate the consequences of primordial non-Gaussian perturbations on galaxy formation/evolution, reionization, and finally on black hole formation/evolution. We use the code GADGET-2, and run several dark matter simulations with either Gaussian or non-Gaussian conditions with several models of the non-Gaussian parameter f_{NL}. Various semi-analytical models are used to paint galaxies, and black holes on dark matter halos.

Chapter 6 concludes on all the studies made in this thesis.

Chapter 2

Numerical simulations

To capture the non-linear evolution of the Universe, numerical simulations are an essential tool. They are designed to study both the formation and evolution of large scale structures, such as filaments, dark matter halos, clusters of galaxies, and physical processes happening at galactic scales, such as galaxy formation and evolution, stellar formation, stellar feedback, but also feedback from black holes. This requires several orders of magnitude in spatial and gas density scales. A fine resolution is needed for dense gas regions, such as halos and galaxies, but is not relevant for large void regions. Cosmological hydrodynamics codes use two main methods to resolve this scale problem: the adaptive mesh refinement (AMR, or Eulerian codes) and smooth particle hydrodynamics (SPH, or Lagrangian codes). The main codes using the AMR techniques are ART (Kravtsov, Klypin & Khokhlov, 1997), Flash (Fryxell et al., 2000), Ramses (Teyssier, 2002), and Enzo (O'Shea et al., 2004). The main codes using the SPH method, are Gasoline (Wadsley, Stadel & Quinn, 2004), Changa (Menon et al., 2015), and Gadget (Springel, Yoshida & White, 2001). Codes, like Arepo (Springel, 2010), which takes the main advantages of both the Eulerian and Lagrangian approaches, have been developed.
In this thesis, we have mainly used the code Ramses. Ramses is a tree-based AMR hydrodynamical scheme coupled with a N-body solver. In the following, we describe in detail the principle of the AMR code Ramses, in term of adaptive mesh refinement, N-body solver, hydrodynamical solver, gas cooling/heating, and the sub-grid physics regarding star formation, SN feedback and black holes. A second part is dedicated to the SPH Gadget, that we have employed for the last chapter of the thesis.

Contents

2.1 RAMSES: a numerical code with adaptive mesh refinement

2.1.1 Adaptive mesh refinement

In the adaptive mesh refinement (AMR) method, grid cells describe the values of density ρ, velocity v, and energy e. The method is Eulerian, meaning that the cells are static, and the gas can flow between them. Higher resolution is achieved in dense regions where the cell sizes are adaptively refined. Conversely, regions with low density are not refined and have a coarser resolution. Dark matter and stars are considered as collisionless particles that only interact gravitationally

The first AMR method, developed in Berger & Oliger (1984), uses an Eulerian hydrodynamics scheme where a hierarchy of nested grids, namely rectangular grid blocks (called patches) of various sizes and resolutions, covers high-resolution regions of the flow. This is the *patch-based* AMR method, the main advantage is that there is no need for domain decomposition, each processor can handle a level or a patch. There is no need to have parent or child cells on the same CPU. However, the lack of real domain decomposition can also be a negative aspect, when doing post-processing analysis, because one CPU does not correspond to a physical region in the simulation box. Contrary to this *patch-based* AMR method used in the codes ENZO and FLASH, the codes ART (Kravtsov, Klypin & Khokhlov, 1997) and RAMSES (Teyssier, 2002) use a *tree-based* AMR method. The tree-based AMR method can be applied to any system, while patches follow clustering. There is a real domain decomposition, therefore a given region is attributed to a given CPU, which makes the post-processing analysis simpler and faster. The data structure is simple, and uses oct-tree, that we represent on Fig. 2.1. In a tree data structure, parent cells can be refined into children cells on a cell-by-cell basis. An oct-tree is a small group of 2^{Ndim} cells, and has 8 associated pointers: 1 parent cell, 6 neighboring parent cells, 8 children octs, and 2 linked list indices. There are then two different types of cells: leaf cells have no children cells and are considered as *active*, and split cells are refined and considered as

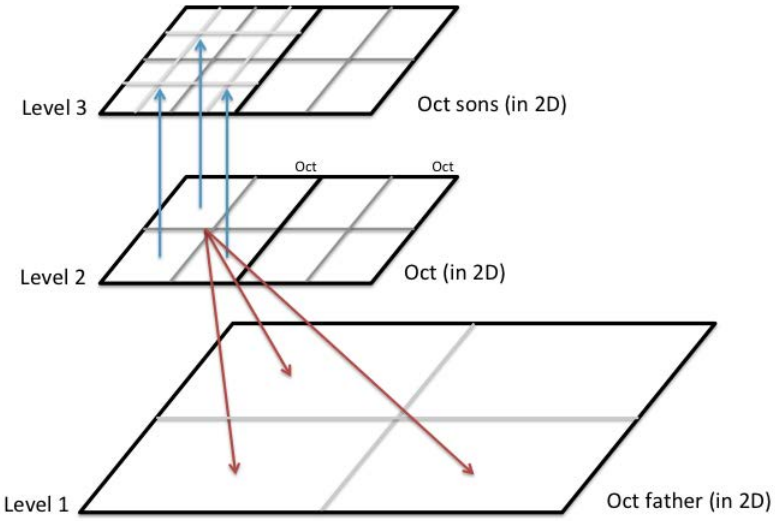

Fig. 2.1 – Oct tree structure, with the main oct (at level 2), pointing at both the parent oct (at level 1), and the children oct (at level 3).

inactive cells. The base of the tree is composed of cells which are all at the same level *levelmin* of refinement, which is called coarse level. The coarse gird is a regular cartesian grid. The drawback of tree-based AMR methods is that data managing is much more complex than in patched-based AMR methods.
A smoothing criterion is applied using the free parameter $n_{\rm expand}$ to refine neighboring cells of a refined cell, in order to avoid large discontinuities in the mesh structure. The refinement can be set up using different criteria, such as particle mass, gas density, and all users can implement their own refinement conditions. We choose to use a mass criterion, if a cell contains more than 8 times the initial mass resolution of the coarse grid, this cell is refined into children cells.
The domain decomposition uses the space-filling curve Peano-Hilbert, this creates a list containing all the cells of the simulation.

2.1.2 Initial conditions

Numerical simulations firstly rely on building initial conditions. A Gaussian (or non-Gaussian, as developed in chapter 5) perturbation field is generated according to a given power spectrum. The initial conditions generated assign initial velocities to all particles on the grid. The simulation code then evolve these particles through cosmic time, according to an N-body and a hydrodynamical solvers that we describe in the following sections.

2.1.3 Adaptive time-stepping

Time-stepping is said *adaptive*, which means that sub-levels can have their own time-step, but the global time-step must be the same than the sum of all the sub time-steps, in order to keep a global evolution of the simulation box at every global time-step. There are 4 conditions that the time-step needs to fulfill, we list them below.

- The time-step Δt must be shorter than the free-fall $t_{\rm ff}$ time $\Delta t < \min(t_{\rm ff})$, where $t_{\rm ff} = \sqrt{3\pi/32G\rho}$, with G the gravitational constant, and ρ the density of the cell.
- A particle, moving at the velocity $v_{\rm part}$, can not travel more than a fraction of the cell size

Δx within one time-step, $\Delta t < \dfrac{\Delta x}{max(v_{\rm part})}$.

- Sound waves can not propagate more than one cell size within one time-step (Courant Friedrich Levy CFL condition, Courant, Friedrichs & Lewy, 1967), $\Delta t < \dfrac{\Delta x}{max(v_{\rm x}+c_{\rm s}, v_{\rm y}+c_{\rm s}, v_{\rm z}+c_{\rm s})}$, with $(v_{\rm x}, v_{\rm y}, v_{\rm z})$ the particle velocity components.
- For cosmological simulations, a last condition is added, that the variation of the expansion factor can not exceed 10% within one time-step, $\Delta t < \dfrac{a_{\rm exp}}{\dot{a}_{\rm exp}}$, with $a_{\rm exp}$ the expansion factor, and its time derivative $\dot{a}_{\rm exp}$.

2.1.4 N-body solver

Dark matter (DM) is one the main ingredients in our Universe, and interacts only through gravity. DM is therefore referred to as collisionless matter interacting via gravity. The evolution of the DM fluid is described by two equations, which are the Vlasov and Poisson equations. Solving gravitational dynamics requires to solve this set of two equations. In cosmological simulations, ideally one would like to model DM with billions of billions of collisionless particles, and to follow each of them individually. Unfortunately this remains impossible with our computational power today. Therefore DM is modeled as a distribution function $f(x,p,t)$ of collisionless particles, particles are described at any time by their position x and velocity v or momentum p. This consists of an approximation of the real evolution of DM, which is more and more exact when the number of DM particles used in the simulation is increased. Vlasov's equation (also know as the collisionless Boltzman equation) is:

$$\frac{\mathrm{df}}{\mathrm{dt}} = \frac{\partial}{\partial \mathrm{t}} f(x,p,t) + \dot{x}\frac{\partial}{\partial \mathrm{x}} f(x,p,t) - m\nabla_x \Phi(x)\frac{\partial}{\partial \mathrm{p}} f(x,p,t) = 0. \tag{2.1}$$

The Poisson equation is written as:

$$\Delta \Phi_x = 4\pi G m \int f(x,p,t)\mathrm{d}^3\mathrm{p}. \tag{2.2}$$

To solve this system of equations, one can use two methods, the first one is a *pure N-body* approach, and the second one a *particle-mesh* (PM) method. The pure N-body approach treats the problem with the entire ensemble of particles. The Poisson integral becomes the direct summation of all the interaction forces between each pair of particles. The problem scales as N^2, with N the number of DM particles. For the PM method, the real space is discretized on a 3D grid (instead of 6D if one discretizes the entire phase-space problem), and it uses particles with real velocities. This method allows one to not compute every particle-particle forces as in the pure N-body method. This speeds up significantly force computation because particles do not interact anymore by pairs, but instead interact with the density field projected on the grid. The problem now scales as $N \times \log(N)$. However, this still leads us with a very large number of particles to deal with, the mass is therefore distributed in particles, which are not physical self-gravitating particles, one numerical "macro" particle accounts for a ensemble of physical particles with a total mass m.

To solve the system of Vlasov and Poisson's equations, main steps are:

- Computing the mass density ρ on the mesh (the grid) using a Cloud-In-Cell (CIC, Hockney & Eastwood, 1981) interpolation scheme. We show in Fig. 2.2 the principle of the CIC

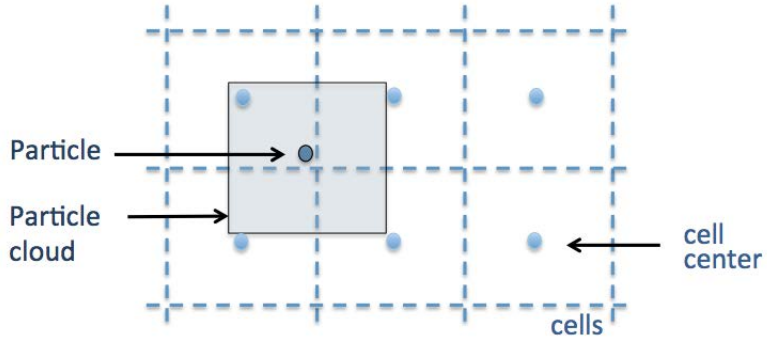

Fig. 2.2 – Principe of the Cloud-In-Cell interpolation scheme. The particle is associated to its corresponding cell, which is the cell overlapping the most with the particle cloud. Particle mass is distributed to the neighboring cells, proportionally to the particle cloud area overlapping them.

interpolation scheme. Indeed, the first thing the code needs to calculate is the potential Φ, which only depends on the density ρ (Poisson's equation). The easiest approach to compute the mass density would be to assign the mass of a particle to the single cell it belongs to, but this would create large fluctuations. Instead, the particle mass is split between the cells around the particle.

- Solving the potential $\Phi(x)$ on the mesh using the Poisson equation. Different types of Poisson solvers can be used, for example the relaxation methods (i.e. the *Jacobi* or *Gauss-Seidel* methods), which are based on iterative procedures. These methods do not need to do massive operations over the whole volume, and do not need the exact solution of Poisson's equation (all solvers can only provide an approximation to the real solution in any case), but only an approximation sufficient at the accuracy level.
  To solve Poisson's equation $\Delta\Phi = 4\pi G\rho$, we can replace second order partial derivatives with second order finite difference approximations, which can be written as $\Phi_{i+1} - 2\Phi_i + \Phi_{i-1} = 4\pi G\rho_i \mathrm{dx}^2$ (in 1D), with i the grid index. Therefore one has to solve an equation of the type $A\Phi = \rho$, with A a square symmetric matrix as:

$$\begin{pmatrix} -2 & 1 & 0 & 0 \\ 1 & . & . & 0 \\ 0 & . & . & 1 \\ 0 & 0 & 1 & -2 \end{pmatrix} \begin{pmatrix} \Phi_1 \\ . \\ . \\ \Phi_n \end{pmatrix} \propto \begin{pmatrix} \rho_1 \\ . \\ . \\ \rho_n \end{pmatrix} \tag{2.3}$$

  Ramses uses the *conjugate gradient* method, which is an iterative method that solves systems of linear equations. Here Φ is the unkown vector, the matrix A and the vector ρ are known. A is symmetrical, so it exists a basis of normal eigenvectors of A. Knowing all the eigenvectors of A leads to the solution Φ, however, when A is a large matrix, solving the problem is complicated. Instead, an iterative procedure can provide us with a sufficiently good approximation of the solution.
  A function f can be defined as $f(\Phi) = \frac{1}{2}\Phi^T A\Phi - \rho^T\Phi$, the vector Φ minimizes the function $f(\Phi)$. The function $f(\Phi)$ is minimized by setting its gradient $f'(\Phi)$ (also called residual) equal to 0. With A symmetric, it writes:

$$f'(\Phi) = A\Phi - \rho. \tag{2.4}$$

  Indeed, if one sets the gradient to 0, with $f'(\Phi) = A\Phi - \rho = 0$, one gets the equation to solve, namely $A\Phi = \rho$. The goal is to get closer to $f'(\Phi) = 0$ in the phase space in 2D. It

start with an initial estimate (an initial "guess" of the solution) of the vector Φ, and each iteration will drive us closer to the solution, namely $f'(\Phi)$ will decrease with every iteration. The initial estimate of the solution is therefore improved by iteratively decreasing the residual $f'(\Phi)$. The search direction could be orthogonal to the previous vector direction, and then it takes the minimum along this direction, and then another iteration would lead to the search in the orthogonal direction of the previous search direction. Instead, to do fewer iterations, the code searches the minimum along the direction which is A-orthogonal. The direction along which we look for the minimum is therefore orthogonal to all the previous directions where the code already has done the minimisation. The old search vectors are kept in memory and used to construct the new direction of search vector, therefore fewer iterations are needed, which is the advantage of this method. The code stops iterating when $\left|\Phi^{n+1} - \Phi^n\right| <$ accuracy, n denotes the iteration index. Some additional iterations can be done in order to verify that the minimum has been found.

- Computing the acceleration on the mesh (meaning for each cell) using a standard finite-difference approximation of the gradient. This allow us to know the gradient of the potential.

- Computing each particle acceleration required to interpolate back the acceleration to the particles using an inverse CIC interpolation scheme, through the relation:

$$\frac{\mathrm{dv_i}}{\mathrm{dt}} = -\nabla\Phi, \tag{2.5}$$

  with i the index of particle.

- Updating each particle velocity according to its acceleration, and each particle position according to its velocity.
  The explicit Euler time integrator can be written as:

$$(x,v)^{n+1} = (x,v)^n + \mathrm{dt\,f((x,v)^n)}, \tag{2.6}$$

  with $f = (mv, -\mathrm{d}\Phi\mathrm{dx})$. This allows us to update the position and velocity of a particle from the time-step n to the next time-step $n+1$. The difficulty arises from the fact that velocity and force are changing during the time-step. The most common time integrator is the *drift-kick-drift*, which is defined by:

$$\vec{x}^{n+\frac{1}{2}} = \vec{x}^n + \frac{\Delta t}{2}\vec{v}^n. \tag{2.7}$$

  The velocity is then computed using the force (which correspond to the acceleration $-\nabla\Phi$) at mid-point, and the position is updated with the new velocity:

$$\vec{v}^{n+1} = \vec{v}^n + \Delta t\frac{\vec{F}}{m}(\vec{x}^{n+\frac{1}{2}}) \tag{2.8}$$

$$\vec{x}^{n+1} = \vec{x}^{n+\frac{1}{2}} + \frac{\Delta t}{2}\vec{v}^{n+1}. \tag{2.9}$$

In this section, we have seen how DM collisionless dynamics is modeled within the N-body solver. The next section is dedicated to the hydrodynamical solver of simulations.

2.1.5 Hydrodynamical solver

The evolution of the hydrodynamical system is governed by Euler's equations, expressed as the three following equations: equation of continuity for the mass, momentum equation and energy equation:

$$\frac{\partial \rho}{\partial t} + \nabla.(\rho \boldsymbol{v}) = 0 \tag{2.10}$$

$$\frac{\partial}{\partial t}(\rho \boldsymbol{v}) + \nabla.(\rho \boldsymbol{v} \otimes \boldsymbol{v}) + \nabla p = -\rho \nabla \Phi \tag{2.11}$$

$$\frac{\partial}{\partial t}(\rho e) + \nabla.[\rho \boldsymbol{v}(e + \frac{p}{\rho})] = -\rho \boldsymbol{v}.\nabla \Phi, \tag{2.12}$$

with ρ the mass density, $\boldsymbol{v}$ the fluid velocity, e the specific total energy, p the thermal pressure. One needs to add a closure equation to identify a unique solution for this system of equations. This is done by the equation-of-state (EOS) of the gas:

$$p = (\gamma - 1)\rho(e - \frac{1}{2}v^2), \tag{2.13}$$

where $\gamma = \dfrac{C_p}{C_v}$ is the gas adiabatic index, with for instance $\gamma = 5/3$ for a monoatomic gas. The energy equation is conservative if we remove the source terms on the right-hand side of the previous equations (for example, here the gravitational term).

We define the vector $\boldsymbol{V}_i$ as a numerical approximation to the cell average value of $(\rho, \rho\boldsymbol{v}, \rho e)$ at time t^n, and for cell i. Therefore, the Euler system of equations, can be written as:

$$\frac{\partial \boldsymbol{V}}{\partial t} + \triangledown.\boldsymbol{F}(\boldsymbol{V}) = 0 \tag{2.14}$$

with $\boldsymbol{F} = (\rho v, \rho v \otimes v, \rho v\,(e + p/\rho))$ the flux. With this discretization, the equations become:

$$\frac{\boldsymbol{V}_i^{n+1} - \boldsymbol{V}_i^n}{\Delta t} + \frac{\boldsymbol{F}_{i+1/2}^{n+1/2} - \boldsymbol{F}_{i-1/2}^{n+1/2}}{\Delta x} = S_i^{n+1/2}, \tag{2.15}$$

where $F_{1+1/2}^{n+1/2}$ is the time centered flux across cell interfaces, and $\boldsymbol{V}_i^n$ the average value of $\boldsymbol{V}$ in one cell at time t^n. The gravitational source term is expressed as:

$$S_i^{n+1/2} = (0, \frac{\rho_i^n \nabla \Phi_i^n + \rho_i^{n+1} \nabla \Phi_i^{n+1}}{2}, \frac{(\rho v)_i^n \nabla \Phi_i^n + (\rho v)_i^{n+1} \nabla \Phi_i^{n+1}}{2}). \tag{2.16}$$

In other words, mass, momentum and energy change in time as a function of incoming flux and/or leaving flux. To determine these fluxes at the interfaces of cells, one needs to solve the Riemann discontinuity at each cell boundary, imposing $S = 0$ (operator splitting). The interpolation method used in RAMSES is a second-order Godunov method, which corresponds to the piecewise-linear interpolation method (PLM) introduced by Van Leer (1979). Other methods have been introduced, such as the piecewise constant method (PCM), or the piecewise parabolic method (PPM). These methods reconstruct the behavior of the system taking into account not only the mean value at the cell boundary, but also the values of the neighboring cells. Boundary conditions are therefore needed, 2 ghost zones are needed in each direction and sides for the PLM method, one oct-tree has 2^{Ndim} cells in RAMSES, therefore $3^{Ndim} - 1$ neighboring octs are needed to constitute the boundary conditions. In total the PLM scheme uses 6^{Ndim} cells. The PLM interpolation method introduces some dispersions and oscillations around discontinuities,

to limit this effect, the slope in the interpolation can be limited. It avoids the formation of new extrema in the flux values, suppressing oscillations. Therefore we use a Harten-Lax-Van Leer Contact Riemann solver (HLLC), with a Min-Mod total variation diminishing scheme to linearly interpolate the cell-centered values to their edge locations. The HLLC solver only considers the two fastest waves out of the three generated waves, which are the rarefaction wave moving to the densest medium, the shock wave moving to the less dense region, and the intermediate contact wave also moving to the less dense region. This is an approximation to the exact resolution of the Riemann problem, the advantages is the fastest calculation of the (approximate) solution.

2.2 Sub-grid physics to study galaxy formation and evolution

To study galaxy formation and evolution, one needs to take into account baryonic processes, which mostly have a role at galaxy scales, beyond what can actually be resolved in cosmological simulations. Sub-grid physics have been developed over the years to account for these un-resolved processes in large scale simulations. In the following, we describe the current sub-grid physics which is implemented in Ramses, and shared by most of the cosmological codes (through different numerical implementations). Our simulations include sub-grid physics for gas cooling, heating, star formation and feedback, BH formation, accretion, and feedback from active galactic nuclei.

2.2.1 Radiative cooling and photoheating by UV background

The temperature of the gas depends on the net cooling function $\Lambda_{\rm net}$, which can be expressed as the sum of a cooling therm Λ, and a heating term $\mathcal{H}$ due to photoionization of the gas from young stars:

$$\Lambda_{\rm net} = \mathcal{H} + \Lambda. \tag{2.17}$$

Radiative cooling is modeled with the cooling curves of Sutherland & Dopita (1993), the gas cools through H, He, and metals (Courty & Alimi, 2004). We show on Fig. 1.7 the cooling rate of primordial environments and environment with metals.

Several radiation cooling processes are considered for gas of primordial composition: collisional excitation between atoms which emit photons when reverting to their ground state, collisional ionization between atoms which lose energy by emitting an electron, electronic recombination with photon emission, bremsstrahlung or free-free (radiation is produced by the deceleration of a charged particle (electron) when deflected by another charged particle, and emitting a photon, the particles are both free, which means that they do not belong to an atom for example), and Compton ionization.

Primordial gas can cool down to $T = 10^4\,\mathrm{K}$, mainly driven by collisional reactions in the ISM. Temperatures of the warm ISM are typically around $T = 10^4 - 10^6\,\mathrm{K}$. The gas around galaxies is hotter, the cooling is there driven by free-free radiation cooling. Star formation takes place in the regions of galaxies at low temperature and high density. To cool below $T = 10^4\,\mathrm{K}$ the gas needs the contribution from metals and molecules. A contribution from metals is included to the cooling function in Ramses.

The metallicity of the gas is modeled as a passive variable ($p \triangledown v = 0$), which makes it easily trackable over the gas flow through cosmic evolution. An initial zero metallicity is assumed for most of the simulations describes in this thesis, but some use a metallicity background of $Z = 10^{-3}\,Z_\odot$. The cooling curve of gas with metals has roughly the same slope of the H_2 cooling curve, therefore we use an initial background in metallicity to mimic H_2 cooling. This consists of

an approximation, and does not exactly reproduce the H_2 cooling curve, and the fact that H_2 formation rate is, for example, dependent of the gas density.
Physical processes, such as SN explosions and star formation, modify and redistribute the metallicity over neighboring cells.
To mimic reionization, photoheating from an uniform ultraviolet radiation background is added (following Haardt & Madau (1996)), taking place after $z = 8.5$ for most of the simulations that we have run.

2.2.2 Star formation

Star formation takes place in sub-parsec regions, in cold molecular gas clouds, which are dense and at low temperatures. Star formation appears as the gas gravitational collapses with a timescale defined by the free-fall time:

$$t_{\rm ff} = \sqrt{\frac{3\pi}{32G\rho}}. \tag{2.18}$$

Observationally, the Kennicutt law (1998) links the star formation rate (SFR) per unit area with the gas surface density. This law can be transformed to give the volume density of stars as a function of the volume gas density. In RAMSES each cell follows the Schmidt law (Rasera & Teyssier, 2006):

$$\frac{d\rho_\star}{dt} = \frac{\rho}{t_\star(\rho)} \quad \text{if } \rho > \rho_0, \tag{2.19}$$

$$\frac{d\rho_\star}{dt} = 0 \quad \text{if } \rho < \rho_0, \tag{2.20}$$

with ρ_0 a free parameter corresponding to the star formation threshold, this parameter is resolution-dependent, and set by the user. The star formation timescale depends on the local overdensity of the gas via the relation:

$$t_\star = t_0 \left(\frac{\rho}{\rho_0}\right)^{-1/2}, \tag{2.21}$$

with t_0 the star formation characteristic time, which can be seen as the efficiency for the gas to collapse and form stars:

$$t_0 = \frac{t_{\rm ff}(\rho_0)}{\epsilon}, \tag{2.22}$$

with

$$\epsilon = \frac{t_{\rm ff}(\rho)}{t_\star(\rho)}. \tag{2.23}$$

The star formation is entirely described by the timescale t_0 and the density threshold ρ_0. At every timestep Δt, in each leaf cell with a density exceeding the user-defined threshold ρ_0, a number of star particles N are created, following a Poissonian random process. The probability to form N star particles is:

$$P(N) = \frac{\lambda}{N!} \exp -\lambda, \tag{2.24}$$

with

$$\lambda = \left(\frac{\rho \Delta x^3}{m_\star}\right) \frac{\Delta t}{t_\star}, \tag{2.25}$$

with Δx the side length of a cell, and $m_\star$ the stellar resolution of the simulation. In star forming cells, all star particles are grouped to form a unique particle, with a mass $N m_\star$. To avoid empty gas cells, only 90 % percent of the gas density can be used to from stars within a single cell.

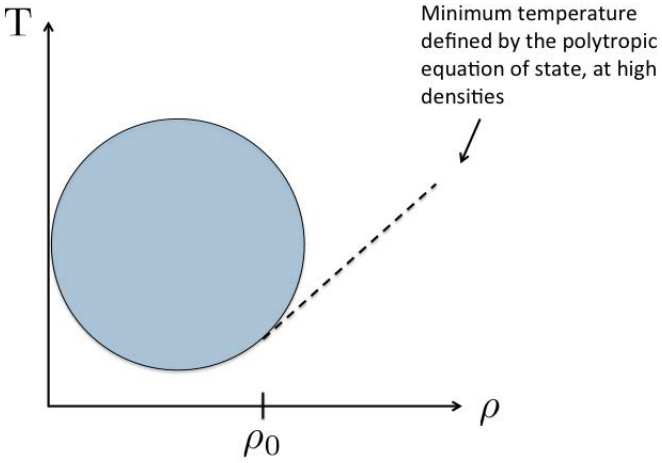

Fig. 2.3 – We use a polytropic equation of state to increase the gas pressure in cells with a high density ($\rho > \rho_0$), to limit excessive gas fragmentation. It mimics the heating of the interstellar medium from stars, and processes that take place at small scales that we do not resolve here.

2.2.3 Equation-of-state

Gas follows an adiabatic equation-of-state (EoS) for monoatomic gas with adiabatic index $\gamma = 5/3$, except at high gas densities $\rho > \rho_0$, where we use a polytropic EoS to increase the gas pressure in dense gas in order to limit excessive gas fragmentation by mimicking heating of the interstellar medium from stars (Springel & Hernquist, 2003):

$$T = T_0 \left(\frac{\rho}{\rho_0}\right)^{\kappa-1}, \tag{2.26}$$

with T the gas temperature, T_0 the temperature threshold, ρ_0 the density threshold, and κ the polytropic index of the gas. We use $\kappa = 1.6$ for the polytropic index, and T_0 depends on the simulation resolution.
For our set of simulations Chunky, which are used in chapter 4, where the spatial resolution is $\sim 80\,\mathrm{pc}$, and the dark matter resolution is $1.6 \times 10^7\,\mathrm{M}_\odot$, we have used a temperature threshold of $T_0 = 10^3\,\mathrm{K}$, and a density threshold $\rho_0 = 1\,\mathrm{H\,cm^{-3}}$. For Tiny, which has a spatial resolution of $\sim 7.6\,\mathrm{pc}$, and a DM resolution of $2082\,\mathrm{M}_\odot$, we have used $T_0 = 10^2\,\mathrm{K}$, and $\rho_0 = 30\,\mathrm{H\,cm^{-3}}$. In chapter 3, we have used three simulations SuperChunky, which have the same spatial resolution and a DM resolution of $1.65 \times 10^6\,\mathrm{M}_\odot$, we have used the same parameters as the simulation Chunky, namely $T_0 = 10^3\,\mathrm{K}$, and $\rho_0 = 1\,\mathrm{H\,cm^{-3}}$.

2.2.4 SN feedback and metal enrichment

A large contribution of the interstellar medium metal enrichment is due to SNe. Massive stars explode into SNe when they die, producing blast waves expanding to larger spatial scales. In cosmological simulations, SN explosions are modeled as sub-grid physics. In this thesis we have used and compared three different SN feedback implementations: a simple thermal SN feedback, a kinetic SN feedback, and a delayed cooling SN feedback.
Current numerical simulations, particularly cosmological simulations, do not resolve star individually. Instead, we use star particles that represent an ensemble of stars. SN feedback is then not done for individual stars, but for a mass fraction of each star particle. Therefore it is crucial to use an IMF, to compute the mass fraction of the star particles that will end up in SNe. We

model type II SNe assuming a Chabrier initial mass function (Chabrier, 2003), where $\eta_{\rm SN} = 20\%$ of the mass fraction of stars end up their life in type II SNe, and release $e_{\rm SN} = 10^{50}\,{\rm erg\,M_\odot^{-1}}$, and return metals with a yield of 0.1. We describe, here, the main characteristics of the three different SN feedback models implemented in RAMSES.

Thermal SN feedback

We use the thermal SN feedback implemented in RAMSES, which is a weak feedback compared to the following ones (as we will see in chapters 3 and 4). The mass ejecta $m_{\rm SN}$ is computed as a fraction of the star particle: $m_{\rm SN} = \eta_{\rm SN} \times m_{\rm star\,particle}$, with $\eta_{\rm SN}$ the mass fraction of stars which end up in type II SNe. The corresponding mass loss is removed from the mass of the star particle. Metals are also distributed into the surrounding cells. Internal specific SN energy $E_{\rm thermal}$ is released in the neighboring cells, it can be expressed by:

$$E_{\rm thermal} = m_{\rm SN} \times e_{\rm SN} = \eta_{\rm SN} \times m_{\rm star\,particle} \times e_{\rm SN}. \tag{2.27}$$

The energy liberated during an SN explosion is resolution-dependent, via $m_{\rm star\,particle}$.

Kinetic SN feedback

The kinetic SN feedback (Dubois & Teyssier, 2008) is modeled to reproduce a Sedov blast wave, where energy, mass and momentum are deposited in the neighborhood. Sedov blast wave is the result of a large energy deposition within a small volume. For each exploding star particle, ejecta are carried out and entrained into the surrounding gas by the blast wave. The maximum radius of the ejecta is set equal to two cells, $r_{\rm max} = 2\Delta x$. Hydrodynamical quantities of cells within $r_{\rm max}$ are updated to account for the Sedov blast wave.

Delayed cooling SN feedback

The third model is called delayed cooling (Teyssier et al., 2013), which we modify in the same way as Dubois et al. (2015) (i.e., parameters are resolution-dependent). After a SN explosion, the coupling of the energy to the gas is not trivial to model, because the energy released by the explosion can be stored by non-thermal processes, such as unresolved turbulence, magnetic fields, cosmic rays, which are not modeled in hydro-dynamical simulations. These processes will dissipate their energy on potentially longer timescales, defined as the dissipative time $t_{\rm diss}$. In order to mimic the energetic and pressure enhancement by the non-thermal component, gas cooling is prevented in gas cells where the non-thermal energy component (or non-thermal velocity dispersion $\sigma_{\rm NT}$) is larger than some user-defined threshold (Stinson et al., 2006 ; Teyssier et al., 2013). We adopt the implementation of Dubois et al. (2015) in order to match the values of $t_{\rm diss}$ and $\sigma_{\rm NT}$ to that required for the blast wave to propagate over a Jeans length (4 high-resolution cells), the parameters are therefore resolution-dependent. We explode only one stellar particle out of 10 stellar particles, with 10 times more SN specific energy to add up stochasticity. The evolution of the non-thermal energy can be written as:

$$\sigma_{\rm NT}^2 = 2\eta_{\rm NT} \frac{10^{51}{\rm erg}}{10{\rm M_\odot}} \frac{t_{\rm diss}}{t_{\rm ff}(\rho)} \epsilon_\star \tag{2.28}$$

$$\sigma_{\rm NT} = \left(2\eta_{\rm NT} \frac{10^{51}{\rm erg}}{10{\rm M_\odot}} N_{\rm cell} \Delta x\right)^{1/3} \left(\frac{32 G \rho_0}{3\pi}\right)^{1/6} \tag{2.29}$$

$$t_{\rm diss} = \left(2\eta_{\rm NT}\frac{10^{51}{\rm erg}}{10{\rm M}_\odot}\epsilon_\star\right)^{-1/3}(N_{\rm cell}\Delta x)^{2/3}\left(\frac{32G\rho_0}{3\pi}\right)^{-1/6}. \quad (2.30)$$

The implementation of SN feedback in numerical simulations has important consequences on metal-enrichment. We can evaluate the radius of the shock $R_{\rm shock}$ (spherical in an homogeneous medium), which is defined by the Sedov blast wave solution:

$$R_{\rm shock} = \xi\left(\frac{e_{\rm SN}\times t^2}{\rho}\right)^{1/5}, \quad (2.31)$$

with ξ a dimensionless parameter of order unity, ρ the density of the medium, $e_{\rm SN}$ the energy of the SN, and t a given time.

This gives us a characteristic length of metal pollution in the medium. We will see that the different implementations of SN directly impact star formation, meta-enrichment, and therefore also BH formation. Indeed, BH form in metal-free environments, therefore the compactness of metal-enriched bubbles allow for more metal-free regions where gravitational collapse may lead to the formation of compact objects, such as BHs. This will be discussed in more detail in chapters 3 and 4.

2.2.5 BH formation

Cosmological simulations have mostly focussed on studying the growth of BHs and AGN feedback, rather than their formation. In order to reproduce succesfuly the AGN luminosity function, various state-of-the-art simulations (e.g. Sijacki, Springel & Haehnelt, 2009; Di Matteo et al., 2012; Hirschmann et al., 2012b; Dubois, Volonteri & Silk, 2014; Sijacki et al., 2015; Volonteri et al., 2016) have seeded halos above a fixed mass threshold (typically $\rm M_\odot$ $10^{10}\,\rm M_\odot$) with $\sim 10^4 - 10^5\,\rm M_\odot$ BHs. Our implementation of BH formation, is different to these models, and is represented in the next chapter in detail. We use sink particles to model the formation of BHs, they are able to accrete gas from surroundings, and to merge together.

2.2.6 BH accretion

The accretion on the BH is described by the minimum between a Bondi-Hoyle-Lyttleton accretion rate and the Eddington accretion rate, with:

$$\dot{\rm M}_{\rm BH} = \frac{4\pi\alpha G^2{\rm M}_{\rm BH}^2\bar{\rho}}{(\bar{c_{\rm s}}^2+\bar{v}^2)^{3/2}},$$

where α is a density dependent boost factor (Booth & Schaye, 2009), G is the gravitational constant, $\rm M_{BH}$ the mass of the BH, $\bar{\rho}$ the average density of the medium, $\bar{c_{\rm s}}$ the average of the sound speed, and $\bar{v}$ the average velocity of the gas relative to the BH. The boost factor α is equal to $(\rho/\rho_0)^2$ when $\rho > \rho_0$ and 1 otherwise.

When a BH forms, namely when its corresponding sink particle is created, it is actually distributed on an ensemble of cloud particles ($\sim$ 2000 cloud particles), equally distributed in space around the sink particle. These cloud particles are important to compute the spatially averaged quantities that we describe below. The quantities $\bar{\rho}$, and $\bar{c_{\rm s}}$, are averaged around the sink particles using the cloud particles. Each cloud particle reads up the value of density, sound speed and velocity from its position in the grid of the simulation, by using the CIC method. A "Bondi-Hoyle radius" value (noted $r_{\rm Bo-Ho}$ in the following) is first computed, this value only depends on the properties of the cell where the sink particle, representing the BH, sits. This Bondi-Hoyle radius is used to

weight the contribution of each cloud particle in the computation of the quantities $\bar{\rho}$, and $\bar{c_s}$. The cell in which each cloud particle is sitting is, therefore, assigned a weight of $w \propto exp(-r^2/r_k^2)$, r is the distance between the cloud particle and the sink particle, and is defined by:

$$r_k = \begin{cases} \dfrac{\Delta x}{4} & \text{if } r_{Bo-Ho} < \dfrac{\Delta x}{4} \\ r_{Bo-Ho} & \text{if } \dfrac{\Delta x}{4} \leqslant r_{Bo-Ho} \leqslant 2\Delta x \\ 2\Delta x & \text{if } r_{Bo-Ho} > 2\Delta x \end{cases} \tag{2.32}$$

with r_{Bo-Ho} the Bondi-Hoyle radius, defined by $r_{Bo-Ho} = G\mathrm{M_{BH}}/\mathrm{c_s^2}$, with c_s measured at the location of the sink particle.
The accretion is limited by the Eddington accretion rate:

$$\dot{\mathrm{M}}_{Edd} = \frac{4\pi G \mathrm{M_{BH}} m_p}{\epsilon_r \sigma_T c},$$

where m_p the proton mass, $\epsilon_r = 0.1$ the radiative efficiency, and σ_T the Thomson cross-section.

2.2.7 AGN feedback

In this thesis, AGN feedback is modeled with an isotropic injection of thermal energy into the surrounding gas, within a sphere of 4 cells ($4 \times \Delta x$) around sink particles (Teyssier et al., 2011; Dubois et al., 2012b). We store the rest-mass energy of the accreted mass into the BH, and release it when the energy is high enough to raise the temperature of the gas around the BH to at least 10^7 K (the model is inspired by Booth & Schaye, 2009). The energy is released as thermal energy, with an efficiency of $\epsilon_f = 0.15$ (calibrated to reproduce the observational $\mathrm{M_{BH}} - \mathrm{M_\star}$ and $\mathrm{M_{BH}} - \sigma_\star$ relations, following Dubois et al., 2012a), within a spherical bubble of 4 cells ($4 \times \Delta x$) centered around the sink particle. Two situations can be distinguished. If the gas environment of the BH is dense and cold, reaching the temperature threshold is more difficult, the energy is accumulated and at some point a burst of energy is released, and impacts the surroundings. In the other hand, if the gas surrounding the BH is hot and less dense, the threshold for AGN feedback is reached faster, and the AGN is more continuously releasing energy into the surroundings.

As said in section 1.5.2, more recent AGN feedback models have been implemented, for example with two modes depending on the accretion rate into the BH. The radio mode or mechanical AGN feedback is effective for $\dot{\mathrm{M}}_{BH}/\dot{\mathrm{M}}_{Edd} \leqslant 0.01$, and is modeled with a kinetic bipolar outflow/jet, where the mass, energy, and momentum are deposited in the surrounding within a cylinder (Dubois et al., 2010, 2011, 2012a). Whereas for the quasar mode or radiative AGN feedback, which is effective for accretion rate onto the BH close to the Eddington limit ($\dot{\mathrm{M}}_{BH}/\dot{\mathrm{M}}_{Edd} > 0.01$), internal energy is deposited into the surroundings to increase the gas temperature, and mimic the heating of the gas (Di Matteo et al., 2008; Teyssier et al., 2011; Dubois et al., 2012a).

2.3 Smoothed particle hydrodynamics code GADGET

Contrary to AMR codes like RAMSES, smoothed particle hydrodynamics code (SPH) codes use a Lagrangian approach. The fluid (namely, DM, star and gas) is discretized into particles, and because Lagrangian, dense regions of the simulation box are naturally refined, and acquire a higher resolution (i.e. it decreases the length between particles). Gas properties are derived via

smoothing of the surrounding particles, anywhere in the simulation box.
In this thesis, we only have used DM only simulations, run with the code GADGET-2, and explained in chapter 5, therefore in the following we only describe briefly the N-body solver, but not the hydrodynamical solver that can be used, neither the sub-grid physics which is used in the hydrodynamical version of the code.
GADGET uses a tree algorithm (or *hierarchical multipole expansion*) to compute gravitational forces on short-range scales, which is coupled to a particle-mesh PM scheme for long-range gravitational forces. This combination of two methods is called a TreePM hydrid method. A N-body solver is used, similar to the one describe in section 2.1.4. Phase-space density is sampled with N particles. Particles are grouped in cells and oct-tree, their gravity is therefore considered as a single multipole force. As in RAMSES, cells are divided into split cells up to leaf cells. The gravitational force is computed from the base of the tree to upper levels. In the optional TreePM method, the potential can be split into long and short-range components, as $\Phi = \Phi_{\rm short} + \Phi_{\rm long}$. The long-range component is computed with mesh-based Fourier methods, whereas the short-range component is computed in real space.

Chapter 3

Pop III remnants and stellar cluster models

Massive BHs inhabit local galaxies, including the Milky Way and some dwarf galaxies. BH formation, occurring at early cosmic times, must account for the properties of BHs in today's galaxies, notably why some galaxies host a BH, and others do not. We investigate the formation, distribution and growth of BH 'seeds' by using the adaptive mesh refinement code Ramses. We develop an implementation of BH formation in dense, low-metallicity environments, as advocated by models invoking the collapse of the first generation of stars, or of dense nuclear star clusters. The seed masses are computed one-by-one on-the-fly, based on the star formation rate and the stellar initial mass function. This self-consistent method to seed BHs allows us to study the distribution of BHs in a cosmological context and their evolution over cosmic time. We find that all high-mass galaxies tend to a host a BH, whereas low-mass counterparts have a lower probability of hosting a BH. After the end of the epoch of BH formation, this probability is modulated by the growth of the galaxy. The simulated BHs connect to low-redshift observational samples, and span a similar range in accretion properties as Lyman-Break Analogs. The growth of BHs in low-mass galaxies is stunted by strong supernova feedback. The properties of BHs in dwarf galaxies thus remain a testbed for BH formation. Simulations with strong supernova feedback, which is able to quench BH accretion in shallow potential wells, produce galaxies and BHs in better agreement with observational constraints.

This chapter is adapted from the publication:

- *Blossoms from black hole seeds: properties and early growth regulated by supernova feedback*, Mélanie Habouzit, Marta Volonteri, and Yohan Dubois, submitted to MNRAS, arXiv:1605.09394

Contents

3.1 Introduction

In this chapter, we aim at understand the properties of BHs in today's galaxies. Massive BHs are found in many local galaxies (Kormendy & Ho, 2013), from massive galaxies to dwarf galaxies (Greene, 2012), some others are lacking of BHs.

So far, we have focussed on understanding and addressing the high-mass end of the BH population, with mass of millions solar masses and above, residing in the center of massive galaxies. State-of-the-art simulations (e.g. Sijacki, Springel & Haehnelt, 2009; Di Matteo et al., 2012; Sijacki et al., 2015; Dubois, Volonteri & Silk, 2014; Hirschmann et al., 2012b), have successfully reproduced the AGN luminosity function, which is dominated by BH with masses $\sim 10^8\,\mathrm{M}_\odot$. However, these simulations, which focus on studying the growth of BHs and AGN feedback rather than BH formation, use very simplistic BH formation models, seeding massive halos with $\approx 10^5\,\mathrm{M}_\odot$.

Today, we are pushing the observational limits, both in term of high redshift galaxies and local low-mass galaxies. We are in a promising period, where observations will provide us new constraints on BH formation. However, a close comparison between these observations and predictions from BH formation models are crucial. Hydrodynamical cosmological simulations, as those proposed in this chapter, are the perfect resource to predict BH and galaxy properties. They allow one to explain BH properties in normal galaxies, and not to only focus on explaining what we were able to observe so far, namely BHs in massive galaxies, quasars and AGN.

As explained in the introduction of this thesis, the imprint of BH formation is not to be found in massive galaxies, where the central BH must have grown by several orders of magnitude. Dwarf galaxies, instead, where neither the galaxy nor the BH can have grown much over cosmic time, provide us a promising laboratory where the mass of the central BH is expected to not differ much from its initial mass (Volonteri, Lodato & Natarajan, 2008; van Wassenhove et al., 2010; Reines, Greene & Geha, 2013). For example, a recent zoom cosmological hydrodynamical

simulation from Dubois et al. (2015) has shown that a strong stellar feedback can suppress the growth of the BH until the galaxy has acquired enough mass at around $\sim 10^9\,\mathrm{M}_\odot$. Below this stellar mass, SN-driven winds are fast enough to overcome the escape velocity of the gravitational potential of the galaxy, and cold gas is routinely removed from the central parts of the galaxy. Low-mass galaxies are also key to distinguish between formation scenarios through a different diagnostic, the occupation fraction, i.e. the probability that a galaxy of a given mass hosts a BH (Volonteri, Lodato & Natarajan, 2008 ; van Wassenhove et al., 2010 ; Greene, 2012). The direct collapse model, requiring very strict conditions, would leave many galaxies bereft of a BH, while less exacting models, such as PopIII star remnant or nuclear cluster models predict that a larger fraction of galaxies are eligible to host a BH. In principle, the mass and the occupation fraction of BHs in low-mass galaxies can therefore constrain BH formation. Of course, one should keep in mind that different models are not mutually exclusive in the Universe (Volonteri & Begelman, 2010 ; Devecchi et al., 2012 ; Lupi et al., 2014).

In this chapter, we implement a model for BH seed formation which mimics the Pop III star remnant and the nuclear cluster models, in the hydrodynamical cosmological code Ramses. In the PopIII star remnant model, BHs are predicted to form in mini-halos ($\mathrm{M_h} \approx 10^5\,\mathrm{M}_\odot$) with gas below a critical metallicity ($Z < 10^{-3.5}\,\mathrm{Z}_\odot$, Bromm et al., 2001 ; Schneider et al., 2002) at redshift $z = 30 - 20$ from the remnants of the first generation of stars (PopIII stars, Madau & Rees, 2001 ; Volonteri, Madau & Haardt, 2003). A massive star $\mathrm{M}_\star \gtrsim 260\,\mathrm{M}_\odot$ can lead to the formation of a BH seed of $\approx 100\,\mathrm{M}_\odot$ (Fryer, Woosley & Heger, 2001), which retained half the mass of the star. Compact nuclear clusters are also thought to be able to collapse and form a very massive star by stellar collisions. In metal-poor gas environment, the newly massive star can as massive as $1000\,\mathrm{M}_\odot$. The nuclear stellar model can lead to the formation of $10^3\,\mathrm{M}_\odot$ BH seeds (Omukai, Schneider & Haiman, 2008 ; Devecchi & Volonteri, 2009 ; Regan & Haehnelt, 2009b ; Katz, Sijacki & Haehnelt, 2015). We develop a new method to seed cosmological simulations with BHs. Our approach is based on the local gaseous and stellar properties, and captures the properties of these two BH formation models. To test BH formation against observations, we compare our sample of BHs with a low-redshift sample of local galaxies (including broad-line AGN, galaxies with dynamical BH mass measurement, and several dwarf galaxies), and with Lyman-Break Analogs (LBAs). LBAs have similar properties to the more distant Lyman Break Galaxies (LBG), but they are local systems that can be studied in much greater detail.

In the first section 3.2, we describe the numerical methods, and our new implementation of BH formation in the code Ramses. We then present our results, on the influence of star formation and metallicity on BH formation (section 3.4), on the BH mass function and the occupation fraction (section 3.5), and finally on the BH growth and the impact of SN feedback in section 3.6. Finally, in section 3.7, we compare the simulated BHs to observations, and we conclude in section 3.8.

3.2 Simulation set up

Simulation parameters, and initial conditions

We only briefly summarize the simulation set-up here, more details can be found in the previous chapter (chapter 2). We have performed three simulations with the code Ramses (Teyssier, 2002), that we call SuperChunky, they only differ by the prescription of SN feedback. We use a Λ cold dark matter cosmology, with total matter density $\Omega_m = 0.276$, dark matter en-

ergy density $\Omega_\Lambda = 0.724$, amplitude of the matter power spectrum $\sigma_8 = 0.811$, spectral index $n_s = 0.961$, baryon density $\Omega_b = 0.045$ and Hubble constant $H_0 = 70.3\,km\,s^{-1}\,Mpc^{-1}$, compatible with WMAP-7 (Komatsu et al., 2011). Simulations are performed in a periodic box of side 10 comoving Mpc (cMpc) with 256^3 dark matter particles, corresponding to a mass resolution of $M_{DM,res} = 1.65 \times 10^6\,M_\odot$. Simulations are run from redshift $z = 100$ to $z = 2$. We use nested grid initial conditions built with the code MUSIC (Hahn & Abel, 2013). The initial mesh is refined with 9 levels of refinement, leading to a spatial resolution of $\Delta x = 76\,pc$.
Our simulations include sub-grid physics for cooling, star formation, SN feedback, AGN feedback. Cooling is modeled with the cooling curves of Sutherland & Dopita (1993), the gas cools through H, He, and metals. The metallicity of the gas is modeled as a passive variable, all the simulations start with a zero-metallicity. To mimic reionization, heating from an uniform UV background is added (following Haardt & Madau, 1996), taking place after $z = 8.5$. Star formation occurs in dense and cold gas, and is modeled with a Kennicutt-Schmidt law.

SN feedback

We model type II SNe assuming a Chabrier initial mass function (Chabrier, 2003), where $\eta_{SN} = 20\%$ of the mass fraction of stars end up their life in type II SNe, and release $e_{SN} = 10^{50}\,erg\,M_\odot^{-1}$, and return metals with a yield of 0.1.
In this chapter, we employ three different SN feedback models implemented in RAMSES:

- Simulation SuperChunky “T”: we use a weak “thermal" SN feedback which releases only internal energy in the neighboring cells (Dubois & Teyssier, 2008).
- Simulation SuperChunky “K”: the kinetic SN feedback (Dubois & Teyssier 2008) is modeled to reproduce a Sedov blast wave, where energy, mass and momentum are deposited in the neighboring gas cells.
- Simulation SuperChunky “D”: This model corresponds to the delayed cooling model (Teyssier et al., 2013 ; Dubois et al., 2015), which prevents the cooling after a SN explosion, to mimic the energetic and pressure enhancement by the non-thermal processes (such as unresolved turbulence, magnetic fields, cosmic rays). We explode only one stellar particle out of 10 stellar particles, with ten times more SN specific energy to add up sochaticity. We use the following resolution-dependent parameters: $M_{SN} = 7.7 \times 10^4\,M_\odot$, non-thermal velocity dispersion $\sigma_{en} = 65\,km\,s^{-1}$, the dissipative time on which non-thermal processes dissipate is set at $t_{diss} = 4.6\,Myr$.

Halo and galaxy finder codes

We construct catalogues of halos using the AdaptaHOP halo finder (Aubert, Pichon & Colombi, 2004), which uses an SPH-like kernel to compute densities at the location of each particle and partitions the ensemble of particles into sub-halos based on saddle points in the density field. Halos contain at least 100 dark matter particles. Galaxies are identified in the same way, galaxies contain at least 100 stellar particles.

3.3 Seeding cosmological simulations with BH seeds

In this section, we describe our implementation to seed BHs in large-scale simulations, with an approach that is inspired by and mimics the Pop III star remnant and nuclear stellar cluster scenarios. Regions to form BHs are not identified on halos properties, but on local environment

properties (see also Bellovary et al., 2011). BH masses are computed one by one, according to the density properties of these local regions.

3.3.1 Selecting BH formation regions

We modify the clump finder routine in RAMSES (Bleuler & Teyssier, 2014), which identifies regions denser than a given threshold. We use $\rho_0 = \rho_\star$, i.e. the threshold for BH formation is the same as for star formation (as the models of BH formation we want to model are based on stars, rather than gas collapse). Thus, the formation of BHs happens in the same dense regions as those of star formation. Two clumps are merged if they share a saddle point, which has a density higher than the density threshold. We then verify several physical criteria: overdensities must be contracting along all axis, must be bound, and no pre-existing BH should exist within the overdensity. We also add a criterion on the metallicity of the gas in the clump, which is crucial to determine the formation rate of BHs in this type of models and its eventual dwindling (Bellovary et al., 2011). The metallicity of the clump is the mass-weighted metallicity of gas cells belonging to the clump. At this stage, collapsing regions with $Z < 10^{-3.5}\,\mathrm{Z}_\odot$ are flagged as possible BH formation sites.

Taylor & Kobayashi (2014) follows a similar approach, where cosmological simulations are seeded with PopIII remnant BHs if a gas particle density exceeds a given density threshold, and is metal-free ($Z = 0$). However, their initial seed BH mass is fixed, whereas our model compute individually each seed BH mass.

3.3.2 Computing BH initial masses

Once we have selected all metal-free collapsing regions in our simulation box, we compute the theoretical mass in low-metallicity stars which can be formed in each clump using the Kennicutt-Schmidt law. We then calculate the probability of forming massive stars, adopting an IMF for the PopIII stars. Since we are focusing on low-metallicity stars ($Z < 10^{-3.5}\,\mathrm{Z}_\odot$), we have considered a logarithmically flat IMF, as suggested by investigations of the formation of PopIII stars (Hirano et al., 2014). The adopted minimum and maximum stellar mass are 1 and 500 $\mathrm{M}_\odot$ respectively. This IMF enters only in the implementation of BH formation and not in the SN feedback implementation. Defining ξ as the IMF per unit of stellar mass, $\xi \equiv \mathrm{m}\dfrac{\mathrm{dN}}{\mathrm{dm}}$, the total mass in stars with masses between m_1 and m_2 is:

$$\mathrm{M}_* = \int_{\mathrm{m}_1}^{\mathrm{m}_2} \mathrm{m}\,\Phi(\mathrm{m})\,\mathrm{dm} = \int_{\mathrm{m}_1}^{\mathrm{m}_2} \xi(\mathrm{m})\,\mathrm{dm}\,.$$

Specifically when we think of the the PopIII remnants scenario, BH seeds are expected to form from stars in two mass ranges (Heger & Woosley 2002): $25 < \mathrm{m} < 140\,\mathrm{M}_\odot$ and $\mathrm{m} > 260\,\mathrm{M}_\odot$. The low-mass range is unlikely to form BHs eligible to become central BHs, as they are not sufficiently massive to remain in the galaxy center (Volonteri, 2010). The high-mass range is more favorable. If the stellar mass in clump is too small, the probability of forming a star with $\mathrm{m} > 260\,\mathrm{M}_\odot$ is smaller than unity. We stochastically sample the IMF and find that the probability of forming a sufficiently massive star becomes close to unity when the stellar mass in the clump is $\sim 10^3\,\mathrm{M}_\odot$. In our simulations gas clumps are always more massive than this value, therefore we can assume that the probability of BH formation is unity in a given mass clump.

We define a parameter f_{BH} to describe the fraction of stellar mass which goes into the BH. We integrate the IMF (in mass) to compute the stellar mass fraction of stars within the range $260 - 500\,\mathrm{M}_\odot$, and find $f_{\mathrm{BH}} = 0.48$. To this, we add an efficiency ϵ_{BH} that accounts for the ratio

of the mass of the BH to its parent star, and we conservatively assume that a BH retains 50% of the stellar mass, and we release metals in the surrounding accordingly. The initial mass of the sink particle is finally expressed by $\mathrm{M_{BH}} = \mathrm{f_{BH}} \times \epsilon_{\mathrm{BH}} \times \mathrm{M}_\star = 0.48 \times 0.50 \times \mathrm{M}_\star = 0.24 \times \mathrm{M}_\star$.

For the nuclear cluster scenario the metallicity range is the key parameter allowing for formation of a BH with mass $\sim 10^3\,\mathrm{M}_\odot$ (Devecchi & Volonteri, 2009), once a dense cluster of stars forms in the clump. As shown in section 4.1 below with the method described above we form already BHs with mass $\sim 10^3\,\mathrm{M}_\odot$, in line with the expectations for this model. We therefore do not differentiate explicitly between the two models, such approach would require even higher resolution simulations that resolve clumps with mass $\ll 10^3\,\mathrm{M}_\odot$. Moreover, because we do not differentiate between the PopIII remnant and stellar cluster models, and that our model is an intermediate model between these two, we assume that all the BHs that could form merge together.

Our approach to seed cosmological simulations, and to compute the initial BH masses, is based on local gas properties. Because the simulations do not include H_2 cooling, and that there is no distinction between the first or second generation of stars in the code Ramses, we do not actually form PopIII stars in the simulations, however we compute the theoretical stellar mass content of every clump based on its local gas density, assuming a Kennicutt-Schmidt law, and a logarithmically flat IMF. Our assumption that the Kennicutt-Schmidt law lies at high redshift for the first generation of stars, may lead to an overestimation of the number of BHs that form, as well as an overestimation of their mass, which is also enhanced by our choice of a logarithmically flat IMF, compared to Salpeter or Kroupa IMF.

3.3.3 BH growth and AGN feedback

The accretion on the BH is described by the minimum between a Bondi-Hoyle-Lyttleton accretion rate and the Eddington accretion rate, with:

$$\dot{\mathrm{M}}_{\mathrm{BH}} = \min\left(\dot{\mathrm{M}}_{\mathrm{BH}}, \dot{\mathrm{M}}_{\mathrm{Edd}}\right) = \min\left(4\pi\alpha G^2 \mathrm{M}_{\mathrm{BH}}^2 \bar{\rho}/(\bar{c_{\mathrm{s}}}^2 + \bar{v}^2)^{3/2}, 4\pi G \mathrm{M}_{\mathrm{BH}} m_{\mathrm{p}}/(\epsilon_r \sigma_{\mathrm{T}} c)\right)$$

where α is a boost factor (Booth & Schaye, 2009), G is the gravitational constant, $\mathrm{M_{BH}}$ the mass of the BH, $\bar{\rho}$ the average density of the medium, c_{s} the average of the sound speed, v the average velocity of the gas relative to the BH, m_{p} the proton mass, $\epsilon_r = 0.1$ the radiative efficiency, σ_{T} the Thomson cross-section, and c the speed of light.

AGN feedback is modeled with an isotropic injection of thermal energy into the surrounding gas, within a sphere of 4 cells ($4 \times \Delta x$) around sink particles (Teyssier et al., 2011 ; Dubois et al., 2012b). We store the rest-mass energy of the accreted mass into the BH, and release it when the energy is high enough to raise the temperature of the gas around the BH to at least 10^7K. The energy is released as thermal energy, with an efficiency of $\epsilon_f = 0.15$ (calibrated to reproduce the observational $\mathrm{M_{BH}} - \mathrm{M}_\star$ and $\mathrm{M_{BH}} - \sigma_\star$ relations), within a spherical bubble of 4 cells ($4 \times \Delta x$) centred around the sink particle.

3.4 The influence of star formation and metallicity on BH formation

In order to test whether star formation is realistic we compare our simulations results to the extrapolation of the model by Behroozi, Wechsler & Conroy (2013), an empirical model of galaxy mass versus halo mass and redshift that extends up to high redshifts ($z = 8$). We extrapolate to even higher redshifts and compare it to our simulation SuperChunky. Fig. 3.1 shows the

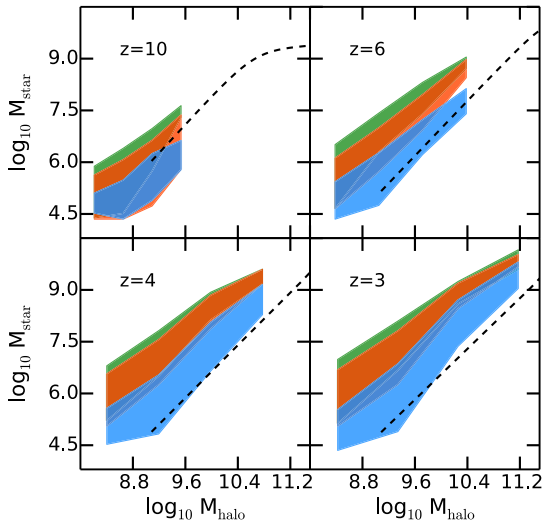

Fig. 3.1 – Stellar-halo mass relation for the SuperChunky simulations, in green with thermal SN feedback (simulation T), in orange with the kinetic SN feedback (simulation K), and in blue with delayed cooling SN feedback (simulation D). We show with black dashed lines an extrapolation of the empirical relation between stellar and halo masses (Behroozi, Wechsler & Conroy, 2013). Simulations with thermal and kinetic SN feedbacks overestimate the stellar mass in halos, while delayed cooling better reproduces the empirical relation.

stellar-halo mass relation for the T (thermal feedback, in green), K (kinetic feedback, in orange), and D (delayed cooling, in blue) simulations, the empirical relation of Behroozi, Wechsler & Conroy (2013) is shown with dashed black curves. We obtain good agreement, particularly with the delayed cooling SN feedback. With the thermal and kinetic SN feedbacks the stellar mass in halos is higher, and overestimated compared to the (extrapolation of) the stellar-halo mass relation. The delayed cooling SN feedback favours a better agreement of the simulation with the empirical model.

More star particles are formed in the T simulation, compared to the K and D simulations. Conversely, more BHs are formed in the D simulation than in the T and K ones. Fig. 3.2 shows the number of BHs formed in the three simulations over time, this correspond to the total number of sink particles at a given time in the simulation. Sink particles do not always form in the centre of galaxies and dark matter halos, and the dynamical evolution, specifically merging and stripping, causes some of the BHs to stray in the outskirts of galaxies. In Fig. 3.2, we include all BHs that form in the simulations, however in the following sections, we will only consider BHs within the virial radius of galaxies.

Three main features are identified in Fig. 3.2, the difference in the number of sink particles in the D simulation versus T and K, the fact that the number of BHs formed for kinetic and thermal SN feedbacks is almost identical, and the asymptotic behaviour at decreasing redshift. In the T and K simulation, more stars are formed, therefore less cold, low-metallicity gas remains available to form a BH. Delayed cooling feedback is stronger, but as less stars are formed within the simulation box, the mean metallicity of haloes is always lower than in the two other simulations, and at all halo masses. The metallicity is highest in the T simulation, and K simulation is intermediate. Regarding the similarity of the curves for the T and K cases, less stars are formed in the K simulation, therefore a larger amount of gas is available to form BHs, but the mean metal enrichment in haloes is very similar in the K and T simulations at the low-mass end. The

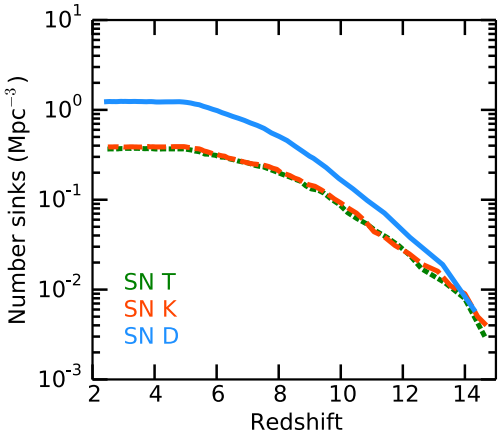

Fig. 3.2 – Number of BHs formed in the three simulations, in green for the thermal simulation, in orange for the kinetic one, and in blue for the delayed cooling one. More stars are formed in the T and K simulation, thus raising the gas metallicity. More cold, pristine gas is still available in the D simulation to form BHs.

gas is more metal-enriched, therefore the number of BHs that formed is reduced, and ends up being similar to the T simulation. The metal enrichment of the T and D simulations is discussed in Habouzit et al. (2016a) (Fig. 2, or Fig. 4.2 in the thesis). Finally, at lower redshifts, the number of forming BHs tapers off; this is due to the metallicity criterion to form BHs, after $z = 6$ the metal-enrichment of the medium is too large to keep forming many BHs (Bellovary et al., 2011). The three simulations follow the same trend with the saturation in the formation of pop III seed BHs below $z < 5$.

Fig. 3.3 shows the initial mass function of BHs which form before $z = 6$, for the three simulations. The initial mass function of the T and K simulations are very similar. The D simulation lead to the formation of more BHs. Most BHs have masses $\sim 10^3\,\mathrm{M}_\odot$ at birth. This mean value of the initial mass of BHs is slightly resolution-dependent, we have tested the dependence with a lower and higher resolution simulations. For the higher resolution simulation, which has a dark matter resolution of $2.3 \times 10^5\,\mathrm{M}_\odot$, we find a mean initial mass of $\sim 3 \times 10^2\,\mathrm{M}_\odot$, whereas for the lower resolution simulation with a dark matter resolution of $1.6 \times 10^7\,\mathrm{M}_\odot$, we find $\sim 6 \times 10^3\,\mathrm{M}_\odot$.

Fig. 3.4 shows a gas density and metallicity map at the same time ($z = 10$). BHs mainly form in halos at the intersection of filaments, i.e. in positively biased regions. This is because high gas densities are required to form and identify a gas clump in the first place. The metallicity criterion, however, acts in the opposite sense, as star formation and metal enrichment occur also in the most biased regions first. BH formation, therefore, mainly occurs in biased regions just before widespread star formation takes place. There are pockets of metals without BHs, these are cases where no sufficiently dense clumps formed before star formation and metal enrichment made the region unsuitable for BH formation.

3.5 Black hole mass function and occupation fraction

We now turn to analyzing the distribution of BHs. Because BHs form in dense regions, but are not forced to stay in the inner part of halos and galaxies, we need to assign BHs and halos, and BHs and galaxies. We consider a BH as the central BH of a halo, if its position is within 10% of the halo virial radius. If several BHs are located within this region, we choose the more massive

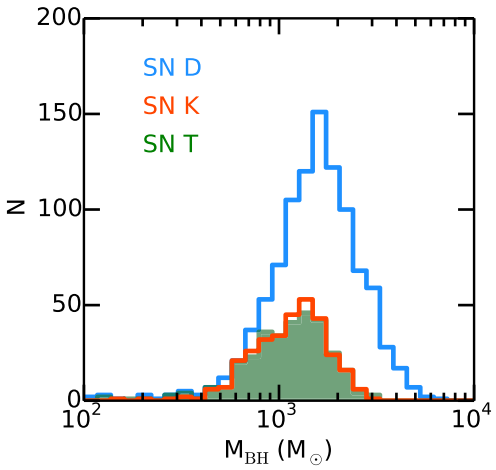

Fig. 3.3 – Initial mass function of BHs for the D (blue), K (orange), and T (green) simulations. The initial mass function of the T and K simulations are very similar. The D simulation leads to the formation of more and more massive BHs.

as the central BH. For galaxies, we proceed in the same way, looking for BHs inside the virial radius of galaxies (with a lower limit of $4 \times \Delta x$).

Fig. 3.5 shows the cumulative mass function of BHs at different redshifts. This differs from the initial mass function of BHs (Fig. 3.3), as we take into account both the seed mass, the mass accreted by the BHs and BH-BH mergers (which are sub-dominant in the mass growth budget). We show in Fig. 3.5 the three different simulations, with the thermal, kinetic, and the delayed cooling SN feedbacks.

The evolution with time is as expected: with increasing cosmic time (decreasing redshift), more and more BHs form, and the already formed BHs grow in mass. Although the mass functions are very similar for the T and K simulations, the low-mass and high-mass ends slightly differ. More central BHs are identified in the kinetic feedback simulation. The high-mass end of the distribution is higher in the T case, showing that the weak thermal SN feedback favours the growth of BHs. The delayed cooling simulation has the largest number of BHs. Conversely, the BHs do not grow in mass as efficiently as in the T and K simulations. The strong SN feedback limits the growth of BHs. In summary, BHs are more numerous in the delayed cooling SN feedback simulation, but their masses are smaller. Only few BHs reach a final mass of $10^6\,M_\odot$ by $z = 3$ with a strong delayed cooling SN feedback. In the T simulation, because the SN feedback is weaker, BHs can grow faster to even higher mass (several BHs reach $10^7\,M_\odot$ by $z = 3$). The impact of SN feedback is discussed in more details in Section 3.6.

Our BH formation model does not necessarily place a BH in each and every galaxy. One of the diagnostics to distinguish between BH formation scenarios, in fact, is the probability that a galaxy or a halo hosts a BH: the occupation fraction. Theoretical studies predict a different occupation fraction of halos for different models, especially in low-mass galaxies and halos. Observing a large sample of low-mass galaxies, and measuring the eventual mass of the central BH will therefore provide constrains on scenarios.

We show in Fig. 3.6 the halo mass function at different redshifts, where we show both the total mass function, and the mass function of halos hosting a BH. As discussed in the previous section, BH formation occurs in the most biased halos first (Bellovary et al., 2011). BH formation, however, does not occur in *all* halos. Large haloes have a higher probability of hosting a BH, whereas this probability drops significantly for low-mass haloes. For the D simulation, the

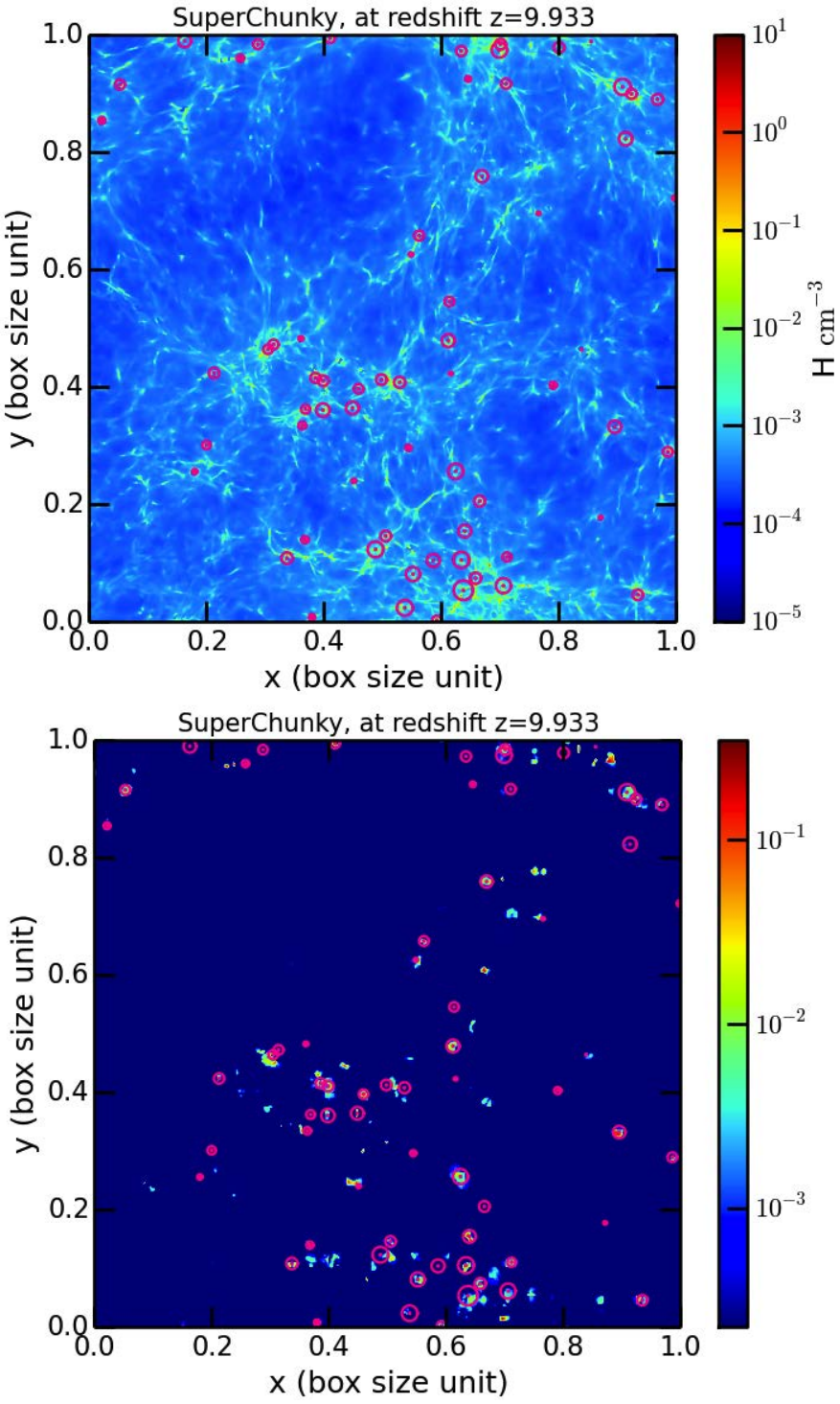

Fig. 3.4 – Gas density (left) and metallicity (right) maps at $z \sim 10$ for the delayed cooling SN feedback simulation. BHs are highlighted with circles, circle sizes are proportional to BH masses. BH formation walks a fine line: the necessity of having high gas densities selects biased regions, the criterion of low-metallicity works in the opposite way. BHs form in biased regions just before they experience a star formation event.

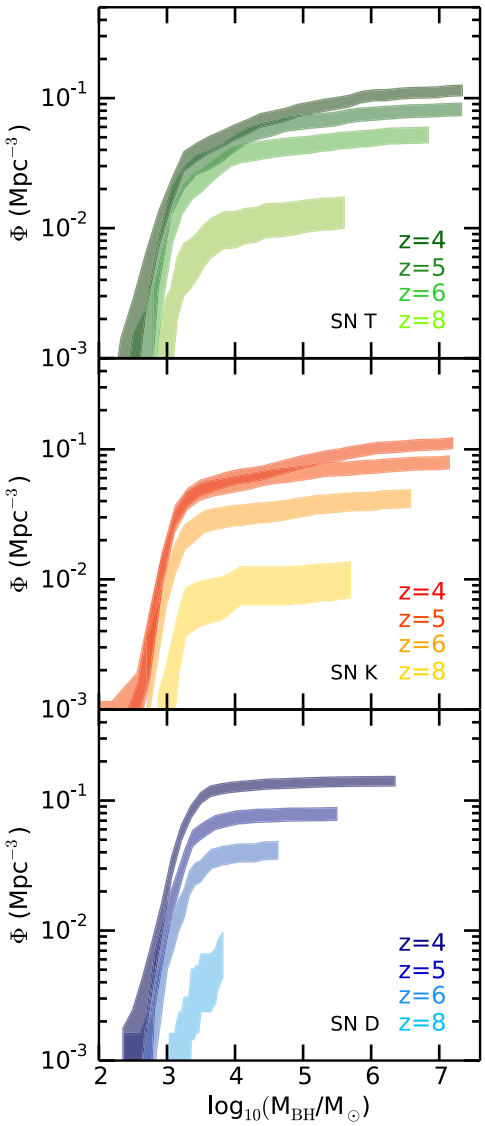

Fig. 3.5 – Cumulative BH mass function for the thermal SN feedback simulation (T, top panel), the kinetic one (K, middle panel), and for the delayed cooling one (D, bottom panel), for redshift $z = 8, 6, 5, 4$. Less BHs are produced in the T and K simulations, but they grow more, up to $\sim 10^7 M_\odot$, about one order of magnitude higher than for the delayed cooling one, which is a signature of SN feedback regulating the growth of low mass BHs in the case of strong feedback (delayed cooling).

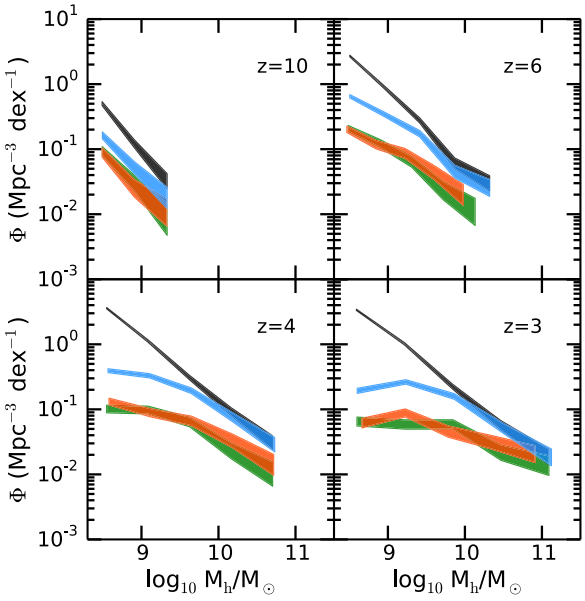

Fig. 3.6 – Total halo mass function (black; shaded areas represent poissonian error bars). The mass function of halos hosting BHs are shown in colours (green for simulation T, orange for K, and blue for D; shaded areas also represent poissonian error bars).

occupation fraction is above 50% only for haloes more massive than $10^{9.5}\,M_\odot$, or galaxies with stellar mass above $10^{7.2}\,M_\odot$. For the T and K simulations, an occupation fraction of 50% is found for higher haloes ($10^{10.5}\,M_\odot$) and galaxy masses (galaxies with stellar mass above $10^{8.8}\,M_\odot$). The mass function of haloes hosting a BH is closer to the total halo mass function for the delayed cooling simulation since more BHs form in this simulation.

We show in Fig. 3.7 the BH occupation fraction as a function of galaxy mass. Here again, the probability for galaxies to host a BH is high at the high-mass end of galaxies, and drops at the low-mass end. At fixed galaxy mass, the occupation fraction is higher for the simulation with the delayed cooling SN feedback, for two reasons. First, because it allows the formation of more BHs, and second, because the strong SN feedback reduces the galaxy stellar mass, therefore the occupation fraction is shifted compared to the other simulations T and K, which have a weaker SN feedback. Regarding the evolution with redshift, the galaxy occupation fraction can increase by mergers of galaxies, and the formation of new BHs. As we have seen that no new BHs are formed since $z \sim 5$, and mergers are few, the evolution with redshift can be explained by the growth in mass of galaxies. At a given galaxy mass, the occupation fraction is lower at lower redshift, because galaxies have grown in mass. The lower redshift occupation fraction is shifted to higher galaxy masses. This occupation fraction can be used to seed with BHs cosmological simulations at lower resolution, which can not resolve the small galaxies where BHs are expected to form.

3.6 Black hole growth regulated by efficient SN feedback

Most BHs in our simulations are growing slowly. The normalized histograms of the BH accretion rate for the three simulation are shown in Fig. 3.8. We have averaged the histogram over few outputs around $z = 4$. The typical accretion rate for the D simulation is highly sub-Eddington. In the kinetic and thermal SN feedback simulations, instead, a significant fraction of the BHs are

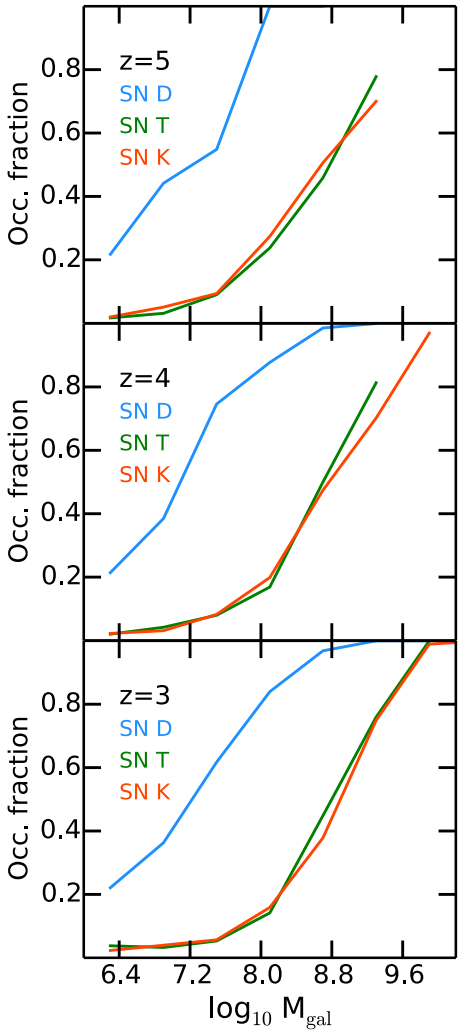

Fig. 3.7 – Probability that a galaxy of a given mass at a given redshift hosts a BH. This occupation fraction for the thermal (T, green), and the kinetic (K, orange) SN feedbacks is similar, and lower than for the delayed cooling SN feedback (D, blue). The occupation fraction for the D simulation is higher because more BHs are formed in this simulations compared to the others, but galaxies are also less massive, because of the stronger SN feedback. With time the occupation fraction shifts to the right because galaxies are becoming more massive with time, but no more BHs are formed below $z = 5$. The number of BHs remains almost identical, but galaxies grow.

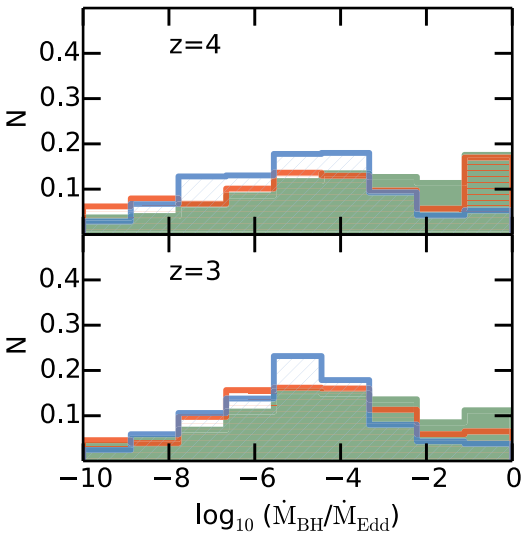

Fig. 3.8 – Normalized distribution of Eddington ratios $\log_{10}(\dot{M}_{BH}/\dot{M}_{Edd})$ at redshift $z = 4$ and $z = 3$ for the delayed cooling (in blue), kinetic (in orange), and thermal (in green) SN feedback simulations. More BHs are accreting at the Eddington limit (when $\log_{10}(\dot{M}_{BH}/\dot{M}_{Edd})$=0) in the T simulation than in the D one.

accreting at the Eddington limit, especially at higher redshifts.

Fig. 3.9 shows the BH mass as a function of the total stellar galaxy mass, at several redshifts ($z = 8, 7, 6, 5, 4, 3.5, 3$), for the thermal SN feedback simulation on the left panel and the delayed cooling one on the right panel. The BH-galaxy mass relation for the kinetic feedback simulation (not shown here) is very similar to that of the thermal feedback case.

In the thermal SN feedback simulation, some massive galaxies host very low-mass BHs. These are BHs that have recently been acquired from a satellite galaxy that merged with a larger galaxy that did not initially host a BH. We do not force BHs to form in massive galaxies, in fact, if in some galaxy wide-spread star formation and metal enrichment occur before the formation of a dense, bound clump that meets all the criteria for BH formation, that galaxy is not seeded with a BH. Fewer BHs form in the thermal and kinetic SN feedback case, as discussed in Section 4.1, therefore more galaxies are BH-less. Some BHs form in relatively small galaxies, which travel to intersections of filaments, and are then captured by a more massive galaxies. If the more massive galaxy does not host its own BH, eventually the BH in the satellite galaxy can become the central BH of the merger remnant. We do not reposition BHs at galaxy centres artificially, but let them evolve under the effect of dynamical friction (see Tremmel et al., 2015, for a detailed discussion on BH dynamics in cosmological simulations). The timescale for a small BH ($\sim 10^3\,M_\odot$) to settle in the galaxy centre is long, of order of a few hundred Myr to Gyr (Binney & Tremaine, 2008), and, during the orbital decay, the rapidly moving BH cannot efficiently accrete gas from its surroundings. Only after the BH has settled long enough in the galaxy centre, it will start accreting and grow, “catching up" with its galaxy. Such population is instead not present in the delayed cooling feedback simulation, simply because a larger fraction of galaxy is initially seeded with their own BH: the BHs initially hosted in satellite galaxies either merge with the pre-existing BH in the main galaxy, or remain stranded in its outskirts without necessarily merging with the central BH (see, e.g., Islam, Taylor & Silk, 2003; Volonteri & Perna, 2005; Volonteri et al., 2016).

Except for the small population of recently captured BHs, we see that “weak” SN feedback (T and K) produces a near-linear BH-galaxy mass relation, while for the “strong” SN feedback (D)

the BH-galaxy mass relation plateaus at low galaxy mass with an ankle at $M_* = 10^9 - 10^{10}\,M_\odot$ and a steep rise above this mass transition. BHs grow faster (see Fig. 3.8) in the T and K simulations than in the D simulation, and as a result the BH masses are larger relative to their galaxy stellar mass. This mechanism was identified in Dubois et al. (2015) as the *SN-regulated growth of BHs in low-mass galaxies* by means of one single zoom cosmological simulation of group progenitor at $z = 2$. We, here, confirm the result with a statistical sample of high-redshift galaxies.

The kinetic and thermal feedbacks are weaker, because the energy released by the SN explosion is distributed in the nearby surrounding cells, however, the cold gas present in dense regions central regions is not destroyed (because of short cooling times) and is still available to form stars, BHs, and also to fuel an existing BH. Dubois et al. (2015) find that this cold gas reservoir fuels the BH efficiently, and accretion occurs at rates close to the Eddington limit. In contrast, with delayed cooling SN feedback, the dense gas clumps in star-forming regions are destroyed by the release of energy after a SN explosions with a SN wind velocity of around $270\,\mathrm{km\,s^{-1}}$. The main effect is to reduce the BH growth (and star formation) in the central regions of the galaxy by routinely removing the dense star-forming gas with SN winds, until the gravitational potential well of the bulge and galaxy is deep enough to confine the cold gas close to the BH. Dubois et al. (2015) show that the growth of the rest of the galaxy is not much impacted (though growing at a slower rate than with inefficient SN feedback), therefore the total stellar mass keeps growing but not the BH mass, nor the bulge mass. It is only when the galaxy mass and bulge stellar mass become massive enough (i.e. with a corresponding escape velocity larger than SN-wind velocity) that the BH can proceed to a rapid near-Eddington growth only altered by the self-regulation due to AGN feedback. They measured that this transition occurred for a galaxy stellar mass of $10^9 - 10^{10}\,M_\odot$ (corresponding to $v_{\rm esc} = 300 - 400\,\mathrm{km\,s^{-1}}$).

In Fig. 3.9 we report also the BH and stellar mass for the objects published by Reines & Volonteri (2015) (dark and light blue points). In this paper, 262 broad-line AGN and 79 galaxies with dynamical BH mass measurement, for redshift $z < 0.055$, are used to investigate the scaling relation between BH mass and the total stellar mass of galaxies. We see that when BHs grow, they eventually connect to the low-redshift sample. In low-mass galaxies, however, BHs are unable to grow, and more so if SN feedback is strong, and BHs remain "stuck" at low mass. Volonteri & Stark (2011) proposed, based on empirical arguments, that if BHs in small galaxies are under-massive and BHs in large galaxies are over-massive, then one can reconcile several observational results, namely that analysis of the BH mass/luminosity function and clustering suggests that either many massive galaxies do not have BHs, or these BHs are less massive than expected (Willott et al., 2010a ; Treister et al., 2013 ; Weigel et al., 2015).

To investigate BH growth in more detail, we track the BHs with mass above $10^6\,M_\odot$ at $z = 3$. The thermal SN feedback simulation has 24 BHs above this mass threshold, the kinetic one 22, and the delayed cooling one only 2. In Fig. 3.10, we show the growth of these BHs with solid lines (left panel for the simulation with the thermal SN feedback, right panel for the delayed cooling one), the theoretical evolution of a BH at the Eddington limit is also showed with a dashed line. All BHs in the thermal and kinetic SN feedback simulations have episodes of accretion at the Eddington limit. In contrast, the growth of BHs in the delayed cooling simulation is smoother, and Eddington-limited phases minimal in particular at early times.

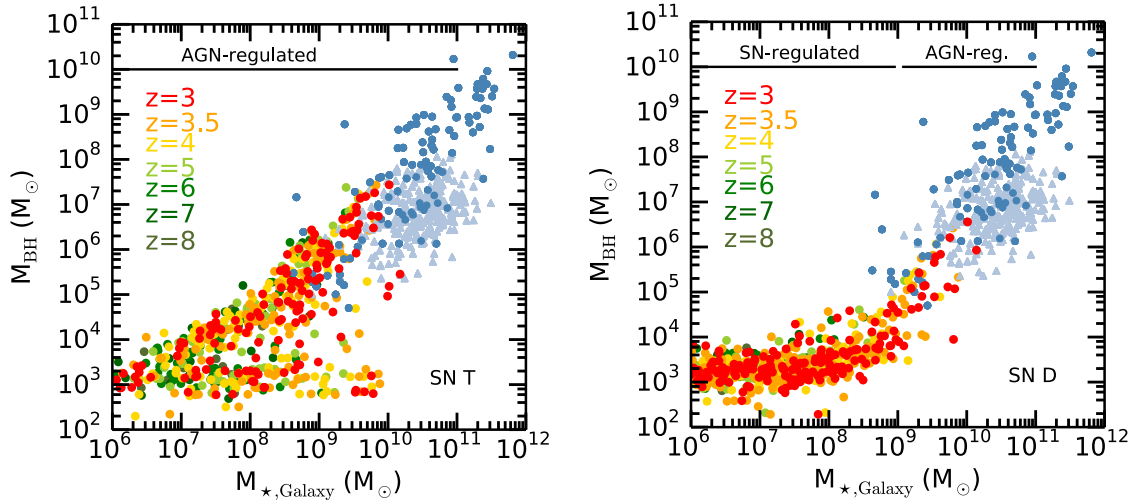

Fig. 3.9 – BH mass as a function of the total galaxy stellar mass for the kinetic SN feedback (left) and the delayed cooling SN feedback (right). BHs in the smallest galaxies have a very hard time to grow because low-mass galaxies have shallow potential wells, and supernova feedback is sufficient to energize gas and suppress BH accretion.

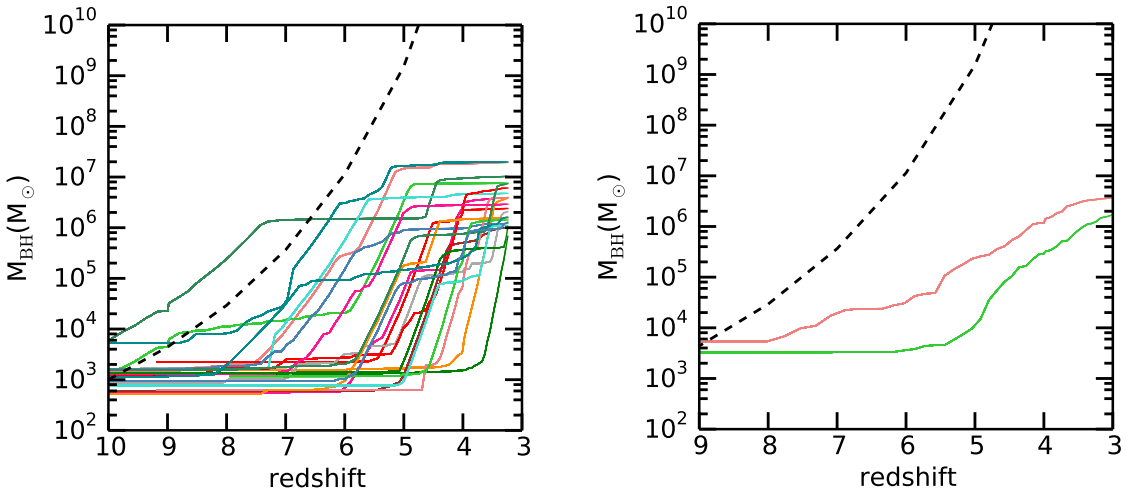

Fig. 3.10 – We show here the BH growth of the most massive BHs, $M_{BH} > 10^6\,M_\odot$ at $z = 3$, for the simulation with thermal SN feedback (left panel) and the one with the delayed cooling SN feedback (right panel). The dashed line represents BH growth at the Eddington limit. For the thermal feedback, BHs grows rapidly with several episodes at the Eddington limit, whereas for the delayed cooling SN feedback simulation, BH growth is smoother. Only two BH in this simulation succeed in growing to $10^6\,M_\odot$ by $z = 3$. We do not show the corresponding plot for the simulation with kinetic SN feedback; it is very similar to the thermal SN feedback simulation.

3.7 Comparisons with a sample of local galaxies, and Lyman-Break Analogs

Over the past decades, an incredible effort has been made to study, theoretically and observationally, the BH, quasars and AGN population in massive galaxies, very often looking for the smoking gun of AGN feedback, thought to impacting the growth and star formation at the high-mass end of the galaxy distribution. In Fig. 3.11 we present the luminosity function of BHs at different redshifts, and compare it to the fit to the bolometric luminosity function compiled by Hopkins, Richards & Hernquist (2007) and its extrapolation (middle and bottom panels on the left in Fig. 3.11), and to the X-ray luminosity (middle and bottom panels on the right, Buchner et al. (2015)). Our low-mass, slowly accreting BHs are well below current observational limits. Future high-sensitivity missions, such as JWST and ATHENA, and proposed ones such as X-ray Surveyor and StarX, can instead start probing the luminosity range where normal high-z BHs in normal galaxies are evolving, instead of the brightest quasars powered by the most massive BHs we can reach today.

The high-mass end of the BH distribution provides us essential information on the growth of BHs. However, as the host galaxies are typically massive, all the clues relating to BH formation have been erased by the growth of BH, through gas accretion and BH-BH mergers (e.g., Dubois, Volonteri & Silk, 2014, and references therein). In order to collect crucial information on BH formation, one has to look at the least evolved galaxies. Lacking observational samples of low-mass galaxies at high-redshift, we compare our simulations to two different types of low-redshift galaxies: dwarf galaxies and local analogs of high-redshift galaxies (LBAs).

In recent years, many studies have started looking for evidence of the presence of BHs in low-mass galaxies (with stellar mass of $M_\star \sim 10^9\,M_\odot$): evidence for accreting BHs with broad Hα line in the SDSS survey (Greene & Ho, 2004, 2007b ; Dong et al., 2012), evidence for narrow-line AGN in low stellar velocity dispersions (favoring the presence of a low mass BH). Reines, Greene & Geha (2013) went further and performed the first systematic search for BHs in galaxies with stellar mass of $M_\star < 3 \times 10^9\,M_\odot$. They found 136 dwarf galaxies harboring evidences of active BHs (photoionization signatures, broad emission lines). The comparison between our high-redshift samples (from $z = 8$ in green to $z = 3$ in red points) and the observations in the local Universe (dark and light blue points) is shown in Fig. 3.9. We discussed how BH growth appears to be stunted in low-mass galaxies by SN winds, but with our high-redshift simulations we can only extrapolate our results to the local Universe provided that the BH to galaxy mass relation show little-to-no evolution with redshift (e.g. Volonteri et al., 2016 for the Horizon-AGN simulation, Dubois et al., 2014); bringing such high-resolution simulation as SuperChunky to $z = 0$ is computationally very expensive.

A fairer comparison can be made with local analogs of high-redshift galaxies. Such LBAs are promising laboratories for constraining BH formation. They have properties similar to the more distant Lyman Break Galaxies (LBGs), in terms of mass, age, size, metallicity, star formation rate, optical extinction, but are much closer to us, thus permitting more detailed studies. AGN in LBAs can then provide us crucial clues on BHs in LBGs and then directly on the high redshift population of BHs. Fig. 3.12 compares the sample of BHs in our simulations with the sample of XMM observation of six LBAs described in Jia et al. (2011a), with $z \leqslant 0.3$. We show the normalized distribution of accretion rate, shown as X-ray luminosity. The accretion rate is similar for the high-z galaxies for the most luminous BHs in the simulation and the LBAs (shown as black triangles in Fig. 3.12) suggesting that the physical conditions are at least comparable.

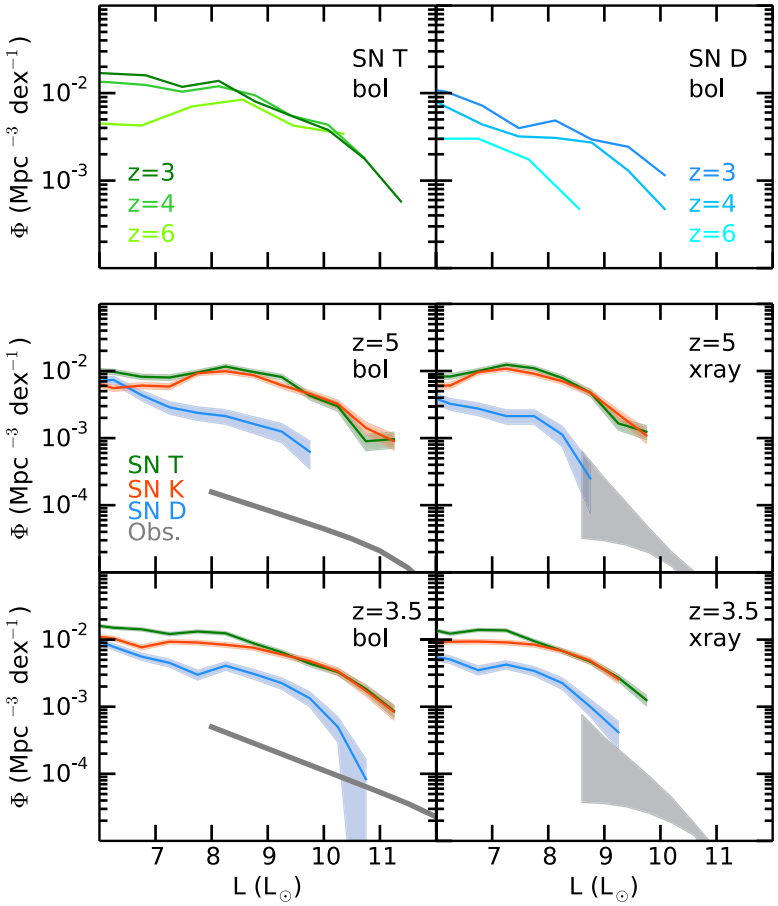

Fig. 3.11 – Luminosity function of simulated BHs, and comparison with observations. In the two top panels, we show the evolution of the bolometric luminosity function of the simulated BHs with time (for $z = 6, 4, 3$) for the simulation T (top left panel) and the simulation D (top right panel). In the 4 bottom panels, we compare the bolometric (left) and the hard X-ray (right) luminosity function of simulated BHs in simulations D (blue), K (orange) ,T (green) with observations (shaded grey regions, Hopkins, Richards & Hernquist (2007), and Buchner et al. (2015)). The middle panels show the comparison at $z = 5$, and bottom panels at $z = 3$.

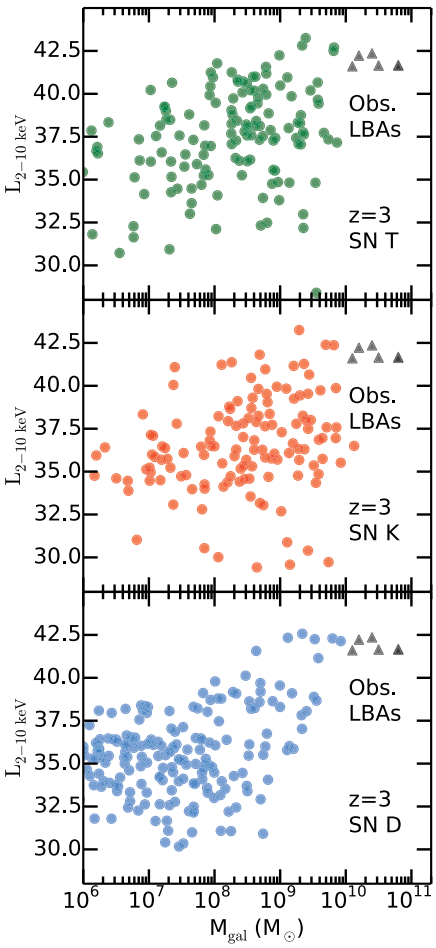

Fig. 3.12 – BH hard X-ray luminosity from the simulations (delayed cooling in blue, kinetic SN feedback in orange, thermal SN feedback in green, at redshift $z = 3$), compared to the observed BHs in LBAs (black triangles). The luminosity, and so the accretion rate, of the most luminous simulated BHs is similar to the LBAs, suggesting that the physical conditions are at least comparable.

3.8 Conclusions

In this chapter, we present a new implementation to seed cosmological simulations with BHs. Our implementation mimics BH formation models based on stellar properties, namely a scenario based on remnants of PopIII stars, and a scenario based on stellar mergers in nuclear star clusters at low metallicity. The seed BHs are relatively small, as expected for the scenario investigated here. Most BHs have masses $\sim 10^3\,M_\odot$ at birth. The lowest mass central BH in a galaxy (ignoring "normal" stellar mass BHs) has a mass estimate of $\sim$ 50,000 $M_\odot$ (Baldassare et al., 2015), and was identified as a low-luminosity AGN in the dwarf galaxy RGG 118 (Reines, Greene & Geha, 2013). Our implementation allows for such low-mass BHs to be accounted for.

This implementation is not based on halo properties, but on the local environment of the BH formation sites. The code first identifies all the local overdensities in the gas density field, selects clumps that are bound and collapsing along all axes. If the gas metallicity is below a critical value, they are flagged as potential sites for BH formation. We compute the stellar mass formed in these dense regions and the probability of forming a BH, based on the IMF and the total stellar mass in the clump. If the stellar mass is low ($< 10^3\,M_\odot$) the probability of forming a BH is less than unity. Once a region is flagged as a site for BH formation, the mass of the BH is computed, directly related to the stellar mass. Therefore each BH in the simulation box has a different mass, assigned on-the-fly. To mimic the formation of these BHs, we use sink particles, which are able to accrete gas from their surroundings, and to merge together.

SN feedback is of paramount importance, as it modulates metal enrichment, as well as the presence and retention of cold gas in low-mass galaxies. We compare three implementations of SN feedback: one of the simulations uses a thermal feedback, another one a kinetic feedback, while the last one uses a delayed cooling feedback. Our main results are as follows.

- We find that a stronger SN feedback, delayed cooling, produces galaxies with stellar masses closer to those predicted by the relation with halo mass.
- We find that with strong SN feedback, more BHs are formed, but their growth is SN-regulated for low-mass galaxies with $M_* < 10^9\,M_\odot$ (Dubois et al., 2015): SN-driven winds remove dense star-forming gas and stunt BH accretion in galaxies with shallow potential wells.
- The lower BH masses and lower accretion rates predicted by the simulation with the strongest SN feedback, delayed cooling, seem to be in better agreement with the paucity of AGN in high-z galaxies (Weigel et al., 2015; Cappelluti et al., 2016, and references therein).
- We provide the probability that a galaxy of a given mass and redshift hosts a BH (Fig. 3.7). This information can be used to seed with BHs lower resolution cosmological simulations.
- The occupation fraction is also used as a diagnostic of BH formation. Our results agree with analytical and semi-analytical studies (Volonteri, Lodato & Natarajan, 2008; van Wassenhove et al., 2010; Devecchi et al., 2012) and with the simulations by Bellovary et al. (2011), in that all high-mass haloes/galaxies tend to host a BH, but low-mass haloes/galaxies have a lower probability of hosting a BH. After BH formation stops at $z \sim 6$, at a given galaxy mass the occupation fraction decreases with time because galaxies grow in mass. We provide the occupation fraction at high redshift, when the diagnostic is for today's low mass galaxies, however low mass galaxies are expected to experience a quieter merger history, and therefore the occupation fraction for low-mass galaxies is

not expected to vary much from high redshift to $z = 0$. One caveat is that our predicted occupation fraction slightly depends on the resolution of the simulations, but the models we provide is in good agreement with several observations, such as the bolometric and x-ray BHs luminosity function, and the number of AGN candidates identified at high redshift in the CDF-S survey.

- We have compared the BH populations from our simulations to a sample of galaxies representative of the local Universe (Reines & Volonteri, 2015) and to LBAs, local analogs of high-redshift LBGs (Jia et al., 2011a). Our simulated BHs connect to the low-redshift observational sample, and span a similar range in accretion properties as LBAs.

3.9 Perspectives: the details of BH growth, and predictions for future observations

3.9.1 BH growth in the delayed cooling SN feedback simulation

In the strongest SN feedback simulation presented in this chapter, those with delayed cooling, we have seen that early BHs growth is regulated by SN feedback. Some of the BHs in the simulation box, however, are still able to growth up to $\sim 10^6\,M_\odot$. What physical process allows some BHs to grow and others to be left behind?

Fig. 3.13, 3.14, and 3.15 show the mass evolution of three BHs (see bottom panels) over cosmic time. Black arrows represent the time at which we show the gas density maps (a,b,c,d,e,f), before and after a high accretion episode. From these figures, it seems that in most of the cases a galaxy merger triggers the episode of high accretion into the BHs. This may imply a dynamical effect, i.e. torques feeding the BH with gas on timescales shorter than star formation, or that the galaxy bulge grows sufficiently to reach the mass needed to retain gas, as suggested by Dubois et al. (2015). We are planning to study in more detail the growth of these BHs, and the evolution of the host galaxies, such as the evolution of star formation, for example.

3.9.2 Need for further comparisons with observations, preparing future observational missions.

Comparisons with observations

The comparison with LBAs so far only includes 5 LBAs (Jia et al., 2011b), and we span a similar range in accretion properties as LBAs. We are lacking of statistics, so we would like to work closely with observers to pursue our comparisons with larger sample of LBAs.

I also want to investigate in more detail the population of BHs in LBGs. Generally very few AGNs are observed in these galaxies. The identification of AGN in LBGs is difficult even for those that show some AGN signatures, e.g. the detection of CIV or HeII can hint either a low-luminosity AGN, as well as a population of hot young stars (Stark et al., 2015 ; Pallottini et al., 2015), the same problem is observed for LBAs (Jia et al., 2011b). Indeed these galaxies often show evidences for composite system, intense starburst or/and obscured AGN, making the AGN signatures questionable. With my simulation, I would like to predict the number of BHs in LBGs, and using theoretical spectra (Feltre, Charlot & Gutkin, 2016), estimate the optical and X-ray signal over star formation rate. It will help us to understand why AGN have not been observed so often in LBGs. BHs in these galaxies could be absent, or at least very faint and therefore not easily observable. In the simulation SuperChunky D, we have indeed see that BHs are stuck at low mass, the growth is stopped partly because of the feedback from supernovae,

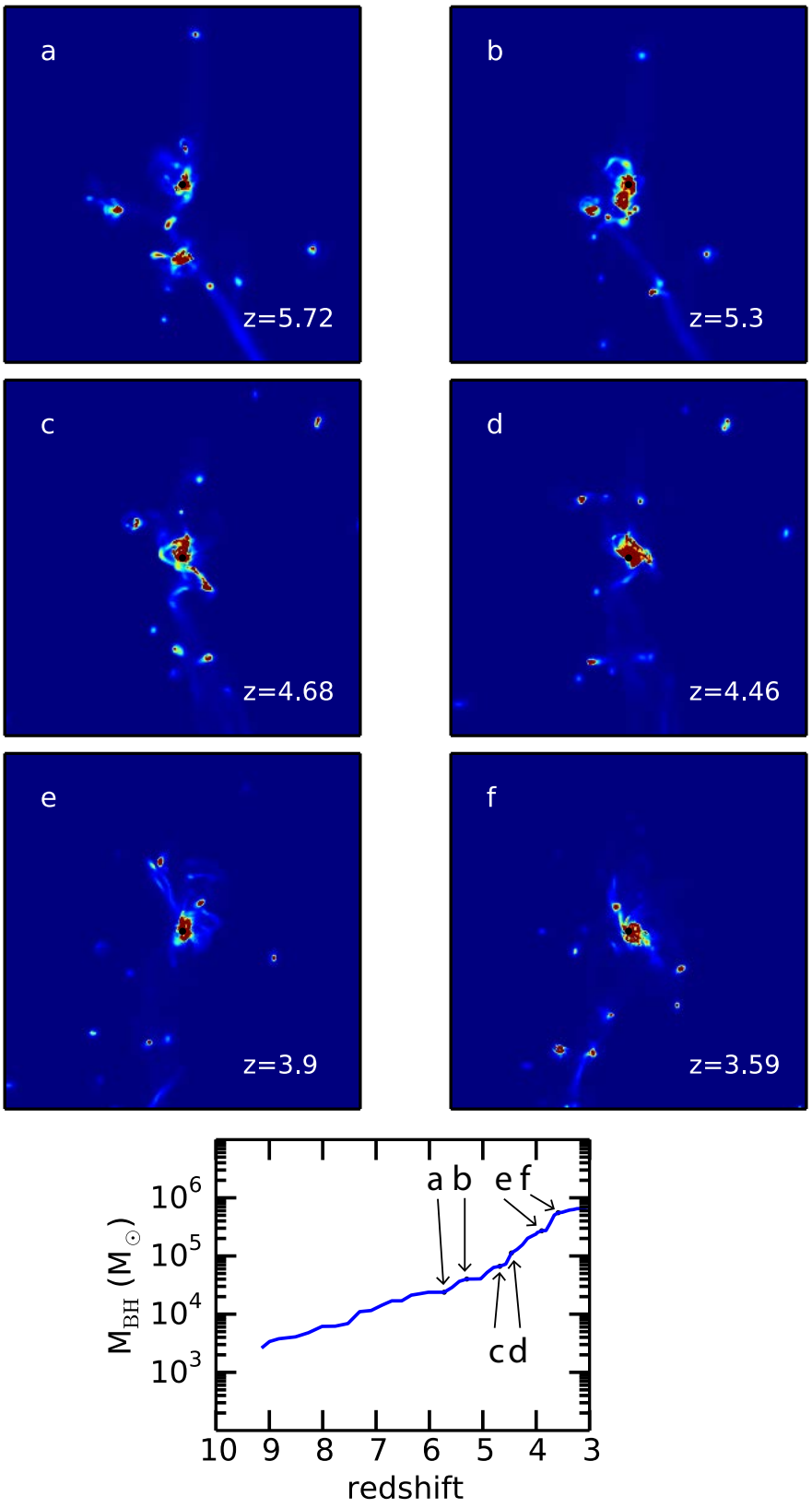

Fig. 3.13 – Black hole growth of one of the most massive BH at $z = 3$. Panel a,b,c,d,e,f show gas density maps centered on the BH position (black point), the figures represent 0.5 cMpc around the BH, colorbar ranges in $10^{-5} - 10$ H/cc. The bottom panel shows the evolution of the BH mass through cosmic time. Black arrows indicate the corresponding gas density map panels.

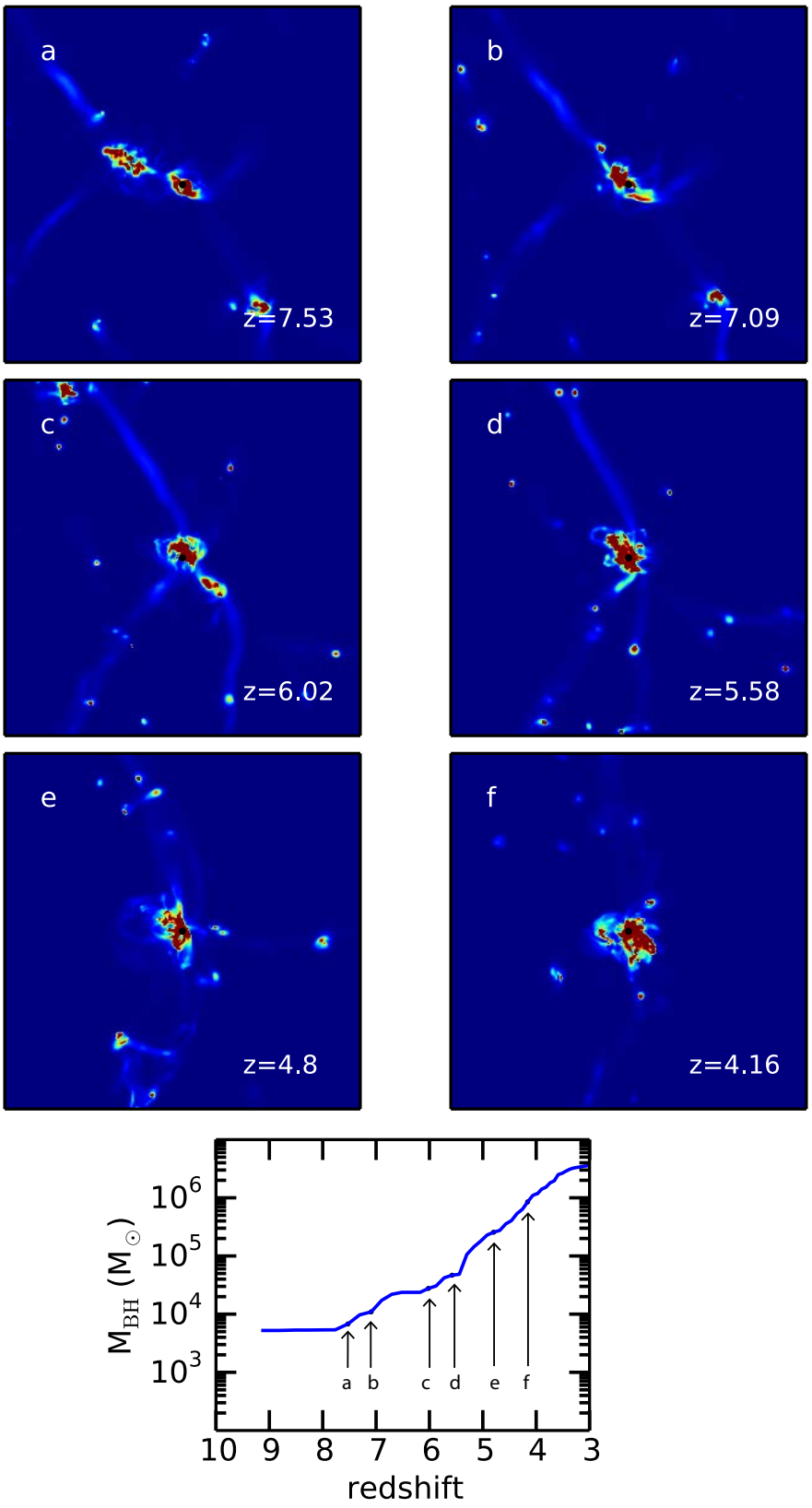

Fig. 3.14 – Black hole growth of one of the most massive BH at $z = 3$. Panel a,b,c,d,e,f show gas density maps centered on the BH position (black point), the figures represent 0.5 cMpc around the BH, colorbar ranges in $10^{-5} - 10$ H/cc. The bottom panel shows the evolution of the BH mass through cosmic time. Black arrows indicate the corresponding gas density map panels.

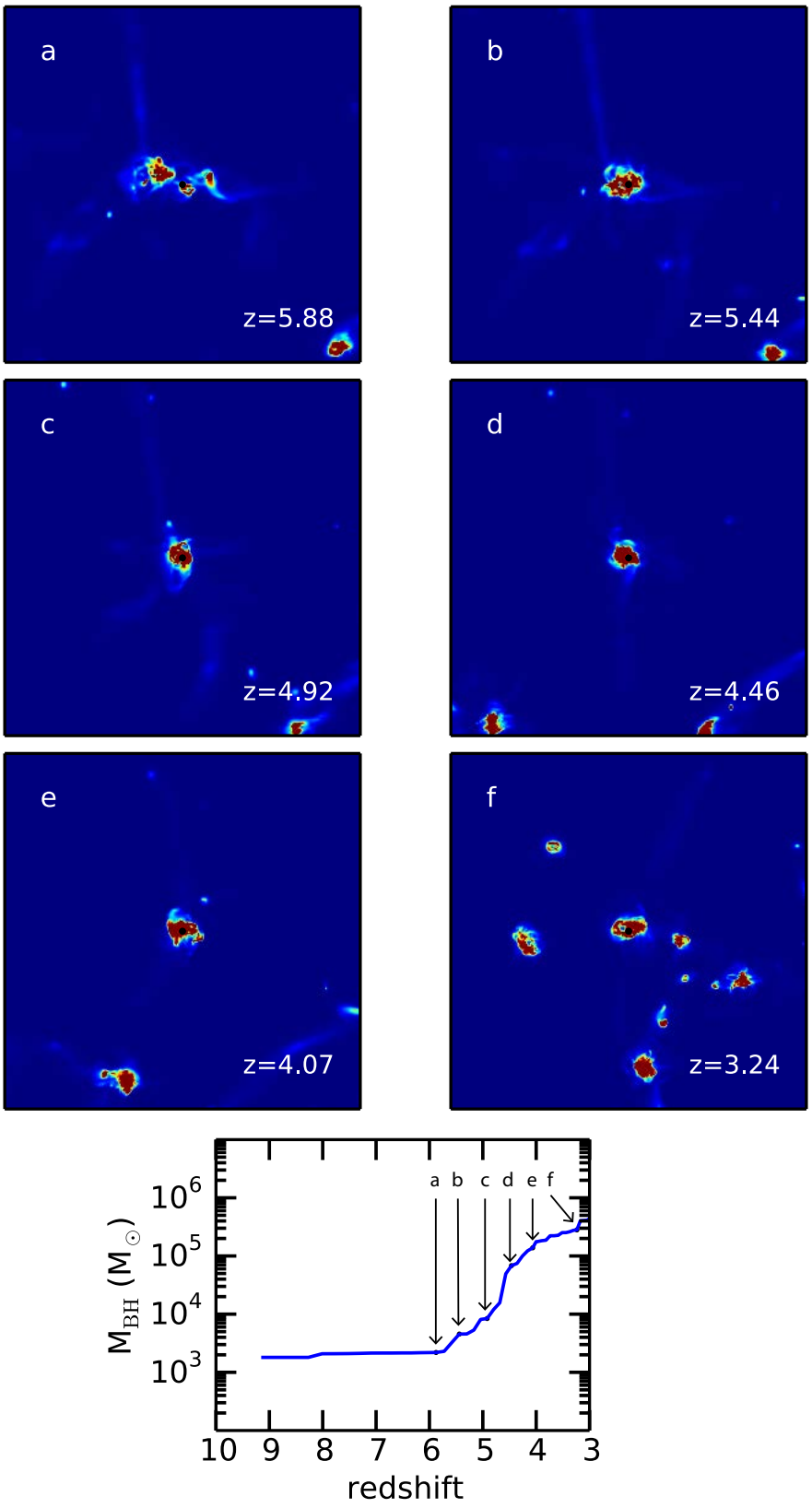

Fig. 3.15 – Black hole growth of one of the most massive BH at $z = 3$. Panel a,b,c,d,e,f show gas density maps centered on the BH position (black point), the figures represent 0.5 cMpc around the BH, colorbar ranges in $10^{-5} - 10$ H/cc. The bottom panel shows the evolution of the BH mass through cosmic time. Black arrows indicate the corresponding gas density map panels.

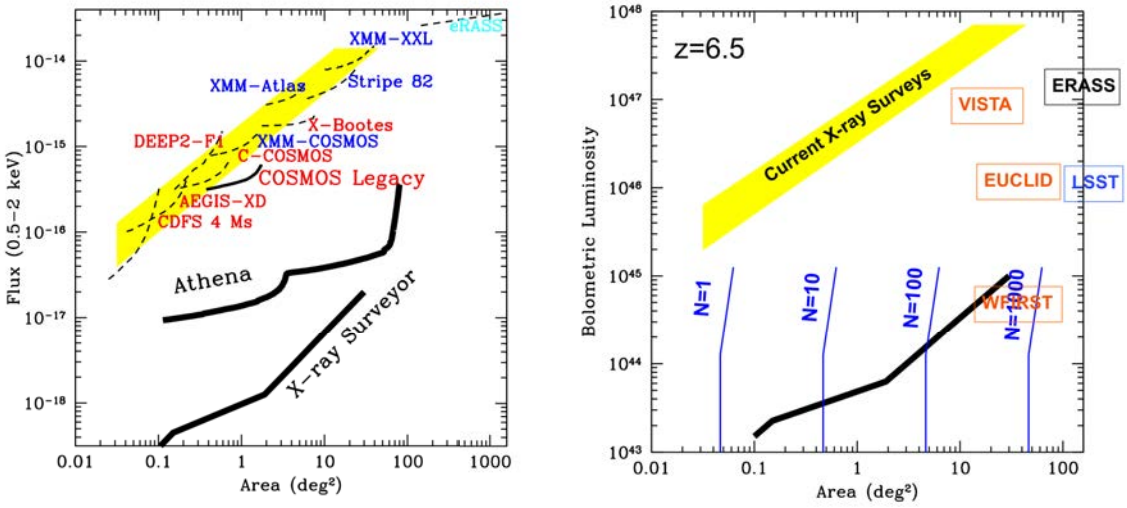

Fig. 3.16 – Figures from Fransceca Civano (adapted from Civano et al. (2015)). The left panel shows all the different X-rays surveys, and the new surveys ATHENA and X-ray Surveyor, which will push observations to much deeper sources. The right panel shows in blue lines the number of observable BHs predicted from my simulation Chunky (previous version of the simulations shown in this chapter) and Horizon-AGN (Volonteri et al., 2016), the black line shows again the X-ray Surveyor survey.

which could lead to a faint population of BHs in LBGs/LBAs.

Predictions for future missions

Fig. 3.16 (left panel, adapted from Civano et al. (2015)) shows the diversity of already existing X-ray missions, and the upcoming or proposed X-ray missions: the large X-ray telescope ATHENA and the X-ray Surveyor. I collaborated with Francesca Civano and we have used my simulations (a previous version of SuperChunky, the simulations used in this chapter) to predict the number density of BHs observable with the X-ray Surveyor survey. The preliminary result of this collaboration is shown in the right panel of Fig. 3.16, where the black line refers to the X-ray mission, and the blue lines to the prediction of observable BHs from my simulation (for high resolution) and the simulation Horizon-AGN of Yohan Dubois (for a lower resolution, see Volonteri et al., 2016).

Chapter 4

Direct collapse model

Supermassive BHs reside in the center of most local galaxies, but they also power active galactic nuclei and quasars, detected up to $z = 7$. These quasars put constraints on early BH growth and the mass of BH seeds. The scenario of "direct collapse" is appealing as it leads to the formation of large mass BH seeds, $10^4 - 10^6 \mathrm{M}_\odot$, which eases explaining how quasars at $z = 6 - 7$ are powered by BHs with masses $> 10^9\,\mathrm{M}_\odot$. Direct collapse, however, appears to be rare, as the conditions required by the scenario are that gas is metal-free, the presence of a strong photo-dissociating Lyman-Werner flux, and large inflows of gas at the center of the halo, sustained for $10 - 100$ Myr. We performed several cosmological hydrodynamical simulations that cover a large range of box sizes and resolutions, thus allowing us to understand the impact of several physical processes on the distribution of direct collapse BHs. We identify halos where direct collapse can happen, and derive the number density of BHs. We also investigate the discrepancies between hydrodynamical simulations, direct or post-processed, and semi-analytical studies. Under optimistic assumptions, we find that for direct collapse to account for BHs in normal galaxies, the critical Lyman-Werner flux required for direct collapse must be about two orders of magnitude lower than predicted by 3D simulations that include detailed chemical models. However, when supernova feedback is relatively weak, enough direct collapse BHs to explain $z = 6 - 7$ quasars can be obtained for Lyman-Werner fluxes about one order of magnitude lower than found in 3D simulations.

This chapter is adapted from its corresponding publications, the chapter follows mostly the first publication:

- *On the number density of "direct collapse" black hole seeds*,
  Mélanie Habouzit, Marta Volonteri, Muhammad Latif, Yohan Dubois, and Sébastien Peirani,
  MNRAS, 2016, vol 463, pages 529-540, arXiv:1601.00557

- *Impact of dust cooling on direct collapse black hole formation*,
  Muhammad Latif, Kazuyuki Omukai, Mélanie Habouzit and Dominik Schleicher, and Marta Volonteri,
  ApJ, 2016, vol 823, page 40, arXiv:1509.07034

Contents

4.1 Introduction

In the last chapter, we have investigated two BH formation models, PopIII remnants and stellar clusters, which are predicted to form light BH seeds. The direct collapse model, instead, predict the formation of more massive BH seeds, of $10^4 - 10^6\,M_\odot$ seeds, making it easier to reproduce the quasar population at $z > 6$. As we have said in the introduction of this thesis, several variants of the model have been studied theoretically. The direct collapse of pristine gas can be triggered by dynamical processes (Loeb & Rasio, 1994; Eisenstein & Loeb, 1995; Koushiappas, Bullock & Dekel, 2004; Begelman, Volonteri & Rees, 2006; Lodato & Natarajan, 2006; Mayer et al., 2010), or can be isothermal in primordial halos (Bromm & Loeb, 2003; Spaans & Silk, 2006; Dijkstra et al., 2008; Latif et al., 2013a). The latter has become the most popular version of the direct collapse scenario.

However, the physical conditions required by the isothermal collapse model are numerous, and make the channel a rare event. One needs a halo that has reached the atomic cooling threshold $\sim 10^7 - 10^8\,M_\odot$, but it is still pristine, i.e., metal-free. One needs that the molecular hydrogen formation has been suppressed throughout the halo's evolution. The two last conditions, namely the absence of metals and molecular hydrogen, ensure that there is no efficient coolant in the gas. Conversely, the presence of metals and molecular hydrogen would decrease the temperature of the gas, and so the Jeans mass. This could lead to the fragmentation of the gas cloud, therefore the formation of only one massive object is unlikely, and the formation of several less massive objects, namely PopIII stars, is instead expected. The destruction and prevention of molecular hydrogen can be accomplished by strong photo-dissociating radiation (Lyman-Werner, LW, photons with energy between 11.2 eV and 13.6 eV). A large inflow rate of gas at the center of the halo, higher than $0.1\,M_\odot/\mathrm{yr}$, and sustained for at least 10 Myr, is also needed to form a supermassive star-like object in the nucleus (Begelman, Volonteri & Rees, 2006; Begelman, Rossi & Armitage, 2008; Begelman, 2010; Ball et al., 2011; Hosokawa, Omukai & Yorke, 2012; Hosokawa et al., 2013; Schleicher et al., 2013). The BH mass can be up to 90% of the stellar mass.

Several aspects, on different physical scales, of the direct collapse scenario have been addressed in the last years. However, so far, studies have focused either on small scale simulations to capture the physical processes leading to the gas collapse, or on semi-analytical studies to derive a DCBH number density. For instance, Latif et al. (2013a) used zoomed cosmological hydrodynamical simulations of single halos to show that when all the conditions listed above are met, collapse

can happen (see also Regan, Johansson & Wise, 2014). Agarwal et al. (2012, A12 thereafter) and Agarwal et al. (2014, A14 thereafter), investigated in post-processing spatial variations in the LW radiation and the importance of the clustering of the LW photon sources, using a 4 comoving Mpc (cMpc) cosmological hydrodynamical simulation. In the meanwhile, semi-analytical studies also derived the number densities of DCBHs, for example Dijkstra et al. (2008, D08 thereafter) computed the probability distribution function of the LW radiation that irradiates halos at redshift $z = 10$, and showed that a small fraction of halos, 10^{-8} to 10^{-6}, may be exposed to radiation higher than 20 times the background radiation (see also Dijkstra, Ferrara & Mesinger, 2014, D14 thereafter). Inayoshi & Tanaka (2015) include the impact of X-rays, and predict a decrease in the formation rate of DCBHs per unit volume with redshift. Agarwal et al. (2015a) and Hartwig et al. (2016) use semi-analytical models with merger trees based on the Extended Press & Schechter formalism. Habouzit et al. (2016b) develop a hybrid model, where they "paint" galaxies, using the prescriptions of D08 and D14, over a dark matter only simulation, in order to include self-consistently the clustering of halos.

On the importance of using hybrid models

With these models has emerged the importance of several physical processes, such as metal enrichment of the medium from galactic winds (Dijkstra, Ferrara & Mesinger, 2014), and the clustering of LW photon sources (Dijkstra et al., 2008 ; Agarwal et al., 2012). These physical aspects rely on spatial information (halo distribution) and unfortunately, can not easily be treated with pure semi-analytical models (SAMs). Pure SAMs use the formalism of the Extended Press-Schechter theory (for example Valiante et al., 2016), where massive halos are decomposed into their higher redshift progenitors. The evolution of dark matter halos is followed on their merger tree.

One key requirement for the formation of DCBHs, through isothermal collapse, is the absence of efficient coolants within eligible DC halos, to keep the gas temperature and so the Jeans mass of halos (which scales as $T^{3/2}$) high enough to avoid fragmentation. The main coolants which operate below $\mathrm{T_{vir}} = 10^4\,\mathrm{K}$ are molecular hydrogen and metals. Therefore the absence of H_2 is required. Nearby star-forming halos emit LW photons that are able to photodissociate H_2 (Omukai, 2001 ; Omukai, Schneider & Haiman, 2008 ; Shang, Bryan & Haiman, 2010 ; Latif et al., 2013a), spatial distance between halos is therefore a crucial ingredient. Cosmological simulations, either dark matter only or hydrodynamical simulations, direclty provide the separation distance between halos. Because DCBH regions are expected to be close to star-forming galaxies to maintain a low abundance of H_2, they are also the first regions which are exposed to metal-pollution from galactic winds driven by SNe. Metal-enrichment is predicted to be very disparate in the early Universe, but some halos could remain metal-free down to $z \sim 6$ (Pallottini et al., 2014 ; Agarwal et al., 2014). The fraction of metal-free halos, or at least halos below the critical metallicity to avoid fragmentation, depends on chemical and mechanical processes (Schneider et al., 2006a,b). The evolution of metal-polluted bubbles escaping from halos can not be modeled easily in pure SAMs, however cosmological hydrodynamical simulations can track self-consistently the evolution of metal-enrichment over the entire simulated volumes (Latif et al., 2016 ; Agarwal et al., 2014 ; Habouzit et al., 2016a). Finally cosmological hydrodynamical simulations offer the advantage of following halo history as a function of time, which is of crucial importance for metal pollution by heritage, for example. A good illustration of the importance of the spatial information is the scenario described in Visbal, Haiman & Bryan (2014), which recently discuss the possibility of forming a DCBH in a synchronized pair halos (see also Dijkstra et al., 2008), without being metal-polluted, but while getting enough LW photons to photodissociate H_2.

Finally hybrid SAMs are the bridge between pure SAMs and cosmological hydrodynamical zoom-in simulations of single halos (Latif et al., 2013a). Such small scale zoom-in simulations are able to capture the physical processes which lead to the gas collapse. However they need to assume external quantities, such as the radiation intensity produced by nearby star-forming galaxies. This artificial intensity is generally taken very high (about one order of magnitude higher than what is needed in hybrid models to form a sufficient number of DCBHs) to ensure the collapse of the gas, but may not be representative of a statistical sample. Hybrid SAMs give us the opportunity to study in more details the feasibility of the DC scenario. They provide a reasonable set of parameters, such as the probability of halos with a given angular momentum, fraction of metal-poor halos, radiation intensity, which can be used as inputs for zoom-in simulations, and give us a first insight on the occurrence of zoom-in physical set up.

Current hybrid models

There are two types of hybrid models, those using spatial information from dark matter only cosmological simulations, and those taking advantage of cosmological hydrodynamical simulations, which provide self-consistently information on metal pollution, star formation, and the spatial distribution of halos. We briefly summarize here the current models that can be found in the literature:

- Agarwal et al. (2012) use a dark matter only cosmological simulation, run in a box of 4.8 cMpc side length, with a resolution of $M_{DM} \sim 6 \times 10^3\,M_\odot h^{-1} \sim 9.3 \times 10^3\,M_\odot$. They derive a number density in the range $10^{-2} - 10^{-1}\,\mathrm{cMpc}^{-3}$ for $J_{crit} = 30$ (see their fiducial model). The LW radiation intensity is modeled as the sum of a background intensity and a local varying intensity, and is computed for each dark matter halos of the simulation box.

- Agarwal et al. (2014) use the same LW model as Agarwal et al. (2012), but this time on top of a hydrodynamical simulation. The simulation FiBY is a 4 cMpc box size simulation, with a resolution of $M_{DM} \sim 6 \times 10^3\,M_\odot$. The simulation FiBY includes self-consistently on-the-fly the treatment of H_2 destruction by LW radiation, and the photo-detachment of H^-. Cooling by H_2 is also included. The simulation offers the possibility to follow self-consistently external metal-pollution, that was not included in Agarwal et al. (2012). The number density of DCBH regions is in the range $10^{-2} - 10^{-1}\,\mathrm{cMpc}^{-3}$ for $J_{crit} = 30$.

- Habouzit et al. (2016b) use two different dark matter only cosmological simulations of size length each, to study the impact of primordial non-Gaussianities in the density field on the number density of DCBHs. A model for LW radiation intensity is used on top of these simulations, and is based on Dijkstra, Ferrara & Mesinger (2014). The analysis is presented in chapter 5.

- Habouzit et al. (2016a): the method and results of this study are presented in the present chapter. The description of the 4 simulations used in this chapter, are described in the next section.

- Chon et al. (2016) use a cosmological hydrodynamical simulation to identify the possible DC regions, and then use zoom-in simulations to follow the dynamical evolution of these regions to see whether they can collapse. A number of 42 regions are first identified with the large scale simulation, out of which only 2 cases are presented as having good chance to lead to the formation of a DCBH. Therefore, the number density ranges in $10^{-4} - 10^{-3}\,\mathrm{cMpc}^{-3}$

for $J_{crit} = 100$ (we have averaged over $\Delta z = 1$ the number of DCBH regions found for $z = 12, 11, 9, 8, 7$, see their Table 1).

In this chapter, we use a hybrid method to compute the number density of BHs in different scale simulations, and to understand the impact of different physical processes as star formation or metal-pollution through SN feedback. Finally we also aim to discuss the discrepancies between different models that have been used to derive the number density of DCBHs, along with SAMs and hybrid models.
In the following, we use a set of three different cosmological hydrodynamical simulations, with increasing box size, allowing us to capture the physical processes on small scales in a small-volume, high-resolution simulation, to derive the number density of BHs and to test the impact of the SN feedback using a larger simulation with intermediate resolution. Finally, a large-volume simulation, with lower resolution, Horizon-noAGN (Peirani et al, in prep), is also used to test whether the direct collapse scenario is able to explain the population of quasars that we observe at redshift $z = 6$. We follow the approach introduced by D08, A12, D14 and A14 and model the LW radiation field on top of all the different simulations. A DCBH region finder code is applied to compute the DCBH number density function on all the simulations, for different redshifts.

The chapter is organized as follows. We first describe, in section 4.2, the simulations we use in this work, and the modeling of the LW radiation intensity, in section 4.3. In section 4.4, we investigate SN feedback and, in section 4.5 how it can alter the number density of DCBH regions derived from simulations. section 4.6 is dedicated to the simulation Horizon-noAGN, for which we derive the number density of DCBH regions, and we investigate the feasibility of the DC scenario for explaining the population of quasars at $z = 6$. In section 4.7, we explore a comparison between the different methods to derive the DCBH number density (which leads to discrepancies of several orders of magnitude), using either semi-analytical methods, or using hydrodynamical simulations. We summarize the results of this work in section 4.8.

4.2 Simulation set up

We have performed a set of simulations with increasing box sizes from 1 cMpc to 142 cMpc, using the adaptive mesh refinement hydrodynamical cosmological code RAMSES (Teyssier, 2002). We summarize in the following the main characteristics of these simulations. Table 4.1 establishes a comparison between all the simulations parameters used in this work. Fig. 4.1 shows gas density maps of our simulations Tiny, Chunky, and Horizon-noAGN. In the density map of Chunky (middle panel), the white square indicates the size of Tiny, and in the Horizon-noAGN map (bottom panel, only a small part of the simulation box is shown here), we show the size of the simulation Chunky.

Simulation Tiny
The smallest simulation, Tiny, is performed in a periodic box of $L_{box} = 1\,$cMpc size length with 256^3 dark matter particles, corresponding to a mass resolution of $M_{DM,res} = 2082\,M_\odot$. The simulation uses a Λ cold dark matter cosmology, with total matter density $\Omega_m = 0.276$, dark matter energy density $\Omega_\Lambda = 0.724$, amplitude of the matter power spectrum $\sigma_8 = 0.811$, spectral index $n_s = 0.961$, baryon density $\Omega_b = 0.045$ and Hubble constant $H_0 = 70.3\,km\,s^{-1}\,Mpc^{-1}$. Simulations are run with 10 levels of refinement ($\ell_{min} = 8$ defines the number of cells on the coarse level, $\ell_{max} = 17$ defines the finest level of refinement), leading to a spatial resolution of

Tab. 4.1 – Simulation parameters for the four simulations used in this chapter: Tiny, the two simulations Chunky, and Horizon-noAGN.

Simulations	Tiny	Chunky	Horizon-noAGN
L_{box} (Mpc)	1	10	142
Particles	256^3	128^3	1024^3
$M_{res,DM}$ ($M_\odot$)	2082	1.6×10^7	8×10^7
Spatial res. (proper pc)	7.63	76.3	1000
$m_{res,\star}$ ($M_\odot$)	2.3×10^2	7.7×10^3	2×10^6

7.6 pc. A new refinement level is allowed only when the expansion factor doubles, namely for $a_{exp} = 0.1, 0.2, 0.4$ and so on.

Simulation Chunky

Two intermediate volume simulations, Chunky, are also run, they differ by the model of SN feedback, in one case we use a “thermal" SN feedback and in the other a “delayed cooling” SN feedback (both SN feedback models are described in Section 2.5.). They use the same cosmology as Tiny. Simulations are performed in a periodic box of side $L_{box} = 10$ cMpc with 128^3 dark matter particles, corresponding to a mass resolution of $M_{DM,res} = 1.6 \times 10^7 M_\odot$. These simulations are run on 11 levels of refinement ($\ell_{min} = 7$, $\ell_{max} = 17$), leading to a spatial resolution of 76.3 pc.

Simulation Horizon-noAGN

We use the Horizon-noAGN simulation (Peirani et al, in prep.), which is a version without BHs and AGN feedback of the Horizon-AGN simulation (Dubois et al., 2014). This simulation has $\Omega_\Lambda = 0.728$, $\Omega_m = 0.272$, $\Omega_b = 0.045$, $\sigma_8 = 0.81$, $n_s = 0.967$, and $H_0 = 70.4\,km\,s^{-1}\,Mpc^{-1}$. Simulations were run with 1024^3 dark matter particles in a $L_{box} = 142$ cMpc size box, leading to a dark matter mass resolution of $M_{DM,res} = 8 \times 10^7 M_\odot$. Simulations are run on 8 levels of refinement ($\ell_{min} = 10$, $\ell_{max} = 17$), leading to a spatial resolution of ~ 1 kpc.

Star formation and physical processes

In all simulations, star formation is allowed in cells with a gas density exceeding the threshold ρ_0 (as described in chapter 2), which is $30\,H\,cm^{-3}$ for Tiny, $1\,H\,cm^{-3}$ for Chunky, and $0.1\,H\,cm^{-3}$ for Horizon-noAGN. The mass resolution of the simulations is $m_{res,\star} = 2.3 \times 10^2\,M_\odot$ for Tiny, $7.7 \times 10^3\,M_\odot$ for Chunky, and $2 \times 10^6\,M_\odot$ for Horizon-noAGN.

To mimic reionization, heating from an uniform UV background is added (following Haardt & Madau (1996)), taking place after redshift $z = 8.5$ for the simulations Chunky and Tiny, and $z = 10$ for Horizon-noAGN. Cooling is modeled with the cooling curves of Sutherland & Dopita (1993), the gas cools through H, He, and metals. Modeling the metallicity as a passive variable makes it easily trackable over the gas flow through redshift evolution. Physical processes, such as SN explosions and star formation, modify and redistribute the metallicity over neighboring cells. An initial zero metallicity is assumed for Chunky. However, for the smallest box size simulation, as we resolve mini-halos below the threshold for atomic hydrogen cooling, we use a metallicity floor of $10^{-3}\,Z_\odot$ in order to mimic cooling by molecular hydrogen. The same metallicity background is employed in Horizon-noAGN. The cooling by metals also mimics here cooling by molecular hydrogen, therefore allowing the formation of stars in mini-halos.

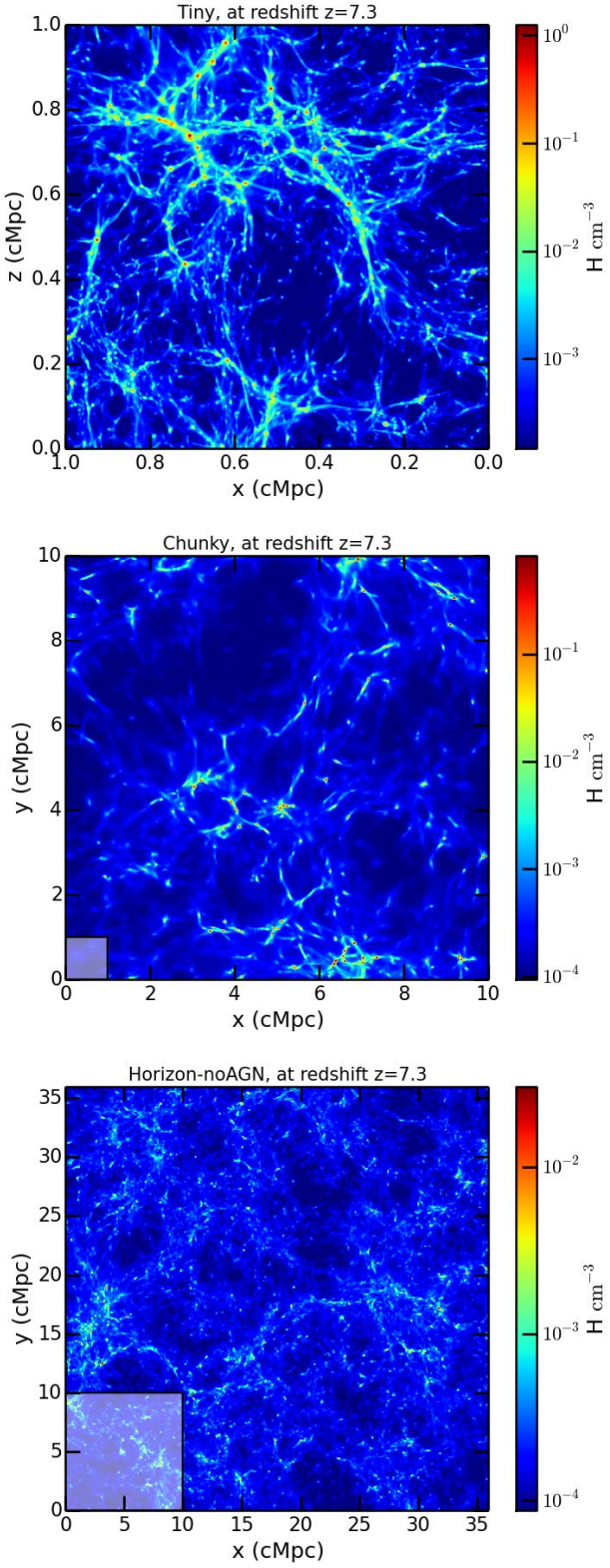

Fig. 4.1 – Gas density maps representing the three simulations used in this work: Tiny ($L_{box} = 1$ cMpc, top panel), Chunky ($L_{box} = 10$ cMpc, middle panel), and Horizon-noAGN ($L_{box} = 142$ cMpc, here we only show a small part of the simulation, a box of ~ 40 cMpc side, bottom panel). The white squares mark the size of the previous simulation: in the gas density map of Chunky (middle panel), we show the size of Tiny, and in Horizon-noAGN map (bottom panel), we show the size of Chunky.

The gas follow an adiabatic equation-of-state (EoS) for monoatomic gas with adiabatic index $\gamma = 5/3$, except at high gas densities $\rho > \rho_0$, where we use a polytropic EoS to increase the gas pressure in dense gas in order to limit excessive gas fragmentation by mimicking heating of the interstellar medium from stars. We use the following parameters that are described in chapter 2: $\kappa = 1.6$ for the polytropic index, and $T_0 = 10^3\,K$ for Chunky, and $T_0 = 10^2\,K$ for Tiny. For Horizon-noAGN, $\kappa = 4/3$ and $T_0 = 10^3\,K$ have been used.

Supernova feedback
Because metallicity and star formation are both a direct product of how SN feedback is modeled in hydrodynamical simulations, and are of the crucial importance when studying the direct collapse scenario, we test two different SN feedback implementations. We model SNe type II assuming a Chabrier initial mass function, where 20% of the mass fraction of stars end up their life in type II SNe, and release $10^{50}\,erg\,M_\odot^{-1}$, and return metals with a yield of 0.1. In this chapter, we use both the thermal and delayed cooling SN feedback implementations. For Chunky, we use the delayed cooling SN feedback parameters (that are described in chapter 2): $M_{gmc} = 7.7 \times 10^4\,M_\odot$, $\sigma_{NT} = 4.3 \times 10^{-4}\,km\,s^{-1}$, $t_{diss} = 4.6\,Myr$. For Tiny, we use: $M_{gmc} = 2.5 \times 10^3\,M_\odot$, $\sigma_{NT} = 2.5 \times 10^{-4}\,km\,s^{-1}$, $t_{diss} = 0.59\,Myr$. Horizon-noAGN includes a "kinetic feedback" with a strength intermediate between these two implementations.

The simulations Chunky and Horizon-noAGN do not resolve mini-halos. The impact of not resolving mini-halos in our simulations is not trivial to predict. On the first hand, we miss the early first episode of star formation that takes place in mini-halos, and consequently the early metal-enrichment. Large regions can be polluted by SN feedback from PopIII star, because their host halos are small. In that sense, we under-estimate the pollution by metals when computing the number of direct collapse halos. On the other hand, we also consider some halos as being pristine when they could be polluted by metals, because we do not capture their earlier star formation episode and metal enrichment. Therefore we also over estimate in that sense the number of halos that are still pristine and could be eligible for the direct collapse model.

Halo catalog and merger trees
We construct catalogues of halos using the AdaptaHOP halo finder (Aubert, Pichon & Colombi, 2004), which uses an SPH-like kernel to compute densities at the location of each particle and partitions the ensemble of particles into sub-halos based on saddle points in the density field. Halos contain at least 20 particles. We study the individual evolution of halos by building merger trees using the code TreeMaker developed by Tweed et al. (2009).

4.3 Method

We post-process the identification of all the regions, in a given simulation, which are eligible for the formation of a DCBH. In large cosmological simulations the main difficulty is to capture both large scales to have statistics and very small scales where the collapse of gas and the formation of a massive central object can be resolved. Several physical processes, playing a crucial role for the direct collapse scenario, such as star formation, metal-enrichment, depend on the simulation resolution. In order to take this into account, we have run our DCBH finder code on three different simulations. Therefore we are covering a large range of resolutions and volumes.

According to the direct collapse scenario, metal-free/metal-poor halos with mass $> 10^7 - 10^8\,M_\odot$ may host DCBHs under specific conditions. An inflow rate (higher than $0.1\,M_\odot/yr$) of gas

at the center of the halo can lead to the formation of a supermassive star-like object in the nucleus. The star can then collapse and form a $10^5 - 10^6\,M_\odot$ BH. In order for the Jeans mass to remain sufficiently high to form only one very massive object, efficient cooling by molecular hydrogen or metals must be prevented. Therefore metal-free conditions and a strong photo-dissociating flux are required.

A12 and A14 model the Lyman-Werner radiation as the sum of a spatial varying component of the radiation produced by young stars and of a background component. The background component is described by:

$$J_{LW,bg,II} = 0.3 \left(\frac{1+z}{16}\right)^3 \left(\frac{\dot{\rho}_{\star,II}}{10^{-3}\,M_\odot\,yr^{-1}Mpc^{-3}}\right) \tag{4.1}$$

in units of $10^{-21}\,erg\,s^{-1}\,cm^{-2}\,Hz^{-1}\,sr^{-1}$, with $\dot{\rho}_{\star,II} = 10^{-3}\,M_\odot\,yr^{-1}Mpc^{-3}$ for the star formation rate (constant with time). The background radiation intensity, however, is negligible compared to the local radiation intensity:

$$J_{LW,local,II} = 3 \sum_{i,stars\leqslant 5Myr} \left(\frac{r_i}{1\,kpc}\right)^{-2} \left(\frac{m_i}{10^3\,M_\odot}\right) \tag{4.2}$$

in units of $10^{-21}\,erg\,s^{-1}\,cm^{-2}\,Hz^{-1}\,sr^{-1}$, with r the distance between the source and the region where we compute the radiation and m the mass of the star. In the following, $J_{LW,crit}$ refers to the critical value of $J_{LW,local,II}$ in units of $10^{-21}\,erg\,s^{-1}\,cm^{-2}\,Hz^{-1}\,sr^{-1}$, which we simplify in J_{LW}. In this study, as we will consider radiation intensity thresholds much above the background level, we do not include the background component to the radiation intensity, which would be negligible compared to the spatially varying component. We have also not included radiation produced by Pop III stars, as their contribution to DCBH formation is highly subdominant compared to the Pop II population (see A12 and A14).

In this work, we do not include self-shielding by molecular hydrogen, self-shielding of halos could decrease the number density of DCBH regions we find in the following sections. We do not include ionizing radiation from reionization. In the presence of an ionizing radiation before the beginning of the collapse of the inner part of halos, infall of gas and accretion in the center can be decreased, which delays collapse, and triggers molecular hydrogen formation. Halos can then reach lower temperatures, which favours star formation instead of DCBH region formation. Johnson et al. (2014) show that the fraction of halos that could experienced this process is very small.

The critical value required for DCBH depends of the spectrum of the stellar population, Wolcott-Green, Haiman & Bryan (2011) argue a $J_{LW,crit} = 1000$ for a Pop III population, Shang, Bryan & Haiman (2010) show that the critical value ranges in $J_{LW,crit} = 30 - 300$ for a Pop II population. A strong radiation is needed in order to not only dissociate the molecular hydrogen in the outer parts of the halo, but also in the center. The critical values cited just above are thought to be sufficient to bring the molecular fraction down to 10^{-8} in 1D simulations. The value of the critical radiation $J_{LW,crit}$ is more likely to be spread on a distribution of possible values rather than equal to a fixed single value (derived from a fixed temperature black body), as shown by Sugimura, Omukai & Inoue (2014) ; Agarwal et al. (2014) ; Agarwal & Khochfar (2015). However in order to be able to compare our results on the number density of DCBH regions to previous literature, we consider a critical value of the radiation intensity of either $J_{LW,crit} = 30$ (Agarwal et al., 2012, 2014), $J_{LW,crit} = 100$ or $J_{LW,crit} = 300$. These values are lower compared to those required by high-resolution 3-D cosmological simulations (Regan, Johansson & Wise, 2014 ; Latif et al., 2014, 2015), which require $J_{LW,crit} > 500 - 1000$. Inclusion of X-rays also increases

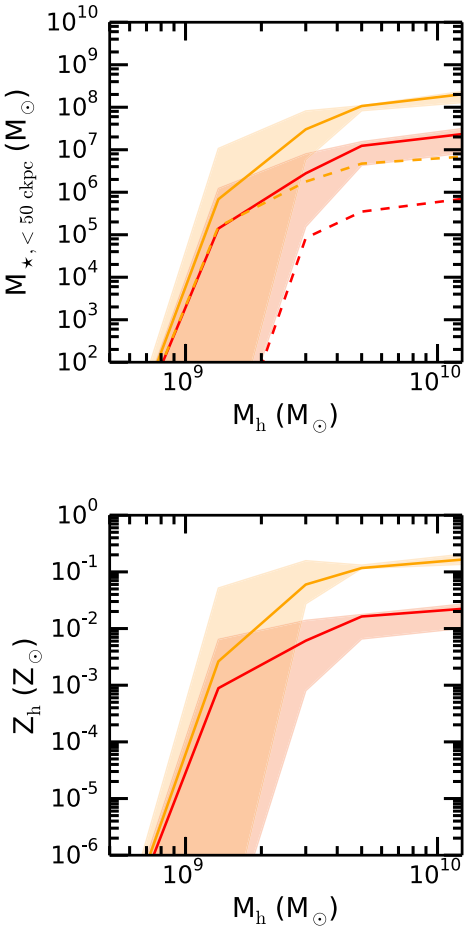

Fig. 4.2 – Top panel: median stellar mass enclosed in a sphere with a radius of 50 ckpc around halos (solid lines, red for the simulation with the delayed cooling SN feedback and yellow for the thermal SN feedback). Dashed lines include only stellar mass in young stars (age $\leqslant 5$ Myr). Bottom panel: Median of the average metallicity of halos in the two Chunky simulations, at redshift $z = 7.33$, binned in mass. Shaded areas extend to the 1σ values. The spread in the metallicity, as well as in the stellar mass, is due to very isolated halos. thermal feedback decreases the probability of having DCBH regions because the number of halos polluted by metals is higher, but it also favours it because the amount of radiation produced by young stars is higher.

the critical flux (Inayoshi & Tanaka, 2015), but the net effect is still unclear (Latif et al., 2015). It will be clear in the following that if we were to consider such values we would not form any DCBH in our volumes. In summary, what we obtain is an upper limit to the number of DCBHs, under optimistic conditions.

4.4 Impact of SN feedback on metallicity and star formation

Metals are created by stars and spread by SN explosions. Therefore SN feedback implementation has a strong impact on the metal-enrichment of the intergalactic medium, and on the number density of BH seeds formed. SN feedback also regulates star formation, therefore modulates the formation of the young stars that can provide Lyman-Werner radiation.

The simulation Tiny allows us to resolve the detailed expansion of the metal-enriched bubbles, but the size of the simulation (1 cMpc) is too small to see, statistically, the impact of SN metal enrichment on the number density of DCBHs. We use Chunky, a simulation with a side length

Tab. 4.2 – Number of direct collapse regions in the simulation Chunky with thermal SN feedback, assuming that collapse requires either 10 Myr, or the full free-fall time of the halo. For reference in Chunky with delayed cooling SN feedback, the only case that gives one candidate, at $z = 7.33$, has $J_{LW,crit} = 30$ and a collapse time of 10 Myr.

Criteria	$z = 10.1$	9.00	8.09	7.33
$J_{LW,crit} = 30$, 10 Myr	1	3	6	17
$J_{LW,crit} = 30$, $t_{Myr,ff}$	0	0	0	3
$J_{LW,crit} = 100$, 10 Myr	0	0	1	3
$J_{LW,crit} = 100$, $t_{Myr,ff}$	0	0	0	0
$J_{LW,crit} = 300$, 10 Myr	0	0	0	0
$J_{LW,crit} = 300$, $t_{Myr,ff}$	0	0	0	0

10 times larger (10 cMpc), to study metal enrichment and star formation rate for a significant volume of the Universe. We have run two identical simulations where only the prescription for the SN feedback is different, as described in Section 4.2. The thermal SN feedback is weaker, compared to delayed cooling. In fact, the total mass in stars in the box is about one order of magnitude larger for the thermal feedback case, at all redshifts.

The direct collapse scenario depends on two main quantities: the metallicity of the halo, and the radiation intensity it is exposed to, which in turn depends on the mass in nearby young stars (< 5 Myr). We compare these two quantities for the two SN feedbacks in Fig. 4.2. We calculate a halo mean metallicity averaging over all the gas leaf cells enclosed in its virial radius, and show the median of these mean metallicity values for all the halos in the two Chunky simulations, with solid lines in Fig. 4.2 (top panel). The shaded areas represent the 1σ values of halos metallicity. Thermal feedback leads to a higher metal enrichment. This is simply due to the larger stellar mass formed when adopting the SN thermal feedback, as evident from the bottom panel of Fig. 4.2, which represents the median stellar mass in the neighborhood of halos (solid lines), in a sphere with a 50 ckpc radius. This median stellar mass is larger with the thermal feedback. The stellar mass in young stars ($\leqslant 5$ Myr), which contribute at a given redshift to the LW radiation, is shown as dashed lines and follows the same trend.

It is difficult to predict the global effect of SN feedback on the number density of DCBHs in a cosmological box because metal enrichment and the amount of stellar mass in young stars have opposite effects. Regarding the former, delayed cooling SN feedback is more favourable to the formation of DCBHs - more halos are metal-poor and therefore eligible for DCBH formation-, regarding the latter, it is the thermal SN feedback implementation that has the advantage - halos are illuminated by stronger radiation because there are more young stars at any given time.

4.5 Number density of direct collapse regions in Chunky

We now turn to identifying the number of regions which are eligible for the direct collapse scenario. These regions must fulfill three criteria: they must be metal-poor, not forming stars, and be illuminated by a LW radiation intensity higher than the threshold $J_{LW,crit} = 30$ (we take here the same value as in A12) during the whole time it takes for the collapse and DCBH formation. D08 use a free-fall time defined by:

$$t_{Myr,ff} \sim 83 \left(\frac{1+z}{11} \right)^{-3/2}, \tag{4.3}$$

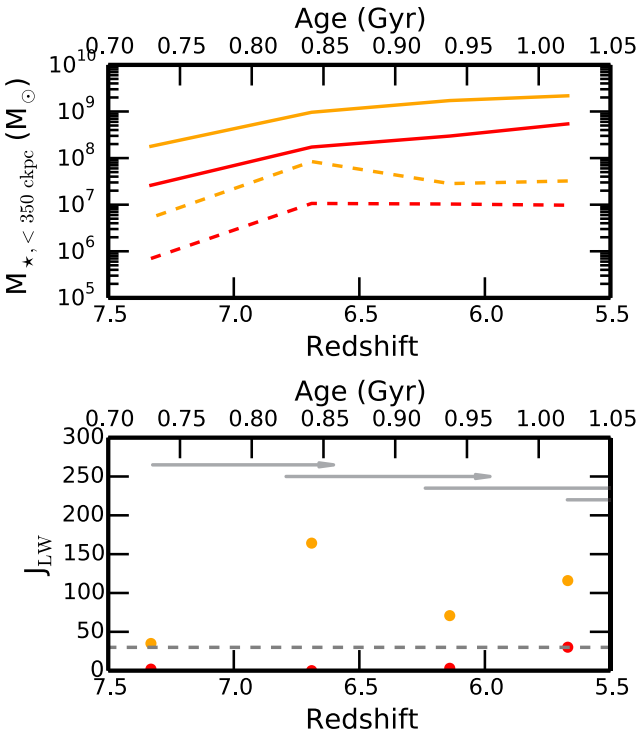

Fig. 4.3 – We compare one DCBH candidate halo in the simulation Chunky with the thermal supernova feedback (in orange) and the corresponding halo in the delayed cooling simulation (in red). Top panel: stellar mass (solid lines), stellar mass in young stars (dashed lines) in the neighborhood of the candidate (in a sphere of 350 ckpc radius). Bottom panel: the radiation intensity (dots) seen by the candidate halo for the two supernova feedbacks. The critical radiation intensity used in A12, $J_{LW,crit} = 30$, is shown as a dashed grey line. Arrows represent the free-fall time used in D08. If a candidate is above the critical LW radiation for the full length of an arrow, it is retained. In this case the orange dot (thermal feedback) remains a candidate, the red dot (delayed cooling feedback) does not.

which assumed $\rho \sim 200 \times \bar{\rho}$. This is the free-fall time at the virial radius. Visbal, Haiman & Bryan (2014) argue instead that the relevant collapse time is that of the gas, on scales 10% of the virial radius, so that the collapse time should be $0.1 \times t_{\rm Myr,ff}$. The length of the collapse in 3D high-resolution simulations of Latif & Volonteri (2015), indeed lasts ∼10 Myr. In this study, we consider both the redshift-dependent collapse time, defined in Eq. 4.3 (D14), and a collapse time of 10 Myr, which appears more realistic, according to recent simulation studies.

We give an example of our technique in the following. We show in Fig. 4.3 one concrete example of a DCBH candidate halo, with a mass of $\rm M_h = 5.2 \times 10^8\,M_\odot$ at $z = 7.33$: the top panel shows the evolution of the stellar mass in the environment of the halo, the total stellar mass is represented with solid lines, the stellar mass in young stars is shown with dashed lines. The corresponding radiation intensity is shown in the bottom panel with dots, the grey dashed line indicates the radiation intensity threshold of $\rm J_{LW,crit} = 30$. The simulation with thermal feedback is shown in orange, and the simulation with the delayed cooling feedback in red. Grey arrows give an idea of the free-fall time at that redshift, computed as in D08. We see that when the stellar mass in young stars increases, the radiation intensity also increases, and when it decreases at redshift $z = 6.6$, the radiation intensity also decreases.

Using this technique, only considering the radiation criterion, for the thermal SN feedback case, 17 regions are identified as potential DCBH sites, at $z = 7.33$. The maximum value of the radiation intensity at that redshift is $\rm J_{LW} = 162.72$. Then we look back in time using merger trees made with TreeMaker (Tweed et al., 2009), in order to check if these candidates have been illuminated by a sufficiently high radiation intensity for at least one collapse time, and how the intensity varies over time. We find that only 4 of the candidates are illuminated by a radiation intensity above the critical value for at least one collapse time, and therefore are still flagged as DCBH candidates. Finally we check the metallicity of the candidates, and find that only one region is not polluted by metals, and 2 regions are partially polluted, which leads to a number density $\rm n_{DCBH} \leqslant 3 \times 10^{-3} cMpc^{-3}$. Zero candidates are found for $\rm J_{LW,crit} = 100$ and $\rm J_{LW,crit} = 300$.

In the previous paragraph, we adopted as collapse time the free-fall time of the halo, defined by Eq. 4.3. However, if we now use a collapse time of 10 Myr, as suggested by Visbal, Haiman & Bryan (2014), for the same $\rm J_{LW,crit} = 30$, we find: 1 halo at $z = 10.1$ with $Z < 10^{-3.5}\,\rm Z_\odot$, 3 regions at $z = 9.00$ (all with $Z = 0$), 6 regions at $z = 8.09$ (3 regions with $Z = 0$, and 3 regions with $Z < 10^{-3.5}\,\rm Z_\odot$), 17 regions at $z = 7.33$ (7 regions with $Z = 0$, and 10 regions with $Z < 10^{-3.5}\,\rm Z_\odot$). All the regions are in halos with $\rm M_h > 10^8\,M_\odot$. With a radiation intensity threshold of $\rm J_{LW,crit} = 100$, the numbers decrease to 1 at 8.09, and 3 at $z = 7.33$, no DCBH halo is found at $z = 10.1$ or $z = 9.00$. Zero candidates are found for $\rm J_{LW,crit} = 300$.

We repeat the same exercise for the simulation with delayed cooling SN feedback, and find only one candidate for the DCBH process, for the case with $\rm J_{LW,crit} = 30$, and assuming a collapse time of 10 Myr. No candidates are found in the other cases. The maximum radiation intensity is $\rm J_{LW} = 30.33$. In conclusion, the lower stellar mass in young stars in the delayed cooling simulation directly impacts the direct collapse scenario, by strongly decreasing the number of regions illuminated by a sufficient radiation intensity, and therefore decreasing the number density of DCBHs. The number density of DC haloes found at a given redshift (not the cumulative number density) in the two Chunky boxes is shown in Fig. 4.4, with orange symbols when using for the collapse time the free-fall time of the halo, violet symbols for a collapse time of 10 Myr, and the number of candidates is reported in Table 4.2.

As a note, no DCBH is found in Tiny, for any subset of criteria. Tiny is the only simulation where we resolve minihalos, and Machacek, Bryan & Abel (2001) ; O'Shea & Norman (2008),

show that a small amount of LW flux is able to delay or temporarily shut down the formation of PopIII stars, and instead favors the formation of second generation stars (Johnson, Dalla Vecchia & Khochfar, 2013). If we included the suppression of PopIII star formation through LW flux, this would increase the number of PopII stars, thus would increase the probability of DCBH formation. As we consider all stars as PopII stars in this work, we are already overestimating the LW radiation (which already mimics the enhancement of PopII formation produced by the suppression of PopIII star formation by LW flux), thus obtaining optimistic results for the occurrence of DCBHs. Since, under optimistic assumptions, we find zero DCBH candidates in Tiny, we expect that including the suppression of Pop III star formation in pristine minihaloes would not change strongly this null result.

Small simulation boxes only allow us to derive a number density of DCBH regions for $J_{LW,crit} = 30$, which appears to be sightly lower than the values derived by D14 or A12, and even lower compared to A14. The differences between implementations causing these discrepancies are analyzed and discussed in Section 4.7. We will only consider the fiducial models of these studies, which are comparable to our study, with an escape fraction of unity, and no additional physical processes, as the effect of galactic winds (D14) or reionization feedback (A12). A12 discuss a case with an additional reionization feedback from hydrogen-ionizing photons (however, with an escape fraction of 0.5, which differs from the other studies and makes a direct comparison problematic), which can strongly decrease the number density by a factor of ~ 15 (from a number density of $0.518\,\mathrm{cMpc}^{-3}$ to $0.035\,\mathrm{cMpc}^{-3}$).
All the regions that we describe above are in halos with $M_h > 10^8 M_\odot$. In Chunky we do not resolve smaller halos that could be still metal-poor, and available to form a DCBH region, neither to capture the early metal-enrichment of the DCBH regions we have identified.

4.6 Horizon-noAGN simulation: Can direct collapse explain the BHs powering $z = 6$ quasars?

We now turn to exploring the number density of BHs in the Horizon-noAGN simulation. This simulation allows us to look at DCBH formation without being biased by the feedback of pre-existing BHs, compared to the sister simulation, Horizon-AGN, which includes BH accretion and feedback. The main advantage of the simulation is that the large box (142 cMpc side length) allows some statistics, at the expense of spatial and mass resolution. We use the same method as for the set of Chunky simulations to compute the radiation intensity illuminating halos.

We first flag all halos illuminated by a radiation intensity higher than $J_{LW,crit} = 30$. We identify 8 regions at redshift $z = 9.83$, and 814 regions at $z = 7.31$. Since we are trying to estimate whether DCBHs can explain the number density of $z > 6$ quasars, we do not need to proceed to lower redshift (the next available output is at $z = 5.87$). This simulation includes a metallicity floor, therefore we rescaled the metallicity accordingly. Halos with a mean metallicity lower than $10^{-3.5} Z_\odot$ are kept as DCBH candidates. We are left with 2 regions at redshift $z = 9.83$, 373 regions at $z = 7.31$. For a radiation intensity of $J_{LW,crit} = 100$ we identify 2 regions at redshift $z = 9.83$ and 153 at $z = 7.31$. Including the metallicity criterion ($Z \leqslant 10^{-3.5} Z_\odot$), there are 0 regions at redshift $z = 9.83$, and 42 at $z = 7.31$. For a radiation threshold of $J_{LW,crit} = 300$ we identify 1 region at redshift $z = 9.83$ and 13 regions at $z = 7.31$. Including the metallicity criterion, we find 0 regions at redshift $z = 9.83$, 2 regions at $z = 7.31$ ($Z \leqslant 10^{-3.5} Z_\odot$), and no region at $z = 9.83$. See Table **??** for a summary. Metallicity appears to be a key parameter in the direct collapse scenario, reducing significantly the number of DCBH candidates (up to 25 % at $z = 9.83$, 45 % at $z = 7.31$).

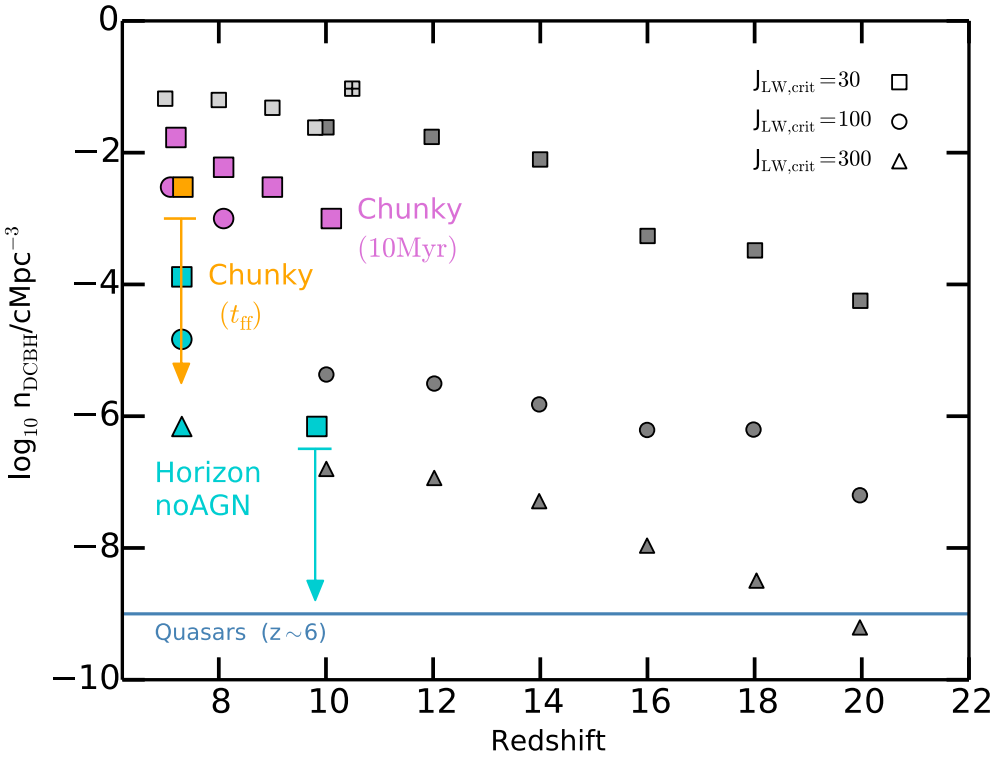

Fig. 4.4 – Number density of halos that can host a DCBH, at a given redshift. To be consistent with previous literature, we show the number density of DCBH regions at a given redshift, this is not a cumulative number density in the sense that we do not add the regions found at higher redshifts. In grey we show the number density from previous studies. Symbols represent different radiation intensity thresholds. Squares: $J_{LW,crit} = 30$, circles: $J_{LW,crit} = 100$, triangles: $J_{LW,crit} = 300$. The top light grey crossed square at $z = 10.5$ is from A14 (post-processing of a hydrodynamical simulation), the light grey squares in the range $z = 10 - 7$ are from A12 (values from private conversation, semi-analytical study), dark grey squares are the results of D14 (analytical). We do not show the number density derived in D08, which is in the range $10^{-6} - 10^{-8}\,\mathrm{cMpc}^{-3}$, similar to the one derived in D14. The orange square shows the number density for Chunky (10 cMpc side box), for the thermal SN feedback (0 regions are identified in the simulation employing the delayed cooling SN feedback), for halos that are illuminated by a high radiation intensity for at least their free-fall time. The purple squares and circles show the number density for Chunky, for halos that are illuminated by a high radiation intensity for at least 10 Myr. The blue squares, circle and triangle represent the large-scale cosmological simulation Horizon-noAGN (142 cMpc side box).

Tab. 4.3 – Number of direct collapse regions in the simulation Horizon-noAGN.

Criteria	$z = 9.83$	$z = 7.31$
$J_{LW,crit} = 30$	8	814
$J_{LW,crit} = 30$, $Z \leqslant 10^{-3.5} Z_\odot$	2	373
$J_{LW,crit} = 100$	2	153
$J_{LW,crit} = 100$, $Z \leqslant 10^{-3.5} Z_\odot$	0	42
$J_{LW,crit} = 300$	1	13
$J_{LW,crit} = 300$, $Z \leqslant 10^{-3.5} Z_\odot$	0	2

It is important to notice here that the time-scale between two outputs in the simulation are larger than the collapse time, either the free-fall time or 10 Myr. Therefore we are missing the time criterion of the direct collapse here: some of the candidates identified could be polluted by metals before the full collapse time has elapsed and therefore before unable to form the DCBH. The radiation intensity could also vary and not be enough to sustain molecular hydrogen dissociation for the full collapse time. Another important caveat is the resolution of the simulation, Δx = 1kpc and $M_{DM,res} = 8 \times 10^7\,M_\odot$, which does not allow us to capture the first metal-enrichment of halos, simply because we do not resolve small halos. Rather than the quantitative numbers, Horizon-noAGN allows us to explore trends in a statistical sense.

Fig. 4.4 shows the number density obtained for the simulation Chunky (in orange, and violet) and Horizon-noAGN (in light blue). All the grey symbols represent previous studies: the light grey top crossed square is for A14, the light squares for A12, dark grey squares for D14, both for $J_{LW,crit} = 30$, dark grey circles are for D14 and $J_{LW,crit} = 300$, dark grey triangles for D14 and $J_{LW,crit} = 300$. We do not show the number density derived in D08 ($10^{-6} - 10^{-8}\,cMpc^{-3}$), because similar to the one obtained in D14.

In Horizon-noAGN, considering the metallicity threshold $Z \leqslant 10^{-3.5}\,Z_\odot$, we find $n_{DCBH} \simeq 10^{-7}\,cMpc^{-3}$ at $z = 9.83$, and $n_{DCBH} \simeq 10^{-4}\,cMpc^{-3}$ at $z = 7.31$ (blue squares in Fig. 4.4), for $J_{LW,crit} = 30$. At $z = 7.31$, for $J_{LW,crit} = 100$, we find $n_{DCBH} \simeq 10^{-5}\,cMpc^{-3}$ (blue circle in Fig. 4.4), and $n_{DCBH} \simeq 10^{-6}\,cMpc^{-3}$ for $J_{LW,crit} = 300$ (blue triangle in Fig. 4.4).

For Horizon-noAGN, our attempt was to see if the conditions on metallicity and on radiation intensity could be meet in more than few halos. Of course, with this simulation, we do not resolve small halos, nor the early metal-enrichment, but it gives us a first picture of the feasibility of the direct collapse scenario on a cosmological scale. For $J_{LW,crit} = 30$, we again find a number density smaller than D14, and A14. However, for the highest thresholds, $J_{LW,crit} = 100$, $J_{LW,crit} = 300$, the number density of DCBH regions are very similar to those found by D14.

Finally, we investigate the probability for massive halos at $z \sim 6$ to be seeded by a DCBH. A massive halo at $z \sim 6$, will host a DCBH if at least one of its progenitors was a DCBH region (namely metal-poor halos, illuminated by a strong photo-dissociating radiation intensity). We start by selecting all the most massive halos in the simulation Horizon-noAGN at $z = 5.8$, namely the 552 halos with $M_h \geqslant 10^{11}\,M_\odot$. We build the merger history of all these halos with TreeMaker (Tweed et al., 2009), with the two previous snapshots of the simulation, at $z = 7.3$ and $z = 9.8$. We compute the mean metallicity of all the progenitors of massive halos at $z = 5.8$, and the photo-dissociating radiation they are illuminated by. Of the 552 halos with $M_h >= 10^{11}\,M_\odot$ at $z = 5.8$, 155 have at least one DCBH progenitor at $z = 7.3$, illuminated by a radiation with an intensity higher than $J_{LW,crit} = 30$ and with a metallicity $Z < 10^{-3.5}\,Z_\odot$. We do not identify any DCBH progenitor at $z = 9.8$. Therefore the fraction of massive halos which can host a DCBH is 155/552=0.28, so 28% of the massive halos. When considering a radiation intensity threshold of $J_{LW,crit} = 100$, only 6.5% of the massive halos can host a DCBH, and it drops to 0.36% for $J_{LW,crit} = 300$.

In summary, about a third of the most massive halos at $z = 6$ have at least one progenitor reaching both the criterion on metallicity ($Z < 10^{-3.5}\,Z_\odot$) and the criterion on radiation intensity ($J_{LW,crit} = 30$). However, this fraction drops significantly down to $\sim 6\%$ for $J_{LW,crit} = 100$, and even more, down to less than 1% for a more realistic value of $J_{LW,crit} = 300$.

Tab. 4.4 – Percentage of massive halos with at least one DCBH progenitor, in the simulation Horizon-noAGN.

Criteria	$Z \leqslant 10^{-3.5}$
$J_{LW,crit} = 30$	28%
$J_{LW,crit} = 100$	6.5%
$J_{LW,crit} = 300$	0.36%

4.7 Comparison between hydro-dynamical simulations and (semi-)analytical models

In this section, we perform a systematic comparison between different models presented in the literature. Analytical and semi-analytical studies have the advantage of investigating with ease the impact of physical processes. Ahn et al. (2008) show that the clustering of halos, which are the sources responsible for the photo-dissociating background, leads to local variations in the LW radiation intensity background. D14 uses a semi-analytical model to investigate the role of galactic outflows, which drive metal-enrichment in the surrounding of star-forming galaxies. DCBH regions need to be close enough to star-forming galaxies in order to be illuminated by a high radiation intensity, whereas the proximity with star-forming regions imply a potential metal-pollution by their galactic winds. Agarwal et al. (2012) and Habouzit et al. (2016b) use a hybrid model where they "paint" galaxies on dark matter only simulations, so that the clustering of halos is naturally taken into account.

Conversely, hydrodynamical simulations have the advantage of tracking the cosmic evolution of metal-enrichment and star formation in a more self-consistent way, where semi-analytical models need to use approximations. However, simulations cannot resolve large and small scales at the same time: small scale simulations allow one to follow the physical processes accurately but suffer from poor statistics (especially considering that the probability of having a DCBH is 10^{-6}, based on the analytical estimates), while large scale simulations provide statistics but do not capture physical details/processes. For instance, Latif et al. (2015) use zoomed simulations of single halos to investigate different values of $J_{LW,crit}$. A14 use a high resolution simulation with a size of 4 cMpc to estimate the density number of DCBHs. Our work covers the scale of A14, and larger scales up to 142 cMpc box size length, at degrading resolution.

We start by comparing different models for the radiation intensity coming from star-forming regions, D14 versus A14 (the latter based on A12), and then move on to the probability for halos to have a given stellar mass, the probability of being star-forming, and the probability of being metal-free.

In D14, the stellar mass of a dark matter halo M_{halo} is assigned as:

$$M_\star = f_\star M_{halo,gas} = f_\star \frac{\Omega_b}{\Omega m} M_{halo}, \tag{4.4}$$

where $f_\star = 0.05$ is the fraction of gas which turns into stars, $M_{halo,gas}$ the gas mass of the halo, M_{halo} the total mass of the halo, Ω_b the baryon density and Ω_m the total matter density. The mean production rate of LW photons per solar mass of star formation is time-dependent, where time is counted from the time t_{Myr} when a burst of star formation occurs, and expressed as:

$$\langle Q_{LW}(t) \rangle = Q_0 \left(1 + \frac{t_{Myr}}{4}\right)^{-3/2} \exp\left(-\frac{t_{Myr}}{300}\right) \tag{4.5}$$

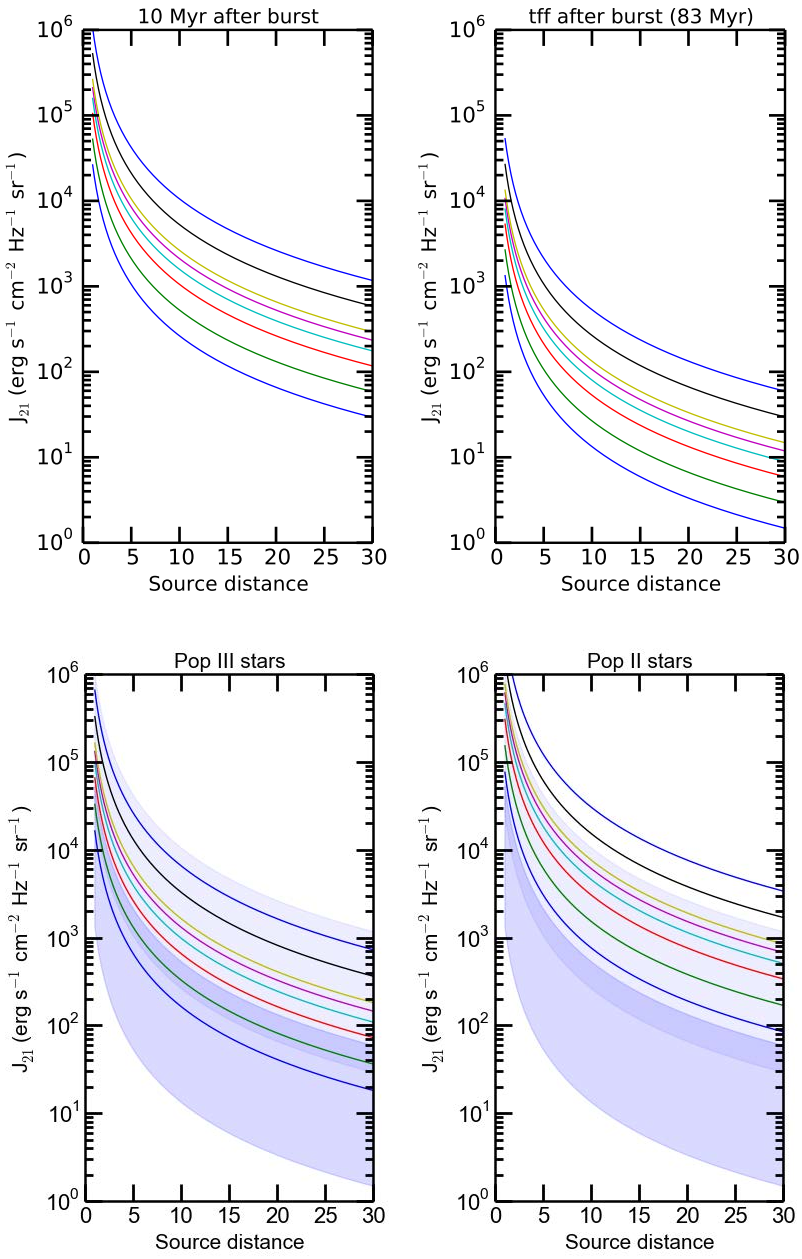

Fig. 4.5 – Top panels: Radiation intensity (in J_{LW} units) provided by a source at a given distance (in proper kpc) for different sources mass at $z = 10$ (halo masses of the source from top to bottom: 4×10^{11}, 2×10^{11}, 10^{11}, 8×10^{10}, 6×10^{10}, 4×10^{10}, 2×10^{10}, $10^{10}\,M_{\odot}$), 10 Myr after the star formation burst (left panel), and 83 Myr after the burst (right panel) using the model by D14. Bottom panels: Radiation intensity (in J_{LW} units) provided by a source at a given distance (in pkpc) for different sources mass, at $z = 10$. The colored curves (colors as in Fig. 4.5, top panels) show the radiation intensity based on A14, considering a stellar population PopIII (left) or PopII (right) as the radiation source. Halo masses of the source from top to bottom: 4×10^{11}, 2×10^{11}, 10^{11}, 8×10^{10}, 6×10^{10}, 4×10^{10}, 2×10^{10}, $10^{10}\,M_{\odot}$. The model by D14 is shown with filled blue regions, the top region corresponds to 10 Myr after the burst, the bottom region to 83 Myr after the burst) for the same stellar masses.

with $Q_0 = 10^{47}\,\mathrm{s}^{-1}\,\mathrm{M}_\odot^{-1}$.

The mean LW photon production rate is computed one free-fall time after the star formation burst (Eq. 4.3). D14 motivate this choice by the requirement that molecular hydrogen is suppressed throughout the collapse. The expression of Q_{LW} is a fit from STARBURST99 (which used a Salpeter IMF in the range $m_{\mathrm{low}}, m_{\mathrm{up}} = 1, 100\,\mathrm{M}_\odot$, an absolute metallicity of $Z = 10^{-3}$ ($0.05\ \mathrm{Z}_\odot$), and a stellar mass of $10^5\,\mathrm{M}_\odot$). The mean LW luminosity density $\langle L_{\mathrm{LW}}(\mathrm{M}, \mathrm{t})\rangle$ is a function of the mean number of LW photons (given by the mean production rate of LW photons per solar masses times the stellar mass of the halo), their energy and the escape fraction of these photons.

$$\langle L_{\mathrm{LW}}(\mathrm{M}, \mathrm{t})\rangle = \frac{h\,\langle\nu\rangle}{\Delta\nu}\,\langle Q_{\mathrm{LW}}(t)\rangle\,f_{\mathrm{esc,LW}}\left(\frac{\mathrm{M}_\star}{\mathrm{M}_\odot}\right). \tag{4.6}$$

The efficiency of LW photons to escape from their halos is highly debated, and can depend on halo mass and stellar feedback. Using hydrodynamical zoom-in simulations of high-redshift mini-halos, Kimm & Cen (2014) find that the escape fraction could be close to 100% at the epoch of reionization. Schauer et al. (2015) recently showed that the escape fraction from PopIII stars can be close to 100% in the "far-field" limit, but can significantly decrease by taking also into account self-shielding by atomic hydrogen. In order to be able to compare our models directly to previous works, which for the most part used an escape fraction of 100%, we adopt the same value.

The flux at a distance r then becomes:

$$\langle J_{\mathrm{LW}}(r, \mathrm{M}, \mathrm{t_{ff}})\rangle = \frac{1}{4\pi}\frac{\langle L_{\mathrm{LW}}(\mathrm{M}, \mathrm{t})\rangle}{4\pi r^2} f_{\mathrm{mod}}(r), \tag{4.7}$$

where the first factor $1/4\pi$ is needed to express $\langle J_{\mathrm{LW}}(r, \mathrm{M}, \mathrm{t_{ff}})\rangle$ in $\mathrm{J_{LW}}$ units ($\mathrm{erg\,s^{-1}\,cm^{-2}\,Hz^{-1}\,sr^{-1}}$). $f_{\mathrm{mod}}(r)$ is used to correct the radiation intensity for the extra dimming introduced by the LW horizon (Ahn et al., 2008):

$$f_{\mathrm{mod}}(r) = 1.7\exp\left(-\left(\frac{r_{cMpc}}{116.29\,\alpha}\right)^{0.68}\right) - 0.7 \qquad \text{if } \mathrm{r_{cMpc}}/\alpha \leq 97.39 \tag{4.8}$$

$$= 0 \qquad \text{otherwise.} \tag{4.9}$$

In Fig. 4.5 (top panels) we show the intensity (y axis in units of $\mathrm{J_{LW}}$) of the radiation coming from a source at a given distance for different stellar masses of the source. In the left panel, we consider the radiation emitted 10 Myr after the star formation burst, while in the right one we use one free-fall time after the burst (∼83 Myr at redshift z=10), as in D14. In Fig. 4.5 (bottom panels), the radiation intensity computed using the model of D14 is shown in blue shades for 10 Myr or 83 Myr, and is compared to the model of A14 for the same stellar masses as in Fig. 4.5(top panels). Sources are considered either as Pop III stars (bottom left panel, in Fig. 4.5), or PopII stars (bottom right panel). We find that the model of A14, considering the source either as a population of PopIII or PopII stars, roughly corresponds to the model of D14 for 10 Myr after the star formation burst, but overestimate D14 for a free-fall time (as computed with Eq. 4.3).

A14 consider a continuous star formation history, with the radiation intensity depending only on the stellar mass of the source (considering only stars younger than 5 Myr, before the production of LW photons drops significantly), and the distance to the stellar source, and therefore it is not explicity time-dependent. The time-dependence is implicit in the choice of using only stars younger that 5 Myr. This differs with respect to the explicit time dependence

used in D14 (in the original paper, the free-fall time at the virial radius, ~ 83 Myr, we also added 10 Myr here, based on the discussion in Visbal et al. 2014) and A12. D14 and A12 provide a time-dependent modeling of the radiation intensity. A12 (erratum), and seemingly A14, used continuous star formation to model the radiation intensity. With a starburst, the emission rate of LW photons drops rapidly. With continuous star formation, it increases rapidly at first, and becomes constant after 80 Myr (cf. Fig. 2 in A12 with Fig. 1 in the erratum of A12, and see Fig. A1 in D14). The radiation intensity of A12 and A14, for continuous star formation, would be higher than the one derived by D14, who adopted a starburst, if we considered a time longer than 5 Myr (e.g., 10 Myr or 83 Myr). Over timescales longer than ~ 10 Myr, however, metals generated by the stars themselves would pollute the regions irradiated by the LW flux (D14, Habouzit et al. (2016b)), making the photon production ineffectual in view of the DCBH process.

We then compare another quantity, the stellar mass per halo. D14 use a linear relation (Eq. 4.4) that overestimates the stellar mass compared to our hydrodynamical simulation. We compare the stellar mass of all halos in the Chunky simulation at $z = 9$ to the theoretical stellar mass derived with D14 formalism. On average the masses of D14 are a factor ~ 70 larger than those in Chunky (albeit with a large scatter). On the other hand, in D14, the probability for a halo to be star-forming is set at $\mathrm{P_{SF}} = 0.1$, i.e., 10 % of halos experience a starburst at the same given time, and contribute to the radiation intensity seen by all the other halos. This probability has a strong impact on the number density of DCBH regions, as a higher star-forming probability implies a higher radiation intensity seen by the neighboring halos. In our simulation, we define a halo as star-forming if young stars ($\leqslant 5$ Myr) are found within its virial radius. The fraction of star-forming halos we find in Chunky is always higher than 10%. Depending on the SN feedback model used, the fraction is between 20 and 35% for the delayed cooling model, and between 25 and 45% in the thermal feedback model.

Finally, we compare the expansion of metal-polluted bubbles in the analytical framework and in simulations, using our highest resolution simulation, Tiny, which has a spatial resolution of 7.6 pc and a dark matter mass resolution of $\sim 2000\,\mathrm{M_\odot}$. Fig. 4.6 shows the evolution of one SN bubble over three different snapshots, corresponding respectively to z =10.11, 9.00, 8.09. Overlaid the metallicity contours from the simulation is the analytical estimate by D14:

$$r_{\mathrm{bubble}} = 3 \times 10^{-2}\,\mathrm{kpc} \left(\frac{\mathrm{M_\star}}{\mathrm{M_\odot}}\right)^{1/5} n^{-1/5} \left(\frac{t}{\mathrm{Myr}}\right)^{2/5}, \tag{4.10}$$

where n is gas 60 times denser than the mean intergalactic value at redshift z, i.e. $n \sim 60 \times \Omega_b\, \rho_{\mathrm{crit}} (1+z)^3 / m_p$. The expansion of the metal-polluted bubble is faster in the hydrodynamical simulation, implying that D14 underestimates the size of polluted regions compared to us. However, the bubble becomes quickly highly asymmetric, therefore the geometry of the halo-halo configuration becomes of importance.

In summary, D14 overestimates the stellar mass, but underestimate the galaxies that can contribute radiation and the extent of metal polluted regions. The net effect is that the effects almost compensate, and explain why our results using hydrodynamical simulations are very close to the results of D14.

4.8 Conclusions

In this chapter, we have addressed the formation of supermassive BHs by the direct collapse scenario. Isothermal collapse is predicted to happen in halos with minimum mass of $\sim 10^7 - 10^8$ $\mathrm{M_\odot}$ that have reached the atomic cooling threshold. To avoid the fragmentation of the

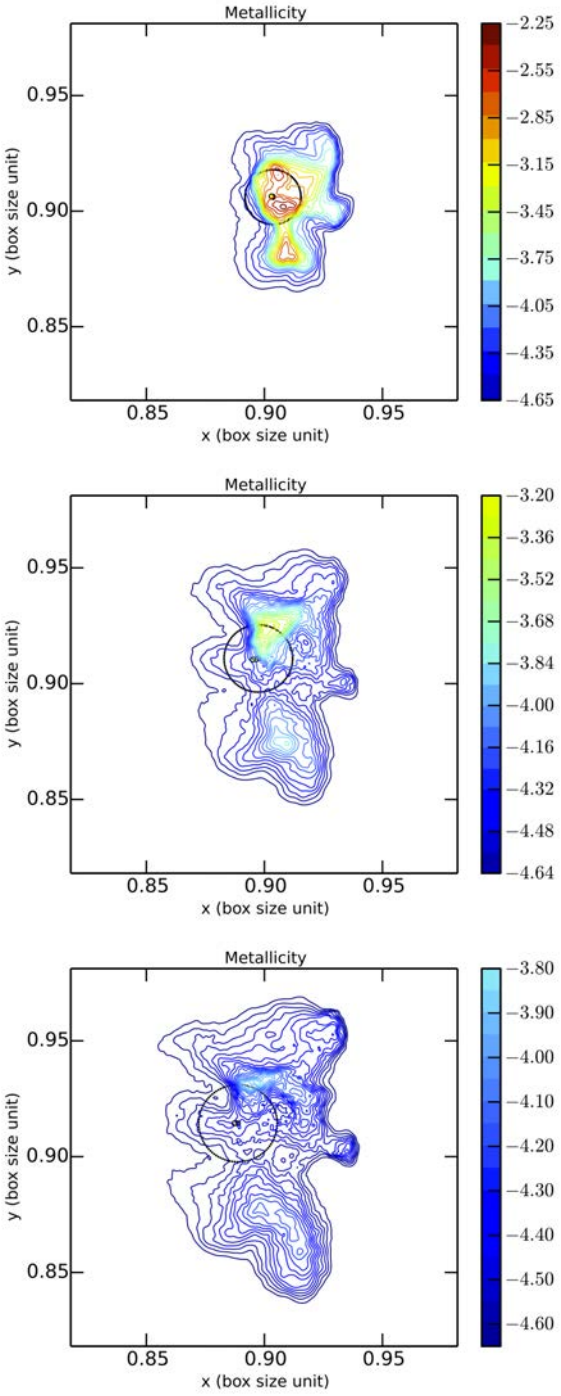

Fig. 4.6 – Contour plot representing the metallicity (log10 of the absolute metallicity) around the SN explosion in the simulation Tiny at redshift z =10.11, 9.00, 8.09 (top to bottom). The black circle marks the analytical estimate by D14.

gas, all the efficient coolants, namely metals and molecular hydrogen, must be absent. The destruction and the prevention of molecular hydrogen can be done by a strong photo-dissociating radiation coming from nearby star-forming galaxies. A large inflow rate of gas at the center of the halo, higher than 0.1 $M_\odot$/yr for at least one free-fall time, is required in order to form a supermassive star-like object.

The feasibility of the direct collapse mechanism is difficult to investigate. Zoom-in simulations investigate the collapse and the accretion properties (e.g., Latif et al., 2013a ; Regan, Johansson & Wise, 2014 ; Hartwig et al., 2015), but use an artificial radiation intensity. Larger scale simulations, such as Chunky or FiBY (the simulation used for A14), instead model the spatially varying radiation intensity but are not able to follow the collapse, the accretion rate in the inner part of the halo, neither to model individually the radiation coming from each star. Employing small hydrodynamical simulation boxes has the advantage of resolving in detail different aspects of the problem (chemistry, mini-halos, early metal-enrichment, for example), but fails to present a large diversity of cosmological regions, biasing the derived number density of DC regions.

In this chapter, we use three sizes of simulation box, from a small box of 1 cMpc side length, a medium box of 10 cMpc with a set of two simulations, and a large simulation box of 142 cMpc. We model the radiation intensity coming from nearby star-forming galaxies in a similar way as D14 and A14. Our attempt was to estimate the number density of regions eligible to host a DCBH, based on the absence of efficient coolants criterion: a high enough radiation intensity to destroy molecular hydrogen and a low metallicity. The idea was not to capture all the physical processes at the same time in the same simulation, but to have a larger picture of the direct collapse scenario by using, for the first time, a suite of large scale hydrodynamical simulations. Another aim was to see if some halos were illuminated by a sufficiently high radiation intensity ($J_{LW,crit} = 100, 300$), more similar to what is obtained as critical value for collapse in 3D zoom-in simulations.

We investigated the impact of SN feedback. We use either a weaker thermal feedback or a stronger delayed cooling feedback. Star formation is lower (by one order of magnitude) in the simulation with delayed cooling SN feedback, and more in line with the predictions of halo occupation distribution (Habouzit, Volonteri & Dubois, 2016). A weak SN feedback allows for more young stars, but also, consequently, for an earlier metal pollution. Using our DCBH finder code (with t_{ff} as in D14 and $J_{LW,crit} = 30$), we do not find any DCBH regions in the simulation Chunky with the delayed cooling feedback, however we do find 3 regions for the thermal SN feedback. The absence of a strong radiation field, caused by the lower star formation rate, therefore, appears to be more important than metal pollution. Besides, in these 10 cMpc side box, we do not find any halo illuminated by a radiation intensity higher than 162.71 in J_{LW} units, down to $z = 7.33$, so no DCBH can form if $J_{LW,crit} \gg 100$. For the delayed cooling SN feedback, the maximum value of the radiation intensity is only $J_{LW} = 30.33$.

The simulation Horizon-noAGN allows us to have a more global view of the direct collapse scenario. The simulation box is large enough to have some statistics (box side length of 142 cMpc), at the price of a lower resolution, and it includes a relatively weak SN feedback. The number density of DCBH regions in this simulation varies from 7×10^{-7} to 10^{-4} cMpc^{-3}. We find similar results as D14, specifically for the two largest thresholds $J_{LW,crit} = 100$ and $J_{LW,crit} = 300$. However, the number density of BHs for the threshold $J_{LW,crit} = 30$ for the Horizon-noAGN simulation is smaller than what D14 and A14 obtained for the same threshold. We do not consider a radiation background, and this can have an impact when considering low intensity thresholds such as $J_{LW,crit} = 30$. Horizon-noAGN also allows us to investigate whether the DC scenario can explain the presence of BHs in massive galaxies at $z = 6$, considered as proxies for

the hosts of quasars. We find that 30% of the halos more massive than $10^{11}\,M_\odot$ at $z = 5.8$, have at least one progenitor eligible to form a DCBH for $J_{LW,crit} = 30$. This probability, however, drops abruptly below 1-10% when considering higher thresholds ($J_{LW,crit} = 100, 300$) for the radiation intensity.

Several approaches have been used in the last few years to determine the number density of direct collapse regions, from post-processing of hydrodynamical simulations to semi-analytical methods. These approaches derive number density which differ by several orders of magnitude (from 10^{-1} to 10^{-9} Mpc^{-3}). We perform a comparison between some of these approaches, specifically with A14 and D14, in order to understand this discrepancy. We find differences in the probability for halos to be star-forming and metal-free, for the propagation of metals in the gas, and finally in the modeling of the radiation intensity itself, which in some cases compensate to produce similar results in the number density, despite the very different single assumptions.

In summary, we find that if DC requires $J_{LW,crit} = 300$, and a halo must be illuminated by such intense field for its full collapse, the number of DCBHs may be sufficient to explain the number of high-z quasars, based on Horizon-noAGN, but not the presence of BHs in normal galaxies. If instead either $J_{LW,crit} \sim 30$ or a halo must be illuminated only during the collapse of the central region, then DCBHs may be common also in normal galaxies, provided that SN feedback is not very strong.

4.9 Perspectives: Applications of hybrid SAMs

Hybrid SAMs as the bridge between SAMs and zoom-in cosmological hydrodynamical simulations

As we have said in the introduction of this chapter, hybrid semi-analytical models are the bridge between pure SAMs and cosmological hydrodynamical zoom-in simulations of single halos. Zoom-in simulations reach high spatial resolution, and are able to follow the gas collapse to high densities. However, they are lacking of validation for the occurrence of a zoom-in physical set up. Hybrid SAMs are therefore needed to provide a set of reasonable parameters, for instance, metallicity, background radiation intensity. They are also crucial to place the zoom-in simulations in a more global context, and to provide an idea of the occurrence of the processes studied in zoom-in simulations. In the following, we give an example of an applications of hydrodynamical simulations: the fraction of metal enriched halos (Latif et al., 2016).

In Latif et al. (2016), we have studied the impact of dust and metal line cooling in massive primordial halos ($M_h > 10^7\,M_\odot$) illuminated by a strong radiation intensity, and polluted by trace amounts of metals and dust. The importance of dust in gas fragmentation has been shown by Schneider et al. (2003) ; Omukai et al. (2005) ; Omukai, Schneider & Haiman (2008), the presence of dust will boost the cooling of the gas, which favors the fragmentation of the gas. Formation of H_2 on dust grains also boosts the cooling of the gas (Omukai, 2001 ; Cazaux & Spaans, 2009 ; Latif, Schleicher & Spaans, 2012). We have performed 3D zoom-in cosmological simulations of two halos with the code Enzo, which includes here cooling and heating from dust grains. The isothermal collapse of the gas is possible, even in the presence of trace metals and dust, until reaching densities of $10^{-16}\,g\,cm^{-3}$, at which dust cooling becomes effective. We find that dust cooling is more efficient for high metallicities. Regarding the inflow rate, which is of paramount importance in the DC BH formation model, we find that inflow rate of $0.1\,M_\odot/yr$ is feasible for $Z \leqslant 10^{-5}\,Z_\odot$, and decreases for higher metallicities. Compared to metal-free halos,

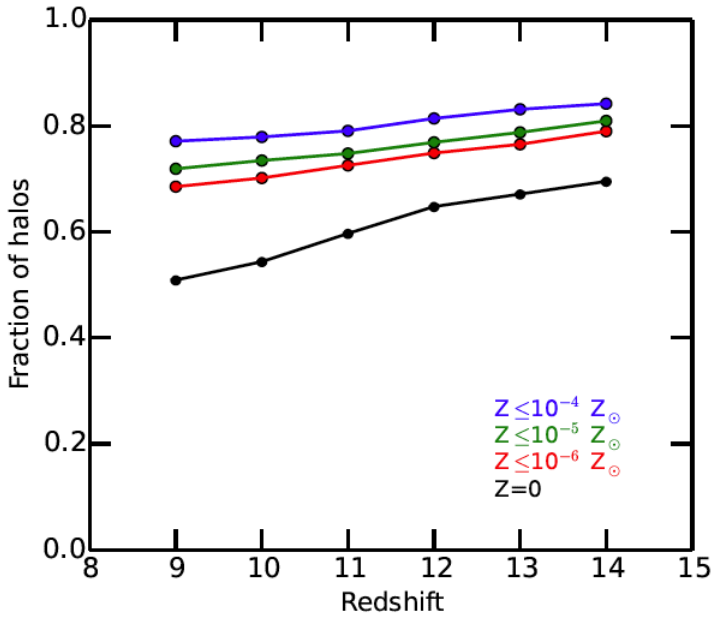

Fig. 4.7 – Fraction of metal below a given mean halo metallicity, $Z < 10^{-4}\,Z_\odot$ in blue, $Z < 10^{-5}\,Z_\odot$ in green, $Z < 10^{-5}\,Z_\odot$ in red, and finally $Z = 0$ in black. Published in (Latif et al., 2016).

by which factor the fraction of DC eligible halos increase for metallicity of $Z \leqslant 10^{-5}\,Z_\odot$?
To answer this question and to give a large scale perspective to this work, we have run a cosmological hydrodynamical simulation Chubby, which is similar to the simulation Chunky, but with a better spatial and dark matter resolution. The box size is $(10\,\mathrm{cMpc})^3$, and allows us to have some statistics. Chubby is very similar to Chunky (described above) in terms of the cosmology used, star formation recipe, AGN feedback, SN feedback. We use the delayed cooling SN feedback implementation, with the parameter $M_{SN} = 3.2 \times 10^3\,M_\odot$, $\sigma_{en} = 54\,\mathrm{km\,s^{-1}}$, $t_{diss} = 0.7\,\mathrm{Myr}$. The box side is again $10\,\mathrm{cMpc}^{-3}$. We run the simulation from $z = 200$ down to $z = 6$, we stop at this redshift because sufficient for the study we described, and also because such a high resolution simulation is very time consuming. The spatial resolution is $\Delta x = 10\,\mathrm{pc}$, and he mass resolution $M_{DM,res} = 2 \times 10^5\,M_\odot$.
With the simulation Chubby, we estimate the fraction of halos that are metal-polluted with $Z < 10^{-4}\,Z_\odot$ (Latif et al., 2016). With HaloMaker, we identify all the halos in the mass range $2 \times 10^7 - 10^8\,M_\odot$ that at least contain 100 dark matter particles. Fig. 4.7 show the fraction of metal below a given mean halo metallicity, $Z < 10^{-4}\,Z_\odot$ in blue, $Z < 10^{-5}\,Z_\odot$ in green, $Z < 10^{-5}\,Z_\odot$ in red, and finally $Z = 0$ in black. The number of halos under a given mean metallicity decreases with decreasing redshift. The fraction of halos polluted with $Z \leqslant 10^{-5}\,Z_\odot$ is ~ 1.5 higher than the fraction of metal-free halos. Therefore, if the DC model is feasible for $Z \leqslant 10^{-5}\,Z_\odot$, the fraction of DC candidate halos is increased by 1.5 compared to metal-free halos.

Hybrid SAMs as template for full self-consistent cosmological hydrodynamical simulations

Hybrid SAMs offer us the advantage of following in time different crucial quantities for the DC BH formation model, such as metal-enrichment of the gas, stellar formation, spatial distribution of halos. This is crucial to determine which halos are eligible for the formation of DCBHs. Unfortunately, following in time the growth of these DCBH is still limited by our inability of

forming DCBHs self-consistently on-the-fly in hydrodynamical simulations. Based on the work we have described in this chapter, we would like to implement in the code RAMSES the DC formation scenario.

The implementation will be based on the metallicity of the local environment of the future BHs, the stellar mass and the distance of nearby star-forming regions, a collapsing time or free-fall time (during which the radiation coming from the star-forming regions has to be higher than a given threshold.) All the regions matching these criteria, will be seeded with a sink particle and flagged as DCBH. Doing it on-the-fly will allow us to self-consistently make predictions on the observational diagnostics for BH formation for the different BH formation models, namely the *light seed* models presented in the previous chapter, and the DC *heavy seed* model: mass of BH, BH-galaxy occupation fraction. Having all these BH formation scenarios implemented in the same simulation code will allow us to study the impact of both the low-mass and high-mass seeds, through AGN feedback, on their host galaxies, for example.

This project will require a larger simulation box size. As we have seen in this chapter, in a simulation box of 10 cMpc side length, only few, if any, DC candidate halos are found, this project will therefore require a larger simulation box size, with a spatial and dark matter resolutions comparable to those of the simulation Chubby.

Chapter 5

Black hole formation and growth with primordial non-Gaussianities

The chapter treats different topics in the fields of galaxy formation and evolution, reionization history, and the formation and growth of supermassive black holes. How do the prescription of the cosmological model affect the evolution of the Universe and the formation of large scale structures, and massive objects? *Planck* mission recently provided strong limits on non-Gaussianity on scales of clusters, but there is still room for considerable non-Gaussianity on galactic scales. We have tested the effect of local non-Gaussianity by running five cosmological N-body simulations down to $z = 6.5$. For these simulations, we adopt the same initial phases, and either Gaussian or scale-dependent non-Gaussian primordial fluctuations, all consistent with the constraints set by *Planck* on cluster scales. We particularly focus on the impact of non-Gaussianities on high-redshift dark matter halos, and galaxy population, on the reionization history of the Universe, and finally on supermassive BH formation and evolution over cosmic time. The main result of the introduction of primordial non-Gaussian fluctuations is the assembly of more low-mass dark matter halos. The galaxy mass function is also enhanced by a maximum of 0.3 dex at the low-mass end. This leads to an increase of the number of sources providing ionizing photons, resulting in an early reionization period. These more numerous low-mass galaxies, are potential extra sites for BH formation, we investigate the two most common BH formation models, the PopIII remnants and the direct collapse models.

This chapter is adapted from its corresponding publications:

- *Testing primordial non-Gaussinities on galactic scales at high-redshift*,
  Mélanie Habouzit, Takahiro Nishimichi, Sébastien Peirani, Yohan Dubois, Gary Mamon, Joseph Silk and Jacopo Chevallard,
  MNRAS, 2014, vol 445, pages L129-L133, arXiv:1407.8192

- *Effect of primordial non-Gaussianities on the far-UV luminosity function of high-redshift*,
  Jacopo Chevallard, Joseph Silk, Takahiro Nishimich, Mélanie Habouzit, Gary Mamon, Sébastien Peirani,
  MNRAS, 2015, vol 446, pages 3235-3252, arXiv:1410.7768

- *Black hole formation and growth with non-Gaussian primordial density perturbations*,
  Mélanie Habouzit, Marta Volonteri, Muhammad Latif, Takahiro Nishimichi, Sébastien Peirani, Yohan Dubois, Gary Mamon, Joseph Silk and Jacopo Chevallard,
  MNRAS, 2016, vol 456, pages 1901-1912, arXiv:1507.05971

Contents

5.1 Introduction on primordial non-Gaussianities

The cosmological principle predicts an uniform and isotropic distribution of matter in the Universe. In order to form large scale structures, one needs to introduce perturbations in the history of the Universe. The Hot Big Bang theory has no explanation for the non-uniform and isotropic distribution of matter, and it is one of the so-called *problems* of this theory (the two others being the flatness problem and the horizon problem). The standard description of the Universe, driven by the general theory of relativity, is expected to break down when the Universe is so dense that quantum effects may be more than important to consider. Inflation theory has been considered to be a natural physical process solving the Hot Big Bang theory's problems, since almost 40 years ago. In addition to solving the Hot Big Bang problems, this accelerated period of our Universe allows the introduction of these quantum processes, which can produce the necessary spectrum of primordial density seed perturbations, that gravitational instability accentuates to produce the large structures we observe today, namely dark matter halos, clusters and galaxies.

Inflation was also able to explain the CMB temperature anisotropies, that is why inflationary theory has became very appealing and studied over the years. The temperature anisotropies of the CMB, measured by *COBE* (Smoot et al., 1992 ; Bennett et al., 1996 ; Gorski et al., 1996), *WMAP* (Spergel et al., 2003 ; Komatsu et al., 2003) and *Planck* (Planck Collaboration et al., 2011, 2015b,a) missions, are relics of density perturbations in the cosmic fluid at the time of last scattering (through the Sachs-Wolfe effect). Primordial perturbations described by a Gaussian distribution is supported, on large scales, by the measurements of these temperature

anisotropies of the CMB, since the first detection of anisotropies by COBE in 2001. *Planck*'s results (Planck Collaboration et al., 2014, 2015b) have made incomparable progress in the accuracy of the estimated cosmological parameters and on our knowledge of the beginning of the Universe. The *Planck* mission has, however, focused on large structures, considering primordial density perturbations on the scale of clusters. Mapping in detail the CMB on the full sky, it has provided very strong constraints on the local non-Gaussian parameter $f_{\rm NL} = 2.7 \pm 5.8$ (Planck Collaboration et al., 2013b), which describes the deviation to a Gaussian distribution of primordial density fluctuations, and will be explained in more detail in the next section. However, as predicted by some inflationary models, non-Gaussianities on smaller scales, beyond the reach of CMB measurements, are still conceivable.

As nicely discussed in Bartolo et al. (2004), the question is not to probe that CMB is consistent with Gaussianities, but rather to ask "How Gaussian is it?". Investigating and testing the Gaussianity of the CMB is a very difficult task, and this is due to the fact that non-Gaussian fluctuations have infinite degrees of freedom (in other words, there is an infinite number of ways of being non-Gaussian). The observed signal of the CMB is the result of a summation of different effects arising from different sources, that all contribute to the observed signal. They can come from non-Gaussianities in the primordial curvature perturbation produced in the very early universe by inflation (the purpose of this work), but also from non-Gaussianity arising after recombination as lensing, or generated by galactic and extra galactic sources. Extracting the information of primordial non-Gaussianity is challenging for these reasons. In this chapter, we will focus only on primordial non-Gaussianities, and investigate their impact on the Universe evolution with cosmological simulations. In the following, we start with a short introduction on primordial non-Gaussianities. We then describe the consequences of non-Gaussianities in the assembly of large structures, both dark matter halos and galaxies, on the reionization history, and finally on black hole formation and evolution.

5.1.1 Primordial bispectrum

Probes of inflation theory come from properties of fluctuations. Standard models of inflation predicts a flat Universe perturbed by nearly Gaussian and scale invariant primordial fluctuations (Gangui et al., 1994 ; Acquaviva et al., 2003 ; Maldacena, 2003). Primordial non-Gaussianities are therefore an important test of how physics shaped the universe at early times, at energies too high to be probed by laboratory experiments. Non-Gaussianities are a promising way to investigate inflation, and specifically the interactions of the field generating inflation.
To define the standard inflationary observables, we characterize the scalar degree of freedom in the primordial density perturbations using the curvature perturbation on a uniform density hypersurface ξ (gauge-invariant, and can be related to the field fluctuations during inflation and the temperature fluctuations in the CMB).
Power spectrum P_ξ is defined by the two-point correlation function and described the statistical properties of the primordial density perturbations:

$$< \xi_{k_1} \xi_{k_2} >= (2\pi)^3 P_\xi(k_1) \delta^{(3)}(\mathbf{k_1} + \mathbf{k_2}), \tag{5.1}$$

k_i the comoving wavevectors, $\delta^{(3)}$ the three dimensional Dirac delta function, ξ_k the Fourier transform of ξ. If ξ is a purely Gaussian field then the two-point correlation function completely defines the statistics of the field. To acceed any departure from a Gaussian field, which is not encoded in the power spectrum P_ξ, one requires to measure higher order of correlations. Therefore for a non-Gaussian field, higher-order correlations are needed, with the three-point

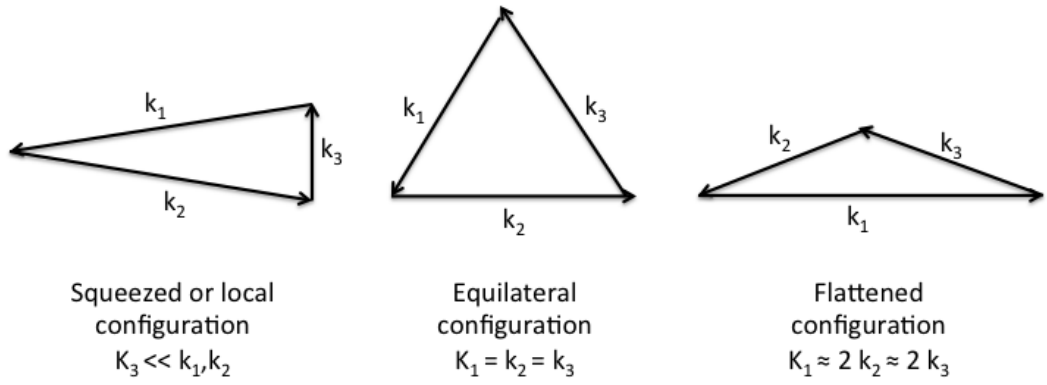

Fig. 5.1 – Representation of the closed triangles formed by the three momenta (k_1, k_2, k_3). On the left, we show the squeesed or local configuration. The equilateral configuration is shown in the middle. On the right, the flattened or folded configuration

correlation function $< \xi_{k_1}\xi_{k_2}\xi_{k_3} >$, that correlates density fluctuations at three points in space, or its counterpart in Fourier space, the bispectrum B_ξ, which correlates the fluctuations with three wave vectors in Fourier space:

$$< \xi_{k_1}\xi_{k_2}\xi_{k_3} >= (2\pi)^3 B_\xi(k_1, k_2, k_3)\delta^{(3)}(\mathbf{k_1} + \mathbf{k_2} + \mathbf{k_3}). \tag{5.2}$$

Every model of inflation has its own predictions for the bispectrum of the primordial perturbations B_ξ. Statistical homogeneity, represented here by the delta function $\delta^{(3)}(\mathbf{k_1} + \mathbf{k_2} + \mathbf{k_3})$, requires the three momenta (k_1, k_2, k_3) to form a closed triangle in Fourier space, with $\mathbf{k_1} + \mathbf{k_2} + \mathbf{k_3} = 0$, whilst statistical isotropy ensures that the bispectrum B_ξ only depends on the magnitude of the momentum $k_i = |\mathbf{k_i}|$, and not their orientations.
Theoretically, there are an infinite number of possible triangles formed by the three wave vectors, every model of inflation has its own. The goal today, is to rule out some of the theoretical models of inflation.

5.1.2 Introduction of $f_{\rm NL}$ parameter

Most of the inflation models, predict non-observable non-Gaussianities. These models verify the 4 following conditions: *single field*, *canonical kinetic energy*, *slow-roll*, and *initial vacuum state*. The first condition tells us that there is only one field driving inflation, and responsible for creating of the initial perturbations. The second condition says that these fluctuations propagate at the speed of light. Slow roll condition says that during inflation, the evolution of the field was very slow compared to the Hubble time. Finally, before the creation of the fluctuations, the quantum field was initially in an adiabatic vacuum state, and this is the last condition. Models that predict, instead, observable non-Gaussinities, assume the violation of one of the above conditions. The type of non-Gaussianity depends on which of the condition is violated. The name of the models generally refer to the violated condition: multi-fields models, or non slow-roll models, for example.

Different relations between the wave vectors k_i, what we call *shape dependence* of the bispectrum, defines different types of non-Gaussianities. The shape is capable of differentiating between physically distinct Lagrangians, and so between non-Gaussianity types.
Below, we list the most common configurations of the triangles:
Flattened configuration The shape has the maximum signal at the flattened configuration, two of

the three wavenumbers are equal and twice the value of the third vector, $k_1 \approx 2\,k_2 \approx 2\,k_3$ (see last figure in Fig. 5.1). This configuration is produced by non-vacuum initial condition.
Equilateral configuration This configuration is characterized by $k_1 = k_2 = k_3$ (representation in the middle of Fig. 5.1). This shape can be produced by non canonical kinetic terms of quantum fields.
Squeezed or local configuration This is produced by considering multiple fields inflation models. The most studied primordial bispectrum is the *local-type model*, also called the squeezed configuration. Interactions that are local in real space (that is why we call them *local non-Gaussianities*) therefore maximize the bispectrum in the squeezed configuration (cf the left panel in Fig. 5.1), when two of the wavenumbers are much greater than the third one $k_3 << k_1, k_2$ (Gangui et al., 1994).

They are two distinct features of the bispectrum that help us probe the inflationary action. The first one is its *overall amplitude*, which is often parametrized (Komatsu & Spergel, 2001) by the non-linearity parameter $f_{\rm NL}$ (for a given model of B_ξ). $f_{\rm NL}$ measures the level of the non-Gaussianity signature.

We can express the bispectrum as a function of the $f_{\rm NL}$ parameter, and a function $T(k_1 k_2, k_3)$ which capture its dependence on the triangle configurations:

$$B_\xi \equiv f_{\rm NL}\, T(k_1 k_2, k_3). \tag{5.3}$$

The magnitude of the non-Gaussianity of local configuration can be parameterized (Komatsu & Spergel, 2001) by the parameter $f_{\rm NL}$, describing the quadratic coupling of the primordial perturbations. The gravitational potential can be split in two components, a Gaussian field given the usual perturbation results, described by $\zeta_{\rm G}(\mathbf{x})$, and a small local non-Gaussian term, described by $\zeta_{\rm G}(\mathbf{x}) = f_{\rm NL}\left(\zeta^2_{\rm G}(\mathbf{x}) - \left\langle \zeta^2_{\rm G}(\mathbf{x})\right\rangle\right)$. The resulting curvature perturbations $\zeta(x)$ at a given position x, can therefore be expressed by:

$$\zeta(\mathbf{x}) = \zeta_{\rm G}(\mathbf{x}) + \frac{3}{5} f_{\rm NL}\left(\zeta^2_{\rm G}(\mathbf{x}) - \left\langle \zeta^2_{\rm G}(\mathbf{x})\right\rangle\right), \tag{5.4}$$

where $\zeta_{\rm G}$ is a Gaussian random field at the same position. In other words, we parametrized non-Gaussianity as a non-linear correction to a Gaussian perturbation $\zeta_{\rm G}$. The factor 3/5 is conventional and comes from the fact that initially the equation was expressed in terms of the Newtonian potential $\Phi(x)$, which is related to ζ by the factor 3/5 during the matter-dominated period.

We need to keep in mind that we have confirmed over the years that inflation has produced primordial fluctuations, however we still have not identified the mechanisms by which these fluctuations are generated. Of course, several scenarios have been proposed. The slow-roll scenario is the standard scenario (fluctuations of the inflation field when it slowly rolls down along its potential, produce the cosmological density fluctuations). This scenario predict $f_{\rm NL} \sim \varepsilon$, where $\varepsilon \ll 1$ is the slow roll parameter, which is independent of scale (Maldacena, 2003). We can also cite the curvaton scenario (Mollerach, 1990 ; Enqvist & Sloth, 2002 ; Lyth & Wands, 2002), but also the inhomogeneous reheating one (Dvali, Gruzinov & Zaldarriaga, 2004), or the ghost inflationary scenario (Arkani-Hamed et al., 2004).

5.1.3 Observational constraints, room for non-Gaussianities at small scales

The primordial density fluctuations evolve with time, and lead to the collapse of dark matter particles, and baryons. A non-Gaussian initial spectrum of density perturbations will then affect the distribution of baryonic structures. The large scale structures of the Universe therefore are the results of the non-linear evolution due to gravitational instability of some initial density perturbations, which are also responsible for the CMB anisotropies. The CMB provides us a map of the density perturbations at the time of decoupling, the earliest information we have about our Universe. Studying CMB anisotropies give us amazing insight of non-Gaussianities.

In the field of cosmological perturbations, measuring the parameter $f_{\rm NL}$ has been one of the primary goals of several spatial missions. The first attempt was with the satellite COsmic Background Explorer (COBE), which was launched on the 18th of November 1989 [1]. In 2001, the data of the Differential Microwave Radiometer instrument DMR allowed a first estimate of $|f_{\rm NL}| < 1500$ (68%), via the angular bispectrum, which is the harmonic counterpart of the three-point correlation function. While this limit has ben obtained for large-scale non-Gaussianities, with the MAXIMA data, a limit at small scales has also been determined, $|f_{\rm NL}| < 950$ (68%). Despite an interesting range of methods to compute a value for the $f_{\rm NL}$ parameter, and different final values, the COBE satellite only gave us a weak constrain.

Wilkinson Microwave Anisotropy Probe (WMAP) satellite has been launched on June 30, 2001. The first results were released in 2003, and further results were released in 2005, 2007, 2009 and 2011. The constraints on the parameter $f_{\rm NL}$ have been highly debated, because of the scatter obtained in the constraints by different teams, but with the same set of data. We only cite here the estimate of Smith, Senatore & Zaldarriaga (2009), with $-4 < f_{\rm NL} < 80$ (95%, WMAP-5years).

The *Planck* satellite was launched in 2009, it has provided a much stronger constraint on the local non-Gaussianity parameter, $f_{\rm NL} = 2.7 \pm 5.8$ (Planck Collaboration et al., 2013b), than did the previous CMB missions. This new constraint on $f_{\rm NL}$ on large scales does not exclude non-Gaussianity on smaller scales, on galactic scales.

5.1.4 Previous work, and the idea of running non-Gaussianities

By appealing to the theory of Press & Schechter (1974) it is straightforward to show that positively skewed ($f_{\rm NL} > 0$) primordial density fluctuations increase the halo mass function (HMF) at large masses with respect to that arising from Gaussian initial conditions (e.g. Matarrese, Verde & Jimenez, 2000). This effect has also been verified with cosmological N-body simulations (Kang, Norberg & Silk, 2007; Grossi et al., 2007; Pillepich, Porciani & Hahn, 2010). Simulations with non-Gaussian initial conditions (nGICs) have been used to probe the halo mass function (Kang, Norberg & Silk, 2007; Grossi et al., 2007; Pillepich, Porciani, & Hahn, 2010), the scale-dependent halo bias (Dalal et al., 2008; Desjacques, Seljak & Iliev, 2009; Grossi et al., 2009) and bispectrum (Nishimichi et al., 2010; Sefusatti, Crocce, & Desjacques, 2010), weak lensing statistics (Pace et al., 2011; Shirasaki, Yoshida, Hamana, & Nishimichi, 2012), the pairwise velocity distribution function (Lam, Nishimichi, & Yoshida, 2011). Hydrodynamical cosmological simulations have been performed with nGICs to study the baryon history (Maio & Iannuzzi, 2011), the gas distribution (Maio, 2011), the gas density profiles (Maio & Khochfar, 2012) and SZ maps (Pace & Maio, 2014).

[1] That was few months after my birth date, meaning that I am as old as COBE satellite

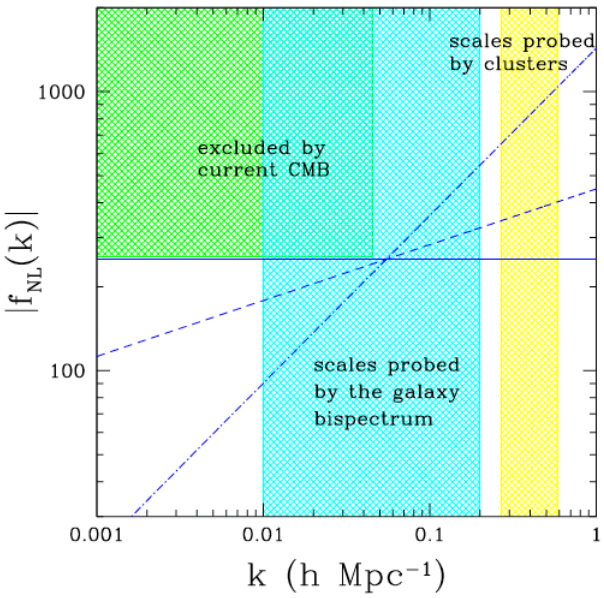

Fig. 5.2 – Example of running models for non-Gaussianity parameter $f_{\rm NL}$ in solid or dashed lines, by LoVerde et al. (2008). Range of scales probed by different observables are also shown in green region for CMB, blue for galaxy bispectrum, and yellow for clusters.

These studies have all used a *scale-independent* value of $f_{\rm NL}$. However, the new constraint on $f_{\rm NL}$ on large scales does not exclude non-Gaussianity on smaller scales, namely on galactic scales. Indeed, the non-Gaussianity might depend on scale, as predicted, e.g., in several inflation models with a variable speed of sound, such as the string-based Dirac-Born-Infeld models (Silverstein & Tong, 2004 ; Alishahiha, Silverstein & Tong, 2004 ; Chen, 2005).
An extra-dependence of scale k, can be described as a *running* prescription for the parameter $f_{\rm NL}$, that we can therefore expressed as:

$$f_{\rm NL}(k) = f_{\rm NL,0} \left(\frac{k}{k_0}\right)^{\alpha}, \tag{5.5}$$

where k_0 is a pivot scale.

It is thus possible that significant non-Gaussianity can lurk on the comoving scales of galaxies without being detected by the *Planck* CMB mission, whose angular resolution effectively limits it to the scales of clusters of galaxies. A *blue* spectrum of *running non-Gaussianity* might enhance low masses instead, if the spectrum is blue enough, i.e. if $\alpha = \mathrm{d}\ln \mathrm{f_{NL}}/\mathrm{d}\ln \mathrm{k}$ is large enough. The effects of scale-dependent non-Gaussianity on the HMF (cluster counts) and on reionization were analytically predicted by LoVerde et al. (2008) and Crociani et al. (2009), respectively. LoVerde et al. (2008) study the possibility of constraining the running parameter α with a coalition of different methods, CMB measurements, but also the measurements of cluster abundance. The range of scales probed by the different observables are shown in Fig.5.2, in green the region excluded by CMB measurements, in blue the scales probed by the galaxy spectrum, and finally in yellow the scales probed by cluster surveys. The scale dependence α of the parameter $f_{\rm NL}$, implies a different level of non-Gaussianities at different scales k. LoVerde et al. (2008) consider an equilateral model here, however the principle remains the same as what we investigate in this chapter with local non-Gaussianity on galactic scales.

Because small scales are still poorly constrained at high redshifts ($z > 6$), cosmological

Tab. 5.1 – Characteristics of $f_{\rm NL}$ models (eq. [5.6])

Model	G	NG1	NG2	NG3	NG4
$f_{\rm NL,0}$	0	82	1000	7357	10000
α	–	1/2	4/3	2	4/3

simulations are key for predicting whether non-Gaussianities have an impact on galactic scales. Only one team has run nG simulations with an *explicit scale-dependence* adjustable by a free parameter (Shandera, Dalal & Huterer, 2011), focusing on halo clustering in the the local Universe. In the following, we describe the method that we use to investigate non-Gaussianity, namely the simulation set-up and the various models of scale-dependent $\rm f_{NL}$ parameter.

5.2 Effects of non-Gaussianities on the Universe structure formation: halo and galaxy mass functions

5.2.1 Numerical methods: from non-Gaussian N-body simulations to galaxy formation model

Initial conditions: prescription for $f_{\rm NL}$ and N-body simulations

We employed a simple model that allows a significant amount of non-Gaussianity on small scales, relevant for early structure formation, while keeping such effects small on large scales to meet the strong constraints obtained by the *Planck* CMB mission (Planck Collaboration et al., 2013b). We model the scale-dependent non-linearity parameter $f_{\rm NL}$ as:

$$f_{\rm NL}(k) = f_{\rm NL,0} \left(\frac{k}{k_0}\right)^{\alpha} \tag{5.6}$$

We explored four different non-Gaussian (nG) models by varying the normalization $f_{\rm NL,0}$ and the slope $\alpha = \mathrm{d\ln f_{NL}/d\ln k}$, in such a way that the non-Gaussianity is significant on galactic scales, yet small enough to meet the current constraints from *Planck* (Planck Collaboration et al., 2013b). Table 5.1 (normalization and slope for $k_0 = 100\,h/\mathrm{Mpc}$) lists our adopted models, while Fig. 5.3 displays these models with current constraints from CMB experiments. We restricted ourselves to positively skewed primordial density fluctuations, i.e. $f_{\rm NL} > 0$, hence $f_{\rm NL,0} > 0$.

We modified the initial condition generator originally developed by Nishimichi et al. (2009), based on second-order Lagrangian perturbation theory (e.g., Scoccimarro, 1998; Crocce, Pueblas & Scoccimarro, 2006), parallelized by Valageas & Nishimichi (2011) and with local-type non-Gaussianities implemented by Nishimichi (2012). We followed Becker, Huterer & Kadota (2011) and realized the generalized local ansatz of equation (5.4) by taking a convolution of the curvature squared and the k-dependent $f_{\rm NL}$ kernel in Fourier space. We used the public Boltzmann code, CAMB (Lewis, Challinor & Lasenby, 2000) to compute the transfer function and multiply it to the curvature perturbations to have the linear density fluctuations.

N-body simulations and halo catalog

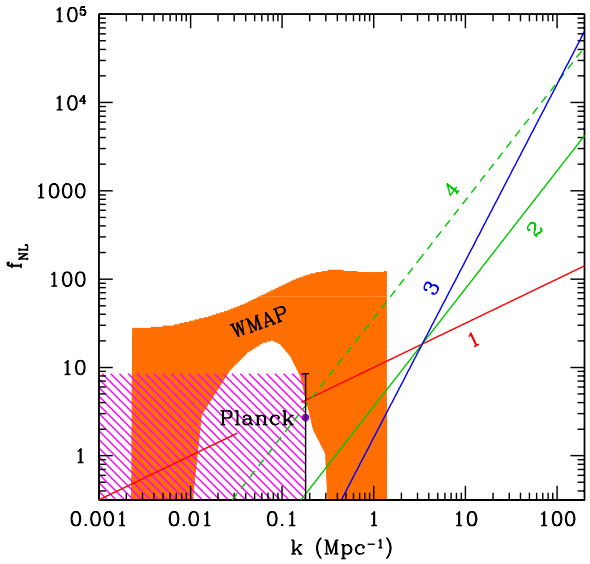

Fig. 5.3 – Models (lines) for the scale-dependent NG parameter f_{NL}^{local}. The orange shaded region represents the allowed values from *WMAP*, within $1\,\sigma$, of the $f_{NL}^{local}(k)$ according to Becker & Huterer (2012). The magenta shaded region shows the *Planck* constraint (Planck Collaboration et al., 2013b). The right edge of the box corresponds to a scale of $2\pi/k \simeq 30\,\mathrm{kpc}$, i.e. the scales of galaxies are to the right of the right edge of the box.

We have performed five cosmological simulations with GADGET-2 (Springel, 2005) for a ΛCDM universe using *Planck* parameters (Planck Collaboration et al., 2013a), namely $\Omega_M = 0.307$, $\Omega_\Lambda = 0.693$, $h = 0.678$ and $\sigma_8 = 0.829$. Each simulation was performed in a periodic box of side $50\,h^{-1}$ Mpc with 1024^3 dark matter particles (e.g. with mass resolution of $\sim 9.9 \times 10^6\,h^{-1}\,\mathrm{M}_\odot$). One simulation (hereafter, 'G') started with Gaussian ICs, while the other four (hereafter, 'NG') began with nGICs (eqs. [5.4] and [5.6], with parameters in Table 5.1), with the same initial phases. The simulations started at $z = 200$ and ended at $z = 6.5$. In each case, the Plummer-equivalent force softening was set to 5% of the mean inter-particle distance ($2.44\,h^{-1}$ kpc in comoving units).

For each snapshot (taken every ~ 40 Myr), catalogues of halos were prepared using ADAPTA-HOP (Aubert, Pichon, & Colombi, 2004), which employs an SPH-like kernel to compute densities at the location of each particle and partitions the ensemble of particles into (sub)halos based on saddle points in the density field. Only halos or subhalos containing at least 20 particles (e.g. $2.9 \times 10^8\mathrm{M}_\odot$) were retained. We then studied the individual evolution of (sub)halos, by building halo merger trees using TREEMAKER (Tweed et al., 2009), which allowed us to accurately derive the mass evolution of each dark matter (sub)halo. This was the basis to compute the evolution of galaxy stellar masses, as we shall see in Sect. 5.2.3.

Galaxy formation and evolution model

Galaxy stellar masses are "painted" on the halos and subhalos using the Behroozi, Wechsler, & Conroy (2013) model that provides the galaxy mass m as a function of halo mass M and redshift z. We could have adopted a *physical* model, such as Cattaneo et al. (2011). We also considered using the *empirical* model of Mutch, Croton, & Poole (2013). The former model is only constrained at $z = 0$, while the latter extends to $z = 4$, which is still insufficient for our purposes. We have thus preferred to adopt the empirical model of Behroozi, Wechsler & Conroy, whose parameters were fit to the galaxy stellar mass functions, specific star formation rates and

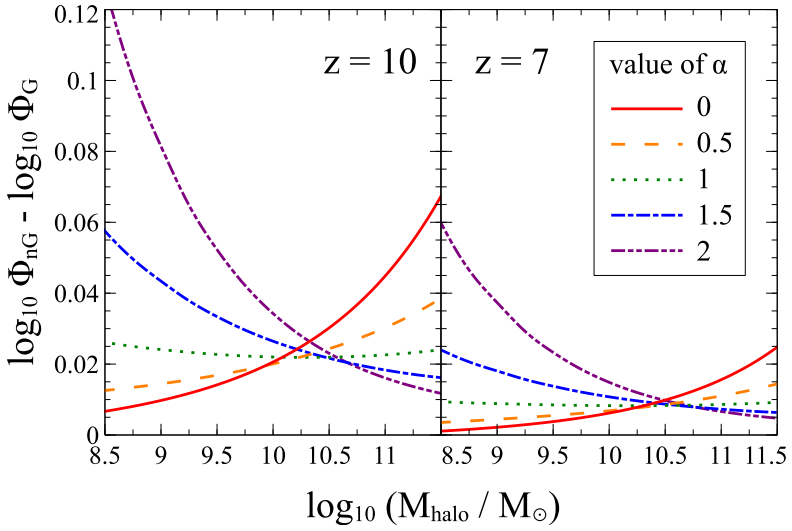

Fig. 5.4 – Analytical predictions of the nG correction to the halo mass function, for different power values of $f_{\rm NL}$. We plot the ratio of the halo mass function with non-Gaussian and Gaussian initial conditions at $z = 10$ (left) and $z = 7$ (right), for different running $f_{\rm NL}(k)$ passing through the pivot point of the first 3 models of Table 5.1 (see Fig. 5.3).

cosmic star formation rate, from $z = 0$ to $z = 8$. In particular, the Behroozi, Wechsler & Conroy model is the only empirical model of galaxy mass vs. halo mass and redshift that extends up to the redshift when reionization is thought to occur. A weakness of our approach is that, for lack of a better simple model, we assume that the Behroozi, Wechsler & Conroy model can be extrapolated beyond $z = 8$ to $z = 17$.

The Behroozi, Wechsler & Conroy model was calibrated with HMFs derived from cosmological simulations with Gaussian ICs. One could argue that their model cannot be applied to simulations with nGICs, without appropriate corrections. Alternatively, one could adopt the Behroozi, Wechsler & Conroy model as a basis to which we can compare the effects of Gaussian vs non-Gaussian ICs, and this is what we do here.

However, we slightly modify the Behroozi, Wechsler & Conroy model, by preventing galaxy masses from decreasing in time. For quiescent (sub)halos, we simply apply $\mathrm{m(M, z)}$, while for merging (sub)halos, we compare the galaxy mass $\mathrm{m(M, z)}$ to the sum over all its progenitors (in the previous timestep). If the galaxy mass from the model is higher than the sum of progenitor masses, we apply $\mathrm{m(M, z)}$; if the galaxy mass is smaller, the new galaxy mass is the sum over all its progenitors.

5.2.2 Predicted halo mass functions from theory

Before discussing the results of our numerical simulations, it is worth presenting analytical predictions to gain insight into the potential consequences of scale-dependent non-Gaussianities on early structure formation. We here adopt a simple model and discuss the effects on the HMF.

We follow the Press-Schechter formalism (Press & Schechter, 1974) for this calculation. Namely, we work with the linear density field, δ_M, smoothed with a spherical top hat window that encompasses a mass M and linearly extrapolated to $z = 0$, and consider that the one-point cumulants of this field uniquely determine the HMF. Assuming that the nG correction is small, we apply the Edgeworth expansion to the one-point density probability distribution function (LoVerde et al., 2008). Up to the skewness order, the non-Gaussian to Gaussian ratio of the

HMF is given by

$$\frac{\mathrm{dn_{nG}/dM}}{\mathrm{dn_G/dM}}(M,z) = 1 + \frac{1}{6}C_M^{(3)}H_3(\nu) + \frac{1}{6}\frac{\mathrm{d}C_M^{(3)}}{\mathrm{d}\ln\sigma_M}\frac{H_2(\nu)}{\nu}, \tag{5.7}$$

where $\sigma^2(M) = \left\langle \delta_M^2 \right\rangle$ is the variance of the density fluctuations δ_M, $C_M^{(3)} = \left\langle \delta_M^3 \right\rangle / \sigma_M^3$ is a measure of the skewness of δ_M, $\nu = \delta_\mathrm{c}(z)/\sigma(M)$ is the peak height, given $\delta_\mathrm{c}(z) = 1.686/D_+(z)$, the threshold density contrast for spherical collapse at redshift z, where $D_+(z)$ is the growth rate, and finally H_n is the Hermite polynomial.

In this model, all the nG correction comes from the skewness, which can be expressed by an integral of the *bispectrum*:

$$\langle \delta_M^3 \rangle = \int \frac{\mathrm{d}^3\mathbf{p}\mathrm{d}^3\mathbf{q}}{(2\pi)^6}\mathcal{M}(p)\mathcal{M}(q)\mathcal{M}(|\mathbf{p}+\mathbf{q}|)B_\zeta(p,q,|\mathbf{p}+\mathbf{q}|), \tag{5.8}$$

where $\mathcal{M}$ stands for the transfer function from the curvature to the density fluctuation smoothed by a mass scale M, and the bispectrum of the curvature ζ in the model (5.4) is given by

$$B_\zeta(k_1,k_2,k_3) = \frac{6}{5}\left[f_\mathrm{NL}(k_1)P_\zeta(k_2)P_\zeta(k_3) + (\mathrm{cyc.}\,2)\right], \tag{5.9}$$

where (cyc. 2) denotes two more terms that are obtained by cyclic permutation of the wavenumbers in the first term. The k dependence of f_NL propagates to the mass dependence of skewness through these equations, making the nG correction to the HMF rather non-trivial. Since we focus on blue f_NL (i.e., $\alpha > 0$), we anticipate that the correction to the HMF gets larger at low masses.

Fig. 5.4 shows the analytical prediction (eq. [5.7]) at $z = 10$ (left) and $z = 7$ (right). We here adopt $k_0 = 5.11\,h/\mathrm{Mpc}$, $f_{\mathrm{NL},0} = 18.5$, which is the intersection of the models 1, 2 and 3 (see Fig. 5.3), and vary the slope α as indicated in the figure legend. There are two noticeable trends in Fig. 5.4. First, the dependence of the HMF ratio on M depends on the slope α: the boost from non-Gaussianity is an increasing function of M for $\alpha < 1$, while a larger α results in a decreasing function of M. This high-mass enhancement of the HMF for small α is consistent with LoVerde et al. (2008). Because of the ν-dependence in equation (5.7), rare objects receive more non-Gaussian effect in these cases. When the k-dependence of f_NL is blue enough, it is the low-mass end of the HMF that is enhanced, so that the mass dependence in $C_M^{(3)}$ overwhelms that of $H_3(\nu)$. Second, the nG correction is more prominent at higher redshift. It is about a factor of two greater at $z = 10$ compared to $z = 7$. Although, not shown here, structure formation at low redshift is almost unaffected with the models that we consider here (i.e., the change of dn/dM is less than 10% at $z < 3$ over the mass range shown in Fig. 5.4). Thus, early structure formation provides us with a unique opportunity to constrain scale-dependent non-Gaussianity, given the very tight *Planck* constraints on large scales.

5.2.3 Results on halo and galaxy mass function

The left-hand panels of Fig. 5.5 show the HMFs obtained from the five cosmological simulations. One sees (upper left panel of Fig. 5.5) that the effects of non-Gaussianity on the HMF are increasingly important with increasing model number (see for example the upper left panel of Fig. 5.5).

Non-Gaussian models NG1 ($\alpha = 1/2$) and NG2 ($\alpha = 4/3$, low normalization) cause only small (less than 0.1 dex) and insignificant enhancements of the HMF (top two left panels of

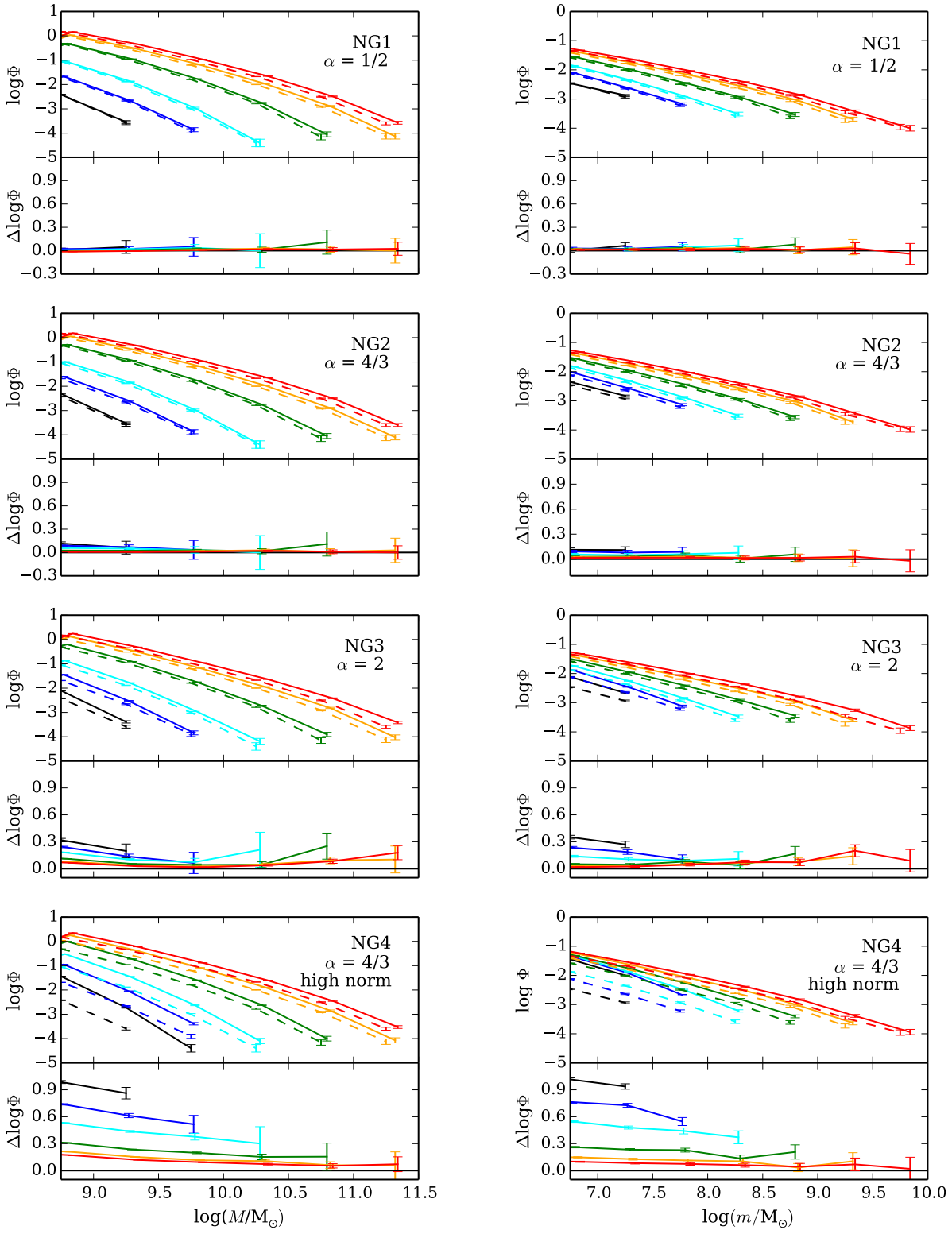

Fig. 5.5 – *Upper panels of boxes*: halo (*left*) and galaxy stellar (*right*) mass functions (in $\mathrm{Mpc}^{-3}\mathrm{dex}^{-1}$) for different initial conditions: Gaussian models (*dashed*), and non-Gaussian models 1 to 4 (from *top* to *bottom*). *Lower panels of boxes*: residuals of the log mass function relative to that of the Gaussian run (the *horizontal line* shows equal non-Gaussian and Gaussian mass functions). The errors are Poisson. The different curves indicate different redshifts (decreasing upwards for the large boxes): $z = 17$ (*black*), $z = 15$ (*blue*), $z = 13$ (*cyan*), $z = 10$ (*green*), $z = 8$ (*orange*), and $z = 7$ (*red*).

Fig. 5.5) and SMF (top two right panels of Fig. 5.5). Non-Gaussian model NG3, with a very steep slope ($\alpha = 2$), produces significant enhancements (left panel in third row of Fig. 5.5) of up to 0.3 dex ($z = 17$) or 0.2 dex ($z = 15$), in the HMF at $\log M/M_\odot = 9$. Finally, model NG4, with a slope 4/3 but a much higher normalization (10 times that of model NG2), produces very large enhancements of the HMFs and SMFs at low masses and high redshifts: greater than 0.3 dex enhancements in the HMF arise for $z \geq 13$ at all halo masses and $z \geq 10$ for $\log M/M_\odot < 9.5$. The corresponding SMF is also enhanced by over 0.3 dex for all galaxy masses at $z \geq 13$ and at galaxy masses $\log m/M_\odot \leq 6.8$ for $z = 10$.

5.2.4 Conclusions

We summarize the results presented in this first part of the chapter. In comparison with the predictions from Gaussian ICs, simulations with ICs that are increasingly non-Gaussian at smaller scales, yet consistent with the CMB constraints from *Planck*, can lead to small, but eventually detectable alterations to the halo and galaxy stellar mass functions. Since constant $f_{\rm NL} > 0$ enhances the HMF principally at large masses, one can think that low slopes of $\alpha = d \ln f_{\rm NL}/d \ln k > 0$ (keeping $f_{\rm NL} > 0$) should also enhance the high-end of the HMF, while a high enough slope should do the opposite and enhance the HMF at the low-mass end. At $\alpha = 2$, the HMF is in fact enhanced, both at the high and low ends (left residual plot of third row of Fig. 5.5, although that of the high end is only marginally significant). However, for the shallower slope ($\alpha = 4/3$), the HMF is only enhanced at the low end. We find that our two strongest non-Gaussian models (NG3, NG4) exhibit the largest differences, up to 0.2 dex for NG3 ($\alpha = 2$), and greater than 0.3 dex (at $z = 10$) for NG4 ($\alpha = 4/3$, $f_{\rm NL,0} = 10000$). These effects of nGICs on our simulated HMFs are close to the theoretical predictions, with some quantitative differences.

Unfortunately, it is difficult to measure the HMF with great accuracy, and considerably easier to measure the SMF. We used the state-of-the-art model of stellar mass versus halo mass and redshift of Behroozi, Wechsler & Conroy (2013) to produce galaxy masses on the (sub)halos of our cosmological N-body simulations. We slightly altered the model to consider halo mergers and prevent galaxy masses from decreasing in time. Comparing the resultant galaxy mass functions of our non-Gaussian models with that of our Gaussian model, we find similar behavior of the enhancements of the galaxy mass function with mass and redshift, i.e. 0.2 dex for NG3, and 0.3 dex (at $z = 10$) for NG4.

The modification of the SMF by nGICs can have profound consequences. In particular, the reionization of the Universe by the first stars and galaxies will be affected, in a different way depending on the slope α. Low mass galaxies are thought to be one of the most powerful sources of ionizing photons at high redshift (Robertson et al., 2013 ; Wise et al., 2014). Using a set of cosmological simulations, we have seen that faint galaxies are the most affected by primordial non-Gaussianities (see Models NG3 with $\alpha = 2$ and NG4 with $\alpha = 4/3$, but high normalization). Therefore primordial non-Gaussian perturbations can then strongly affect the thermal history of the intergalactic medium. Effects on the far-UV luminosity function and the reionization history are discussed in the next section.

5.3 Consequence of primordial non-Gaussianities on the reionization history of the Universe

Using the same set of simulations, in Chevallard et al. (2015), we went further to address the implications of scale-dependent non-Gaussianities on cosmic reionization. We only briefly describe the method of the study, the models that we have used and the main results.
Reionization is thought to be mainly driven by UV radiation emitted by massive stars born in the first galaxies, and particularly by the low-mass galaxies, because hydrogen ionizing photons can escape more easily from low mass halos than high mass ones. The number of ionizing photons emitted by early galaxies depends on their number density, i.e. on their far-UV galaxy luminosity function. We employed different reionization models (a fixed escape fraction $f_{\rm esc} = 0.2$, and two different escape fractions varying with redshift, and different far-UV absolute magnitude limits) to investigate the ionization fraction of the Universe as a function of redshift. We quantify the impact of the non-Gaussian primordial perturbations on the Universe reionization history, and on the optical depth of electrons to Thomson scattering.

5.3.1 Far-UV luminosity function and reionization models

Far-UV luminosity function

Instead of using the Behroozi model, this time we consider a modified semi-analytical galaxy formation model based on Mutch, Croton & Poole (2013) to compute the stellar mass assembly in each dark matter halo. The stellar mass is linked to dark matter halo mass via two functions:

$$\frac{\mathrm{dM_\star}}{\mathrm{dt}} = \mathrm{F_{growth}} \times \mathrm{F_{phys}}. \tag{5.10}$$

The growth function $\mathrm{F_{growth}}$ gives the amount of baryons available to form stars,

$$\mathrm{F_{growth}} = \mathrm{f_b} \frac{\mathrm{dM_{halo}}}{\mathrm{dt}}, \tag{5.11}$$

where we take $f_{\rm b} = 0.17$ the baryon fraction of the Universe. $\mathrm{F_{phys}}$ described the fraction of baryons actually converted into stars. Instead of taking a log-normal function as in Mutch, Croton & Poole (2013), we use a log-Cauchy function, where the parameters are chosen to match the observed far-UV luminosity function of Bouwens et al. 2014 at $z = 7$.
The Bruzual & Charlot (2003) stellar population synthesis code is used to compute the far-UV luminosity function for redshifts in the range $7 \leq z \leq 15$. The effect of non-Gaussianities on the far-UV luminosity function is very similar to the effect on the halo and galaxy mass function.

Reionization models

We consider a "standard" reionization model in order to compute the reionization of the Universe. We can write the equation expressing the competition between processes of hydrogen ionization by Lyman-continuum photons, and hydrogen recombination:

$$\frac{\mathrm{dQ_{HII}}}{\mathrm{dt}} = \frac{\dot{n}_{\rm ion}}{\langle n_{\rm H} \rangle} - \frac{Q_{\rm HII}}{t_{\rm rec}}, \tag{5.12}$$

where $Q_{\rm HII}$ is the volume filling fraction of ionized hydrogen. $\dot{n}_{\rm ion}$ is the comoving production rate of hydrogen ionizing photons within galaxies, and can be expressed as:

$$\dot{\mathrm{n}}_{\rm ion} = \mathrm{f_{esc}}\, \xi_{\rm ion}\, \rho_{\rm UV}. \tag{5.13}$$

We assumed here that reionization is mainly driven by UV radiation emitted by massive stars in early galaxies, therefore the comoving production rate of hydrogen depends on the UV galaxy luminosity function density, of the rate of Lyman-continuum photons per unit UV luminosity (computed at the wavelength 1500 Å). The UV luminosity density $\rho_{\rm UV}$ is computed by integrating the Schechter fit to the UV luminosity function obtained for the different Gaussian and non-Gaussian simulations, and depends on the minimum galaxy luminosity. For the latter we also use two different values in the following, because it is an uncertain parameter as observations are currently only able to probe the bright end of the UV luminosity function at high redshift. $f_{\rm esc}$ is the escape fraction of these photons into the IGM, two different models of the escape fraction are assumed in this work, and detailed in the following. $\langle n_{\rm H} \rangle$ is the comoving average number density of hydrogen atoms:

$$\langle n_{\rm H} \rangle = \frac{X_{\rm p}\, \Sigma_{\rm b}\, \rho_{\rm c}}{m_{\rm H}} \tag{5.14}$$

Finally, $\rm t_{rec}$ is the average recombination of time of hydrogen:

$$t_{\rm rec} = (\alpha_{\rm B}(T)\, n_{\rm e}\, C_{\rm HII})^{-1} \tag{5.15}$$

with $\alpha_{\rm B}$ the hydrogen recombination coefficient, $C_{\rm HII}$ the clumping factor which account for inhomogeneities in the density field, and $n_{\rm e}$ the number density of free electrons, which can be expressed as a function of redshift, $\langle n_{\rm H} \rangle$, and the fraction $f_{\rm e}$ of free electrons per hydrogen nucleus in the ionized IGM, via the relation $n_{\rm e} = f_{\rm e}\, \langle n_{\rm H} \rangle\, (1+z)^3$.

The fraction of Lyman-continuum photons escaping their galaxies is one of the most uncertain parameter of cosmic reionization. In this study we use three different models of reionization:

- Model A: the escape fraction is a constant $f_{\rm esc} = 0.2$, we consider here a far-UV absolute magnitude limit of $M_{\rm FUV}^{\rm lim} = -12$.
- Model B: the escape fraction varies with redshift. We consider here a far-UV absolute magnitude limit of $M_{\rm FUV}^{\rm lim} = -12$.

  $$f_{\rm esc}(z) = f_{\rm esc,0} \left(\frac{1+z}{5} \right)^k, \tag{5.16}$$

  with $f_{\rm esc,0} = 0.054$, and $k = 2.4$ (Kuhlen & Faucher-Giguère, 2012 ; Robertson et al., 2013). We consider here a far-UV absolute magnitude limit of $M_{\rm FUV}^{\rm lim} = -12$.
- Model C: We assume the same varying escape fraction than Model B, but we set the far-UV absolute magnitude limit at $M_{\rm FUV}^{\rm lim} = -7$.

5.3.2 Fraction of ionized volume of the Universe

On Fig. 5.6 we show the faction of ionized volume of the Universe as a function of redshift for the different models, black curve is for the Gaussian simulation, colored lines correspond to different level of non-Gaussianitiy, solid lines to the models of reionization A and C, whereas dashed lines correspond to the model of reionization B. At a given redshift, the fraction of IGM ionized is larger for the simulation with the more important level of non-Gaussianity (NG4, yellow lines on Fig. 5.6), this is directly due to the larger number of low-mass galaxies formed in the NG4 simulation, which at each redshift, increases the number of photons available for hydrogen ionization. NG4 always produces an ionizing fraction higher than the other simulations, independently of the reionization model.

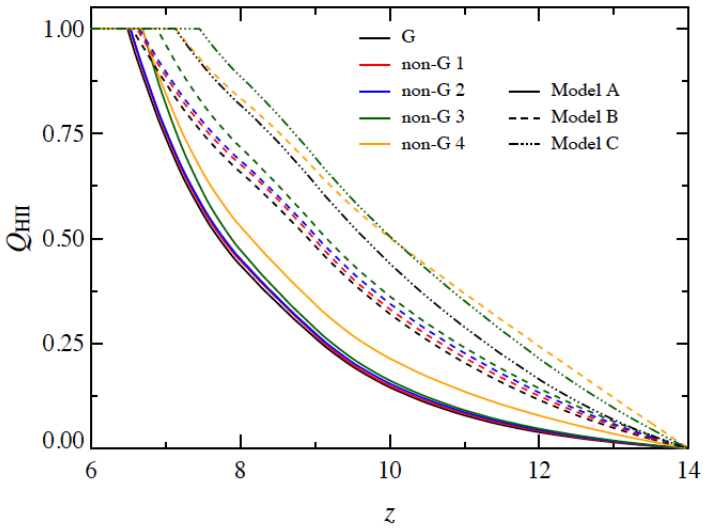

Fig. 5.6 – Ionization fraction of the Universe as a function of redshift obtained for the Gaussian and non-Gaussian simulations: Gaussian simulation in black, non-Gaussian simulation 1 in red, non-Gaussian simulation 2 in blue, non-Gaussian simulation 3 in dark green, non-Gaussian simulation 4 in orange. Types of line refer to different reionization models: A ($f_{\rm esc} = 0.2$ and $M_{\rm FUV}^{\rm lim} = -12$), B ($f_{\rm esc}$ increasing with redshift and $M_{\rm FUV}^{\rm lim} = -12$), C ($f_{\rm esc}$ increasing with redshift and $M_{\rm FUV}^{\rm lim} = -7$).

Model A, with a fixed escape fraction of 0.2, leads to the smallest ionization fraction of the Universe, increasing with decreasing redshift. Model B assumes an escape fraction increasing with increasing redshift, this makes the fraction of ionized IGM to increase more rapidly at high redshift, because more photons are available for hydrogen ionization at higher redshift. This model with the varying escape fraction with redshift, boosts the impact of non-Gaussianities on the Universe reionization. For model C, we only plot the Gaussian and non-Gaussian NG3 results, the limit $M_{\rm FUV}^{\rm lim}$ is higher, the magnitude goes to fainter galaxies, which increases the weight of very faint galaxies, where non-Gaussinities have the most important effect. This results to higher values of the ionization fraction of the Universe.

5.3.3 Electron Thomson scattering optical depth

Optical depth of electrons to Thomson scattering is an important constraint on cosmic reionization, because it depends on the ionizing fraction $\rm Q_{HII}$, and can be measured with CMB photons. It can be written as:

$$\tau_{\rm e} = \int_0^\infty {\rm d}z \frac{c\,(1+z)^2}{H(z)} Q_{\rm HII}(z)\,\sigma_{\rm T}\,\langle n_{\rm H}\rangle\,f_{\rm e} \tag{5.17}$$

with c the speed of light, $H(z)$ the Hubble parameter, $\sigma_{\rm T}$ the cross-section of electrons to Thomson scattering. Planck mission have estimated the optical depth at $\tau_{\rm e} = 0.089 \pm 0.032$ (68%, *Planck*+lensing) (Planck Collaboration et al., 2014) [2], that we show in solid black line on Fig. 5.7, the shaded area shows the confidence limits at 68%.

Model A is shown with the solid lines (the most bottom lines on the figure) assumes a constant escape fraction of 0.2, and leads to an optical depth $\tau_{\rm e}$ lower than the current observational constraints from Planck. We have seen that model B boosts the effect of non-Gaussianities, and we see that also in Fig. 5.7, where the dashed curves for model B are above the solid ones for

[2] The last result of Planck indicates a lower estimate for the optical depth, of $\tau_{\rm e} = 0.066 \pm 0.016$ (Planck Collaboration et al., 2015b), we discuss this in the next section.

model A. The last model C, accounts for fainter galaxies, and therefore boosts even more the effect of non-Gaussian primordial perturbations. This suggests that a higher escape fraction and/or a fainter limiting UV magnitude are required to reionize earlier the Universe and obtain an optical depth in agreement with *Planck* constraints (Planck Collaboration et al., 2014), model C is able to reproduce the observations.

5.3.4 Conclusions

The effect of non-Gaussian primordial fluctuations on the reionization history depends on the adopted reionization model, namely on the escape fraction and the far-UV magnitude limit, which are both uncertain ingredients of the reionization today. We have computed both the ionization fraction of the Universe $Q_{\rm HII}$ and the electron Thomson scattering optical depth, as a function of redshift. For all the reionization models that we have employed, we find that the most non-Gaussian simulation (NG4) produces the bigger effects on these two diagnostics. Therefore the presence of non-Gaussian primordial perturbations leads to a higher ionization fraction, the Universe is reionized earlier compare to a Gaussian model for the primordial perturbations.
At the time of publication, we were also finding that a model of varying escape fraction with redshift, produces a better match to the observational constraint on optical depth, obtained from Planck mission ($\tau_{\rm e} = 0.089 \pm 0.032$ (68%, *Planck*+lensing) (Planck Collaboration et al., 2014)). However, the optical depth measurement of the *Planck* 2015 release, is lower, and estimated to $\tau_{\rm e} = 0.066 \pm 0.016$ (Planck Collaboration et al., 2015b). This would, instead, favor our reionization model A, with a low escape fraction $f_{\rm esc} = 0.2$, and a far-UV magnitude limit of $M_{\rm FUV}^{lim} = -12$.
This could be a potential way of descriminating between primordial perturbation models, through the effect of non-Gaussianties on the optical depth is small in Model A. In any case, for this we first need to understand better the escape fraction ingredient, and to have a clearer observational picture of the faint-end of the galaxy luminosity function of the Universe.

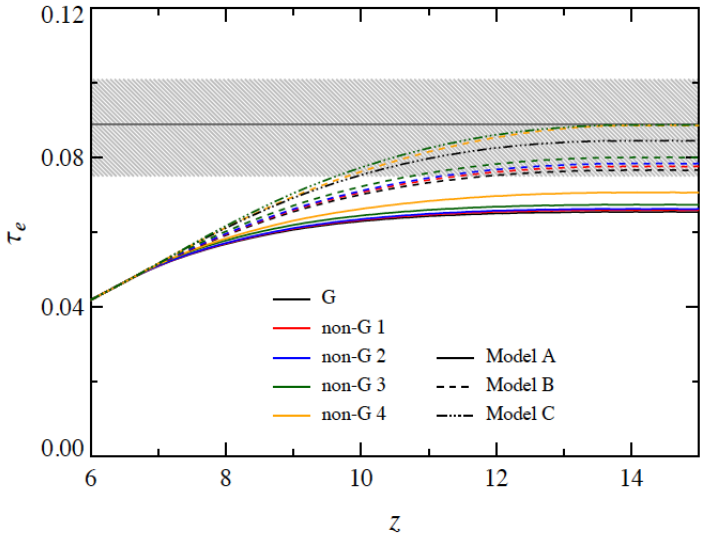

Fig. 5.7 – Optical depth of electrons to Thomson scattering as a function of redshift. The dark-grey solid line indicates the "best-fit" value of τ_e along with the 68 % confidence limits (grey hatched region), obtained by *Planck*. Lines of different colours refer to different simulations:Gaussian simulation in black, non-Gaussian simulation 1 in red, non-Gaussian simulation 2 in blue, non-Gaussian simulation 3 in dark green, non-Gaussian simulation 4 in orange. Types of lines refer to different reionization models: A ($f_{esc} = 0.2$ and $M_{FUV}^{lim} = -12$), B (f_{esc} increasing with redshift and $M_{FUV}^{lim} = -12$), C (f_{esc} increasing with redshift and $M_{FUV}^{lim} = -7$).

5.4 BH formation and growth with primordial non-Gaussianities

The formation and growth of BHs in a cosmology including non-Gaussian primordial density fluctuations can be altered in several ways. In the first place, a larger number of galaxies may be able to form a BH. Most theories (for a review, see Volonteri, 2010, and references therein) link BH formation to the first generation of galaxies, either via the first stars (Pop III stars, stars without heavier elements than hydrogen and helium, Madau & Rees, 2001 ; Volonteri, Haardt & Madau, 2003), or via gas collapse in metal-free halos illuminated by strong photo-dissociating flux (Loeb & Rasio, 1994 ; Bromm & Loeb, 2003 ; Spaans & Silk, 2006 ; Begelman, Volonteri & Rees, 2006 ; Dijkstra et al., 2008 ; Latif et al., 2013a). The formation of BHs in the cosmology we propose could be impacted in two ways; the enhancement at the low-mass end of the galaxy mass function at high redshift could increase the number of halos producing stars, thus boosting the formation of BHs as Pop III remnants. Regarding the DC scenario, the number of halos illuminated by dissociating radiation could also be enhanced because of the higher star formation. On the other hand, the enhanced stellar production would also lead to increased metal pollution, suppressing the “eligibility" of a fraction of halos. Therefore some BH formation mechanisms would be boosted, and other may be suppressed in a way non-trivial to predict.
The growth of BHs is also impacted. There are two channels for BHs to grow in mass: the first one is by BH-BH mergers, the second one by accretion of gas, which can be strongly increased during galaxies merger episodes. Both channels are facilitated in the presence of non-Gaussianities, because of the increased number of low-mass galaxies, which increases the number of galaxy mergers, and of BH mergers as well [3].

[3] A small fraction of merging BHs may however be ejected from the host halos because of the gravitational wave induced recoil, (e.g., Redmount & Rees, 1989 ; Schnittman, 2007) thus lowering the ‘positive’ contribution of BH-BH mergers

We compare the formation and growth of BHs in the Gaussian simulation G and the most non-Gaussian simulation NG4. We investigate the formation of BHs through two formation scenarios: DC (Section 5.4.1) and the remnants of the first generation of stars (Section 5.4.2). We build a model to compute the Lyman-Werner radiation that may impinge on each halo in the two simulations. Looking at all halos evolving under a radiation higher than $J_{21,crit}$, we are able to estimate where DC BHs can form for the two simulations. Similarly, Section 5.4.2 is devoted to the study of the number density of BHs formed via the remnants of the first generation of stars. In Section 5.4.3, we follow the most massive halos in both simulations with the aid of merger trees to perform an analysis addressing the growth of BHs over cosmic time.

5.4.1 BHs formed through direct collapse

In this section, we study whether the probability of forming BHs in the DC scenario (Loeb & Rasio, 1994; Bromm & Loeb, 2003; Koushiappas, Bullock & Dekel, 2004; Begelman, Volonteri & Rees, 2006; Lodato & Natarajan, 2006; Dijkstra et al., 2008; Latif et al., 2013a) is higher or lower when scale-dependent non-gaussianities produce more low-mass halos .
The DC scenario is very appealing as it may lead to the formation of large $10^4 - 10^6\,M_\odot$ seeds, that ease the growth constraints for the sample of $z > 6$ quasars, but required several conditions: atomic cooling metal-free halos, no efficient coolants such as metals or molecular hydrogen, and large mass inflow toward the center of the halos. A strong photo-dissociating radiation (Lyman-Werner, LW, photons $11.2\,\mathrm{eV} < E_{\mathrm{LW\,photons}} < 13.6\,\mathrm{eV}$) is needed to destroy molecular hydrogen and prevent its formation.
DC scenario is a rare process, and recently some studies have shown that it could be even rarer. Latif & Volonteri (2015) use zoomed cosmological simulations of single halos to find that complete molecular hydrogen dissociation may not be necessary, while Latif et al. (2015) and Inayoshi & Tanaka (2015) include the impact of X-rays on molecular hydrogen dissociation and show that X-rays make DC BHs rarer than previously expected, less than the number density of $\sim 1\ \mathrm{Gpc}^{-3}$ necessary to explain the population of $z > 6$ quasars. However, non-Gaussianities provide an enhancement in the low-mass end of the halo/galaxy mass function, therefore they can increase the probability of having halo/galaxy clustered regions, hence boosting the number density of eligible DC regions in the early Universe.

The model

Our model is a modification of D14, where we adopt dark matter simulations to obtain the clustering of halos and their redshift evolution, rather than analytical prescriptions (see Inayoshi & Tanaka, 2015, for a discussion of the uncertainties in clustering assumptions). To identify halos which can potentially form a DC BH we use the LW radiation model of D14, described in the following.
The stellar mass of a dark matter halo M_h is assigned as:

$$M_\star = f_\star M_{h,gas} = f_\star \frac{\Omega_b}{\Omega_m} M_h, \tag{5.18}$$

where $f_\star = 0.05$ is the fraction of gas which turns into stars, $M_{h,gas}$ the gas mass of the halo, M_h the total mass of the halo, Ω_b the baryon density and Ω_m the total matter density. The mean production rate of LW photons per solar mass of star formation is time-dependent, where time is

counted from the time $t_{\rm Myr}$ when a burst of star formation occurs, and expressed as

$$\langle Q_{\rm LW}(t)\rangle = Q_0 \left(1+\frac{t_{\rm Myr}}{4}\right)^{-3/2} \exp\left(-\frac{t_{\rm Myr}}{300}\right) \quad {\rm s}^{-1}\,{\rm M}_\odot^{-1}. \tag{5.19}$$

with $Q_0 = 10^{47}{\rm M}_\odot\,{\rm s}^{-1}$.
The mean production rate is computed one free-fall time after the star formation burst. Assuming that $t_{\rm ff} = \sqrt{3\pi/(32\,G\,\rho)} = \sqrt{3\pi/(32\,G\,200\,\rho_{\rm c})} = \sqrt{3\pi/(32\,G\,200\,(1+z)^3\,\rho_{\rm c,0})}$, the free-fall time can be expressed as:

$$t_{\rm Myr,ff} \sim 83\left(\frac{1+z}{11}\right)^{-3/2}. \tag{5.20}$$

D14 motivate this choice by the requirement that the molecular hydrogen is suppressed throughout the collapse. The expression of $Q_{\rm LW}$ is a fit from STARBURST99 (which used a Salpeter IMF in the range $m_{\rm low}, m_{\rm up} = 1, 100\,{\rm M}_\odot$, an absolute metallicity of $Z = 10^{-3}$ (0.05 ${\rm Z}_\odot$), and a stellar mass of $10^5\,{\rm M}_\odot$). The mean LW luminosity density $\langle L_{\rm LW}({\rm M,t})\rangle$ is a function of the mean number of LW photons (given by the mean production rate of LW photons per solar masses times the stellar mass of the halo), their energy and the escape fraction of these photons (we assume $f_{\rm esc} = 1$ in this study to be able to compare with the fiducial model of D14):

$$\langle L_{\rm LW}({\rm M,t})\rangle = \frac{h\,\langle\nu\rangle}{\Delta\nu}\,\langle Q_{\rm LW}(t)\rangle\,f_{\rm esc,LW}\left(\frac{{\rm M}_\star}{{\rm M}_\odot}\right). \tag{5.21}$$

The flux at a distance r then becomes:

$$\langle J_{\rm LW}(r,{\rm M},{\rm t_{ff}})\rangle = \frac{1}{4\pi}\frac{\langle L_{\rm LW}({\rm M,t})\rangle}{4\pi r^2} f_{\rm mod}(r), \tag{5.22}$$

where the first factor $1/4\pi$ is required to express $\langle J_{\rm LW}(r,{\rm M},{\rm t_{ff}})\rangle$ in ${\rm J}_{21}$ units (erg s^{-1} cm^{-2} Hz^{-1} sr^{-1}). $f_{\rm mod}(r)$ is used to correct the radiation intensity for the extra dimming introduced by the LW horizon (Ahn et al., 2008):

$$f_{\rm mod}(r) = 1.7\exp\left(-\left(\frac{r_{\rm cMpc}}{116.29\alpha}\right)^{0.68}\right) - 0.7 \qquad \text{if } {\rm r_{cMpc}}/\alpha \leq 97.39 \tag{5.23}$$

$$= 0 \qquad \text{otherwise.} \tag{5.24}$$

Where the size is expressed in comoving Mpc (cMpc). We assume in our study that each halo has a 10% probability of being star forming for all redshifts, $P_{\rm SF} = 0.1$, in agreement with Dijkstra et al. (2008). Therefore, only 10% of the halos in the box are considered to compute the radiation intensity, and only 10% of nearby halos contribute to this radiation intensity. Halos are chosen randomly. The experiment is repeated 40 times to take into account the random choice of halos which are flagged as star-forming.

Two main opposite factors influence the number of potential eligible DC regions: the LW radiation intensity coming from nearby star-forming regions illuminating halos and the metal pollution they can be exposed to. Halos irradiated by the LW flux coming from a nearby star forming halo can also be polluted by metals released at the end of the lives of the same stars which produce the radiation. Halos that are metal-enriched would be able to cool too efficiently to be potential DC regions anymore. The metal pollution of a halo can come from three different contributions: (i) the contamination by the halo itself if it is star-forming, (ii) the contamination from the past history of the halo, and (iii) the potential contamination by close star-forming regions because of SN-driven galactic winds which spread metals in their surroundings.

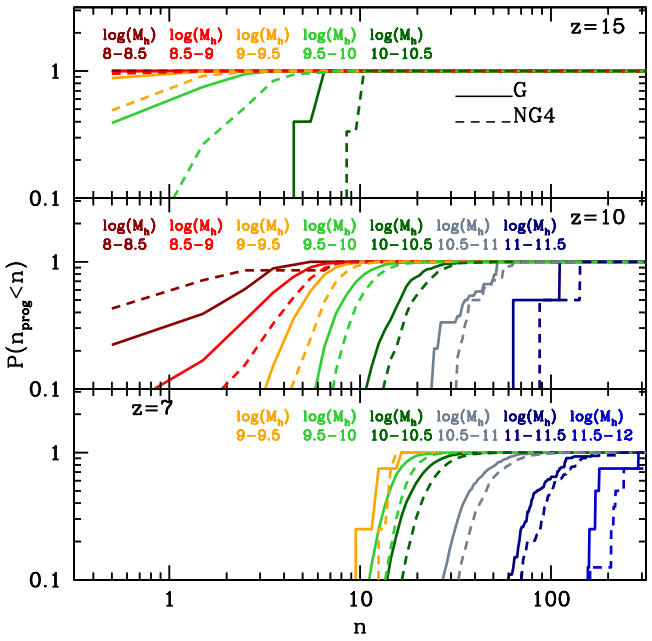

Fig. 5.8 – Probability of having given number of progenitors for halos in a given mass range and at a given redshift ($z = 15$, $z = 10$, $z = 7$ from the top to the bottom panel). The Gaussian simulation is represented with lines, whereas dashed lines are for the non-Gaussian simulation NG4. The typical number of progenitors is larger for NG4 at almost all masses and redshifts.

To account for the first source of pollution (i), we eliminate from the list of potential DC candidates the halos which are star-forming at the current time, with the probability of being star-forming $P_{\rm SF} = 0.1$ as described above. To account for the second contamination (ii), we estimate the probability that a halo had a progenitor which was star-forming in the past. In a hierarchical theory of structure formation, halos are formed through the continuous merging of smaller structures, which may have already encountered supernova-driven metal-enrichment episodes, making the present halo metal-polluted. Therefore the probability for a halo to be metal-polluted increases with the number of their progenitors. For a halo of a given mass and at a given redshift, the number of progenitors is on average larger for NG4 (dashed curves), than for G. For instance, at $z = 15$ halos with mass $10^{10} - 3.16 \times 10^{10}\,{\rm M}_\odot$ have a 50% probability of having less than 5 progenitors in G, and a 50% probability of having less than 10 progenitors in NG4. In order to account for this effect we compute the mean number of progenitors per halo, for different halo mass bins, and redshifts, shown in Fig. 5.8. The mean number of progenitors is derived from the merger trees described in section 5.4.3.

The probability for a halo to be metal-polluted by heritage, i.e. to have metal-polluted progenitors $P_{\rm SF\ progenitor}|_{\rm M_h,z}$ is described by:

$$P_{\rm SF\ progenitor}|_{\rm M_h,z} = P_{\rm SF} \times \langle \text{number of progenitors} \rangle\,|_{\rm M_h,z}. \tag{5.25}$$

We keep as potential DC candidates only those halos which, after Monte Carlo sampling this probability, result metal-free.

Regarding the last source of metal pollution (iii), D14 conclude that metal pollution from nearby galaxies, through galactic winds, could be an important aspect of the halo candidates contamination. Including the redshift dependence of density and free-fall time in the expression provided by D14 for the bubble radius, in proper kpc (pkpc), of a metal polluted bubble one free-fall time after the SF burst:

$$r_{\rm bubble} = 22\,{\rm pkpc} \left(\frac{\rm M_h}{10^{11}\,{\rm M}_\odot}\right)^{1/5} \left(\frac{1+z}{11}\right)^{-6/5}, \tag{5.26}$$

while the radius $r_{\rm rad}$ of the sphere where $\rm J_{21,LW} = 100$ one free-fall time after the star-formation burst scales as:

$$\begin{aligned} r_{\rm rad} =& 126\,{\rm pkpc} \times \left(\left(1 + \frac{83}{4}\left(\frac{1+z}{11}\right)^{-3/2}\right)^{-3/2} \exp\left(-\frac{83}{300}\left(\frac{1+z}{11}\right)^{-3/2}\right)\right)^{1/2} \\ & \times \left(\frac{\rm M_h}{10^{11}{\rm M}_\odot}\right)^{1/2} \left(\frac{J_{\rm 21,LW}}{100}\right)^{-1/2} \left(\frac{f_{\rm mod}}{1}\right)^{1/2}. \end{aligned} \tag{5.27}$$

Fig. 5.9 compares the radius of the metal polluted sphere ($r_{\rm bubble}$) to the sphere ($r_{\rm rad}$) where $\rm J_{21,LW} = 100$ or $\rm J_{21,LW} = 300$.

A correction that accounts for galactic winds coming from nearby star-forming galaxies is then added: if the distance between the halo we are considering as a DC candidate and a SF halo is less than $r_{\rm bubble}$, then the candidate halo would be metal-polluted, hence not an eligible DC region anymore. Fig. 5.9, however, shows that only halos with mass $\sim 10^{11} M_\odot$ at $z > 13$ can act as catalysts of a DC process in a nearby halo if $\rm J_{21,LW,crit} \leqslant 100$. At lower masses and redshift the metal polluted bubble is always larger than the bubble irradiated by sufficiently high UV flux. In our simulations, we do not have any halos with mass $> 10^{11} M_\odot$ at $z \geq 11$ or $> 10^{10} M_\odot$ at $z > 16$, and for lower-mass halos at lower redshift, as shown in Fig. 5.9, the bubble size is larger than the sphere irradiated by $\rm J_{21,LW} = 100$ or $\rm J_{21,LW} = 300$. Adding this correction, therefore, would leave no DC candidate in the simulation box.

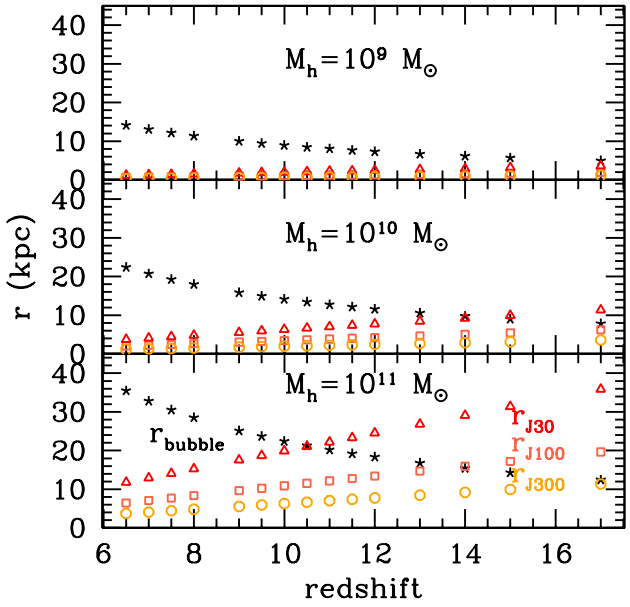

Fig. 5.9 – Metal polluted bubble radius (black stars), and radius of the regions where $J_{21,LW} = 30$ (red triangle), $J_{21,LW} = 100$ (orange squares) or $J_{21,LW} = 300$ (yellow circles) vs redshift for different halo masses ($10^9, 10^{10}, 10^{11} M_\odot$). All quantities are computed one free-fall time after the star-formation burst. Only regions which are at a distance above the distance given by r_{bubble}, and below the r_{rad} are illuminated by the given radiation intensity and are not polluted by galactic winds. For instance, halos with mass $10^{11} M_\odot$ at $z = 15$ can irradiate a nearby halo at a distance of ~ 17 kpc with an intensity $J_{21,LW} = 100$ without polluting it (the metal bubble has reached only a distance of ~ 14 kpc).

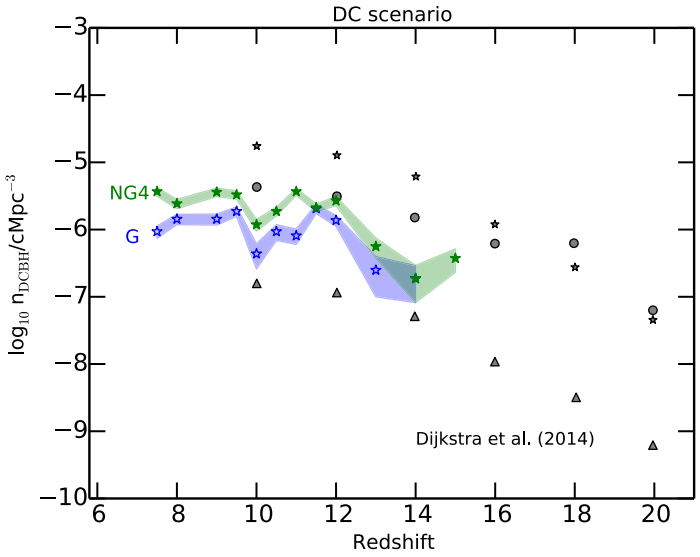

Fig. 5.10 – Number density of DC regions identified at a given redshift in the Gaussian (blue star symbols) and non-Gaussian (green star symbols) simulations. Blue and green stars are derived from a model which does not account for direct pollution by galactic outflows, and where we use the radiation intensity threshold $J_{21,LW,crit} = 300$. Shaded areas represent the Poissonian errorbars derived from 40 realizations of the process. The D14 results are shown in grey symbols: triangles correspond to their fiducial model where $J_{21,LW,crit} = 300$ and account for galactic winds pollution, circles to $J_{21,LW,crit} = 100$, and stars to $J_{21,LW,crit} = 300$ without considering galactic winds pollution. Blue and green star symbols in our study can be compared with star symbols in D14 as they use the same modeling for the radiation intensity (the only differences being the probability of genetic pollution, and the use of an analytical model versus a cosmological simulation). Errorbars represent the uncertainty of the mean value of the number density of BHs.

Results on the number density of potential DC regions

The number density of DC regions obtained in this study is shown in Fig. 5.10, for both G and NG4. Blue star symbols represent the number density of DC regions in G and green star symbols in NG4, using a model where we consider $J_{21,LW,crit} = 300$.

In Fig. 5.10 we also reproduce the results of the three main models used in D14: triangles correspond to their fiducial model where $J_{21,LW,crit} = 300$ and galactic wind pollution is included, circles to a model with $J_{21,LW,crit} = 100$ and galactic wind pollution, and stars to a model with $J_{21,LW,crit} = 300$ without considering galactic wind pollution. Star symbols in our study and in D14 can be directly compared as they use the same modeling for the radiation intensity. The two differences between the two studies are that we use a dark matter simulation to obtain the spatial distribution of halos, rather than an analytical prescription, and that we have derived the probability for a halo to be metal-free from the mean number of progenitors (from the merger tree history) in halo mass and redshift bins, whereas D14 use an analytical prescription. Despite these differences, our study is in good agreement with D14.

It is worth noting that our model does not include a treatment for galactic wind pollution (at the current time or in the past). If we included these effects, as discussed in section 5.4.1, we would not identify any DC regions in our simulation boxes, in either G or NG4. Indeed, if we estimate the number of DC candidates N_{DCBH} in our simulation box from the model by D14, which includes galactic wind pollution, we find that N_{DCBH} is less than one ($N_{DCBH} = n_{DCBH} \times V_{box} \approx 10^{-7} \times V_{box} = 0.04$ with V_{box} the simulation box volume).

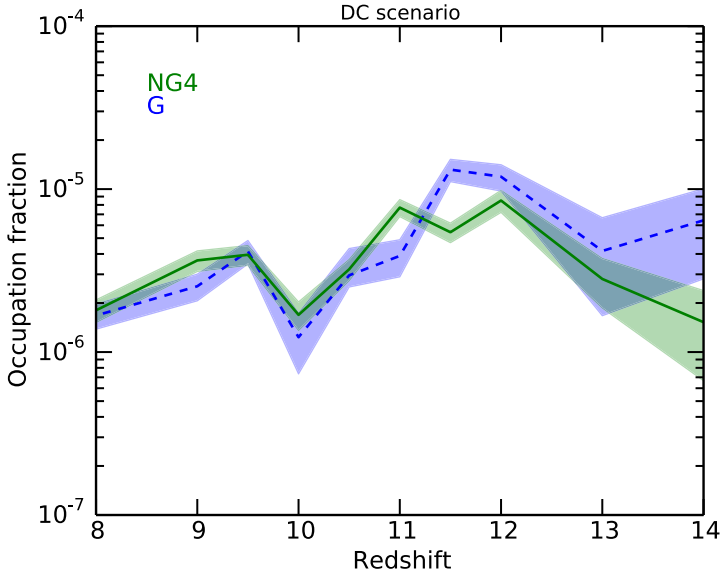

Fig. 5.11 – Halo occupation fraction of newly formed BHs for the Gaussian (dashed blue line) and non-Gaussian (solid green line) simulations, as a function of redshift, for the DC scenario (without taking into account the metal-pollution from galactic winds). This is not a cumulative probability, but the probability that a BH forms in a halo at a given redshift. Errorbars represent the uncertainty of the mean value of the occupation fraction.

With our model, we find that NG4 (green star symbols on Fig. 5.10) host a number density of DC regions slightly larger than the Gaussian simulation (blue star symbols) for the whole range of redshifts, although the differences at the largest redshifts are within the $1-\sigma$ uncertainty. The cumulative number density of BHs at redshift z=7.5 is 1.1×10^{-5} cMpc^{-3} for G, while in NG4 the cumulative number density is almost twice, with 2.3×10^{-5} cMpc^{-3}. The cumulative number densities of the two simulations differ by more than $1-\sigma$.

While the number density of BHs in NG4 is larger, so is the number of halos. In fact, when we estimate the occupation fraction of newly formed BHs, i.e., the fraction of halos as a function of redshift where a BH is potentially formed (Fig. 5.11, this occupation fraction is not cumulative, i.e., we calculate it for newly formed BHs only) we find that the probability of a halo being seeded with a BH is almost identical in the two simulations, although at the highest redshifts the occupation fraction in the Gaussian case is slightly above the non-Gaussian one. This can be explained as follows: since the number of progenitors is larger in the non-Gaussian simulation (see Fig. 5.8), halos in the non-Gaussian simulation have a higher probability of being metal polluted because of heritage pollution. In summary, scale-dependent non-gaussianities boost the overall number of potential DC BHs in the Universe, but not the probability that a halo hosts or not a BH.

In the vicinity of the two most massive halos

The analysis presented in the previous section highlights the difficulty of finding a significant number of DC regions. In order to have a clearer picture of the interplay between irradiation and metal-pollution in the model by D14, we focus here on the halos neighbouring the two most massive halos in our simulation volume. The reason for this choice is that according to the model described in section 5.4.1, only halos more massive than 10^{11}M$_\odot$ can provide an intensity higher than $J_{21,LW} = 300$ at a distance of 10 pkpc one free-fall time after the star formation burst.

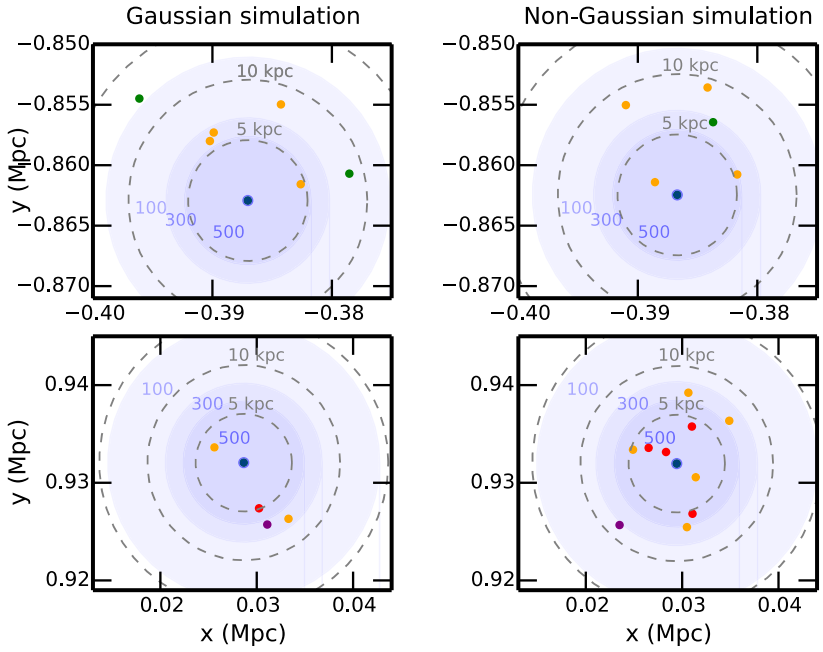

Fig. 5.12 – The two most massive halos of the Gaussian and non-Gaussian simulations at redshift z=10 are presented in blue dots. On the top left panel, we show a halo with a mass of 1.17×10^{11} (ID 54335), on the top right 1.65×10^{11} (ID 61371), on the bottom left 1.22×10^{11} (ID 104966) and no the bottom right $1.75 \times 10^{11} M_{\odot}$ (ID 118759). Indicative radii of 5 kpc, 10 kpc, and 15 kpc are shown with grey dashed lines in the (x, y) plane. The radiation intensity from these massive halos is shown in blue contours, the innermost area has intensity higher than $J_{21,LW} = 500$, the second by $J_{21,LW} = 300$ and outermost $J_{21,LW} = 100$. Finally, the projection of halos in the plane (x, y) is shown in colours indicating the radiation intensity they experience (in 3D): in green $J_{21,LW} < 100$, in orange $J_{21,LW} \geq 100$, in purple $J_{21,LW} \geq 300$, in red $J_{21,LW} \geq 500$.

Critically, a common critical intensity value suggested by simulations (Bromm & Loeb, 2003; Sugimura, Omukai & Inoue, 2014; Latif & Volonteri, 2015; Regan, Johansson & Wise, 2014) is $J_{21,LW,crit} \sim 10^3$.

We therefore select the two halos more massive than $10^{11} M_{\odot}$ at redshift $z = 10$ in the G and NG4 simulations. These two halos match one another in the two simulations. Only these two halos are able to produce sufficient radiation to efficiently dissociate molecular hydrogen on ~ 20 pkpc distances. We consider all the halos inside a 20 pkpc radius centred on each of the most massive halos and compute the radiation intensity illuminating them.

In Fig. 5.12, halos shown in red are illuminated by a radiation intensity higher than $J_{21,LW} = 500$. The number of halos is higher for the non-Gaussian simulation, as well as the number of halos exposed to a high radiation intensity. In NG4, which forms more low-mass halos, the potential number of DC regions is increased. However, if we account for SN-driven metal-pollution using Eq. 5.26, 1 Myr after the SN explosion, the metals in the massive halo are already spread over 4 pkpc. After 2 Myr, the metal-polluted sphere reaches 5-6 pkpc. At this time all halos illuminated by a LW intensity $J_{21,LW} > 300$ are inside this sphere and therefore polluted by metals, making the DC process unfeasible.
Within the formalism we have adopted here, we can not identify a difference between G and NG4. However, this model includes several simplifications, for instance the expansion of the metal bubble in a real Universe may not be spherical, and P_{SF} may well be a function of redshift and

halo mass. We argue that the non-Gaussian simulation, having more low-mass halos irradiated by a strong UV flux, could represent a more favourable environment for this scenario.

5.4.2 BHs formed from the remnants of the first generation of stars.

Pop III star remnants is another popular scenario to explain the formation of BH seeds in the early Universe (Madau & Rees, 2001 ; Volonteri, Madau & Haardt, 2003). BHs are predicted to form in metal-free mini-halos ($M_h \sim 10^5\,M_\odot$) at redshift $z = 20 - 30$ from the remnants of the first generation of stars. If some of these stars are sufficiently massive ($> 260\,M_\odot$), BHs retaining up to half the stellar mass are formed, leading to the formation of a BH seed of $\sim 100 M_\odot$(Fryer, Woosley & Heger, 2001).
In this section we want to estimate the number density of BHs and the fraction of halos where a BH can form via the Pop III stars scenario for G and NG4. We stress that our simulations do not have the resolution needed to resolve mini-halos, therefore the following experiment can only be used to assess trends. However, since the model we consider in this work has stronger non-Gaussianity on smaller scales (and thus on less massive halos), we can expect that the impact of non-Gaussianities on mini-halos can be even larger than what we find (in the following paragraphs) for more massive halos.
According to the PopIII star scenario, only metal-free halos can host the first generation of stars. We therefore identify all the star-forming and metal-free halos in the two simulations using the same approach described in section 5.4.1. The probability of a halo being star-forming is again $P_{SF} = 0.1$, identical for all redshifts, meaning that only 10% of the halos are selected in the first place as potential hosts of a Pop III remnant BH seed. Additionally, we ensure that these halos are not metal-polluted from the past history of the halo (heritage pollution), nor from galactic winds coming from neighboring halos at a coeval redshift.
Regarding the second aspect, we account for the probability of having a star-forming neighbor $P_{SF} = 0.1$ on a distance scale r_{bubble} defined in Eq. 5.26, this distance is redshift and halo mass dependent. We also consider the probability for the neighboring halos (on the same distance scale) to have spread metals in their past history, which could also have introduced metals in the considered halo, making it ineligible to form PopIII star in a metal-free environment. We perform 40 realizations of the model.

Fig. 5.13 represents the mean number density of potential BHs formed via the Pop III star remnant scenario for the two simulations (Gaussian in blue, non-Gaussian in green). The trends of the two curves are similar, but NG4 hosts more BHs. The enhancement in the number density of BHs increases with redshift, while at $z = 7.5$ the two curves are almost overlapping. However the cumulative number density of BHs for NG4 is again almost twice as large (G: 0.17 cMpc^{-3}, NG4: 0.34 cMpc^{-3}). The cumulative number density in the two cases differs by more than $1 - \sigma$. The occupation fraction of halos where BHs form via this scenario is shown in Fig. 5.14. The blue line indicates the occupation fraction for G, and the green line NG4. We note that the occupation fraction is almost identical for the two simulations: it is $\sim 10^{-1}$ at $z = 17$ and drops to $\sim 10^{-2}$ at $z = 8$ before increasing again (we account for forming BHs only, not the cumulative occupation fraction). The Gaussian case is slightly above the non-Gaussian one. This can be explained with the same arguments as those discussed for the DC case, and, moreover, halos in NG4 have also a number of neighbours slightly higher than halos in G, increasing the probability of being polluted by galactic winds. As noted above, our simulations do not resolve mini-halos, but since our model for f_{NL} enhances the number of low-mass halos at a given redshift, there will be more mini-halos in the non-Gaussian case, favouring the formation of PopIII stars at even higher redshifts than those considered here. Therefore, also at higher redshift, the number of

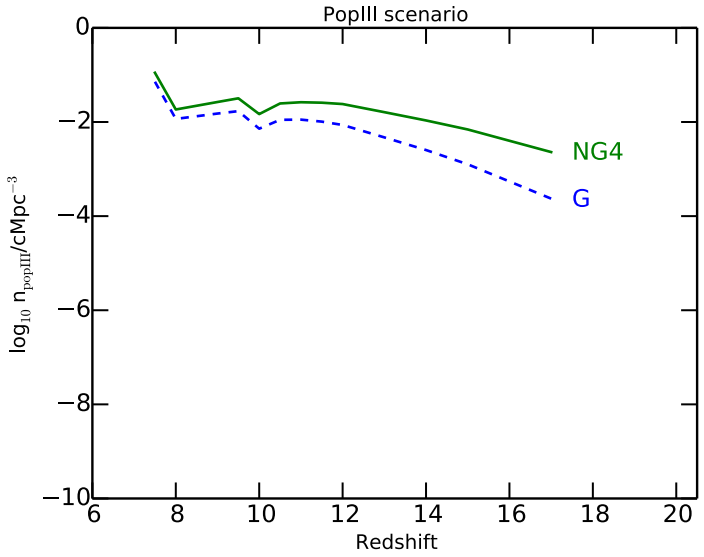

Fig. 5.13 – Number density of Pop III star remnant BHs formed at a given redshift for the Gaussian (dashed blue line) and the non-Gaussian (solid green line) simulations. Errorbars represent the uncertainty of the mean value of the number density, the uncertainty is here too small to be seen.

BHs formed throughout the PopIII remnant scenario would be higher in the non-Gaussian case until metal pollution starts dominating the environment. Our results can therefore be considered a lower limit to the enhancement in the BH population.

5.4.3 BHs in the most massive halos at $z = 6.5$

We now turn to exploring the possibility that the different growth histories of halos in Gaussian and non-Gaussian models affect the assembly of BHs at the high mass end. Using merger trees made with TreeMaker, we derive the history of the most massive halos in all simulation boxes at redshift $z = 6.5$. From the mass evolution of these halos, we derive the evolution that a hypothetical BH in these halos could have.

To probe the *cumulative* effect that a different early evolution has on the BH population, we evolve the BH masses in the merger trees. Rather than assigning a BH mass simply based on the halo mass at a given time we seed the highest redshift progenitor halos of the $z = 6.5$ halos with BH 'seeds' and evolve their mass over cosmic time adopting simple prescriptions. Our goal is to explore how the dominant differences in halo growth histories caused by non-Gaussian initial conditions affect the assembly of the BHs. The main diagnostics will be the mean BH mass as a function of time and the number of BHs with mass above some minimum threshold. The latter diagnostic is important as we are currently able to detect only the most massive BHs ($\sim 10^9\,\mathrm{M}_\odot$). Even in the future, at such high redshift, we will always pick the most massive BHs, although the mass threshold will decrease. For instance, the future X-ray mission ATHENA[4] is expected to be able to detect BHs with masses above $10^6 - 10^7\ \mathrm{M}_\odot$ up to $z \sim 8 - 10$ (Aird et al., 2013).

Specifically, first we analyse the merger trees of all halos with mass $> 10^{11}\,\mathrm{M}_\odot$ at $z = 6.5$ to find the effects of non-Gaussianities. There are 125 such halos in simulation G and 133 in NG4. The main differences we find in the halo growth are in the total number of progenitors, and in the number of mergers involving similarly sized halos, i.e., with mass ratio > 0.1 ('major mergers' hereafter). We perform a Kolmogorov-Smirnov test (Fig. 5.15) and find that the probability that

[4] http://sci.esa.int/cosmic-vision/54517-athena/

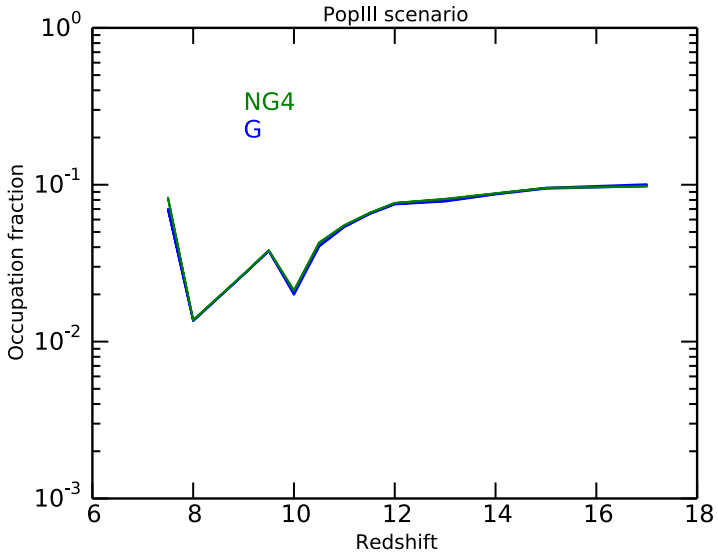

Fig. 5.14 – Newly formed BH-halo occupation fraction for the Gaussian (blue line) and the non-Gaussian (green line) simulations, as a function of redshift, for the remnants of the first generation of stars scenario. As in Fig. 5.11, this is not a cumulative probability. Errorbars represent the uncertainty of the mean value of the occupation fraction, the uncertainty is here too small to be seen.

the progenitor number distributions come from the same parent distribution is less than 10^{-6}. The evidence for differences in the major merger distributions is weaker, with a probability of 0.14, because of the small-number statistics. The mean number of progenitors for the $> 10^{11}\,\mathrm{M}_\odot$ at $z = 6.5$ halos is 95 for model G and 120 for NG4. The mean number of major mergers is 16 (G) and 20 (NG4).

We then model, in a simplified way, the evolution of hypothetical BHs over the cosmic history of these halos. Two main factors linked to the different number of halos and progenitors in G and NG4 would influence the BH distribution (masses and number) at $z = 6.5$: (i) how many halos host BHs, and (ii) the number of major mergers for merger-driven BH growth. Regarding the first point, it is expected that BH formation is not ubiquitous in all halos as specific conditions are required (see sections 5.4.1 and 5.4.2 and Volonteri, 2010, for a review). Therefore, if each halo has a given probability of hosting a BH, the larger the number of the progenitors of a halo, the higher the probability that a halo without a BH acquires a BH through a merger with a halo seeded by a BH (Menou, Haiman & Narayanan, 2001). Regarding the second point, major galaxy mergers trigger torques that destabilize the gas in a galaxy, causing nuclear inflows that trigger BH accretion episodes (Kauffmann & Haehnelt, 2000 ; Hopkins et al., 2006). If a BH is hosted in a galaxy that experiences a larger number of major mergers, its growth will be boosted.

To test how the different merger histories of Gaussian and non-Gaussian models affect the BH growth in this way, we perform a first experiment where we assume that each halo starts with a $10^2\mathrm{M}_\odot$ BH, and, after each major merger, the BHs also accrete at the Eddington limit, assuming a radiative efficiency of 10%, for one dynamical time (Tanaka, 2014), while the masses of the BHs in the merging halos are summed. The results are shown in Fig. 5.16, top panel. NG4 has a consistently higher mean BH mass and a higher number of BHs with mass above a minimum threshold, e.g., $10^4\,\mathrm{M}_\odot$ at $z = 6.5$. Simulation NG4 hosts 58 BHs with mass $> 10^4\,\mathrm{M}_\odot$ at $z = 6.5$, while G hosts 57. The BHs with mass $> 10^5\mathrm{M}_\odot$ are 8 and 3 respectively.

We perform a second experiment (Fig. 5.16, middle panel) where we assume that each halo has a 10% probability of hosting a $10^2\,\mathrm{M}_\odot$ BH when it enters the merger tree. We use here the

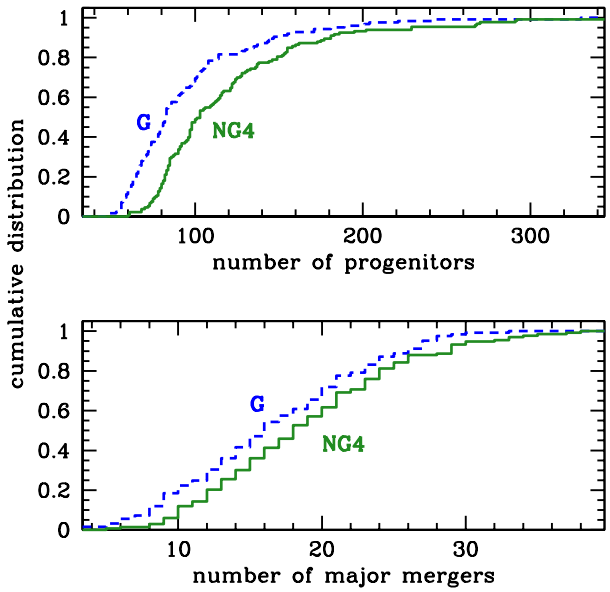

Fig. 5.15 – Cumulative distribution of the number of progenitors (top) and halo mergers with mass ratio > 0.1 for all halos with mass $> 10^{11}\,M_\odot$ at $z = 6.5$ in the Gaussian (G, dotted blue histogram) and the non-Gaussian (NG4, green, solid histogram) simulations. The probability that the progenitor distributions come from the same parent distribution is less than 10^{-6}. The evidence for differences in the major merger distributions is weaker, 0.14.

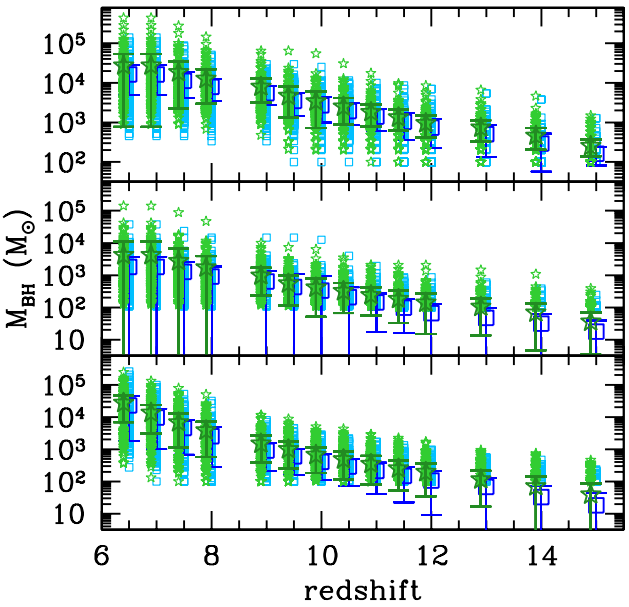

Fig. 5.16 – Top: Evolution of the BH mass for all halos with mass $> 10^{11}\,M_{odot}$ at $z = 6.5$, assuming that accretion is only merger-driven. Middle: assuming the probability that a halo hosts a BH is 10%, and accretion is only merger-driven. Bottom: assuming that the probability that a halo hosts a BH is 10% and BHs grow in mass through random accretion. Simulations: G (blue asterisks); NG4 (green stars). Each halo is represented by a point at each simulation output, and we calculate mean and variance at each output redshift (shown as a larger point with errorbar).

occupation fraction of the Pop III star remnant case in order to have some statistics. We note that if we increased the seed mass by a given factor, the results shown below would scale by the same factor. Given the results of sections 5.4.1 and 5.4.2, we adopt the same probability for both G and NG4. If the main halo already hosts a BH, the masses of the BHs in the main and merging halo are summed. BHs also accrete at the Eddington limit for one dynamical time after each major merger. Simulation NG4 has 12 BHs with mass $> 10^4\,\mathrm{M}_\odot$ at $z = 6.5$, while G has 3. Above $10^5\,\mathrm{M}_\odot$ are 1 and 0 respectively. By $z = 6.5$ 80% of the halos host a BH in G, while this fraction is 90% for NG4, despite starting with the same occupation fraction of 10% in each case (see Menou, Haiman & Narayanan, 2001).

The final experiment is to forego major-merger driven accretion and assign to each BH an accretion rate based on a distribution probability calculated in a large scale cosmological simulation, Horizon-AGN (Dubois et al., 2014). In Fig. 5.16, bottom panel, we show a model where we assume that each halo has a 10% probability of hosting a $10^2\,\mathrm{M}_\odot$ BH when it enters the merger tree, and if the main halo already hosts a BH, their masses are summed. The BHs also accrete over a timestep with an accretion rate randomly drawn from the distribution of Eddington rate, λ, calculated from all the BHs at $6 < z < 8$ in the Horizon-AGN simulation: $\mathrm{dN/dlog}\lambda = 10^{(\log\lambda+2)}/10^2$. In this case, simulation NG4 hosts 67 BHs with mass $> 10^4\,\mathrm{M}_\odot$ at $z = 6.5$ while G hosts 51. The BHs with mass $> 10^5\,\mathrm{M}_\odot$ are 10 and 9 respectively. Again, at $z = 6.5$ 80% of the halos host a BH in G, while this fraction is 90% for NG4.

The main conclusion is that in NG4 the number of the most massive BHs is larger, and the mean BH mass at $z = 6.5$ increases by 0.08, 0.22 and 0.36 dex for the third, first and second experiment respectively. In the Eddington rate formalism, a mass difference of a factor of two corresponds to a change in the growth time of 70%, because of the exponential dependence. While in all the experiments the statistical significance of the difference between G and NG4 is low (they are compatible within $1 - \sigma$) the trends are always consistent: if all conditions for BH growth are equal, i.e., BH physics is the same, a population of BHs in NG4 would grow faster and have more more massive BHs. In the example shown here, however, the small high-redshift seeds do not grow much more than to a few $\times 10^5\,\mathrm{M}_\odot$ at $z = 6.5$. We have tested the difference with a case where the initial seed mass is $10^5\,\mathrm{M}_\odot$ (keeping all other assumptions equal), and we find that, in that case, BHs can grow up to several $10^8\,\mathrm{M}_\odot$, less than the masses of $z > 6$ quasars. This is not surprising, given the absence, in our simulation box, of the sufficiently massive dark matter halos, $\sim 10^{13}\ \mathrm{M}_\odot$ expected to be hosting these extremely massive BHs. To explain the observed quasars, with mass $> 10^9\,\mathrm{M}_\odot$, large seeds or additional growth channels (e.g., super-Eddington accretion), and sustained accretion at the Eddington level (Di Matteo et al., 2012; Dubois et al., 2012b) would be needed.

5.4.4 Conclusions

In this section, we have addressed the formation and the growth of supermassive BHs in the presence of scale-dependent non-Gaussianities. We use two identical simulations except for their initial conditions, with either Gaussian or scale-dependent non-Gaussian primordial perturbations ($f_{\mathrm{NL}}(k) = f_{\mathrm{NL},0}\ (k/k_0)^\alpha$, with $\alpha = 4/3$ and $f_{\mathrm{NL},0} = 10^4$). The introduction of these non-Gaussianities on galactic scales, consistent at larger scales with the Planck results, produces an enhancement in the low-mass end of the halo and galaxy mass functions, increasing with redshift. As a consequence, changes in the BH population arise as well. We explore the impact of scale-dependent non-Gaussian primordial perturbations on two models of BH formation, and on the growth of the putative BHs. Sherkatghanad & Brandenberger (2015) also investigate local-type non-Gaussianities, i.e. with both skewness (f_{NL}) and kurtosis (described by the parameter

$g_{\rm NL}$), in the context of BH formation. They do not include scale-dependent non-Gaussianities, and conclude that non-Gaussianities do not strongly affect the number density of dark matter halos at high redshifts (and of BHs as a consequence). This is in agreement with our previous work (Habouzit et al., 2014) where we showed that non-Gaussian models closest to a non-scale dependent $f_{\rm NL}$ do not show significant differences in halo and stellar mass functions compared to the Gaussian model. On a related note, Hirano et al. (2015) find that varying the slope of the primordial power spectrum impacts the formation of structures as well: an enhanced power spectrum at small length scales (or blue-tilted power spectrum) pushes to the formation of the first stars at much higher redshifts, and the higher CMB temperature leads to more massive stars, which can be precursor of massive BHs.

The formation of DC BHs is predicted to happen in metal-poor regions illuminated by a UV radiation intensity higher than a critical value (here we use $\rm J_{21,LW,crit} = 100$). We have implemented a model to identify these regions, inspired by D14, to compute the radiation intensity emitted from galaxies forming in dark matter halos. The increase in the galaxy mass function, particularly at the low-mass end, in the non-Gaussian simulation leads to a larger number density of potential DC regions. This is due to the increase of the number of galaxies for two reasons, there are statistically more regions that can collapse forming a BH, but also because more galaxies can act as radiation sources to illuminate dense regions where the collapse may happen. Conversely, the presence of more galaxies can also lead to a stronger metal enrichment, making a halo unavailable for the DC process. This last aspect has been difficult to study: we have implemented a model for the metal-pollution coming from close star-forming regions, in the current time and the past history of the regions. Taking into account the pollution coming from galactic winds reveals a metal pollution of all the previously identified DC regions, making any comparison between the Gaussian and non-Gaussian simulations impossible. A larger simulation box would be needed to test in further detail the impact of the enhancement in the low-mass end of the galaxy mass function on the metal-enrichment of potential DC regions by galactic winds.

However, as the critical value for the radiation intensity is still highly debated, and may be as high as $\rm J_{21,LW,crit} = 10^3$, only halos as massive as $10^{11}\rm M_\odot$ or larger could provide sufficiently high radiation to suppress molecular hydrogen in their neighbourhood. The number of neighbours in the vicinity of the two halos more massive than $10^{11}\rm M_\odot$ in the non-Gaussian simulation is larger, up to a factor 4, for halos seeing a radiation intensity $> J_{\rm 21,LW} = 500$ in the example shown in Fig. 5.12. This illustrates the effect of primordial non-Gaussianities in increasing the number density of DC regions. Metal pollution remains, however, a concern. Two factors may alleviate the importance of metal pollution: in the first place, SN bubbles may not be spherical, as assumed in D14 and our calculation, once a realistic gas and DM distribution is taken into account. Additionally, we and D14 have assumed, following Madau, Ferrara & Rees (2001) a simplified evolution of the bubble radius (see also section 5 in D14). A third approximation we and D14 have made is that the probability of a halo being star-forming is constant with redshift and halo mass.

A second path for BH formation we have explored hinges on the remnants of the first generation of stars, in metal-free mini-halos. In order to test the impact of primordial density perturbations on this scenario, we have modified the scheme we have adopted for the direct collapse scenario (same probability for a halo to be star-forming, and the same contributions for the metal-pollution, namely pollution from heritage of the considered halo itself, and from

galactic winds coming from neighboring star-forming halos). Only star-forming and metal-free halos are considered as eligible site to form BHs. While our simulations have a much lower resolution than needed to resolve mini-halos, we can at least identify some trends. We find that non-Gaussianities do not have a strong effect on the newly formed BH-halo occupation fraction, in both cases the occupation fraction drops from 10^{-1} at $z = 20$ to 10^{-2} at $z = 8$. Conversely, the number density of BHs is increased at the highest redshifts in the presence of non-Gaussianities, up to one order of magnitude. The larger number of progenitors and neighbours in the non-Gaussian simulation imply a larger probability for a halo to be/become polluted by metals.

The growth of supermassive BHs is also altered when considering non-Gaussianities. After deriving the merger history of the most massive halos at $z = 6.5$ in both the Gaussian and non-Gaussian simulations, we study the evolution of BHs in massive halos down to $z = 6.5$. To investigate the cumulative effect over cosmic times on the BHs assembly, we model the growth of BHs in three different ways. Different probabilities for a halo of hosting a seed BH, and different accretion models (either each BH accretes at the Eddington limit for a dynamical time after a major merger or using an accretion rate based on a distribution probability derived from a large-scale hydrodynamical simulation) are adopted. We have not included in our models the effects of “kicks" caused by asymmetric emission of gravitational waves, which have been proposed to be possibly responsible for ejecting BHs from halos with shallow potential wells, thus halting or reducing the growth of high-redshift BHs hosted in small halos (e.g. Yoo & Miralda-Escudé, 2004 ; Volonteri & Rees, 2006 ; Tanaka & Haiman, 2009). This effect, however, seems to affect less than 10% of binaries and it becomes negligible for BH mergers at $z < 10$ (Volonteri & Rees, 2006). We find that non-Gaussianities imply a larger number of massive BHs and also an increase in the mean BH mass (up to 0.36 in the most favourable experiment). A population of supermassive BHs will then grow faster and to higher masses in a universe with scale-dependent non-Gaussian primordial density fluctuations. If the seed masses are similar to those of PopIII star remnants, BHs will not be able to grow above few $\times 10^5\,\mathrm{M}_\odot$ by $z = 6$. However, our simulations do not resolve mini-halos, and we may underestimate the growth of seeds at earlier times. We argue that, in a simulation resolving mini-halos, BHs would have formed earlier through the PopIII remnant scenario, leading to a longer time for them to grow in mass. If we assumed that PopIII remnant seeds with mass $100\,\mathrm{M}_\odot$ form at $z \sim 30$ in halos unresolved in our simulations, they would have grown, assuming, optimistically, constant growth at the Eddington rate (but see Johnson & Bromm, 2007 ; Alvarez, Wise & Abel, 2009 ; Milosavljević, Couch & Bromm, 2009 ; Park & Ricotti, 2011) to $\sim 10^3$ $\mathrm{M}_\odot$ by $z = 18$, where we start our analysis. The final BH mass at $z = 6$ would then be $\sim$ one order of magnitude larger, a few $\times 10^6\,\mathrm{M}_\odot$, still short of the $\sim 10^9$ $\mathrm{M}_\odot$ required. The very limited growth obtained for the PopIII remnant case suggests that large seeds or super-Eddington accretion (see Volonteri, Silk & Dubus, 2015, and references therein) may be necessary for successful BH growth. We have done the same experiments on BH growth starting with initial 10^5 $\mathrm{M}_\odot$ BH masses (not shown here, but see section 5.4.1). In this case we found that it is much easier for BHs to grow to higher BH masses, but still only to several $10^8\,\mathrm{M}_\odot$. This is not unexpected, because our simulation box does not contain the very rare and biased dark matter halos with masses $\sim 10^{13}$ $\mathrm{M}_\odot$ believed to be hosting these extreme BHs.

Note:
The relative coherent motions between baryons and dark matter, that we call streaming, could in principle affect the formation of supermassive black holes by both the popIII remnant scenario and the direct collapse one. Indeed, the star formation can be delayed by few Myr in mini halos,

the abundance of popIII star regions can also be decreased because the virial mass needed for H_2 cooling is increased. The delay in star formation can favor the direct collapse scenario. However, Latif, Niemeyer & Schleicher (2014) use simulations of halos with different streaming velocities and show that for halos more massive than $10^7\,M_\odot$, the effect is negligible (it is more difficult for the gas to escape from a deep potential well) compared to mini-halos. Our simulations do not resolve mini-halos, and in any case we expect the impact of streaming velocities to be the same in the Gaussian and non-Gaussian simulations. Also, the conditions where streaming velocities can have an impact on the BH formation are very rare (very high velocity >90 km s-1, and so very high redshift as the streaming velocity decays with time), therefore the consequences on black holes formation are, in conclusion, thought to be small, and should not affect the difference found in the number density of black holes between the Gaussian and non-Gaussian simulations. Regarding the growth of supermassive black holes, streaming velocities are also thought to have a negligible effect (Greif et al., 2011 ; Naoz, Yoshida & Gnedin, 2013 ; Tanaka, Li & Haiman, 2013).

Chapter 6

Conclusions

The main subject of this thesis is the formation of supermassive BHs. The thesis aims at understanding the population of BHs in today's galaxies, and to determine their properties, by answering some of the following questions. Why do some galaxies host a BH, and some others lack BHs? What is the minimum mass of a BH? What are the physical processes responsible for the formation of BHs? What is the minimum galaxy mass where a BH can be found? How many low mass BHs exist in the high redshift Universe? Can we explain the population of BHs in local galaxies, or the population of high redshift quasars with the current theoretical BH formation models?
During the last three years, I explored BH formation in the early Universe, I particularly focussed on the three following aspects:

- I have studied the formation of BHs in low-mass galaxies, which constitute the most promising laboratory of pristine environment we can observe today. I have presented the results of this investigation in chapter 3.
- In the second part of this thesis, in chapter 4, I have explored the feasibility of the DC BH formation model.
- BH formation and growth has been studied in a cosmology with non-Gaussian primordial density perturbations in chapter 5.

In the following, I will briefly summarize the purpose of these investigations, and the different results we have obtained, and suggest some future extensions. During my thesis, I implemented, performed and analyzed full-physics cosmological hydrodynamical simulations with the code Ramses, which is a hydrodynamical adaptive mesh refinement code. For the last project (chapter 5), I analyzed a set of 5 cosmological simulations, run with the code Gadget 2, which is a smoothed particle hydrodynamics code. We have explained the main features of these two codes in chapter 2.

Supermassive black holes are found in many galaxies, from massive galaxies to dwarf galaxies, when some other galaxies seem to not host BHs. BHs are not only present in our local Universe, the observation of quasars, powerful objects powered by massive BHs, have confirmed the presence of BHs in the early Universe too, less than 1 Gyr after its beginning. The observation of quasars in the early Universe, gave us the first insight of BH formation: BHs must have been formed in the early Universe to acquire masses above a billion solar masses within 1 Gyr.

Today, our ability of observing the Universe is increasing, we are pushing the observational limits, both in terms of local low-mass galaxies, and high redshift galaxies. We are in a promising

period, where observations will provide us new constraints on BH formation. Low-mass galaxies are among the most pristine galaxies that we can observe locally, and therefore they can provide us crucial information on BH formation, in analogy with “galactic archeology" for metal enrichment and star formation histories. BH seeds form in the very early stages of the Universe, most of their initial properties are erased by accretion, dynamics and mergers of their host galaxies. Dwarf galaxies, which are thought to experience a quieter growth history, may have conserved the initial properties of BHs. Moreover low-mass galaxies can also help us to distinguish among BH formation scenarios by two main diagnostics: BH mass measurement is a direct clue of the initial BH seed mass, and the occupation fraction of these galaxies is predicted to differ for different BH formation models.

However, the modeling of BH formation processes in simulations is still limited. For example, most of the cosmological state-of-the-art simulations seed only massive halos with a fixed BH mass of $\sim 10^5\,\mathrm{M}_\odot$. We have, instead, implemented a new method to seed cosmological simulations in the code Ramses, based on local environment properties, following theoretical prescriptions of the PopIII remnants and nuclear stellar clusters BH formation models. BH form in dense, collapsing, bound, and metal-poor regions. The code computes the mass of each BH individually, according to the density of the region, and a given IMF of PopIII stars.

To test our BH formation model against observations, we have compared our simulated BH sample to the local sample of Reines & Volonteri (2015) ($z \leqslant 0.055$). With this comparison, we have seen that our high redshift simulated BHs connect to the low redshift sample of local BHs. However, some of the simulated BHs are stuck at low-mass, some of them however are able to grow up to $\sim 10^6\,\mathrm{M}_\odot$ by redshift $z = 3$ and to connect the observations. We find that SN feedback has a strong impact on the formation and early growth of the simulated BHs. A stronger SN feedback implementation produces galaxies with stellar masses closer to those predicted by the relation with halo mass, derived by the empirical model of Behroozi, Conroy & Wechsler (2010). BHs in low-mass galaxies, under the impact of such strong SN feedback, clearly have a very hard time to grow, because these galaxies have shallow potential wells, and SN feedback is sufficient to energize gas and suppress gas accretion onto BHs. Our BH formation model, combined with the prescription of the strong SN feedback, seems to be in better agreement with the AGN luminosity function and the lack of AGN detections in high redshift galaxies (Willott et al., 2010b ; Weigel et al., 2015).

Furthermore, the hard X-ray luminosity of the most luminous BHs in our simulated sample, is similar to the luminosity of six Lyman-Break Analogs (Jia et al., 2011b). Properties of LBAs, are very similar to their high redshift analogs, the Lyman Break Galaxies, in terms of metallicity, morphology, star formation, etc. Therefore LBAs could be a promising new laboratory for us to study the properties of BHs in galaxies, which look like primordial ones, but are much closer to us, thus easier to observe in detail. Our comparison, as it is today, is obviously lacking statistics, but we would like to continue investigating the comparison between our BH formation model and the LBAs population. This comparison would help us to investigate in more detail the population of BHs in LBGs. Generally very few AGN are observed in these galaxies. The identification of AGN in LBGs is difficult even for those that show AGN signatures, e.g. the detection of CIV or HeII can hint either a low-luminosity AGN, as well as a population of hot young stars (Stark et al., 2015 ; Pallottini et al., 2015), the same problem is actually observed for LBAs. Indeed these galaxies often show evidences for composite system, intense starburst or/and obscured AGN, making the AGN signatures questionable. The next step with my simulations, would be to predict the number of BHs in LBGs, and to estimate the optical and X-ray signal over star formation rate, using theoretical spectra (Feltre, Charlot & Gutkin, 2016). It will certainly help

us to understand why AGN have not been observed (yet?) in LBGs. BHs in these galaxies could be absent, or at least very faint and therefore not easily observable, as the BHs that remain at low mass in our simulations.

Over the last decade, the direct collapse BH formation model has become more popular, and subject of several investigations. This scenario is appealing, as it predicts the formation of massive BH seeds, of $\sim 10^4 - 10^6\,\mathrm{M}_\odot$ in the early Universe, thus helping explaining the presence of the billion solar mass BHs powering quasars at $z > 6$. In this thesis, we have studied the isothermal collapse variant of the DC model, which requires that the halo has reached the atomic cooling threshold, the absence of efficient coolants to avoid the fragmentation of the gas, and a large inflow rate at the center of the halo. This makes the formation of BH through this channel a rare event. To study the feasibility of the DC model, we have developed a hybrid model, which combines a model to compute the radiation intensity seen by every halos, and hydrodynamical simulations (taking advantage of the self-consistent evolution of metallicity, halo history, halo spatial distribution). We have performed a set of simulations with a large range of simulation box sizes, and resolutions, that allowed us to investigate different aspects of the scenario: the number density of direct collapse regions, but also the properties of these regions (host halo mass, metallicity and metal-enrichment of halos, clustering of the regions) and the impact of SN feedback. DCBH regions are identified by computing the local varying radiation intensity, following (Agarwal et al., 2012), and by verifying the conditions required by the theoretical model.

We found that SN feedback has a crucial role in the stellar formation and in the spread of metals by SNe, and that it strongly impacts the number of regions eligible as DCBH sites. With our strong implementation of SN feedback no DCBH region are identified in the 10 cMpc box length simulation, 3 candidates are identified with the weak SN feedback. Metal pollution of halos is therefore crucial, as well as the radiation intensity needed to maintain a sufficiently low molecular hydrogen fraction in order to avoid the fragmentation of the gas. The large scale state-of-the-art cosmological simulation Horizon-noAGN offered us the possibility of discussing the feasibility of the DC model in a more global fashion, at the expense of resolution. It allowed us to explore a larger range of critical radiation intensity values ($\mathrm{J}_{\mathrm{crit}} = 30, 100, 300$). The main point here was to understand if the population of high redshift quasars that we observe at $z = 6$ could have been powered by DCBHs. We found that slightly less than a third of halos more massive than $10^{11}\,\mathrm{M}_\odot$ at $z = 6$, have a high redshift progenitor eligible for the DCBH process, considering $\mathrm{J}_{\mathrm{crit}} = 30$. However, the number of halos at $z = 6$, which could host a DCBH, drops significantly if we consider higher radiation intensity ($\mathrm{J}_{\mathrm{crit}} = 100, 300$).
We can summarize our results by saying that if the DC model requires halos to be illuminated by high radiation intensity of $J_{\mathrm{crit}} = 300$, the number of DCBHs may perhaps be sufficient to explain the population of high redshift quasars, but not the presence of DCBHs in normal galaxies. However, if less radiation intensity is required ($\mathrm{J}_{\mathrm{crit}} = 30$), and under the assumption of weak SN feedback, then DCBHs could be common in normal galaxies.

One caveat of the hybrid models today, is that the analysis of the LW radiation distribution is done in post-processing, and BHs are actually not formed on-the-fly in the simulation. One can not follow these BHs over time self-consistently within the simulation. We are planning to implement in the code Ramses the DC scenario, based on the same properties as for the present post-processing study. This will require a larger simulation box, and a better dark matter resolution. We will be able to study what is missing in hybrid models, namely the growth of DCBHs, their clustering/spatial distribution, but also their feedback on their host galaxies, and

the properties of these host galaxies. This will give us crucial clues on whether the DC model can reproduce/probe the population of high redshift quasars, and in normal galaxies, and how they evolve through cosmic time.

In the last part of this thesis, we have addressed the impact of changing the cosmology on BH formation and growth. The *Planck* mission recently provided unprecedented accuracy of the estimated cosmological parameters, and of the local non-Gaussian parameter $f_{\rm NL}$, which describes the deviation of initial density perturbations to a Gaussian distribution. *Planck* has, however, focused on large scales, mapping the CMB on the full sky, and therefore considered primordial density perturbations on the scale of clusters. However, some inflationary models predict non-Gaussianities on smaller scales, beyond the reach of CMB measurements.

In this thesis, we investigated the presence of non-Gaussinities on galactic scales, by running 5 different simulations, with either Gaussian or scale-dependent non-Gaussian initial conditions, all consistent with *Planck*'s constraints at large scales. The presence of non-Gaussianities on galactic scales lead to the formation of more low-mass dark matter halos, this enhancement propagates to the galaxy mass function, with an increase at the low-mass end of the distribution. The enhancement in the halo and galaxy mass function, depends on the prescription of the parameter $f_{\rm NL}$ (in normalization and slope). The enhancement is small, but eventually detectable, it reaches 0.3 dex in the low-mass end of the galaxy luminosity function at $z = 10$. We have shown that the presence of these non-Gaussianities also have strong consequences on the reionization history of the Universe: the ionized fraction of the Universe is higher compared to the simulation with Gaussian initial conditions, at the same redshift. Because of the large uncertainties of different parameters, and the difficulty to accurately model them, such as the escape fraction or the far-UV magnitude limit, we cannot easily favour or rule out a cosmology including non-Gaussian primordial fluctuations. For example, all our models fit within the uncertainty of *Planck*'s Thomson scattering measurement.

We have also used our set of numerical simulations to investigate the formation of BHs through the PopIII remnants and the DC models. For the DC model, we modeled the local varying radiation intensity, combined with theoretical predictions of the scenario, to compute the number of eligible regions for the DC model. We found that the increase in the halo clustering, led to an enhancement in the number of DCBH regions by a factor of 2. Recent improvements on the DC BH formation model tend to conclude that this model is very rare. For example, the impact of X-rays could significantly decrease the number density of BHs (Inayoshi & Omukai, 2011 ; Latif et al., 2015). The presence of non-Gaussianities seems, instead, to boost the feasibility of the model (see also Hirano et al., 2015 ; Sherkatghanad & Brandenberger, 2015). Similarly, for the PopIII remnants model, we found that the presence of primordial non-Gaussianities boosts the number density of BHs by one order of magnitude at high redshift. However, the BH number density in the Gaussian simulation catches up with the non-Gaussian one at later times, and erase the difference in the BH formation. PopIII remnant BHs form in metal-poor regions, and in the non-Gaussian simulation the probability for a halo to be polluted is larger due to the higher number of progenitors. The occupation fraction in the Gaussian and non-Gaussian simulations remain the same for both BH formation scenarios. We found that non-Gaussianities also impact BH growth, indeed the mean mass of BHs in the non-Gaussian simulations and the number of the most massive BHs at $z = 6.5$ are both increased by a factor 2, which may be considered helpful in explaining how billion solar masses BHs got in place by $z \sim 6 - 7$.

Appendix A

Monitorat at Palais de la Découverte

During my PhD, I also worked at the *Palais de la Découverte*, which is the museum of science in Paris. The museum was built in the 1930s, with the main goal of making science available for everyone. For this purpose, permanent expositions are presented in different fields, such as astrophysics, biology, mathematics, but also temporary expositions, where scientists are asked to explain their current research, or the upcoming spatial missions, for example. For three years, I gave conferences on supermassive black holes every week end, for a large audience from children to senior people. I also wrote two publications for the review *Découverte* of the museum, which are listed below.

List of publications

- *Les trous noirs: monstres massifs de l'Univers*
  Habouzit, M.
  2016, *Découverte* N399
- *Les ondes gravitationnelles: le cas GW150914*
  Habouzit, M.
  2016, *Découverte* N407

Fig. A.1 – Palais de la Découverte - Paris museum of science.

Fig. A.2 – Cover of the magazine *Découverte* N399.

List of Figures

List of Tables

List of Publications

Valiante, R., Agarwal, B., Habouzit, M., Pezzulli, E.
High redshift supermassive black hole formation models
2016, PASA review, submitted

Habouzit, M., Volonteri, M., Dubois, Y.
Blossoms from black hole seeds: properties and early growth regulated by supernova feedback
2016, arXiv:1605.09394

Latif, M. A., Omukai, K., Habouzit, M., Schleicher, D. R. G., Volonteri, M.
Impact of dust cooling on direct collapse black hole formation
2016, ApJ, 823, 40

Habouzit, M., Volonteri, M., Latif, M., Nishimichi, T., Peirani, S., Dubois, Y., Mamon, G.A., Silk, J., Chevallard, J.
Black hole formation and growth with non-Gaussian primordial density perturbations
2016, MNRAS, 456, 1901

Habouzit, M., Volonteri, M., Latif, M., Dubois, Y., Peirani, S.
On the number density of "direct collapse" black hole seeds
2016, MNRAS, 463, 529

Volonteri, M., Habouzit, M., Pacucci, F., Tremmel, M.
The evolution of high-redshift massive black holes
2015, arXiv:1511.02588 - Proceeding

Chevallard, J., Silk, J., Nishimichi, T., Habouzit, M., Mamon, G.A., Peirani, S.
Effect of primordial non-Gaussianities on the far-UV luminosity function of high-redshift galaxies: implications for cosmic reionization
2015, MNRAS, 446, 3235

Habouzit, M., Nishimichi, T., Peirani, S., Mamon, G.A., Silk, J., Chevallard, J.
Testing primordial non-Gaussianities on galactic scales at high redshift
2014, MNRAS, 445, L129

Bibliography

Abel T., Bryan G. L., Norman M. L., 2002, Science, 295, 93

Abramowicz M. A., 2005, in Growing Black Holes: Accretion in a Cosmological Context, Merloni A., Nayakshin S., Sunyaev R. A., eds., pp. 257–273

Abramowicz M. A., Czerny B., Lasota J. P., Szuszkiewicz E., 1988, ApJ, 332, 646

Abramowicz M. A., Lasota J.-P., 1995, Comments on Astrophysics, 18, 141

Acquaviva V., Bartolo N., Matarrese S., Riotto A., 2003, Nuclear Physics B, 667, 119

Ade P. A. R., et al., 2015

Agarwal B., Dalla Vecchia C., Johnson J. L., Khochfar S., Paardekooper J.-P., 2014, MNRAS, 443, 648

Agarwal B., Johnson J. L., Zackrisson E., Labbe I., van den Bosch F. C., Natarajan P., Khochfar S., 2015a, ArXiv e-prints, arXiv: 1510.01733

Agarwal B., Khochfar S., 2015, MNRAS, 446, 160

Agarwal B., Khochfar S., Johnson J. L., Neistein E., Dalla Vecchia C., Livio M., 2012, MNRAS, 425, 2854

Agarwal B., Smith B., Glover S., Natarajan P., Khochfar S., 2015b, ArXiv e-prints

Ahn K., Shapiro P. R., Iliev I. T., Mellema G., Pen U.-L., 2008, AIP Conf.Proc., 990, 374

Aird J. et al., 2013, ArXiv:1306.2325

Albrecht A., Steinhardt P. J., 1982, Physical Review Letters, 48, 1220

Alishahiha M., Silverstein E., Tong D., 2004, Phys. Rev. D, 70, 123505

Alvarez M. A., Wise J. H., Abel T., 2009, ApJ, 701, L133

Arkani-Hamed N., Creminelli P., Mukohyama S., Zaldarriaga M., 2004, J. Cosmology Astropart. Phys., 4, 001

Assef R. J. et al., 2013, ApJ, 772, 26

Aubert D., Pichon C., Colombi S., 2004, MNRAS, 352, 376

Baldassare V. F., Reines A. E., Gallo E., Greene J. E., 2015, ApJ, 809, L14

Baldwin J. A., Phillips M. M., Terlevich R., 1981, PASP, 93, 5

Ball W. H., Tout C. A., Żytkow A. N., Eldridge J. J., 2011, MNRAS, 414, 2751

Barnes J. E., Hernquist L., 1996, ApJ, 471, 115

Barnes J. E., Hernquist L. E., 1991, ApJ, 370, L65

Barth A. J., Greene J. E., Ho L. C., 2008, AJ, 136, 1179

Barth A. J., Ho L. C., Rutledge R. E., Sargent W. L. W., 2004, ApJ, 607, 90

Barth A. J., Strigari L. E., Bentz M. C., Greene J. E., Ho L. C., 2009, ApJ, 690, 1031

Bartolo N., Komatsu E., Matarrese S., Riotto A., 2004, Phys. Rep., 402, 103

Becker A., Huterer D., Kadota K., 2011, J. Cosmology Astropart. Phys., 1, 6

Becker R. H. et al., 2001, AJ, 122, 2850

Begelman M. C., 2004, Coevolution of Black Holes and Galaxies, 374

Begelman M. C., 2010, MNRAS, 402, 673

Begelman M. C., Cioffi D. F., 1989, ApJ, 345, L21

Begelman M. C., Rossi E. M., Armitage P. J., 2008, Mon.Not.Roy.Astron.Soc., 387, 1649

Begelman M. C., Shlosman I., 2009, ApJ, 702, L5

Begelman M. C., Volonteri M., Rees M. J., 2006, MNRAS, 370, 289

Behroozi P. S., Conroy C., Wechsler R. H., 2010, ApJ, 717, 379

Behroozi P. S., Wechsler R. H., Conroy C., 2013, ApJ, 770, 57

Belczynski K., Dominik M., Bulik T., O'Shaughnessy R., Fryer C., Holz D. E., 2010, ApJ, 715, L138

Bellovary J., Volonteri M., Governato F., Shen S., Quinn T., Wadsley J., 2011, ArXiv e-prints

Bennett C. L. et al., 1996, ApJ, 464, L1

Bieri R., Dubois Y., Silk J., Mamon G. A., Gaibler V., 2016, MNRAS, 455, 4166

Binney J., Tremaine S., 2008, Galactic Dynamics: Second Edition. Galactic Dynamics: Second Edition, by James Binney and Scott Tremaine. ISBN 978-0-691-13026-2 (HB). Published by Princeton University Press, Princeton, NJ USA, 2008.

Bleuler A., Teyssier R., 2014, MNRAS, 445, 4015

Booth C. M., Schaye J., 2009, MNRAS, 398, 53

Bouwens R. J., Illingworth G. D., 2006, Nature, 443, 189

Bouwens R. J. et al., 2015, ApJ, 803, 34

Bromm V., 2013, Reports on Progress in Physics, 76, 112901

Bromm V., Ferrara A., Coppi P. S., Larson R. B., 2001, MNRAS, 328, 969

Bromm V., Kudritzki R. P., Loeb A., 2001, ApJ, 552, 464

Bromm V., Loeb A., 2003, ApJ, 596, 34

Bromm V., Yoshida N., 2011, ARA&A, 49, 373

Bruzual G., Charlot S., 2003, Mon.Not.Roy.Astron.Soc., 344, 1000

Buchner J. et al., 2015, ApJ, 802, 89

Cappelluti N. et al., 2016, ApJ, 823, 95

Carr B. J., 2003, in Lecture Notes in Physics, Berlin Springer Verlag, Vol. 631, Quantum Gravity: From Theory to Experimental Search, Giulini D., Kiefer C., Laemmerzahl C., eds., pp. 301–321

Carr B. J., Bond J. R., Arnett W. D., 1984, ApJ, 277, 445

Cattaneo A., Mamon G. A., Warnick K., Knebe A., 2011, A&A, 533, A5

Cazaux S., Spaans M., 2009, A&A, 496, 365

Chabrier G., 2003, PASP, 115, 763

Chen X., 2005, Phys. Rev. D, 72, 123518

Chevallard J., Silk J., Nishimichi T., Habouzit M., Mamon G. A., et al., 2015, Mon.Not.Roy.Astron.Soc., 446, 3235

Chon S., Hirano S., Hosokawa T., Yoshida N., 2016, ArXiv e-prints

Churazov E., Sazonov S., Sunyaev R., Forman W., Jones C., Böhringer H., 2005, MNRAS, 363, L91

Civano F. et al., 2015, ApJ, 808, 185

Collin S., Boisson C., Mouchet M., Dumont A.-M., Coupé S., Porquet D., Rokaki E., 2002, A&A, 388, 771

Courant R., Friedrichs K., Lewy H., 1967, IBM Journal of Research and Development, 11, 215

Courty S., Alimi J. M., 2004, A&A, 416, 875

Crocce M., Pueblas S., Scoccimarro R., 2006, MNRAS, 373, 369

Crociani D., Moscardini L., Viel M., Matarrese S., 2009, MNRAS, 394, 133

Dalal N., Doré O., Huterer D., Shirokov A., 2008, Phys. Rev. D, 77, 123514

Desjacques V., Seljak U., Iliev I. T., 2009, MNRAS, 396, 85

Devecchi B., Volonteri M., 2009, ApJ, 694, 302

Devecchi B., Volonteri M., Rossi E. M., Colpi M., Portegies Zwart S., 2012, MNRAS, 421, 1465

Di Matteo T., Colberg J., Springel V., Hernquist L., Sijacki D., 2008, ApJ, 676, 33

Di Matteo T., Khandai N., DeGraf C., Feng Y., Croft R. A. C., Lopez J., Springel V., 2012, ApJ, 745, L29

Di Matteo T., Springel V., Hernquist L., 2005, Nature, 433, 604

Dicke R. H., Peebles P. J. E., Roll P. G., Wilkinson D. T., 1965, ApJ, 142, 414

Dijkstra M., Ferrara A., Mesinger A., 2014, MNRAS, 442, 2036

Dijkstra M., Haiman Z., Mesinger A., Wyithe J. S. B., 2008, MNRAS, 391, 1961

Djorgovski S. G., Castro S., Stern D., Mahabal A. A., 2001, ApJ, 560, L5

Dong R., Greene J. E., Ho L. C., 2012, ApJ, 761, 73

Dong X.-B., Ho L. C., Yuan W., Wang T.-G., Fan X., Zhou H., Jiang N., 2012, ApJ, 755, 167

Dubois Y., Devriendt J., Slyz A., Teyssier R., 2010, MNRAS, 409, 985

Dubois Y., Devriendt J., Slyz A., Teyssier R., 2012a, MNRAS, 420, 2662

Dubois Y., Devriendt J., Teyssier R., Slyz A., 2011, MNRAS, 417, 1853

Dubois Y., Pichon C., Haehnelt M., Kimm T., Slyz A., Devriendt J., Pogosyan D., 2012b, MNRAS, 423, 3616

Dubois Y. et al., 2014, MNRAS, 444, 1453

Dubois Y., Teyssier R., 2008, A&A, 477, 79

Dubois Y., Volonteri M., Silk J., 2014, MNRAS, 440, 1590

Dubois Y., Volonteri M., Silk J., Devriendt J., Slyz A., Teyssier R., 2015, MNRAS, 452, 1502

Dvali G., Gruzinov A., Zaldarriaga M., 2004, Phys. Rev. D, 69, 083505

Edri H., Rafter S. E., Chelouche D., Kaspi S., Behar E., 2012, ApJ, 756, 73

Eisenstein D. J., Loeb A., 1995, ApJ, 443, 11

Enqvist K., Sloth M. S., 2002, Nuclear Physics B, 626, 395

Fabian A. C., 1999, MNRAS, 308, L39

Fabian A. C., Iwasawa K., 1999, MNRAS, 303, L34

Fabian A. C., Sanders J. S., Taylor G. B., Allen S. W., Crawford C. S., Johnstone R. M., Iwasawa K., 2006, MNRAS, 366, 417

Fan X., 2006, New A Rev., 50, 665

Fan X., Narayanan V. K., Strauss M. A., White R. L., Becker R. H., Pentericci L., Rix H.-W., 2002, AJ, 123, 1247

Fan X. et al., 2006a, AJ, 132, 117

Fan X., Strauss M. A., Richards G. T., Hennawi J. F., Becker R. H., White R. L., Diamond-Stanic A. M., 2006b, AJ, 131, 1203

Fan X., Strauss M. A., Schneider D. P., Becker R. H., White R. L., Haiman Z., Gregg M., 2003, AJ, 125, 1649

Fan X. e. a., 2001, AJ, 121, 54

Feltre A., Charlot S., Gutkin J., 2016, MNRAS, 456, 3354

Ferrarese L., 2002, ApJ, 578, 90

Ferrarese L., Merritt D., 2000, ApJ, 539, L9

Filippenko A. V., Ho L. C., 2003, ApJ, 588, L13

Friedmann A., 1922, Zeitschrift fur Physik, 10, 377

Fryer C. L., Woosley S. E., Heger A., 2001, ApJ, 550, 372

Fryxell B. et al., 2000, ApJS, 131, 273

Gaibler V., Khochfar S., Krause M., Silk J., 2012, MNRAS, 425, 438

Gallo E., Treu T., Jacob J., Woo J.-H., Marshall P. J., Antonucci R., 2008, ApJ, 680, 154

Gallo E., Treu T., Marshall P. J., Woo J.-H., Leipski C., Antonucci R., 2010, ApJ, 714, 25

Gangui A., Lucchin F., Matarrese S., Mollerach S., 1994, ApJ, 430, 447

Gebhardt K. et al., 2000, ApJ, 539, L13

Gebhardt K. et al., 2001, AJ, 122, 2469

Gorski K. M., Banday A. J., Bennett C. L., Hinshaw G., Kogut A., Smoot G. F., Wright E. L., 1996, ApJ, 464, L11

Greene J. E., 2012, Nature Communications, 3, 1304

Greene J. E., Ho L. C., 2004, ApJ, 610, 722

Greene J. E., Ho L. C., 2005, ApJ, 630, 122

Greene J. E., Ho L. C., 2007a, ApJ, 670, 92

Greene J. E., Ho L. C., 2007b, ApJ, 667, 131

Greenstein J. L., 1963, Nature, 197, 1041

Greif T. H., 2015, Computational Astrophysics and Cosmology, 2, 3

Greif T. H., Bromm V., Clark P. C., Glover S. C. O., Smith R. J., Klessen R. S., Yoshida N., Springel V., 2012, MNRAS, 424, 399

Greif T. H., Johnson J. L., Klessen R. S., Bromm V., 2008, MNRAS, 387, 1021

Greif T. H., White S. D. M., Klessen R. S., Springel V., 2011, ApJ, 736, 147

Grossi M., Dolag K., Branchini E., Matarrese S., Moscardini L., 2007, MNRAS, 382, 1261

Grossi M., Verde L., Carbone C., Dolag K., Branchini E., Iannuzzi F., Matarrese S., Moscardini L., 2009, MNRAS, 398, 321

Guth A. H., 1981, Phys. Rev. D, 23, 347

Haardt F., Madau P., 1996, ApJ, 461, 20

Habouzit M., Nishimichi T., Peirani S., Mamon G. A., Silk J., et al., 2014, Mon.Not.Roy.Astron.Soc., 445, 129

Habouzit M., Volonteri M., Dubois Y., 2016, ArXiv:1605.09394

Habouzit M., Volonteri M., Latif M., Dubois Y., Peirani S., 2016a, MNRAS, 463, 529

Habouzit M. et al., 2016b, MNRAS, 456, 1901

Hahn O., Abel T., 2013, MUSIC: MUlti-Scale Initial Conditions. Astrophysics Source Code Library

Harrison E. R., 1970, Phys. Rev. D, 1, 2726

Hartwig T., Glover S. C. O., Klessen R. S., Latif M. A., Volonteri M., 2015, MNRAS, 452, 1233

Hartwig T. et al., 2016, MNRAS, 462, 2184

Hazard C., Mackey M. B., Shimmins A. J., 1963, Nature, 197, 1037

Heger A., Fryer C. L., Woosley S. E., Langer N., Hartmann D. H., 2003, ApJ, 591, 288

Herschel J. F. W., 1864, Philosophical Transactions of the Royal Society of London Series I, 154, 1

Hirano S., Hosokawa T., Yoshida N., Umeda H., Omukai K., Chiaki G., Yorke H. W., 2014, ApJ, 781, 60

Hirano S., Zhu N., Yoshida N., Spergel D., Yorke H. W., 2015

Hirschmann M., Naab T., Somerville R. S., Burkert A., Oser L., 2012a, MNRAS, 419, 3200

Hirschmann M., Somerville R. S., Naab T., Burkert A., 2012b, MNRAS, 426, 237

Hockney R. W., Eastwood J. W., 1981, Computer Simulation Using Particles

Hopkins P. F., Hernquist L., Cox T. J., Di Matteo T., Robertson B., Springel V., 2006, ApJs, 163, 1

Hopkins P. F., Richards G. T., Hernquist L., 2007, ApJ, 654, 731

Hosokawa T., Omukai K., Yorke H. W., 2012, ApJ, 756, 93

Hosokawa T., Yorke H. W., Inayoshi K., Omukai K., Yoshida N., 2013, ApJ, 778, 178

Hubble E., 1929, Proceedings of the National Academy of Science, 15, 168

Hubble E. P., 1925, The Observatory, 48, 139

Inayoshi K., Haiman Z., Ostriker J. P., 2016, MNRAS, 459, 3738

Inayoshi K., Omukai K., 2011, MNRAS, 416, 2748

Inayoshi K., Tanaka T. L., 2015, MNRAS, 450, 4350

Islam R. R., Taylor J. E., Silk J., 2003, MNRAS, 340, 647

Izotov Y. I., Guseva N. G., Fricke K. J., Henkel C., 2014, A&A, 561, A33

Jarrett T. H. et al., 2011, ApJ, 735, 112

Jia J., Ptak A., Heckman T. M., Overzier R. A., Hornschemeier A., LaMassa S. M., 2011a, ApJ, 731, 55

Jia J., Ptak A., Heckman T. M., Overzier R. A., Hornschemeier A., LaMassa S. M., 2011b, ApJ, 731, 55

Jiang L., et al.,, 2009, AJ, 138, 305

Johnson J. L., Bromm V., 2007, MNRAS, 374, 1557

Johnson J. L., Dalla Vecchia C., Khochfar S., 2013, MNRAS, 428, 1857

Johnson J. L., Whalen D. J., Agarwal B., Paardekooper J.-P., Khochfar S., 2014, Mon. Not. Roy. Astron. Soc., 445, 686

Johnson J. L., Whalen D. J., Fryer C. L., Li H., 2012, ApJ, 750, 66

Johnson J. L., Whalen D. J., Li H., Holz D. E., 2013, ApJ, 771, 116

Kang X., Norberg P., Silk J., 2007, MNRAS, 376, 343

Katz H., Sijacki D., Haehnelt M. G., 2015, ArXiv e-prints:1502.03448

Kauffmann G., Haehnelt M., 2000, MNRAS, 311, 576

Kimm T., Cen R., 2014, ApJ, 788, 121

Komatsu E. et al., 2003, ApJS, 148, 119

Komatsu E. et al., 2011, ApJS, 192, 18

Komatsu E., Spergel D. N., 2001, Phys. Rev. D, 63, 063002

Kormendy J., Bender R., 2011, Nature, 469, 377

Kormendy J., Ho L. C., 2013, ARA&A, 51, 511

Kormendy J., Richstone D., 1995, ARA&A, 33, 581

Koushiappas S. M., Bullock J. S., Dekel A., 2004, MNRAS, 354, 292

Kravtsov A. V., Klypin A. A., Khokhlov A. M., 1997, ApJS, 111, 73

Kuhlen M., Faucher-Giguère C.-A., 2012, MNRAS, 423, 862

Lam T. Y., Nishimichi T., Yoshida N., 2011, MNRAS, 414, 289

Latif M. A., Bovino S., Grassi T., Schleicher D. R. G., Spaans M., 2015, MNRAS, 446, 3163

Latif M. A., Niemeyer J. C., Schleicher D. R. G., 2014, MNRAS, 440, 2969

Latif M. A., Omukai K., Habouzit M., Schleicher D. R. G., Volonteri M., 2016, ApJ, 823, 40

Latif M. A., Schleicher D. R. G., Bovino S., Grassi T., Spaans M., 2014, ApJ, 792, 78

Latif M. A., Schleicher D. R. G., Schmidt W., Niemeyer J., 2013a, MNRAS, 433, 1607

Latif M. A., Schleicher D. R. G., Schmidt W., Niemeyer J., 2013b, ApJ, 772, L3

Latif M. A., Schleicher D. R. G., Spaans M., 2012, A&A, 540, A101

Latif M. A., Volonteri M., 2015, MNRAS, 452, 1026

Leavitt H. S., 1908, Annals of Harvard College Observatory, 60, 87

Lemaître G., 1927, Annales de la Societe Scientifique de Bruxelles, 47, 49

Lemons S. M., Reines A. E., Plotkin R. M., Gallo E., Greene J. E., 2015, ApJ, 805, 12

Lewis A., Challinor A., Lasenby A., 2000, ApJ, 538, 473

Linde A. D., 1982, Physics Letters B, 108, 389

Lodato G., Natarajan P., 2006, MNRAS, 371, 1813

Loeb A., Rasio F. A., 1994, ApJ, 432, 52

LoVerde M., Miller A., Shandera S., Verde L., 2008, J. Cosmology Astropart. Phys., 4, 14

Lupi A., Colpi M., Devecchi B., Galanti G., Volonteri M., 2014, MNRAS, 442, 3616

Lupi A., Haardt F., Dotti M., Fiacconi D., Mayer L., Madau P., 2016, MNRAS, 456, 2993

Lyth D. H., Wands D., 2002, Physics Letters B, 524, 5

Machacek M. E., Bryan G. L., Abel T., 2001, ApJ, 548, 509

Madau P., Ferrara A., Rees M. J., 2001, ApJ, 555, 92

Madau P., Haardt F., Dotti M., 2014, ApJ, 784, L38

Madau P., Rees M. J., 2001, ApJL, 551, L27

Magorrian J. et al., 1998, AJ, 115, 2285

Maio U., 2011, Classical and Quantum Gravity, 28, 225015

Maio U., Iannuzzi F., 2011, MNRAS, 415, 3021

Maio U., Khochfar S., 2012, MNRAS, 421, 1113

Maldacena J., 2003, Journal of High Energy Physics, 5, 13

Mapelli M., Colpi M., Zampieri L., 2009, MNRAS, 395, L71

Mapelli M., Zampieri L., Ripamonti E., Bressan A., 2013, MNRAS, 429, 2298

Marconi A., Hunt L. K., 2003, ApJ, 589, L21

Matarrese S., Verde L., Jimenez R., 2000, ApJ, 541, 10

Matthews T. A., Sandage A. R., 1963, ApJ, 138, 30

Mayer L., Fiacconi D., Bonoli S., Quinn T., Roskar R., Shen S., Wadsley J., 2014, ArXiv e-prints:1411.5683

Mayer L., Kazantzidis S., Escala A., Callegari S., 2010, Nature, 466, 1082

McConnell N. J., Ma C.-P., 2013, ApJ, 764, 184

McConnell N. J., Ma C.-P., Gebhardt K., Wright S. A., Murphy J. D., Lauer T. R., Graham J. R., Richstone D. O., 2011, Nature, 480, 215

McLure R. J., Dunlop J. S., 2001, MNRAS, 327, 199

Menon H., Wesolowski L., Zheng G., Jetley P., Kale L., Quinn T., Governato F., 2015, Computational Astrophysics and Cosmology, 2, 1

Menou K., Haiman Z., Narayanan V. K., 2001, ApJ, 558, 535

Merloni A., Heinz S., di Matteo T., 2003, MNRAS, 345, 1057

Merritt D., Ferrarese L., Joseph C. L., 2001, Science, 293, 1116

Messier C., 1781, Catalogue des Nebuleuses et des amas d'Etoiles (Catalog of Nebulae and Star Clusters). Tech. rep.

Mezcua M., Civano F., Fabbiano G., Miyaji T., Marchesi S., 2016, ApJ, 817, 20

Miller B., Gallo E., Treu T., Woo J.-H., 2012, ApJ, 747, 57

Miller B. P., Gallo E., Greene J. E., Kelly B. C., Treu T., Woo J.-H., Baldassare V., 2015, ApJ, 799, 98

Milosavljevic M., Bromm V., Couch S. M., Oh S. P., 2009, Astrophys. J., 698, 766

Milosavljević M., Couch S. M., Bromm V., 2009, ApJL, 696, L146

Mollerach S., 1990, Phys. Rev. D, 42, 313

Moran E. C., Shahinyan K., Sugarman H. R., Vélez D. O., Eracleous M., 2014, AJ, 148, 136

Mortlock D. J. et al., 2011, Nature, 474, 616

Mutch S. J., Croton D. J., Poole G. B., 2013, Mon.Not.Roy.Astron.Soc., 435, 2445

Naoz S., Yoshida N., Gnedin N. Y., 2013, ApJ, 763, 27

Nishimichi T., 2012, J. Cosmology Astropart. Phys., 8, 37

Nishimichi T. et al., 2009, PASJ, 61, 321

Nishimichi T., Taruya A., Koyama K., Sabiu C., 2010, J. Cosmology Astropart. Phys., 7, 2

Oh S. P., Haiman Z., 2002, ApJ, 569, 558

Oke J. B., 1963, Nature, 197, 1040

Omukai K., 2001, ApJ, 546, 635

Omukai K., Schneider R., Haiman Z., 2008, ApJ, 686, 801

Omukai K., Tsuribe T., Schneider R., Ferrara A., 2005, ApJ, 626, 627

O'Shea B. W., Bryan G., Bordner J., Norman M. L., Abel T., Harkness R., Kritsuk A., 2004, ArXiv Astrophysics e-prints 0403044

O'Shea B. W., Norman M. L., 2008, ApJ, 673, 14

Pace F., Maio U., 2014, MNRAS, 437, 1308

Pace F., Moscardini L., Bartelmann M., Branchini E., Dolag K., Grossi M., Matarrese S., 2011, MNRAS, 411, 595

Pacucci F., Ferrara A., Volonteri M., Dubus G., 2015, ArXiv e-prints

Pacucci F., Volonteri M., Ferrara A., 2015, MNRAS, 452, 1922

Palla F., Salpeter E. E., Stahler S. W., 1983, ApJ, 271, 632

Pallottini A., Ferrara A., Gallerani S., Salvadori S., D'Odorico V., 2014, MNRAS, 440, 2498

Pallottini A. et al., 2015

Pardo K. et al., 2016, ApJ, 831, 203

Park K., Ricotti M., 2011, ApJ, 739, 2

Peebles P. J. E., 1969, ApJ, 155, 393

Peebles P. J. E., Yu J. T., 1970, ApJ, 162, 815

Pelupessy F. I., Di Matteo T., Ciardi B., 2007, ApJ, 665, 107

Penzias A. A., Wilson R. W., 1965, ApJ, 142, 419

Perlmutter S. et al., 1999, ApJ, 517, 565

Peterson B. M. et al., 2005, ApJ, 632, 799

Pillepich A., Porciani C., Hahn O., 2010, MNRAS, 402, 191

Planck Collaboration et al., 2013a, arXiv:1303.5076

Planck Collaboration et al., 2013b, arXiv:1303.5084

Planck Collaboration et al., 2014, A&A, 571, A16

Planck Collaboration et al., 2015a, ArXiv:1502.01592

Planck Collaboration et al., 2011, A&A, 536, A1

Planck Collaboration et al., 2015b, ArXiv:1502.01589

Portegies Zwart S. F., Makino J., McMillan S. L. W., Hut P., 1999, A&A, 348, 117

Press W. H., Schechter P., 1974, ApJ, 187, 425

Rasera Y., Teyssier R., 2006, A&A, 445, 1

Redmount I. H., Rees M. J., 1989, Comments on Astrophysics, 14, 165

Rees M. J., 1978, The Observatory, 98, 210

Rees M. J., 1984, ARA&A, 22, 471

Rees M. J., 1989, MNRAS, 239, 1P

Regan J. A., Haehnelt M. G., 2009a, MNRAS, 396, 343

Regan J. A., Haehnelt M. G., 2009b, MNRAS, 393, 858

Regan J. A., Johansson P. H., Wise J. H., 2014, ApJ, 795, 137

Reines A. E., 2015, in American Astronomical Society Meeting Abstracts, Vol. 225, American Astronomical Society Meeting Abstracts, p. 320.07

Reines A. E., Deller A. T., 2012, ApJ, 750, L24

Reines A. E., Greene J. E., Geha M., 2013, ApJ, 775, 116

Reines A. E., Plotkin R. M., Russell T. D., Mezcua M., Condon J. J., Sivakoff G. R., Johnson K. E., 2014, ApJ, 787, L30

Reines A. E., Sivakoff G. R., Johnson K. E., Brogan C. L., 2011, Nature, 470, 66

Reines A. E., Volonteri M., 2015, ArXiv e-prints

Robertson B. E., Ellis R. S., Dunlop J. S., McLure R. J., Stark D. P., 2010, Nature, 468, 49

Robertson B. E. et al., 2013, ApJ, 768, 71

Schaerer D., 2002, A&A, 382, 28

Schauer A. T. P., Whalen D. J., Glover S. C. O., Klessen R. S., 2015, MNRAS, 454, 2441

Schleicher D. R. G., Palla F., Ferrara A., Galli D., Latif M., 2013, A&A, 558, A59

Schmidt M., 1963, Nature, 197, 1040

Schneider R., Ferrara A., Natarajan P., Omukai K., 2002, ApJ, 571, 30

Schneider R., Ferrara A., Salvaterra R., Omukai K., Bromm V., 2003, Nature, 422, 869

Schneider R., Omukai K., Inoue A. K., Ferrara A., 2006a, MNRAS, 369, 1437

Schneider R., Salvaterra R., Ferrara A., Ciardi B., 2006b, MNRAS, 369, 825

Schnittman J. D., 2007, ApJ, 667, L133

Schramm M. et al., 2013, ApJ, 773, 150

Scoccimarro R., 1998, MNRAS, 299, 1097

Sefusatti E., Crocce M., Desjacques V., 2010, MNRAS, 406, 1014

Seth A. C. et al., 2010, ApJ, 714, 713

Shakura N. I., Sunyaev R. A., 1973, A&A, 24, 337

Shandera S., Dalal N., Huterer D., 2011, J. Cosmology Astropart. Phys., 3, 17

Shang C., Bryan G. L., Haiman Z., 2010, MNRAS, 402, 1249

Sherkatghanad Z., Brandenberger R. H., 2015, ArXiv:1508.00968

Shih D. C., Iwasawa K., Fabian A. C., 2003, MNRAS, 341, 973

Shirasaki M., Yoshida N., Hamana T., Nishimichi T., 2012, ApJ, 760, 45

Shlosman I., Frank J., Begelman M. C., 1989, Nature, 338, 45

Sijacki D., Springel V., Haehnelt M. G., 2009, MNRAS, 400, 100

Sijacki D., Vogelsberger M., Genel S., Springel V., Torrey P., Snyder G. F., Nelson D., Hernquist L., 2015, MNRAS, 452, 575

Silk J., 2013, ApJ, 772, 112

Silk J., Mamon G. A., 2012, Research in Astronomy and Astrophysics, 12, 917

Silk J., Rees M. J., 1998, A&A, 331, L1

Silverstein E., Tong D., 2004, Phys. Rev. D, 70, 103505

Slipher V. M., 1917, Proceedings of the American Philosophical Society, 56, 403

Smith H. J., Hoffleit D., 1963, AJ, 68, 292

Smith K. M., Senatore L., Zaldarriaga M., 2009, J. Cosmology Astropart. Phys., 9, 006

Smoot G. F. et al., 1992, ApJ, 396, L1

Soltan A., 1982, MNRAS, 200, 115

Somerville R. S., Hopkins P. F., Cox T. J., Robertson B. E., Hernquist L., 2008, MNRAS, 391, 481

Spaans M., Silk J., 2006, ApJ, 652, 902

Spera M., Mapelli M., Bressan A., 2015, MNRAS, 451, 4086

Spergel D. N. et al., 2003, ApJS, 148, 175

Springel V., 2005, MNRAS, 364, 1105

Springel V., 2010, MNRAS, 401, 791

Springel V., Hernquist L., 2003, MNRAS, 339, 289

Springel V., Yoshida N., White S. D. M., 2001, New Astronomy, 6, 79

Stark D. P. et al., 2015, MNRAS, 454, 1393

Stern D. et al., 2012, ApJ, 753, 30

Stinson G., Seth A., Katz N., Wadsley J., Governato F., Quinn T., 2006, MNRAS, 373, 1074

Sugimura K., Omukai K., Inoue A. K., 2014, MNRAS, 445, 544

Sutherland R. S., Dopita M. A., 1993, ApJS, 88, 253

Tanaka T., Haiman Z., 2009, ApJ, 696, 1798

Tanaka T. L., 2014, Classical and Quantum Gravity, 31, 244005

Tanaka T. L., Li M., Haiman Z., 2013, MNRAS, 435, 3559

Taylor P., Kobayashi C., 2014, MNRAS, 442, 2751

Tegmark M., Silk J., Rees M. J., Blanchard A., Abel T., Palla F., 1997, ApJ, 474, 1

Teyssier R., 2002, A&A, 385, 337

Teyssier R., Moore B., Martizzi D., Dubois Y., Mayer L., 2011, MNRAS, 414, 195

Teyssier R., Pontzen A., Dubois Y., Read J. I., 2013, MNRAS, 429, 3068

Tornatore L., Ferrara A., Schneider R., 2007, MNRAS, 382, 945

Treister E., Schawinski K., Volonteri M., Natarajan P., 2013, ApJ, 778, 130

Tremaine S. et al., 2002, ApJ, 574, 740

Tremmel M., Governato F., Volonteri M., Quinn T. R., 2015, MNRAS, 451, 1868

Tweed D., Devriendt J., Blaizot J., Colombi S., Slyz A., 2009, A&A, 506, 647

Valageas P., Nishimichi T., 2011, A&A, 527, A87

Valiante R., Schneider R., Volonteri M., Omukai K., 2016, MNRAS, 457, 3356

Valluri M., Ferrarese L., Merritt D., Joseph C. L., 2005, ApJ, 628, 137

van Wassenhove S., Volonteri M., Walker M. G., Gair J. R., 2010, MNRAS, 408, 1139

Vink J. S., 2008, New A Rev., 52, 419

Visbal E., Haiman Z., Bryan G. L., 2014, MNRAS, 445, 1056

Volonteri M., 2010, A&AR, 18, 279

Volonteri M., Begelman M. C., 2010, MNRAS, 409, 1398

Volonteri M., Dubois Y., Pichon C., Devriendt J., 2016, MNRAS, 460, 2979

Volonteri M., Haardt F., Madau P., 2003, ApJ, 582, 559

Volonteri M., Lodato G., Natarajan P., 2008, MNRAS, 383, 1079

Volonteri M., Madau P., Haardt F., 2003, ApJ, 593, 661

Volonteri M., Natarajan P., 2009, MNRAS, 400, 1911

Volonteri M., Perna R., 2005, MNRAS, 358, 913

Volonteri M., Rees M. J., 2006, ApJ, 650, 669

Volonteri M., Silk J., Dubus G., 2015, ApJ, 804, 148

Volonteri M., Stark D. P., 2011, MNRAS, 417, 2085

Wadsley J. W., Stadel J., Quinn T., 2004, New Astronomy, 9, 137

Weigel A. K., Schawinski K., Treister E., Urry C. M., Koss M., Trakhtenbrot B., 2015, MNRAS, 448, 3167

White R. L., Becker R. H., Fan X., Strauss M. A., 2003, AJ, 126, 1

Willott C. J. et al., 2010a, AJ, 140, 546

Willott C. J. et al., 2007, AJ, 134, 2435

Willott C. J. et al., 2010b, AJ, 139, 906

Wise J. H., Demchenko V. G., Halicek M. T., Norman M. L., Turk M. J., Abel T., Smith B. D., 2014, MNRAS, 442, 2560

Wise J. H., Turk M. J., Abel T., 2008, ApJ, 682, 745

Wolcott-Green J., Haiman Z., Bryan G. L., 2011, MNRAS, 418, 838

Wrobel J. M., Ho L. C., 2006, ApJ, 646, L95

Yoo J., Miralda-Escudé J., 2004, ApJL, 614, L25

York D. G. et al., 2000, AJ, 120, 1579

Yoshida N., Bromm V., Hernquist L., 2004, ApJ, 605, 579

Yoshida N., Omukai K., Hernquist L., 2008, Science, 321, 669

Yu Q., Tremaine S., 2002, MNRAS, 335, 965

Yuan W., Zhou H., Dou L., Dong X.-B., Fan X., Wang T.-G., 2014, ApJ, 782, 55

Yungelson L. R., van den Heuvel E. P. J., Vink J. S., Portegies Zwart S. F., de Koter A., 2008, A&A, 477, 223

Zeldovich Y. B., 1972, MNRAS, 160, 1P

Zwicky F., 1933, Helvetica Physica Acta, 6, 110